AD

USAAMRDL TECHNICAL REPORT 71-73

INVESTIGATION OF BOUNDARY LAYERS AND TIP FLOWS OF HELICOPTER ROTOR BLADES

By

H. R. Velkoff
J. D. Hoffman
D. A. Blaser

MAY 1972

EUSTIS DIRECTORATE
U. S. ARMY AIR MOBILITY RESEARCH AND DEVELOPMENT LABORATORY
FORT EUSTIS, VIRGINIA

CONTRACT DAAJ02-69-C-0068
THE OHIO STATE UNIVERSITY
RESEARCH FOUNDATION
COLUMBUS, OHIO

DISCLAIMERS

The findings in this report are not to be construed as an official Department of the Army position unless so designated by other authorized documents.

When Government drawings, specifications, or other data are used for any purpose other than in connection with a definitely related Government procurement operation, the United States Government thereby incurs no responsibility nor any obligation whatsoever; and the fact that the Government may have formulated, furnished, or in any way supplied the said drawings, specifications, or other data is not to be regarded by implication or otherwise as in any manner licensing the holder or any other person or corporation, or conveying any rights or permission, to manufacture, use, or sell any patented invention that may in any way be related thereto.

Trade names cited in this report do not constitute an official endorsement or approval of the use of such commercial hardware or software.

DISPOSITION INSTRUCTIONS

Destroy this report when no longer needed. Do not return it to the originator.

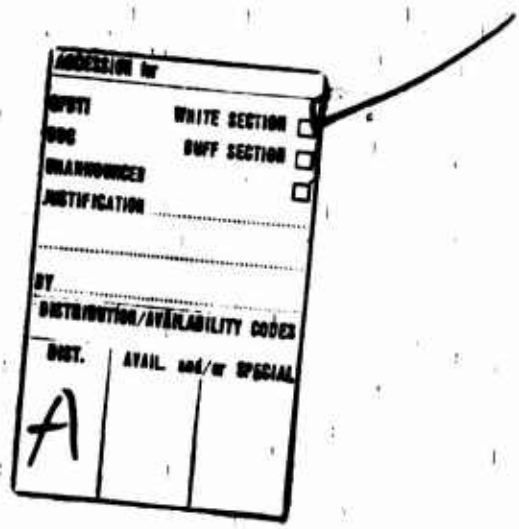

DEPARTMENT OF THE ARMY
U. S. ARMY AIR MOBILITY RESEARCH & DEVELOPMENT LABORATORY
EUSTIS DIRECTORATE
FORT EUSTIS, VIRGINIA 23604

This report has been reviewed by the Eustis Directorate, U. S. Army Air Mobility Research and Development Laboratory and is published for the exchange of information and the stimulation of ideas.

The purpose of this program was to conduct an experimental and analytical study on the nature of rotor blade boundary layers and flow over rotor blade tips in both hovering and forward flight conditions.

This program was under the technical management of Lt. Robert A. Booker, Mr. William T. Yeager, Jr., and Mr. Paul H. Mirick of the Aeromechanics Division of this Directorate.

ic

Task 1F162204A14234
Contract DAAJ02-69-C-0068
USAAMRDL Technical Report 71-73
May 1972

INVESTIGATION OF BOUNDARY LAYERS AND TIP FLOWS OF HELICOPTER ROTOR BLADES

Final Report

By

H. R. Velkoff
D. A. Blaser
J. D. Hoffman

Prepared by

The Ohio State University
Research Foundation
Columbus, Ohio

for

EUSTIS DIRECTORATE
U. S. ARMY AIR MOBILITY RESEARCH AND DEVELOPMENT LABORATORY
FORT EUSTIS, VIRGINIA

ABSTRACT

An experimental and analytical study was conducted on the nature of rotor blade boundary layers and flow over rotor blade tips. The experimental study of boundary layers was conducted using a model rotor and included both hovering and forward flight conditions. Flow visualization using an ammonia trace technique and hot-wire anemometry were used to determine the boundary layer flow. Both chordwise and spanwise velocity distributions were obtained through the boundary layer. Velocity profile data were obtained at selected chordwise and spanwise locations. The profiles obtained appeared to be consistent with boundary layer behavior. In hovering, the boundary layer flow in the vicinity of a separation bubble was mapped out.

The analytical phase of the study was based upon a three-dimensional application of the momentum-integral techniques of handling boundary layer analysis. The study was directed at the hovering condition and included consideration of NACA 0012 and NACA 0015 airfoils. The solutions obtained were found to agree quite well with a prior numerical analysis and to correlate reasonably well with the hot-wire data obtained from the experimental work.

The study of flow over the tip of a rotor blade used the ammonia trace technique. Five different tip shapes were tested in hover over a range of rotor speeds. Tests with the square shaped tip indicated the presence of secondary vortices at the end face of the rotor blade.

TABLE OF CONTENTS

		Page
ABSTRACT		iii
LIST OF ILLUSTRATIONS		vii
LIST OF SYMBOLS		xx
I	INTRODUCTION	1
	1.1 General Background Information	1
	1.2 Approach to the Boundary Layer Study in Hovering	2
	1.3 Approach to the Tip Vortex Study	3
	1.4 Approach to the Study of Boundary Layers in Forward Flight	
II	ANALYTICAL BOUNDARY LAYER STUDY--HOVER	4
	2.1 Introduction	4
	2.2 Method of Solution	12
	2.3 Potential Flow Solution	27
	2.4 Boundary Layer Results and Discussion	37
III	EXPERIMENTAL STUDIES OF ROTOR BOUNDARY LAYERS--HOVER	59
	3.1 Testing Equipment	59
	3.2 Calibration Systems	74
	3.3 Testing Procedures	90
	3.4 Test Results and Discussion	96
IV	COMPARISON OF ANALYSIS AND EXPERIMENTS--HOVER	108
V	TIP FLOW STUDY--HOVER	116
	5.1 Background	116
	5.2 Experimental Program	117
	5.3 Results	128
	5.4 Discussion of Results of Tip Study	177
VI	EXPERIMENTAL BOUNDARY LAYER STUDY--FORWARD FLIGHT	187
	6.1 Testing Equipment	187
	6.2 Calibration Systems	188
	6.3 Testing Procedure	194
	6.4 Test Results and Discussion	195
VII	CONCLUSIONS AND RECOMMENDATIONS	213
	7.1 Conclusions	213
	7.2 Recommendations	214

TABLE OF CONTENTS (Continued)

		Page
LITERATURE CITED		216
APPENDIXES		
I	CALIBRATION OF THE HOT-WIRE FLOW JET	219
II	ADDITIONAL AMMONIA TRACE DATA--HOVER CONDITION . . .	224
III	ADDITIONAL HOT-WIRE VELOCITY DATA--HOVER CONDITION .	231
IV	EVALUATION OF ACCURACY OF HOT-WIRE DATA.	243
V	TIP SHAPES	245
DISTRIBUTION		251

LIST OF ILLUSTRATIONS

Figure		Page
1	Coordinate Systems	7
2	Chordwise or Primary Flow	8
3	Spanwise or Secondary Flow	8
4	Calculation Grid Network	21
5	Variation of the Parameter Δ on a Flat Plate	23
6	Stability of Numerical Technique Near the Stagnation Line of an NACA 0012 Airfoil	26
7	Chordwise Potential Flow for an NACA 0012 Airfoil at Zero Lift	32
8	Surface Geometry for an NACA 0012 Airfoil	32
9	Chordwise Potential Flow for an NACA 0015 Airfoil at Zero Lift	36
10	Surface Geometry for an NACA 0015 Airfoil	36
11	Lines of Similarity for a Rotating Flat Plate	39
12	Profile Parameter Variation for a Rotating Flat Plate	40
13	Pohlhausen Parameter Variation for a Rotating Flat Plate	41
14	Wall Shear Stress Parameter Variation for a Rotating Flat Plate	42
15	Chordwise Velocity Profiles for a Rotating Flat Plate	44
16	Spanwise Velocity Profiles for a Rotating Flat Plate	44
17	Comparison of Chordwise Profiles With Reference 11 for a Flat Plate	45
18	Comparison of Spanwise Profiles With Reference 11 for a Flat Plate	45

LIST OF ILLUSTRATIONS (Continued)

Figure		Page
19	Chordwise Shear Stress Variation for a Rotating Flat Plate	47
20	Ratio of Spanwise to Chordwise Wall Shear Stresses for a Rotating Flat Plate	48
21	Comparison of Separation Lines for a Linearly Decelerated Flow, Rotating and Nonrotating Cases	50
22	Comparison of Chordwise Velocity Profile With Reference 11 for an NACA 0012 Airfoil	52
23	Comparison of Spanwise Velocity Profile With Reference 11 for an NACA 0012 Airfoil	52
24	Comparison of Separation Lines With Reference 11 for an NACA 0012 Airfoil	54
25	Spanwise Distribution of Chordwise Shear on a Rotating NACA 0012 Airfoil	55
26	Chordwise Distribution of Chordwise Shear on a Rotating NACA 0012 Airfoil	55
27	Chordwise Velocity Profiles for an NACA 0015 Airfoil	57
28	Spanwise Velocity Profile for an NACA 0015 Airfoil	57
29	Comparison of Separation Lines for Rotating NACA 0012 and 0015 Airfoils	58
30	Hover Test Stand	60
31	Single-Blade Rotor on Hover Test Stand	61
32	Rotor Blade for Flow Visualization Studies	62
33	Pressure Transducer and Mounting Pad Assembly	64
34	Pressure Blade Showing Transducer Mounting Technique	66
35	Amplifier Package for Twelve Pressure Transducers	67

LIST OF ILLUSTRATIONS (Continued)

Figure		Page
36	Dual Constant-Temperature Anemometer Package	69
37	Anemometer Linearizer Unit	70
38	X-Configuration Hot-Wire Boundary Layer Probe	71
39	X-Configuration With About 40X Magnification.	72
40	Side View of X-Probe Showing Wire Spacing	73
41	V-Configuration With About 20X Magnification.	74
42	Pressure Transducer Calibration Chamber	76
43	Pressure Transducer Calibration Apparatus	77
44	Calibration Device for Pressure Transducers Mounted in Rotor Blade	78
45	Calibration of a Typical Pressure Transducer	79
46	Hot-Wire Calibration Device	81
47	V-Configuration Hot-Wire Probe Geometry	82
48	V-DIRECTION Versus V-MAGNITUDE	85
49	V-MAGNITUDE Versus Wire Reynolds Number	86
50	V-DIRECTION Versus Probe Body Angle	87
51	V-MAGNITUDE Versus Probe Body Angle	88
52	V-DIRECTION Versus Wire Reynolds Number	89
53	Ammonia Feed Apparatus for Visualization Tests	92
54	Hot-Wire Probe Mounted on Rotor Blade as Viewed From the Blade Tip	93
55	Hot-Wire Probe Mounted on Rotor Blade as Viewed From the Leading Edge	94
56	Traversing Microscope Attached to Rotor Blade During Probe Height Measurement	95

LIST OF ILLUSTRATIONS (Continued)

Figure		Page
57	Ammonia Trace Data; θ = 12°, 250 rpm	97
58	Ammonia Trace Data; θ = 12°, 700 rpm	98
59	Ammonia Trace Data; θ = 12°, 990 rpm	99
60	Surface Static Pressure Data at 70% Radius	101
61	Surface Static Pressure Data at 93% Radius	102
62	Velocity Data at 72% Radius, θ = 10°, and 100 rpm . . .	104
63	Velocity Data at 72% Radius, θ = 10°, and 400 rpm . . .	105
64	Location of Hot-Wire Data on Rotor Blade	108
65	Chordwise Profiles on an NACA 0012 at x/c = 0.115 and z/c = 3.87	110
66	Chordwise Profiles on an NACA 0012 at x/c = 0.165 and z/c = 3.87	110
67	Chordwise Profiles on an NACA 0012 at x/c = 0.215 and z/c = 3.87	111
68	Chordwise Profiles on an NACA 0012 at x/c = 0.265 and z/c = 3.87	111
69	Chordwise Profiles on an NACA 0012 at x/c = 0.165 and z/c = 4.92	112
70	Chordwise Profiles on an NACA 0012 at x/c = 0.265 and z/c = 4.92	112
71	Spanwise Profiles on an NACA 0012 at x/c = 0.115 and z/c = 3.87	113
72	Approximate Potential Streamlines on a Rotating NACA 0012 Airfoil Near the Leading Edge	115
73	Pulleys and Belts at Base of Rotor Shaft	119
74	Torque Measuring Device	119
75	Thrust Measuring Device	120

UNCLASSIFIED

Security Classification

DOCUMENT CONTROL DATA - R & D

(Security classification of title, body of abstract and indexing annotation must be entered when the overall report is classified)

1 ORIGINATING ACTIVITY (Corporate author) The Ohio State University Research Foundation 1314 Kinnear Road, Columbus, Ohio	2a. REPORT SECURITY CLASSIFICATION Unclassified 2b. GROUP N/A

3 REPORT TITLE

INVESTIGATION OF BOUNDARY LAYERS AND TIP FLOWS OF HELICOPTER ROTOR BLADES

4 DESCRIPTIVE NOTES (Type of report and inclusive dates)

Final April 15, 1969 - June 15, 1971

5 AUTHOR(S) (First name, middle initial, last name)

Henry R. Velkoff, Dwight A. Blaser, John D. Hoffman

6 REPORT DATE May 1972	7a. TOTAL NO. OF PAGES 275	7b. NO. OF REFS 37
8a. CONTRACT OR GRANT NO DAAJ02-69-C-0068 b. PROJECT NO c. Task 1F162204A14234 d.	9a. ORIGINATOR'S REPORT NUMBER(S) USAAMRDL Technical Report 71-73 9b. OTHER REPORT NO(S) (Any other numbers that may be assigned this report)	

10 DISTRIBUTION STATEMENT

Approved for public release; distribution unlimited.

11 SUPPLEMENTARY NOTES	12. SPONSORING MILITARY ACTIVITY Eustis Directorate U. S. Army Air Mobility Research & Development Laboratory, Fort Eustis, Va.

13 ABSTRACT

An experimental and analytical study was conducted on the nature of rotor blade boundary layers and flow over rotor blade tips. The experimental study of boundary layers was conducted using a model rotor and included both hovering and forward flight conditions. Flow visualization using an ammonia trace technique and hot-wire anemometry were used to determine the boundary layer flow. Both chordwise and spanwise velocity distributions were obtained through the boundary layer. Velocity profile data were obtained at selected chordwise and spanwise locations. The profiles obtained appeared to be consistent with boundary layer behavior. In hovering, the boundary layer flow in the vicinity of a separation bubble was mapped out.

The analytical phase of the study was based upon a three-dimensional application of the momentum-integral techniques of handling boundary layer analysis. The study was directed at the hovering condition and included consideration of NACA 0012 and NACA 0015 airfoils. The solutions obtained were found to agree quite well with a prior numerical analysis and to correlate reasonably well with the hot-wire data obtained from the experimental work.

The study of flow over the tip of a rotor blade used the ammonia trace technique. Five different tip shapes were tested in hover over a range of rotor speeds. Tests with the square-shaped tip indicated the presence of secondary vortices at the end face of the rotor blade.

DD FORM 1 NOV 68 1473

UNCLASSIFIED

Security Classification

14 KEY WORDS	LINK A		LINK B		LINK C	
	ROLE	WT	ROLE	WT	ROLE	WT
Rotor blade						
Boundary layers						
Hovering						
Hot-wire anemometry						
Ammonia trace technique						
Blade tips						

6268-72

LIST OF ILLUSTRATIONS (Continued)

Figure		Page
76	Thrust Ring and Strain Gages	120
77	Ammonia Transfer Ring	121
78	Blade With Tip Removed	122
79	Top View of Square Tip (No. 1)	122
80	End View of Square Tip (No. 1)	123
81	Top View of Standard Tip (No. 2)	123
82	End View of Standard Tip (No. 2)	124
83	Top View of Swept-Aft Tip (No. 3)	124
84	Top View of Trapezoidal Tip (No. 4)	126
85	Top View of Cusp Tip (No. 5)	126
86a	Top View of Square Tip at 400 rpm and 0° Pitch Angle	130
86b	Bottom View of Square Tip at 400 rpm and 0° Pitch Angle	130
86c	Top View of Square Tip at 400 rpm and 2° Pitch Angle	131
86d	Bottom View of Square Tip at 400 rpm and 2° Pitch Angle	131
86e	Top View of Square Tip at 400 rpm and 4° Pitch Angle	132
86f	Bottom View of Square Tip at 400 rpm and 4° Pitch Angle	132
86g	Top View of Square Tip at 400 rpm and 6° Pitch Angle	133
86h	Bottom View of Square Tip at 400 rpm and 6° Pitch Angle	133
86i	Top View of Square Tip at 400 rpm and 8° Pitch Angle	134

LIST OF ILLUSTRATIONS (Continued)

Figure		Page
86j	Bottom View of Square Tip at 400 rpm and 8° Pitch Angle	134
86k	Top View of Square Tip at 400 rpm and 10° Pitch Angle	135
86l	Bottom View of Square Tip at 400 rpm and 10° Pitch Angle	135
86m	Top View of Square Tip at 400 rpm and 12° Pitch Angle	136
86n	Bottom View of Square Tip at 400 rpm and 12° Pitch Angle	136
86o	Top View of Square Tip at 400 rpm and 14° Pitch Angle	137
86p	Bottom View of Square Tip at 400 rpm and 14° Pitch Angle	137
86q	Top View of Square Tip at 400 rpm and 16° Pitch Angle	138
86r	Bottom View of Square Tip at 400 rpm and 16° Pitch Angle	138
87	Point at Which Traces Change Direction From Inward to Outward on Upper Surface of Square Tip Versus Pitch Angle	139
88a	Top View of Square Tip at 500 rpm and 12° Pitch Angle	141
88b	Top View of Square Tip at 600 rpm and 12° Pitch Angle	141
89a	Top View of Standard Tip at 500 rpm and 0° Pitch Angle	142
89b	Bottom View of Standard Tip at 500 rpm and 0° Pitch Angle	142
89c	Top View of Standard Tip at 500 rpm and 4° Pitch Angle	143

LIST OF ILLUSTRATIONS (Continued)

Figure		Page
89d	Bottom View of Standard Tip at 500 rpm and 4° Pitch Angle	143
89e	Top View of Standard Tip at 500 rpm and 8° Pitch Angle	144
89f	Bottom View of Standard Tip at 500 rpm and 8° Pitch Angle	144
89g	Top View of Standard Tip at 500 rpm and 12° Pitch Angle	145
89h	Bottom View of Standard Tip at 500 rpm and 12° Pitch Angle	145
89i	Top View of Standard Tip at 500 rpm and 16° Pitch Angle	146
89j	Bottom View of Standard Tip at 500 rpm and 16° Pitch Angle	146
89k	Top View of Standard Tip at 500 rpm and 18° Pitch Angle	147
89l	Bottom View of Standard Tip at 500 rpm and 18° Pitch Angle	147
89m	End View of Standard Tip at 500 rpm and 18° Pitch Angle	148
90a	Top View of Standard Tip at 1000 rpm and 0° Pitch Angle	150
90b	Bottom View of Standard Tip at 1000 rpm and 0° Pitch Angle	150
90c	Top View of Standard Tip at 1000 rpm and 4° Pitch Angle	151
90d	Bottom View of Standard Tip at 1000 rpm and 4° Pitch Angle	151
90e	Top View of Standard Tip at 1000 rpm and 8° Pitch Angle	152
90f	Bottom View of Standard Tip at 1000 rpm and 8° Pitch Angle	152

LIST OF ILLUSTRATIONS (Continued)

Figure		Page
90g	Top View of Standard Tip at 1000 rpm and 12° Pitch Angle	153
90h	Bottom View of Standard Tip at 1000 rpm and 12° Pitch Angle	153
90i	Top View of Standard Tip at 1000 rpm and 16° Pitch Angle	154
90j	Bottom View of Standard Tip at 1000 rpm and 16° Pitch Angle	154
91a	Top View of Swept-Aft Tip at 500 rpm and 0° Pitch Angle	156
91b	Bottom View of Swept-Aft Tip at 500 rpm and 0° Pitch Angle	156
91c	Top View of Swept-Aft Tip at 500 rpm and 4° Pitch Angle	157
91d	Bottom View of Swept-Aft Tip at 500 rpm and 4° Pitch Angle	157
91e	Top View of Swept-Aft Tip at 500 rpm and 8° Pitch Angle	158
91f	Bottom View of Swept-Aft Tip at 500 rpm and 8° Pitch Angle	158
91g	Top View of Swept-Aft Tip at 500 rpm and 12° Pitch Angle	159
91h	Bottom View of Swept-Aft Tip at 500 rpm and 12° Pitch Angle	159
91i	Top View of Swept-Aft Tip at 500 rpm and 16° Pitch Angle	160
91j	Bottom View of Swept-Aft Tip at 500 rpm and 16° Pitch Angle	160
92a	Top View of Trapezoidal Tip at 500 rpm and 0° Pitch Angle	161
92b	Bottom View of Trapezoidal Tip at 500 rpm and 0° Pitch Angle	161

LIST OF ILLUSTRATIONS (Continued)

Figure		Page
92c	Top View of Trapezoidal Tip at 500 rpm and 4° Pitch Angle	162
92d	Bottom View of Trapezoidal Tip at 500 rpm and 4° Pitch Angle	162
92e	Top View of Trapezoidal Tip at 500 rpm and 8° Pitch Angle	163
92f	Bottom View of Trapezoidal Tip at 500 rpm and 8° Pitch Angle	163
92g	Top View of Trapezoidal Tip at 500 rpm and 12° Pitch Angle	164
92h	Bottom View of Trapezoidal Tip at 500 rpm and 12° Pitch Angle	164
92i	Top View of Trapezoidal Tip at 500 rpm and 16° Pitch Angle	165
92j	Bottom View of Trapezoidal Tip at 500 rpm and 16° Pitch Angle	165
93a	Top View of Cusp Tip at 500 rpm and 0° Pitch Angle	166
93b	Bottom View of Cusp Tip at 500 rpm and 0° Pitch Angle	166
93c	Top View of Cusp Tip at 500 rpm and 4° Pitch Angle	167
93d	Bottom View of Cusp Tip at 500 rpm and 4° Pitch Angle	167
93e	Top View of Cusp Tip at 500 rpm and 8° Pitch Angle	168
93f	Bottom View of Cusp Tip at 500 rpm and 8° Pitch Angle	168
93g	Top View of Cusp Tip at 500 rpm and 12° Pitch Angle	169
93h	Bottom View of Cusp Tip at 500 rpm and 12° Pitch Angle	169

LIST OF ILLUSTRATIONS (Continued)

Figure		Page
93i	Top View of Cusp Tip at 500 rpm and 16° Pitch Angle	170
93j	Bottom View of Cusp Tip at 500 rpm and 16° Pitch Angle	170
94a	Top View of 7-Inch-Chord Standard Tip at 500 rpm and 0° Pitch Angle	172
94b	Bottom View of 7-Inch-Chord Standard Tip at 500 rpm and 0° Pitch Angle	172
94c	Top View of 7-Inch-Chord Standard Tip at 500 rpm and 4° Pitch Angle	173
94d	Bottom View of 7-Inch-Chord Standard Tip at 500 rpm and 4° Pitch Angle	173
94e	Top View of 7-Inch-Chord Standard Tip at 500 rpm and 8° Pitch Angle	174
94f	Bottom View of 7-Inch-Chord Standard Tip at 500 rpm and 8° Pitch Angle	174
94g	Top View of 7-Inch-Chord Standard Tip at 500 rpm and 12° Pitch Angle	175
94h	Bottom View of 7-Inch-Chord Standard Tip at 500 rpm and 12° Pitch Angle	175
94i	Top View of 7-Inch-Chord Standard Tip at 500 rpm and 16° Pitch Angle	176
94j	Bottom View of 7-Inch-Chord Standard Tip at 500 rpm and 16° Pitch Angle	176
95a	C_T Versus C_Q for Square Tip	178
95b	C_T Versus C_Q for Standard Tip	179
95c	C_T Versus C_Q for Swept-Aft Tip	180
95d	C_T Versus C_Q for Trapezoidal Tip	181
95e	C_T Versus C_Q for Cusp Tip	182

LIST OF ILLUSTRATIONS (Continued)

Figure		Page
96	Sketch of Flow Patterns Around Square Tip	183
97	Sketch of Flow Patterns Around Standard Tip	185
98	Flow Channel Used for Forward Flight Simulation Tests	187
99	Ammonia Pulse Valve Used in Forward Flight Visualization Tests	189
100	Pulse Duration Versus Supply Pressure.	191
101	Delay Time Versus Distance from Valve to Hole	192
102	Typical Shape of the Pulse During Calibration	193
103	Test Equipment Used During the Forward Flight Hot-Wire Velocity Measurements	196
104	Ammonia Traces at 400 rpm, $\mu = 0.3$, $C_{\ell_m} = 0.5$, and $\psi = 180°$	197
105	Velocity Magnitude Versus Azimuth for 15% Chord, 63% Radius, and $\mu = 0.2$	200
106	Outflow Angle Versus Azimuth for 15% Chord, 63% Radius, and $\mu = 0.2$	201
107	Velocity Data at 63% Radius, 15% Chord, and $\mu = 0.2$	203
108	Velocity Data at 63% Radius, 20% Chord, and $\mu = 0.2$	204
109	Velocity Data at 63% Radius, 25% Chord, and $\mu = 0.2$	205
110	Velocity Data at 63% Radius, 15% Chord, and $\mu = 0.25$	206
111	Velocity Data at 63% Radius, 20% Chord, and $\mu = 0.25$	207
112	Velocity Data at 63% Radius, 25% Chord, and $\mu = 0.25$	208

LIST OF ILLUSTRATIONS (Continued)

Figure		Page
113	Velocity Data at 63% Radius, 15% Chord, and $\mu = 0.3$	209
114	Velocity Data at 63% Radius, 20% Chord, and $\mu = 0.3$	210
115	Velocity Data at 63% Radius, 25% Chord, and $\mu = 0.3$	211
116	Exit Velocity Versus Chamber Pressure for Hot-Wire Calibration Device	220
117	Center Line Pressure Decay Versus Distance From Jet Exit Plane	221
118	Velocity Profile of Jet at Various Distances From Jet Exit Plane	222
119	Ammonia Trace Data; $\theta = 13.5°$, 250 rpm	225
120	Ammonia Trace Data; $\theta = 13.5°$, 700 rpm	226
121	Ammonia Trace Data; $\theta = 13.5°$, 920 rpm	227
122	Ammonia Trace Data; $\theta = 15°$, 250 rpm	228
123	Ammonia Trace Data; $\theta = 15°$, 700 rpm	229
124	Ammonia Trace Data; $\theta = 15°$, 855 rpm	230
125	Velocity Data at 72% Radius, $\theta = 0°$, and 100 rpm	232
126	Velocity Data at 72% Radius, $\theta = 5°$, and 100 rpm	233
127	Velocity Data at 72% Radius, $\theta = 15°$, and 100 rpm	234
128	Velocity Data at 72% Radius, $\theta = 0°$, and 400 rpm	235
129	Velocity Data at 72% Radius, $\theta = 5°$, and 400 rpm	236
130	Velocity Data at 72% Radius, $\theta = 15°$, and 400 rpm	237

LIST OF ILLUSTRATIONS (Continued)

Figure		Page
131	Velocity Data at 92% Radius, θ = 0°, and 100 rpm	238
132	Velocity Data at 92% Radius, θ = 5°, and 100 rpm	239
133	Velocity Data at 92% Radius, θ = 0°, and 400 rpm	240
134	Velocity Data at 92% Radius, θ = 5°, and 400 rpm	241

LIST OF SYMBOLS

a_n	the coefficients of the Tchebychef polynomials used to curve-fit the function $1/\Delta$ in equation (50)
A_1, A_2, A_3	coefficients in equation (78), used to approximate the potential flow and the surface curvature of airfoils
b	value of intercept in torque equation
C_T	thrust coefficient
C_Q	torque coefficient
c	the chord of the airfoil; units of length
c_p	pressure coefficient, p dynamic pressure
d	hot-wire sensor diameter, units of length
f_{11}, f_{12}, f_{13}, f_{14}, f_{15}	coefficients in the x-momentum-integral equation defined by equations (40) through (44)
f_{21}, f_{22}, f_{23}, f_{24}, f_{25}	coefficients in the z-momentum-integral equation defined by equations (45) through (49)
F, G, H,	velocity profile functions defined by equations (19)
g_1, g_2, h_1, h_2,	potential flow functions defined by equations (24) through (27)
h	boundary layer height
k	a constant used to represent a linear adverse pressure gradient in equation (74); units of length^{-1}
K	the curvature of the airfoil surface; units of length^{-1}
m	value of slope in torque equation
p	pressure; units of force/length^2

LIST OF SYMBOLS (Continued)

$\vec{q}$	the velocity vector relative to the rotating blade; units of length/time
Q	measured torque; units of force x length
r	the radial distance from the axis of rotation to a point on the blade; units of length
R	radius to blade tip; units of length
Re	the Reynolds number based on blade chord and the free-stream chordwise velocity
Re_w	the Reynolds number used in the hot-wire calibration based on calibration jet exit velocity and hot-wire sensor diameter
T	measured thrust; units of force
T_n, T_n'	Tchebychef polynomials and their derivatives, respectively
u, v, w,	local velocities in the x,y,z system of coordinates; units of length/time
U, V, W	potential velocities in the x,y,z system of coordinates; units of length/time
V_A, V_B	components of velocity normal to hot-wire sensors A and B, respectively; units of length/time
v_A, v_B	output voltages of anemometers A and B, respectively; units of volts
X, Y, Z	the Cartesian coordinate system that rotates with the blade; all units of length
x	the distance from the leading edge of the blade, measured in the chordwise direction along the surface of the blade; units of length
y	the distance from the surface of the blade, measured along a normal to the surface; units of length
z	the distance from the axis of rotation, measured along the span of the blade; units of length

LIST OF SYMBOLS (Continued)

α	the angle between the normal to the surface of the blade and a normal to the chord line of the blade
α_1, α_2	coefficients in equation (78), used to approximate the potential flow and the surface curvature of airfoils
β_1, β_2	velocity profile parameters defined by equations (21) and (23)
γ	the outflow angle, or the angle between the local flow velocity vector and the chord line of the blade measured positively in the increasing span direction
δ	three-dimensional rotating boundary layer thickness; units of length
δ_B	two-dimensional nonrotating boundary layer thickness; units of length
δ_x^*, δ_z^*	boundary layer displacement thicknesses in the u and w profiles, respectively; units of length
$\bar{\delta}_x^*$, $\bar{\delta}_z^*$	ratios of displacement thickness to the boundary layer thickness
Δ	boundary layer thickness parameter, $\Omega\delta^2/\upsilon$
Δ_x, Δ_z	partial derivatives of Δ with respect to x and z, respectively; units of length^{-1}
ϵ	wall shear stress parameter
ϵ_x, ϵ_z	partial derivatives of ϵ with respect to x and z, respectively; units of length^{-1}
η	a dimensionless distance above the blade surface measured along a normal to the surface, y/δ
θ	blade pitch angle, or the angle between a normal to the blade chord and the axis of rotation

LIST OF SYMBOLS (Continued)

θ_x, θ_z, θ_{xz}, θ_{zx}	boundary layer momentum thicknesses in the u and w profiles; units of length
$\bar{\theta}_x$, $\bar{\theta}_z$, $\bar{\theta}_{xz}$, $\bar{\theta}_{zx}$	ratios of momentum thickness to boundary layer thickness
Λ_1, Λ_2	velocity profile parameters defined by equations (20) and (22)
μ	the viscosity; units of mass/length-time
ν	the kinematic viscosity, μ/ρ; units of length^2/time
ρ	the density of the fluid; units of mass/length^3
τ_B	two-dimensional, nonrotating surface shear stress; units of force/length^2
τ_{or}	component of wall shear stress along the radial direction; units of force/length^2
$\tau_{o\theta}$	component of wall shear stress along the tangential direction; units of force/length^2
τ_{ox}	component of wall shear stress along the x chordwise coordinate; units of force/length^2
$\bar{\tau}_{ox}$	dimensionless chordwise wall shear stress, $\tau_{ox}\delta/\mu U$
τ_{oz}	component of wall shear stress along the z spanwise coordinate; units of force/length^2
ϕ	velocity potential for plane steady flow past the blade placed in a parallel stream of unit speed; units of length
$\vec{\Omega}$	the rotational velocity vector; units of time^{-1}
Ω	the magnitude of the rotational velocity vector or, the rotor speed; units of time^{-1}

LIST OF SYMBOLS (Continued)

Additional symbols used:

$O(\ )$	meaning "of order", i.e., $O(1)$ and $O(\delta)$
Σ	used to represent a summation of terms which follow the symbol
$\underline{\Delta}x$, $\underline{\Delta}z$	grid spacing increments used in numerical integration in the x and z directions, units in percent of chord.

I. INTRODUCTION

1.1 GENERAL BACKGROUND INFORMATION

The design of rotor blades has relied heavily upon the use of two-dimensional airfoil data. By assuming that individual blade elements produce lift independently, a so-called "blade element theory" was developed in the early stages of rotor design. With this theory, it was possible to make estimates of the rotor thrust and power requirements without requiring a thorough knowledge of the mechanisms by which lift and drag were being produced. Since that time, many refinements to this theory have been incorporated into rotor designs, including tip vortex effects, wake interaction, and nonsteady flow effects; however, the reliance upon two-dimensional airfoil data has not been eliminated.

Experimental rotor data have given indications that rotor lift coefficients much greater than those predicted by two-dimensional airfoil data exist in certain regions at the rotor disk plane. Additionally, the onset of blade stall has been qualitatively determined to occur at a higher blade loading condition than expected two-dimensionally. Since blade stall limits the performance of the helicopter because of increased power requirements, aircraft roughness vibration, and control loads, a knowledge of the mechanism by which rotor blade stall develops is needed. Blade stall, however, depends on the nature of the boundary layer which exists on an airfoil.

For a helicopter in steady forward flight, many actions occur simultaneously which tend to promote three-dimensionality and time dependence within the rotor boundary layer. The primary action is the chordwise boundary layer flow in the presence of a given chordwise pressure distribution. A secondary flow, the spanwise flow component, exists. This secondary flow forces the total boundary layer flow to be examined as a vector quantity having magnitude and direction. The magnitude and direction of the flow at the edge of the boundary layer are continually changing, as do the spanwise pressure gradients which exist. The fluid particles within the boundary layers may experience centrifugal and Coriolis accelerations caused by rotation. Compressible flow effects can occur near the tips of the advancing blade, and a reversed flow occurs in the inboard regions of the retreating blade. Very rapid changes in angle of attack can lead to unusual pressure gradient actions in the boundary layers. Periodic stall flutter on retreating blades has also been given recent intensive study. To further complicate the flow, the blades interact with their own tip vortices from the preceding revolution.

The simultaneous occurrence of all of these actions has made rotor boundary layers so complex that until recently, investigation of the very nature of these boundary layers has been discouraged.

This investigation was initiated to examine the basic nature of the boundary layers on a rotor blade in hovering and forward flight.

A second phase of this investigation was directed toward seeking an understanding of the flow around helicopter rotor blade tips. Because of the nature of the generation of lift of a rotor blade, a strong vortex is trailed from the region of the tip. This vortex can influence the blade boundary layer flow and the performance of the rotor itself. In an effort to further the understanding of the basic flow phenomena over the tips of helicopter rotors, an experimental program was conducted with the following objectives:

1. To investigate the development of the flow around the tips of helicopter rotor blades from surface flow visualization of the boundary layer, and to define the point of inception of the vortex on the tip.

2. To determine the effects of the shape of the tip on the flow around the tip.

3. To measure the effects of tip shape on thrust and torque coefficients of the rotor.

1.2 APPROACH TO THE BOUNDARY LAYER STUDY IN HOVERING

The investigation consists of an analytical phase and an experimental phase directed toward determining the basic nature of a boundary layer on a helicopter rotor in hover.

The analytical phase of the work consists of applying momentum-integral techniques to the solution of the three-dimensional boundary layer problem. Initially, the flat plate or zero pressure gradient case was considered. Then, following a successful solution to this case, the method was extended to include nonzero pressure gradients and airfoils of finite thickness with blunt leading edges. Due to the complexity of the potential flow, only airfoils at zero lift were examined. The solution is presented for a flat plate, an NACA 0012 airfoil and an NACA 0015 airfoil. The analytical solution obtained by this method is compared with the full computer solution obtained by Dwyer and McCroskey.

The experimental phase consists of hover tests using The Ohio State University hover stand. The investigation employed three experimental techniques to measure flow and pressure characteristics on the rotor blades.

The first experimental technique involved a flow visualization process developed at The Ohio State University. The technique is an ammonia-azo process which allows visual observation of the flow direction near the surface of a rotating airfoil.

The second experimental technique involved the use of miniature diaphragm pressure transducers submerged within the blade surface. These transducers were used to measure the surface static pressures at various blade positions and hover conditions.

The third and most informative experimental technique employed hot-wire anemometry. Dual sensor probes were mounted at various distances above the blade surface of the rotor blade to indicate the magnitude and direction of the local flow.

The experimental data are compared with existing two-dimensional data where possible. A comparison of the theoretical model and the hot-wire data is made for the zero lift condition.

1.3 APPROACH TO THE TIP VORTEX STUDY

The tip vortex study concentrated on the behavior of air flow in the vicinity of the blade surface near the tip of the blade. The ammonia-azo process was used throughout this study to provide flow visualization. Ammonia vapor was passed through small orifices in the tips and over a diazonium salt solution sprayed onto the tips. The ammonia, flowing with the local air streamlines, left dark traces on the tips which were then photographed.

1.4 APPROACH TO THE STUDY OF BOUNDARY LAYERS IN FORWARD FLIGHT

The study of forward flight operations was concerned with the experimental determinations of the boundary layer and surface pressure distributions. No attempts were made to study tip vortex flow. The rotor blades used and the instrumentation techniques were essentially the same as those used in the hovering boundary layer studies described in Section 1.2. No theoretical work was performed for the forward flight case.

II. ANALYTICAL BOUNDARY LAYER STUDY--HOVER

2.1 INTRODUCTION

Although the boundary layer theory formulated by L. Prandtl in 1904 is of great importance in practical aerodynamics, the difficulties presented by the nonlinearity of the boundary layer equations has limited the classes of solutions to flows which exhibit special symmetry. Most of the cases which have been treated to date are two-dimensional in character; solutions of three-dimensional boundary layer flows are quite rare.

One of the practically important types of three-dimensional boundary layer flows is the flow on rotating blades such as turbine, helicopter, and propeller blades. In the case where the blade is rotating steadily in an incompressible fluid, the boundary layer flow is governed by the chordwise and spanwise pressure distributions and the centrifugal and Coriolis accelerations. These actions couple the chordwise and spanwise equations of motion and force them to be solved simultaneously.

The theoretical portion of this study involves the development of an approximate method for calculating the laminar boundary layer flow over a cylindrical blade which is rotating steadily about an axis perpendicular to its leading edge.

2.1.1 Review of Literature

Many investigators have made notable contributions to the field of rotating boundary layer flows. The assumptions and results of a few of these researchers are summarized below.

In order to examine the boundary layer flow, the inviscid or potential flow that serves as an outer boundary condition to this region of flow must be known. Sears[1] found a simple but powerful transform that derives the potential flow for the rotating cylinder from the two-dimensional chordwise potential flow across the same cylindrical section. The original result was for the case of infinite blades rotating steadily without circulation; however, Sears and Fogarty[2] and McCroskey and Yaggy[3] have extended this solution to include the effects of translation of the axis of rotation (forward flight) and circulation about the cylindrical section (rotors with lift).

Following the potential solution by Sears, a number of his co-workers began examining the boundary layer of a cylindrical blade rotating steadily in an incompressible fluid. Among these were Fogarty, Tan, Graham, Rott, Smith and Liu. In each case (except Graham) the curvature of the blade was neglected and the surface normal was assumed to be parallel to the axis of rotation.

Fogarty[4] uncoupled the motion equations by introducing the assumption of small cross-flow, or that $W/U \ll 1$. His results indicated that the effects of rotation were small; however, his assumptions limited the validity of his theory to several chord lengths from the axis of rotation where the flow is nearly two-dimensional.

Tan[5] removed Fogarty's assumption of small cross-flow by expanding his solution in powers of x/z and obtaining successive approximations to the differential equations for the case of a rotating flat plate. Unfortunately, this leads to the solution of a large number of differential equations and thus involves a great amount of work to obtain accurate results at large distances from the leading edge.

Graham[6] employed the small cross-flow assumption and then used momentum-integral techniques to obtain approximate calculations of the boundary layer on rotating cylinders. Due to the small cross-flow assumption, the chordwise momentum-integral equation became identical to the standard two-dimensional flow case. This forced the separation point (based on zero chordwise velocity gradient at the wall) to coincide with two-dimensional calculations. Graham's solution did serve to estimate the cross-flow profile shape for a number of examples including that of a circular cylinder and a laminar airfoil section.

Rott and Smith[7] followed the technique employed by Tan[5] and examined the wedge-type flows characterized by the Falkner-Skan potential flow. Calculations were obtained for both positive and negative chordwise pressure gradients. The results indicated spanwise outflow for all cases; however, the greatest outflow was found for retarded flow.

Liu[8] further complicated the problem by allowing the axis of rotation to be arbitrarily located with respect to the leading edge of the blade. A perturbation procedure was set up expressing the velocity components in terms of locations on the blade and location of the axis of rotation relative to the blade. Following a great amount of algebraic manipulation, the equations were formulated and numerical solutions were obtained through the $(x/z)^2$ order terms. The results indicated that the development of the boundary layer from the leading edge of a flat plate is apparently independent of the location of the axis of rotation. For the case of a cylindrical blade of small thickness, the deviations of the results from infinite-cylinder flow are found to be caused mainly by the modification of the outstanding pressure gradient due to the location of the axis of rotation.

Banks and Gadd[9] used momentum-integral techniques to calculate the boundary layer on a flat sector with a linear adverse external-velocity gradient. The effects of rotation were found to postpone separation of the tangential boundary layer flow. This is one of the clearest indications of the stabilizing nature of rotation on the boundary layer.

Velkoff[10] performed an integral analysis and was the first to include the effect of translation. His results indicated a general thinning of the boundary layer for an outward radial flow and thickening for an inward radial flow.

The first major contribution to the analysis of three-dimensional boundary layers on helicopter rotors in forward flight was made by McCroskey and Yaggy[3]. They performed a regular perturbation expansion of the unsteady, three-dimensional incompressible boundary layer equations for small cross-flow. The results reveal that the effects of rotation can be large in regions of incipient separation, but elsewhere, the boundary layer generally resembles the viscous flow over a swept wing. The detailed structure of the spanwise flow was found to depend upon whether the primary flow is accelerating or decelerating.

A direct numerical integration of the three-dimensional or two-dimensional time-dependent boundary layer equations was performed by Dwyer and McCroskey.[11] The three-dimensional hover analysis included the flow near the hub for thin airfoils and circular cylinders. The time-dependent investigations simulated the unsteady effects occurring in forward flight on the outer portions of the rotor. A brute-force method was used assuming velocity profiles and iterating until a local solution was obtained. Each major action was examined independently to determine the order of magnitude of its contribution to the boundary layer flow.

Young and Williams[12] and Young[13] conducted a theoretical study to determine the effects of rotation, downflow, and forward flight on the development of the laminar boundary layer on a helicopter rotor. An 11.9-percent-thick symmetrical Joukowski airfoil was examined. The essential feature of the analysis was the scaling of the chordwise coordinate so that the separation line is invariant with span and time. The transformed equations were expanded in an asymptotic series in span and solved by the Hartree-Wormsley method. The effects of rotation were found to delay separation the greatest amount near the axis of rotation. Forward flight caused an oscillation about this separation line, so that the delay is greatest in the first and fourth quadrants.

Beyond the above-listed investigations, little, if anything, has been done to explain why actual rotors have been observed to perform better than would be expected on the basis of steady-state, two-dimensional section characteristics of the blades as illustrated by Himmelskamp[14] and Harris.[15]

2.1.2 Coordinate Systems

The present analysis is restricted to blades which are rotated about an axis normal to the axis of the blade. The blade is assumed infinitely long so that there are no end effects. The coordinate system is shown in Figures 1 through 3. The blade chord lies in the X-Z plane with the Z-axis located at the blade leading edge. The Y-axis is the axis of rotation and is located at the leading edge of the blade. The axes are fixed with respect to the blade so that they rotate with constant angular speed, Ω. Note that they form a left-hand coordinate system so that the standard two-dimensional terminology, u and v for the primary flow and w for the cross-flow, may be retained. The z-axis is chosen to coincide with the leading edge in conformity with the usual practice in boundary layer analysis. Typically, in two-dimensional boundary layer studies of a flat plate, the boundary layer is assumed to start from the leading edge, and hence the coordinate system is located there. In studies of airfoils the coordinate system

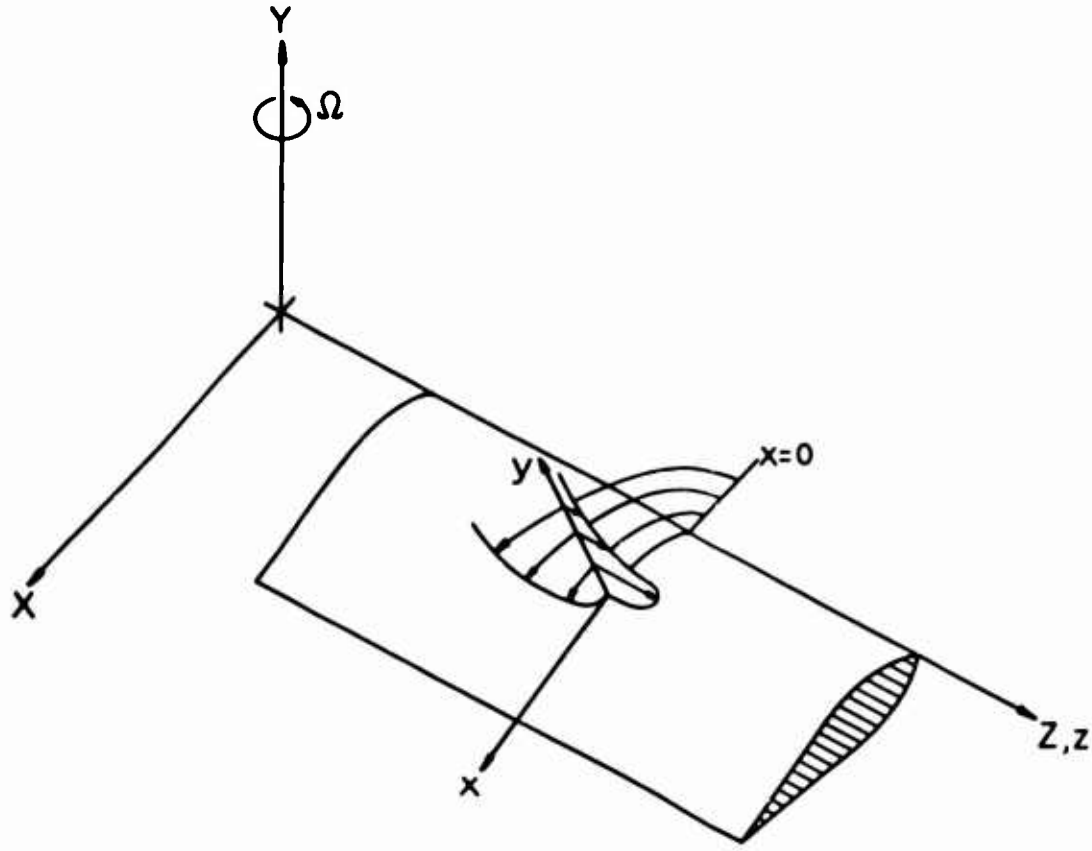

Figure 1. Coordinate Systems.

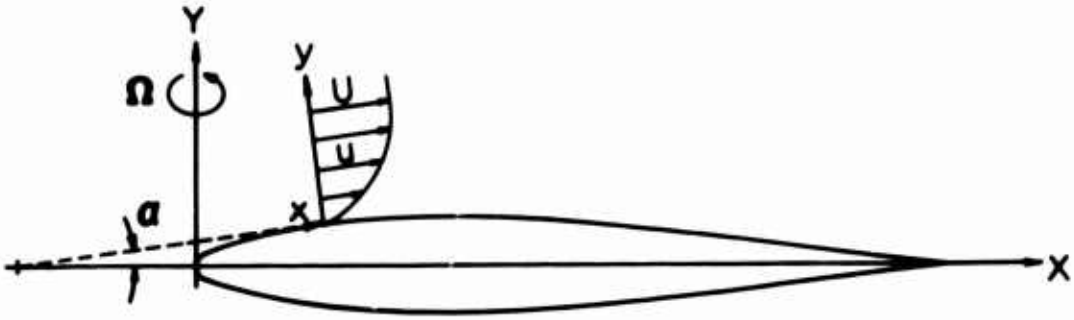

Figure 2. Chordwise or Primary Flow.

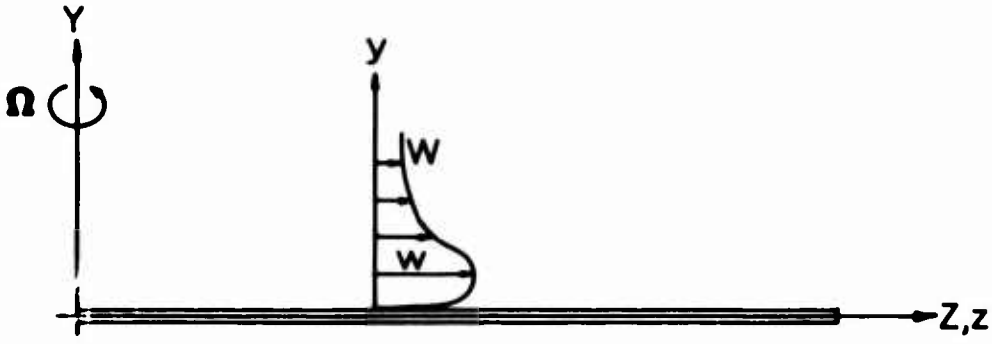

Figure 3. Spanwise or Secondary Flow.

usually is located at the leading edge stagnation point, as has been the case with the previous analyses conducted of rotor blade boundary layers indicated previously.

For boundary layer calculations, it is necessary to define the curvilinear surface coordinate system (x,y,z). The z axis coincides with the elements of the cylinder while the x and y axes are parallel and perpendicular to the blade surface, respectively, as shown in Figure 2. The boundary layer velocity components corresponding to the curvilinear coordinate system (x,y,z) will be denoted by (u,v,w).

The relationships between the Cartesian and curvilinear coordinates can be obtained from Figure 2 and are given below.

$$X = \int_0^x \cos\alpha \, dx - y \sin\alpha \tag{1}$$

$$Y = \int_0^x \sin\alpha \, dx + y \cos\alpha \tag{2}$$

$$Z = z \tag{3}$$

The angle $\alpha(x)$ represents the slope of the surface of the airfoil with respect to the X-axis or midchord line.

2.1.3 Boundary Layer Equations

The boundary layer equations are obtained from the three-dimensional Navier-Stokes equations for a viscous incompressible fluid. Throughout this analysis, the flow is assumed to be laminar. Fogarty[4] presents a derivation of these equations that is valid over the region of the blade where the blade surface is nearly normal to the axis of rotation. This means that the equations are not valid near the stagnation point of an airfoil-shaped blade. This restriction was not imposed by Graham,[6] and thus the essential steps of her derivation are described below.

The time dependence in the Navier-Stokes equations, since the blade is rotating steadily, is eliminated by using coordinates fixed to the blade. With this transformation, centrifugal and Coriolis accelerations appear. In a second transformation, the equations are written in curvilinear coordinates x,y,z, where x and z lie on the blade and y is normal to the surface. (See Figure 1.) These Navier-Stokes equations are reduced to boundary layer equations by the usual assumptions consistent with confining the viscous effects to a thin layer over the blade surface. That is, within this layer of thickness, δ, the following orders of magnitude are assumed.

$x = O(1)$	$u = O(1)$	
$y = O(\delta)$	$v = O(\delta)$	$\delta = O(\sqrt{\nu})$
$z = O(1)$	$w = O(1)$	

Then if the radius of curvature of the blade surface is large compared to the boundary layer thickness, the following boundary layer equations are obtained by neglecting terms $O(\delta)$ and higher:

$$uu_x + vu_y + wu_z - 2\Omega w \cos\alpha - \Omega^2 x \cos\alpha = -p_x/\rho + \nu u_{yy} \tag{4}$$

$$- Ku^2 + 2\Omega w \sin\alpha + \Omega^2 x \sin\alpha = -p_y/\rho \tag{5}$$

$$uw_x + vw_y + ww_z + 2\Omega u \cos\alpha - \Omega^2 z = -p_z/\rho + \nu w_{yy} \tag{6}$$

where K is the blade surface curvature. In like manner, the continuity equation becomes

$$u_x + v_y + w_z = 0 \tag{7}$$

Since the left-hand side of equation (5) is $O(1)$, the pressure can vary at most by an amount $O(\delta)$ within the boundary layer. It is reasonable then to neglect this variation and determine the pressure solely by the potential flow outside the boundary layer. (An identical argument is made for two-dimensional equations governing the boundary layer flow over a curved surface.)

The easiest way to determine the relationships between the pressure gradients p_x and p_z and the potential velocity components U and W is to examine the boundary layer equations near the outer edge of the boundary layer. In this region it may be assumed that $v = 0$, $\partial/\partial y = 0$, $u = U$, and $w = W$, so that equations (4) and (6) become

$$\begin{aligned} -p_x/\rho &= UU_x + WU_z - 2\Omega W \cos\alpha - \Omega^2 x \cos\alpha \\ &= UU_x + WW_x - \Omega^2 x \cos\alpha \end{aligned} \tag{8}$$

$$\begin{aligned} -p_z/\rho &= UW_x + WW_z + 2\Omega U \cos\alpha - \Omega^2 z \\ &= UU_z + WW_z - \Omega^2 z \end{aligned} \tag{9}$$

The second portions of equations (8) and (9) follow from the potential flow solution given in section 2.3.1 as equation (71). Substitution of the pressure gradient expressions into equations (4) and (6) yields the following final form of boundary layer equations:

$$uu_x + vu_y + wu_z - 2\Omega w \cos\alpha = UU_x + WU_z - 2\Omega W \cos\alpha + \nu u_{yy} \tag{10}$$

$$uw_x + vw_y + ww_z + 2\Omega u \cos\alpha = UW_x + WW_z + 2\Omega U \cos\alpha + \nu w_{yy} \tag{11}$$

2.1.4 Momentum-Integral Equations

Because of the great difficulties involved in solving equations (7), (10), and (11), an alternative approximate method was examined. In this approximate method, the boundary layer equations are not satisfied at each point in the boundary layer; instead, the average value of each equation across the boundary layer is maintained. The essential steps of the derivation of the three-dimensional momentum-integral equations are described below.

The y-component of the boundary layer velocity, v, is eliminated from equations (10) and (11) by making use of the continuity equation (7) in the following form:

$$v = -\int_0^y (u_x + w_z)\, dy \tag{12}$$

Then equations (10) and (11) are integrated across the boundary layer from y = 0 to y = h, where h is a constant such that $h \geq \delta$. After making the following standard definitions for displacement and momentum thicknesses and shear stresses,

$$\delta_x^* = \int_0^h \left(1 - \frac{u}{U}\right) dy \qquad \delta_z^* = \int_0^h \left(1 - \frac{w}{W}\right) dy$$

$$\theta_x = \int_0^h \frac{u}{U}\left(1 - \frac{u}{U}\right) dy \qquad \theta_z = \int_0^h \frac{w}{W}\left(1 - \frac{w}{W}\right) dy$$

$$\theta_{xz} = \int_0^h \frac{w}{W}\left(1 - \frac{u}{U}\right) dy \qquad \theta_{zx} = \int_0^h \frac{u}{U}\left(1 - \frac{w}{W}\right) dy$$

$$\tau_{ox} = \mu \left.\frac{\partial u}{\partial y}\right|_{y=0} \qquad \tau_{oz} = \mu \left.\frac{\partial w}{\partial y}\right|_{y=0} \tag{13}$$

the momentum-integral equations may be written in the form given below.

$$\frac{\partial}{\partial x}(U^2\ \theta_x) + \frac{\partial}{\partial z}(UW\ \theta_{xz}) + UU_x\ \delta_x^* + WW_x\ \delta_z^* = \tau_{ox}/\rho \tag{14}$$

$$\frac{\partial}{\partial x}(UW\ \theta_{zx}) + \frac{\partial}{\partial z}(W^2\ \theta_z) + UU_z\ \delta_x^* + WW_z\ \delta_z^* = \tau_{oz}/\rho \tag{15}$$

Equations (14) and (15) will be referred to as the momentum-integral equations throughout the remaining sections. The solution of these equations will indicate an averaged behavior of the boundary layer flow.

2.2 METHOD OF SOLUTION

Since solutions of the three-dimensional momentum-integral equations are rare and quite complex, it would seem appropriate to examine the ability of these equations to accurately describe three-dimensional boundary layer flows.

Although the validity of the momentum-integral method is well established in two-dimensional boundary layer flow, the use of this method in three-dimensional boundary layer flow demands the assumptions that the velocities in the boundary layer preserve, essentially, the corresponding directions at the stream lines in the external flow[16]. This demand is compatible with the requirement that only a weak secondary flow exist in the boundary layer. A portion of the effort

in this analysis was devoted to making predictions of boundary layer separation. Near separation the primary flow is diminished and the secondary flow becomes proportionately stronger. For this reason, the results of a three-dimensional momentum-integral analysis can only be used qualitatively to predict separation.

This limitation near flow separation does not imply that an integral technique is worthless in this flow region. Before this technique can be criticized, the alternative techniques must be thoroughly examined. For example, a finite difference technique could be applied to the complete Navier-Stokes equations similar to Dwyer and McCroskey.[11] However, as separation is approached and the differences (derivatives) become larger and larger, the grid spacing would need to be lessened to a point where the calculations would no longer be possible without great expense. Thus, even the so-called "exact" methods of solution of boundary layer problems have drawbacks near separation.

2.2.1 Extension of the Pohlhausen Technique

Pohlhausen[17] was first to introduce a general method of solution of the two-dimensional momentum-integral equation. A complete description of the method in a more modern form is presented by Schlichting;[16] however, a brief outline of the Pohlhausen method will follow.

First, the two-dimensional momentum-integral condition results in the following single, ordinary differential equation.

$$U^2\frac{d\theta_x}{dx} + (2\theta_x + \delta_x^*)UU_x = \tau_{ox}/\rho \qquad (16)$$

The technique introduced by Pohlhausen was initiated by assuming a velocity profile function which contained an undetermined parameter. The parameter was determined at each location on the wall surface by solving the ordinary differential equation (16).

In contrast, the three-dimensional momentum-integral condition results in two partial differential equations, (38) and (39). The extension of Pohlhausen's technique for three dimensions involves assuming profile functions for the two velocity components, u and w, which may contain a total of two undetermined parameters. These parameters are subsequently determined by solving the partial differential equations over the wall surface. The following sections are devoted to the systematic definition of the velocity profile functions and the two profile parameters, the derivation of the partial differential equations, and the integration technique employed to obtain a solution to these equations.

2.2.2 Velocity Profiles

The momentum-integral method hinges on an approximate description of the velocity profiles within the boundary layer. To insure that the approximate velocity profiles closely represent those that actually occur, a number of conditions derived from the differential equations (4, 5, 6) and boundary conditions are imposed at the surface as well as at the junction with the external flow. Those conditions satisfied in this analysis follow.

Conditions at the surface:

$$u = 0 \qquad w = 0$$

$$u_{yy} = \frac{1}{\nu}\left(\frac{1}{\rho} p_x - \Omega^2 x \cos\alpha\right) \qquad w_{yy} = \frac{1}{\nu}\left(\frac{1}{\rho} p_z - \Omega^2 z\right)$$

Conditions at the junction with the external flow:

$$u = U \qquad w = W$$

$$u_y = 0 \qquad w_y = 0$$

$$u_{yy} = 0 \qquad w_{yy} = 0$$

These conditions insure that, at both edges of the boundary layer, the approximate velocity profiles have the appropriate behavior. Consequently, the greater the number of conditions, the better the approximation.

The accuracy of the approximation is also dependent to some extent on the characteristic parameters selected by the investigator since these parameters allow the profiles to assume different forms. In two-dimensional boundary layer problems, it is conventional to use some measure of the boundary layer thickness as one such parameter. In three-dimensional boundary layer problems, there are two such profiles which have directed some investigators into choosing two thicknesses defining the distances above the surface at which the $u = U$ and $w = W$, respectively. One such investigation was performed by Cooke.[18] On the other hand, if it is assumed that a single boundary layer thickness defines a certain viscous region, that is, that both velocity profiles are equally thick, then it is logical to seek the second parameter at the other extremity of the boundary layer; for example, many investigators, such as Prandtl[19] and Taylor,[20] have chosen the ratio of the wall frictional forces. In the present analysis, a single boundary layer thickness, δ, and a wall shear stress parameter, ϵ, were selected to represent the growth of the boundary layer on a

rotating cylinder. The wall shear stress parameter will be defined by the boundary conditions imposed at the surface.

The velocity profiles for the chordwise and spanwise components of boundary layer flow follow.

$$\frac{u}{U} = F(\eta) + \Lambda_1 G(\eta) + \beta_1 H(\eta) \tag{17}$$

$$\frac{w}{W} = F(\eta) + \Lambda_2 G(\eta) + \beta_2 H(\eta) \tag{18}$$

The following definitions are in order.

$$\eta = y/\delta$$

$$F(\eta) = 2\eta - 2\eta^3 + \eta^4 = 1 - (1+\eta)(1-\eta)^3$$

$$G(\eta) = \frac{1}{6}(\eta - 3\eta^2 + 3\eta^3 - \eta^4) = \frac{\eta}{6}(1-\eta)^3$$

$$H(\eta) = 2(\eta - 6\eta^3 + 8\eta^4 - 3\eta^5) = 2\eta(1+3\eta)(1-\eta)^3 \tag{19}$$

The profile parameters Λ_1, β_1, Λ_2, and β_2 are functions of the boundary layer parameters δ and ϵ, and the potential flow according to the following relations:

$$\Lambda_1 = \left(\frac{UU_x + WW_x}{\Omega U} \right) \frac{\Omega\delta^2}{\nu} \tag{20}$$

$$\beta_1 = -\frac{W}{U}\epsilon \tag{21}$$

$$\Lambda_2 = \left(\frac{UU_z + WW_z}{\Omega W} \right) \frac{\Omega\delta^2}{\nu} \tag{22}$$

$$\beta_2 = \frac{U}{W}\epsilon \tag{23}$$

To simplify the presentation as much as possible, the following definitions will be used.

$$h_1(x,z) = (\Omega^2 x \cos\alpha - p_x/\rho)/\Omega U = (UU_x + WW_x)/\Omega U \tag{24}$$

$$h_2(x,z) = (\Omega^2 z - p_z/\rho)/\Omega W = (UU_z + WW_z)/\Omega W \tag{25}$$

$$g_1(x,z) = -W/U \tag{26}$$

$$g_2(x,z) = U/W \tag{27}$$

$$\Delta = \Omega\delta^2/\nu \tag{28}$$

Thus, equations (20) through (23) may be written in the simplified form given below:

$$\begin{aligned} \Lambda_1 &= h_1\,\Delta & \beta_1 &= g_1\,\epsilon \\ \Lambda_2 &= h_2\,\Delta & \beta_2 &= g_2\,\epsilon \end{aligned} \tag{29}$$

The profile shape parameters Λ_1 and Λ_2 evolve directly from the second boundary conditions at the surface. These conditions are obtained by evaluating the chordwise and spanwise Navier-Stokes equations at $y = 0$, and are analogous to the condition used by K. Pohlhausen[17] in the development of a general two-dimensional momentum-integral method outlined earlier.

These parameters allow the shape of the velocity profiles to be influenced by their corresponding pressure gradients and will be referred to as "Pohlhausen" profile shape parameters. For example, if the pressure gradient is strongly adverse, these parameters will force the profiles to contain inflection points that are found in exact two-dimensional flows and are expected to occur in certain three-dimensional boundary layer flows.

The "symmetry" in the ϵ portions of the profile representations of the chordwise and spanwise velocities was not accidental. Indeed, the first attempt at calculating the boundary layer on a rotating flat plate at zero incidence incorporated profiles quite similar to those used by Prandtl.[19] In this initial analysis, ϵ was defined as the ratio of the spanwise to the chordwise wall shear stresses and was included only in the spanwise profile. This led to "nonsymmetric" forms for the two profiles. Numerical integration of the equations was performed and the results were compared with those of previous investigators. Near the leading edge of the flat plate the results

compared favorably; however, at a value of $x/z = 0.5$, the solution indicated that a singularity may exist. These calculations were then repeated using rotating polar coordinates where ϵ was defined as the ratio of the radial to the tangential wall shear stresses. In this case the numerical integration was stable for all values of x/z.

Since the calculations cannot depend upon the coordinate system used to represent the physical problem, it was apparent that the differences in the results must be attributed to the two definitions of the parameter ϵ. To confirm these conclusions, ϵ was defined to be the ratio of the radial to the tangential wall shear stresses; however, the calculations were made using a Cartesian coordinate system. This forced the chordwise and spanwise profiles to be "symmetric" with respect to the parameter ϵ. The results were identical to those obtained using polar coordinates, as would be expected.

The velocity profile functions given by equations (17) and (18) are generalizations of those used for the initial flat plate analysis. For this reason, ϵ is no longer the ratio of radial to tangential wall shear stresses unless $\Delta = 0$. Further discussion of this parameter for a flat plate is included with the results.

2.2.3 Formulation of the Mathematical Equations

The mathematical problem was formulated as follows. The momentum-integral equations, (14) and (15), have allowed the choice of two free parameters in the velocity profiles. These parameters are δ, the boundary layer thickness, and ϵ, a wall shear stress parameter. Throughout this analysis, $\Delta = \Omega\delta^2/\nu$, a dimensionless form of boundary layer thickness, will be used in place of δ for the first parameter.

Substitution of the velocity profile expressions, equations (17) through (19), into the equations (13) yields the following polynomials for the displacement and momentum thicknesses and the wall shear stresses:

$$\bar{\delta}^*_x = \frac{\delta^*_x}{\delta} = \frac{3}{10} - \frac{1}{120}\Lambda_1 - \frac{1}{5}\beta_1 \tag{30}$$

$$\bar{\theta}_x = \frac{\theta_x}{\delta} = \frac{37}{315}\left(1 - \frac{1}{111}\Lambda_1 - \frac{16}{37}\beta_1 - \frac{19}{444}\Lambda_1\beta_1 - \frac{5}{5328}\Lambda_1^2 - \frac{208}{407}\beta_1^2\right) \tag{31}$$

$$\bar{\theta}_{xz} = \frac{\theta_{xz}}{\delta} = \frac{37}{315}\left(1 - \frac{71}{1776}\Lambda_1 + \frac{55}{1776}\Lambda_2 - \frac{79}{74}\beta_1 + \frac{47}{74}\beta_2 - \frac{19}{888}\Lambda_1\beta_2 - \frac{19}{888}\Lambda_2\beta_1 - \frac{5}{5328}\Lambda_1\Lambda_2 - \frac{208}{407}\beta_1\beta_2\right) \tag{32}$$

$$\bar{\delta}^*_z = \frac{\delta^*_z}{\delta} = \frac{3}{10} - \frac{1}{120}\Lambda_2 - \frac{1}{5}\beta_2 \tag{33}$$

$$\bar{\theta}_z = \frac{\theta_z}{\delta} = \frac{37}{315}\left(1 - \frac{1}{111}\Lambda_2 - \frac{16}{37}\beta_2 - \frac{19}{444}\Lambda_2\beta_2 - \frac{5}{5328}\Lambda_2^2 - \frac{208}{407}\beta_2^2\right) \tag{34}$$

$$\bar{\theta}_{zx} = \frac{\theta_{zx}}{\delta} = \frac{37}{315}\left(1 + \frac{55}{1776}\Lambda_1 - \frac{71}{1776}\Lambda_2 + \frac{47}{74}\beta_1 - \frac{79}{74}\beta_2 - \frac{19}{888}\Lambda_1\beta_2 - \frac{19}{888}\Lambda_2\beta_1 - \frac{5}{5328}\Lambda_1\Lambda_2 - \frac{208}{407}\beta_1\beta_2\right) \tag{35}$$

$$\bar{\tau}_{ox} = \frac{\tau_{ox}\delta}{\mu U} = 2\left(1 + \frac{1}{12}\Lambda_1 + \beta_1\right) \tag{36}$$

$$\bar{\tau}_{oz} = \frac{\tau_{oz}\delta}{\mu W} = 2\left(1 + \frac{1}{12}\Lambda_2 + \beta_2\right) \tag{37}$$

Note that the "symmetric" forms of the two velocity profiles force symmetry in the above expressions. For example, $\bar{\theta}_{zx}$ can be obtained from $\bar{\theta}_{xz}$ by interchanging subscripts 1 and 2.

Substitution of equations (30) through (37) into the two momentum-integral equations results in a pair of equations from which Δ and ϵ are to be obtained as functions of x and z. After a great amount of algebraic manipulation, the equations were written in the following form:

$$f_{11}\,\Delta_x + f_{12}\,\Delta_z + f_{13}\,\epsilon_x + f_{14}\,\epsilon_z = f_{18} \tag{38}$$

$$f_{21}\,\Delta_x + f_{22}\,\Delta_z + f_{23}\,\epsilon_x + f_{24}\,\epsilon_z = f_{28} \tag{39}$$

where the functions f_{ij} are rather complicated functionx of x, z, Δ, ϵ, and the potential flow. These functions are listed below:

$$f_{11} = \frac{U}{\Omega}\left(\overline{\sigma}_x + 2\,\Lambda_1 \frac{\partial \overline{\sigma}_x}{\partial \Lambda_1}\right) \tag{40}$$

$$f_{12} = \frac{W}{\Omega}\left[\overline{\sigma}_{xz} + 2\left(\Lambda_1 \frac{\partial \overline{\sigma}_{xz}}{\partial \Lambda_1} + \Lambda_2 \frac{\partial \overline{\sigma}_{xz}}{\partial \Lambda_2}\right)\right] \tag{41}$$

$$f_{13} = 2\,\frac{U}{\Omega}\,\Delta\, g_1 \frac{\partial \overline{\sigma}_x}{\partial \beta_1} \tag{42}$$

$$f_{14} = 2\,\frac{W}{\Omega}\,\Delta\left(g_1 \frac{\partial \overline{\sigma}_{xz}}{\partial \beta_1} + g_2 \frac{\partial \overline{\sigma}_{xz}}{\partial \beta_2}\right) \tag{43}$$

$$\begin{aligned} f_{18} = &- 2\,\Delta\left[\frac{U_x}{\Omega}\,(2\,\overline{\sigma}_x + \overline{\sigma}^a_x) + \frac{WW_x}{\Omega U}\,\overline{\sigma}^a_z + \left(\frac{W_z}{\Omega} + \frac{WU_z}{\Omega U}\right)\overline{\sigma}_{xz}\right] \\ &- 2\,\Delta^2\left[\frac{U}{\Omega}\frac{\partial \overline{\sigma}_x}{\partial \Lambda_1}\frac{\partial h_1}{\partial x} + \frac{W}{\Omega}\left(\frac{\partial \overline{\sigma}_{xz}}{\partial \Lambda_1}\frac{\partial h_1}{\partial z} + \frac{\partial \overline{\sigma}_{xz}}{\partial \Lambda_2}\frac{\partial h_2}{\partial z}\right)\right] \\ &- 2\,\Delta\,\epsilon\left[\frac{U}{\Omega}\frac{\partial \overline{\sigma}_x}{\partial \beta_1}\frac{\partial g_1}{\partial x} + \frac{W}{\Omega}\left(\frac{\partial \overline{\sigma}_{xz}}{\partial \beta_1}\frac{\partial g_1}{\partial z} + \frac{\partial \overline{\sigma}_{xz}}{\partial \beta_2}\frac{\partial g_2}{\partial z}\right)\right] \\ &+ 2\,\overline{\tau}_{ox} \end{aligned} \tag{44}$$

$$f_{21} = \frac{U}{\Omega}\left[\bar{\sigma}_{zx} + 2\left(\Lambda_1 \frac{\partial \bar{\sigma}_{zx}}{\partial \Lambda_1} + \Lambda_2 \frac{\partial \bar{\sigma}_{zx}}{\partial \Lambda_2}\right)\right] \tag{45}$$

$$f_{22} = \frac{W}{\Omega}\left(\bar{\sigma}_z + 2\,\Lambda_2 \frac{\partial \bar{\sigma}_z}{\partial \Lambda_2}\right) \tag{46}$$

$$f_{23} = 2\,\frac{U}{\Omega}\,\Delta\left(g_1 \frac{\partial \bar{\sigma}_{zx}}{\partial \beta_1} + g_2 \frac{\partial \bar{\sigma}_{zx}}{\partial \beta_2}\right) \tag{47}$$

$$f_{24} = 2\,\frac{W}{\Omega}\,\Delta\, g_2 \frac{\partial \bar{\sigma}_z}{\partial \beta_2} \tag{48}$$

$$\begin{aligned} f_{25} = {} & 2\,\bar{\tau}_{oz} - 2\,\Delta\left[\frac{W_z}{\Omega}\left(2\,\bar{\sigma}_z + \bar{\sigma}^*_z\right) + \frac{UU_z}{\Omega W}\,\bar{\sigma}^*_x\right. \\ & \left. + \left(\frac{U_x}{\Omega} + \frac{UW_x}{\Omega W}\right)\bar{\sigma}_{zx}\right] - 2\,\Delta^2\left[\frac{U}{\Omega}\left(\frac{\partial \bar{\sigma}_{zx}}{\partial \Lambda_1}\frac{\partial h_1}{\partial x}\right.\right. \\ & \left.\left. + \frac{\partial \bar{\sigma}_{zx}}{\partial \Lambda_2}\frac{\partial h_2}{\partial x}\right) + \frac{W}{\Omega}\frac{\partial \bar{\sigma}_z}{\partial \Lambda_2}\frac{\partial h_2}{\partial z}\right] - 2\,\Delta\,\epsilon\left[\frac{U}{\Omega}\left(\frac{\partial \bar{\sigma}_{zx}}{\partial \beta_1}\frac{\partial g_1}{\partial x}\right.\right. \\ & \left.\left. + \frac{\partial \bar{\sigma}_{zx}}{\partial \beta_2}\frac{\partial g_2}{\partial x}\right) + \frac{W}{\Omega}\frac{\partial \bar{\sigma}_z}{\partial \beta_2}\frac{\partial g_2}{\partial z}\right] \end{aligned} \tag{49}$$

2.2.4 Numerical Integration Technique

Equations (38) and (39) may be described mathematically as two coupled, quasi-linear, first-order, partial differential equations. The solutions of these equations involve the determination of the functions $\Delta(x,z)$ and $\epsilon(x,z)$. These two functions cannot be determined explicitly due to the nonlinearity of the differential equations. For this reason, an approximate integration technique was developed which determines values of Δ and ϵ at a discrete number of locations on the blade surface. This technique will be described in detail, since it provides the results for the theoretical analysis portion of this study.

The grid network used throughout this analysis is illustrated in Figure 4. A uniform spanwise grid spacing, $\Delta z = 0.5$ chord, was chosen to provide a reasonable number of spanwise locations for data interpolation. The spanwise locations were located from 0.5 chord to

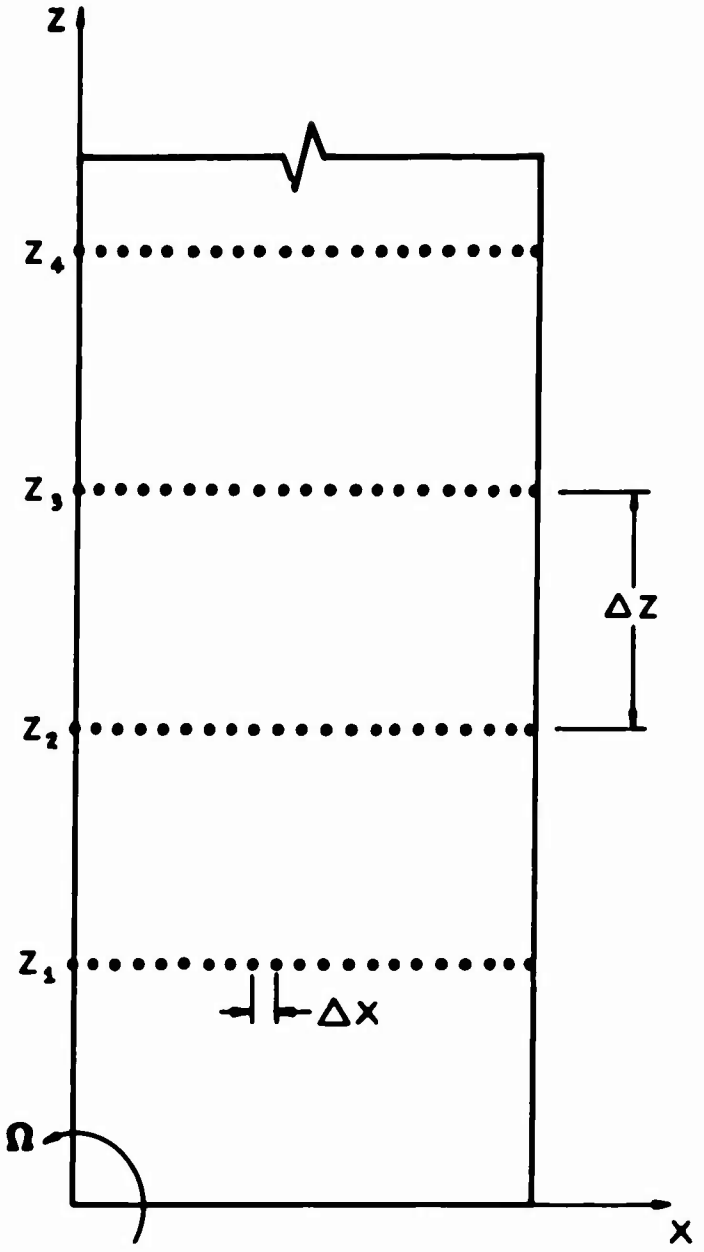

Figure 4. Calculation Grid Network.

20 chords to map the flow over the entire portion of a typical rotor blade. The singularity of the flow in the vicinity of the axis of rotation prevents calculations at spanwise positions near z = 0. This was not considered to be a drawback to the results, since most rotors do not extend their blade sections into this region due to inefficient lift production in the hub interference area. The chordwise grid spacing, Δx, was continually adjusted to maintain a specified computing accuracy during the numerical integration.

The problem was formulated as an initial value problem. The values of $\Delta(0,z_i)$ and $\epsilon(0,z_i)$, where z_i denotes the distance to the i^{th} spanwise grid point, are known from power series expansions for small x discussed in section 2.2.5. For example, for a sharp leading edge blade, both $\Delta(0,z_i)$ and $\epsilon(0,z_i)$ vanish for all spanwise grid points. The values of $\Delta_z(0,z_i)$ and $\epsilon_z(0,z_i)$ can also be evaluated from these power series. With the leading edge values known, the calculations may be stepped a distance Δx in the chordwise direction by using equations (38) and (39) to calculate $\Delta_x(0,z_i)$ and $\epsilon_x(0,z_i)$ and employing a Runge-Kutta integration routine.

With the values $\Delta(\Delta x,z_i)$ and $\epsilon(\Delta x,z_i)$ known, the next step becomes more complicated since $\Delta_z(\Delta x,z_i)$ and $\epsilon_z(\Delta x,z_i)$ are no longer known as they were at the leading edge. To determine these new values of Δ_z and ϵ_z, a numerical curve-fitting routine was developed. Once $\Delta_z(\Delta x,z_i)$ and $\epsilon_z(\Delta x,z_i)$ are known, equations (38) and (39) are again used to calculate $\Delta_x(\Delta x,z_i)$ and $\epsilon_x(\Delta x,z_i)$. Then the Runge-Kutta integration routine steps the calculations to a distance of $2\Delta x$ from the leading edge. Repetition of these calculations results in an approximate solution to the momentum-integral equations.

The numerical integration along the chordwise direction at each spanwise grid point was performed on an IBM 360/75 computer. An IBM application program was selected from the System/360 Scientific Subroutine Package. This subroutine, labeled DHPCG, uses Hamming's modified predictor-corrector method for the solution of general initial-value problems.[21] It is a fourth-order integration procedure which can estimate the local truncation error at each step and properly adjust the step size Δx. Hamming's predictor-corrector method itself is not self-starting; therefore, DHPCG employs a special Runge-Kutta procedure to obtain starting values. DHPCG is a double-precision subroutine which carries at least sixteen significant digits throughout all calculations. Double precision was required primarily for initiating the calculations near the stagnation point of blunt leading edge blades where the equations are singular.

A numerical differentiation routine was developed to calculate Δ_z and ϵ_z at each chordwise position. A typical spanwise variation of the parameter Δ for a rotating flat plate is illustrated in Figure 5 for fixed chordwise positions. The variations are greatest for small values of z. In order to employ a standard polynomial least-square

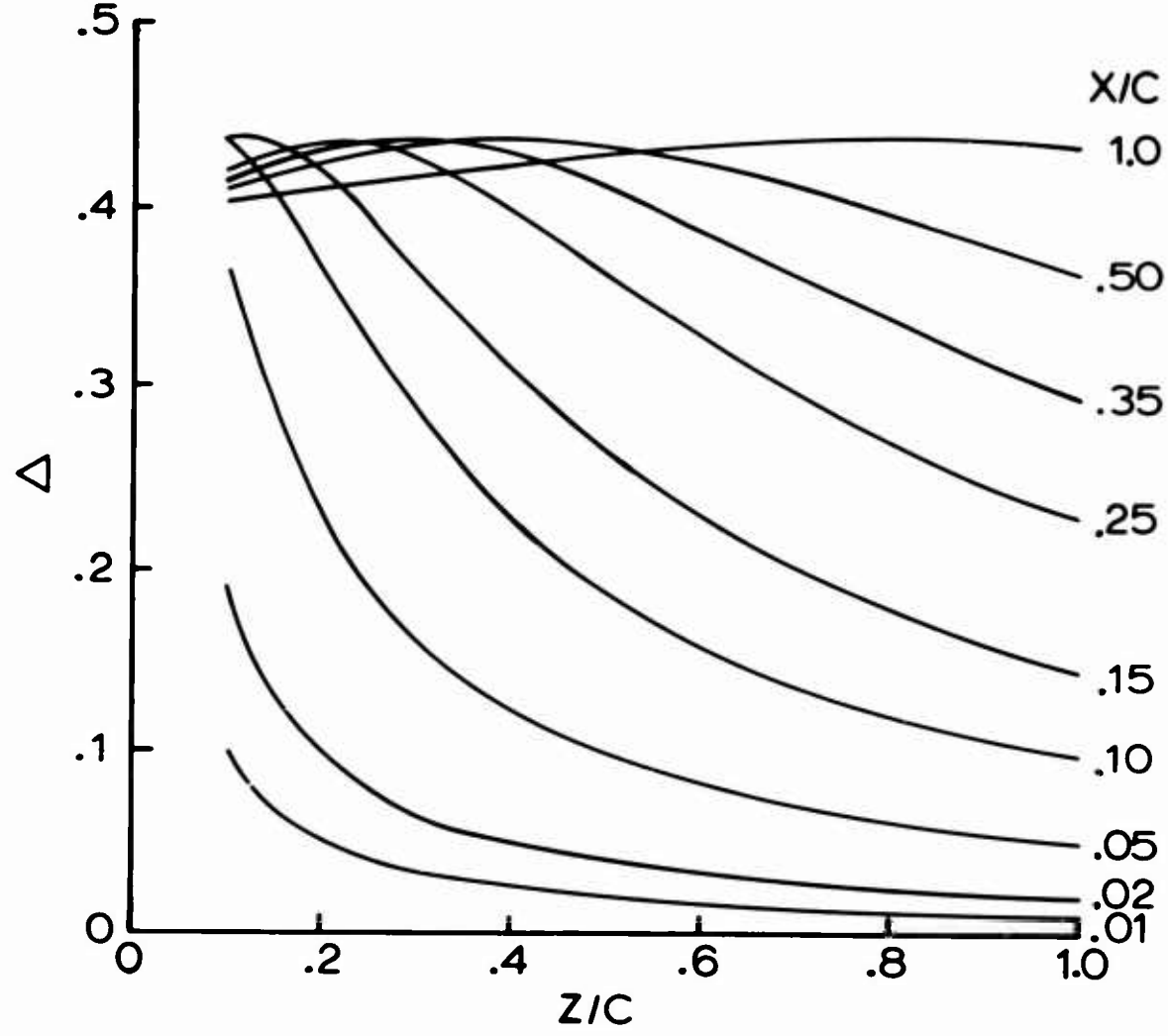

Figure 5. Variation of the Parameter Δ on a Flat Plate.

curve fit routine, it was convenient to first invert the parameter and then apply a curve-fitting technique. In this manner, the following approximation was used:

$$\frac{1}{\Delta} = \sum_{n=1}^{N} a_n T_n(z) \tag{50}$$

where $T_n(z)$ is the Tchebychef polynomial of order n, and a_n is the coefficient of $T_n(z)$ determined from a least-square-error criterion. To obtain Δ_z, equation (50) was differentiated, yielding

$$\Delta_z = -\Delta^2 \sum_{n=1}^{N} a_n T_n'(z) \tag{51}$$

The parameter ϵ had a similar variation with span, and consequently ϵ_z was determined according to an expression equivalent to equation (51). The standard deviations for the curve fit expressions ranged from 10^{-3} to 10^{-5} for both Δ and ϵ.

2.2.5 Leading Edge Starting Values

At the leading edge, the flow is two-dimensional in character and the solutions become identical to the two-dimensional momentum-integral solutions. In solving equations (38) and (39) for Δ_x and ϵ_x, the resulting right sides of both equations are quite complex. To evaluate the nature of the solution in the vicinity of the leading edge, a power series approximation technique was employed. The form of these series varies widely depending upon whether the airfoil has a "sharp" or a "blunt" leading edge.

For the case of a sharp leading edge, the first terms in the series representations of the functions Δ and ϵ are as follows:

$$\Delta = 34.0540\ x/z + 0(x^3) \tag{52}$$

$$\epsilon = -0.907491\ x/z + 0(x^3) \tag{53}$$

These series expansions were used to evaluate Δ_x and ϵ_x at the leading edge. Beyond the leading edge, the complete forms of equations (38) and (39) were evaluated to obtain Δ_x and ϵ_x.

The blunt leading edge case was more difficult since the right sides of the equations for Δ_x and ϵ_x at the leading edge are indeterminate; that is, the numerators and denominators vanish at the stagnation line along the leading edge. Once again, a power series expansion was used and the first terms were evaluated and given by equations (54) and (55):

$$\Delta = \frac{7.05232\ \Omega}{U_x(0,z)} + 0(x^2) \tag{54}$$

$$\epsilon = \left(-0.0578311 + 0.102213\ \frac{z\ W_{xx}(0,z)}{U_x(0,z)}\right)\frac{x}{z} + 0(x^3) \tag{55}$$

For the blunt leading edge airfoil, the initial value of Δ and the initial chordwise slope of ϵ depend upon the form of the potential flow and consequently the shape of the blade surface at the leading edge.

However, the calculation of the value of Δ_x near the leading edge requires the second term in the power series expansion. The algebra involved in computing this second term is rather complex; thus, a second and more approximate method was used. First, calculations were initiated with $\Delta_x(x_\epsilon,z) = 0$, where x_ϵ is a small value of x on the order of x/c of 0.01. The complete expressions were used for $x > x_\epsilon$. The stability of the computer solution for such a calculation is illustrated in Figure 6 by examining the variation in Δ_x. From the power series method, it is known that the second term in the power series expansion of Δ is of order x^2 as shown in equation (54). Thus, Δ_x should start with zero at the leading edge and vary linearly for $x \leq x_\epsilon$. The slope of this linear portion of curve was then determined by extrapolating the well-behaved portion of the curve back to the origin. The second set of calculations was initiated with the slope of Δ_x for $x < x_\epsilon$ being forced to follow the extrapolated slope shown on Figure 6 in the region $0.0 < x/c < 0.01$. The results of this second calculation show some excursion from the extrapolated slope in Figure 6 in the region of $0.01 < x/c < 0.03$. However, aft of x/c of 0.03 the results appear to be independent of any instability or excursion from the extrapolation slope since both runs agree quite accurately.

In summary, it was found that considerable insight to the analysis could be obtained from a power series solution in the vicinity of the leading edge; however, the major disadvantage of the power series method is the vast amount of algebraic manipulations that must be performed.

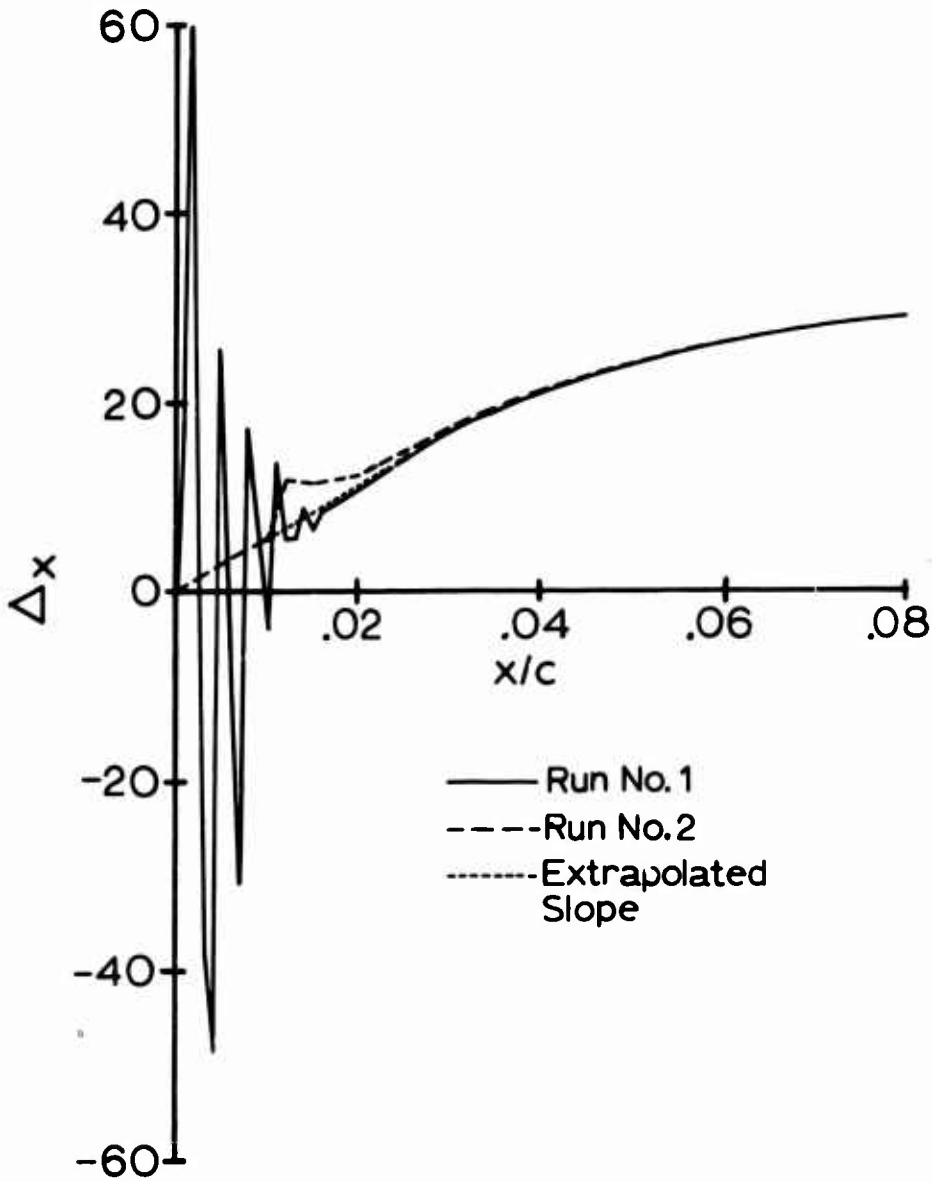

Figure 6. Stability of Numerical Technique Near the Stagnation Line of an NACA 0012 Airfoil.

2.3 POTENTIAL FLOW SOLUTION

The potential flow solution can be viewed as a solution to Navier-Stokes equations, equation (4) through (6) for the special case where viscous effects are neglected. In this type of idealistic flow the "no-slip" condition at the blade surface is relaxed and the convective motions of the flow are governed solely by the existing pressure gradients.

Although the potential flow is, at best, a first approximation for air flows, it is important since it represents the outer condition for the viscous flow. This potential solution must be matched by the boundary layer solution at the outer edge of the boundary layer.

2.3.1 General Solution of Sears

The potential flow solution for the case of an infinitely long cylinder, steadily rotating about an axis normal to it, was first solved by Sears.[1] The results are given by equations (56) through (58), which are the three components of the potential velocity along the Cartesian coordinates shown in Figures 1 through 3.

$$U = \Omega Z \frac{\partial \phi}{\partial X} \tag{56}$$

$$V = \Omega Z \frac{\partial \phi}{\partial Y} \tag{57}$$

$$W = \Omega(\phi - 2X) \tag{58}$$

The function $\phi(X,Z)$ denotes the velocity potential for plane, steady flow past the cylinder placed in a parallel stream of unit speed.

For this analysis it is necessary to have the potential velocity components along the curvilinear or boundary layer coordinates. To obtain approximate expressions along these coordinates, a portion of the derivation presented in Sears' paper will be repeated to make the necessary adjustments to the curvilinear coordinate system.

In any coordinate system rotating with the blade, the potential flow must satisfy the following expressions:

$$\text{div } \vec{q} = 0 \tag{59}$$

$$\text{curl } \vec{q} = 2 \vec{\Omega} \tag{60}$$

where $\vec{q}$ is the velocity vector relative to the rotating blade and $\vec{\Omega}$ is the angular velocity vector of the blade. Equation (59) is the expression for continuity while equation (60) expresses the fact that the potential flow is irrotational with respect to some nonrotating set of coordinates.

Using the equations developed by Mager[22] for representing equations (59) and (60) in terms of orthogonal curvilinear coordinates, the following four equations were obtained:

$$\frac{U_x}{1+Ky} + V_y + \frac{KV}{1+Ky} + W_z = 0 \tag{61}$$

$$W_y - V_z = 2\Omega_x = 2\Omega \sin\alpha \tag{62}$$

$$U_z - \frac{W_x}{1+Ky} = 2\Omega_y = 2\Omega \cos\alpha \tag{63}$$

$$\frac{V_x}{1+Ky} - U_y - \frac{KU}{1+Ky} = 2\Omega_z = 0 \tag{64}$$

K is the curvature of the blade surface and may be represented in terms of the physical data by the following equation:

$$K = -\frac{d\alpha}{dx} \tag{65}$$

The assumption imposed at this point in the analysis is that the radius of curvature of the blade is large in comparison to the boundary layer thickness, or that $1/K \gg \delta$. Also, the primary use of the potential flow is to provide the outer condition for the boundary layer flow; therefore, the region of interest in the potential flow is restricted to that region very near the blade surface. With this in mind, equations (61) through (64) can be simplified to equations (66) through (69) by assuming that $1 + Ky \simeq 1$ and $V \simeq 0$:

$$U_x + V_y + W_z = 0 \tag{66}$$

$$W_y = 2\Omega \sin\alpha \tag{67}$$

$$U_z - W_x = 2\Omega \cos \alpha \tag{68}$$

$$U_y = 0 \tag{69}$$

One further assumption made in the analysis is that the spanwise flow component, W, is not a function of z. From equation (67), it can be seen that this implies that $\sin\alpha$, which is satisfied only by thin airfoils, is very small. Near the leading edge of blunt airfoils, this assumption is not valid; however, the magnitude of the spanwise flow in this assumption will not greatly affect the results of the momentum-integral technique.

One major result of the preceding assumption may be observed by examining equation (58). The potential function ϕ, even in curvilinear coordinates, is only a function of x and y because there was no "mixing" of the z coordinate in the coordinate transformations. Thus, with the assumption that $W_y \simeq 0$, the spanwise potential flow becomes solely a function of the chordwise coordinate. With this in mind, the continuity equation for the potential flow becomes

$$U_x + V_y = 0 \tag{70}$$

and the irrotational flow condition results in the following single component condition:

$$U_z - W_x = 2\Omega \cos \alpha \tag{71}$$

The continuity equation expresses the fact that if a pressure gradient exists in the chordwise flow, the resulting acceleration or deceleration of the primary flow will necessarily be balanced by a deceleration or acceleration in the flow normal to the surface. It must be reemphasized that in a momentum-integral analysis, this potential velocity component normal to the surface is completely neglected. Thus, the continuity equation is not satisfied for the potential flow. An intuitive physical description of equation (71) is that it guarantees that the potential flow relative to fixed coordinates has no component of rotation about the y-axis.

2.3.2 Flat Plate (Zero Pressure Gradient)

The simple case of a flat plate blade at zero angle of attack provides an ideal starting point for this analysis. Subsequently, additional effects of pressure gradients and blade thickness will be included. The potential flow for this case is almost trivial, since without viscous effects and a pressure gradient, the flow is not influenced by the presence of the blade.

Therefore, the potential streamlines are circles relative to the rotating coordinates, and the velocity components are as follows:

$$U = \Omega z \tag{72}$$

$$W = -\Omega x \tag{73}$$

The chordwise profile can be obtained from equation (56) by recognizing that $\phi = 1$. The spanwise profile can be obtained from equation (71) by recognizing that $\alpha = 0$.

2.3.3 Flat Plate (Adverse Pressure Gradient)

Prior to examining an airfoil with thickness, it was recognized that for many airfoils the two-dimensional chordwise velocity is decelerated at approximately a constant rate over the aft 50 to 70 percent of the airfoil. To make the progression from a flat plate to an airfoil less abrupt, the second case examined in this study is that of a flat plate with a linearly decelerating chordwise flow. For this case, the chordwise velocity component, U, is given by the form

$$U = \Omega z \ (1 - kx) \tag{74}$$

where k is to be taken as a given constant. The spanwise component, W, is obtained by integrating equation (71) while assuming that $\alpha \simeq 0$. This spanwise component is given by equation (75):

$$W = -\Omega x \left(1 + \frac{1}{2} kx\right) \tag{75}$$

2.3.4 NACA 0012 at Zero Incidence

The most common method used to calculate the two-dimensional potential flow about an airfoil was introduced by Theodorsen.[23] This method involves the complex transformation of an arbitrary airfoil shape into a circular cylinder using approximate numerical techniques. The potential flow calculations for an NACA 0012 using this method have been tabulated by Abbott and von Doenhoff.[24] The chordwise velocity profile was obtained from this latter reference and is plotted in Figure 7. The abscissa is the distance from the leading edge along the airfoil contour.

Since these data were obtained using an approximate numerical technique, only a discrete number of data points are known; however, a solid curve is indicated. Unfortunately, the momentum-integral analysis requires that the first two derivatives of this velocity component be supplied, as well as the velocity itself. Since $U/\Omega z$ is such a rapidly varying function of z near the leading edge, a polynomial curve fit routine cannot match this data without many oscillations about the curve. These oscillations would produce first and second derivatives that could be in error by an order of magnitude. To maintain a "smooth" functional curve fit that would produce continuous derivatives with a minimum amount of numerical calculations, the following technique was developed.

The solid line in Figure 7 can be grossly approximated by two straight lines. The first line would pass through the origin and represent the two-dimensional potential velocity in the vicinity of a stagnation point as given by equation (76):

$$\frac{U}{\Omega z} = A_1 x \tag{76}$$

The second straight line would be analogous to the potential flow of section 2.3.3. This represents a linearly decelerating flow and may be given by equation (77):

$$\frac{U}{\Omega z} = A_2 x + A_3 \tag{77}$$

The Kutta condition at the trailing edge which forces the velocity to return to zero will be ignored in this approximation, since the laminar flow should separate prior to reaching this point.

In general, the actual velocity distribution is a combination of these two straight lines. It was proposed that the complete curve (barring the trailing edge) could be approximated by the following combination of the above straight lines:

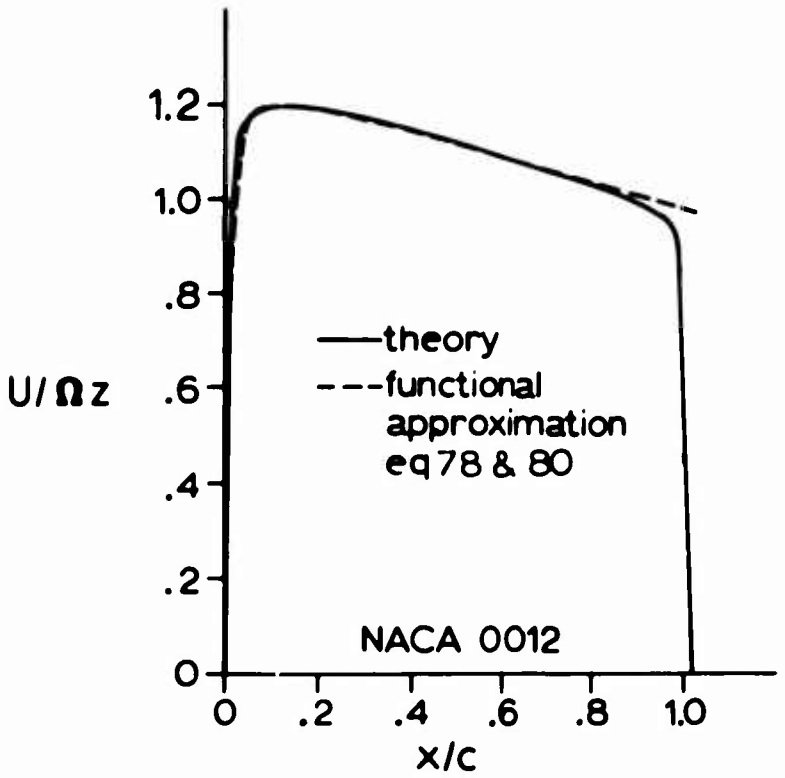

Figure 7. Chordwise Potential Flow for an NACA 0012 Airfoil at Zero Lift.

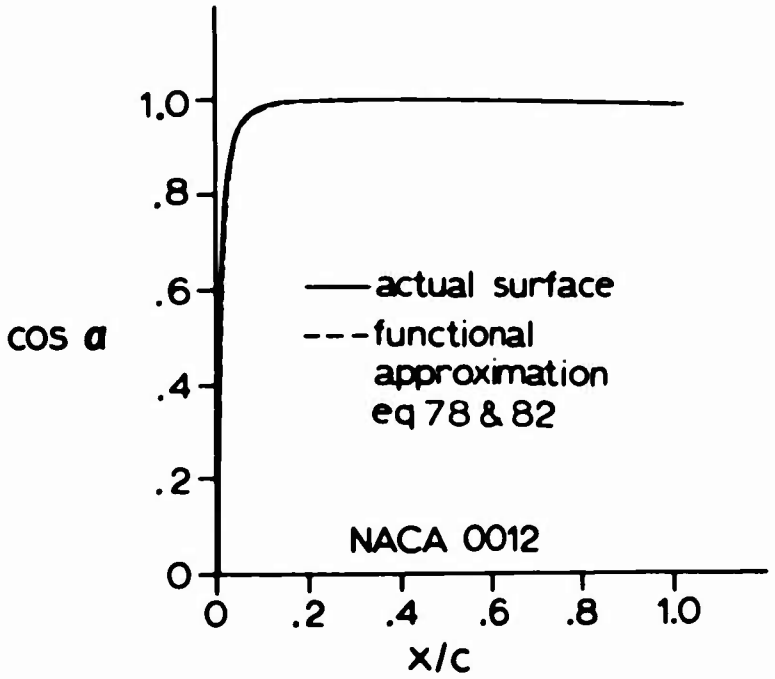

Figure 8. Surface Geometry for an NACA 0012 Airfoil.

$$\frac{U}{\Omega z} = A_1 \, x/c \, e^{-\alpha_1 x/c} + (A_2 \, x/c + A_3)(1 - e^{-\alpha_2 x/c}) \tag{78}$$

When x is small, the second half of this expression is small and the first half is approximately $A_1 x$. Also, when x is large, the first half of this equation is small and the second half is approximately $A_2 x + A_3$. In order to determine the best set of coefficients A_1, A_2, A_3, α_1, and α_2 to match the 0012 velocity distribution, the following conditions were enforced:

$$\begin{aligned}
&\frac{d}{dx/c}\left(\frac{U}{\Omega z}\right)\Big|_{x=0} = 70.0 \\
&\left(\frac{U}{\Omega z}\right)\Big|_{x\to\infty} = -0.267\, x + 1.245 \\
&\frac{d}{dx/c}\left(\frac{U}{\Omega z}\right)\Big|_{x=.133} = 0 \\
&\left(\frac{U}{\Omega z}\right)\Big|_{x=.133} = 1.188
\end{aligned} \tag{79}$$

The coefficients satisfying conditions (79) are as follows:

$$\begin{aligned}
A_1 &= 41.0 & \alpha_1 &= 38.42 \\
A_2 &= -0.267 & \alpha_2 &= 23.32 \\
A_3 &= 1.245
\end{aligned} \tag{80}$$

The final functional representation of the chordwise velocity distribution for an NACA 0012 airfoil at zero lift is given by equation (78) with the coefficients defined in (80). This approximation is plotted as a broken line in Figure 7. The agreement is accurate to within 2 percent over the major portion of the distribution. The accuracy is much better than this for the adverse pressure gradient region which is most critical for boundary layer calculations.

In order to determine an expression for the spanwise profile, equation (71) must be integrated. To accomplish this integration, $\cos\alpha$ must be represented in a functional form. The data for $\cos\alpha$ were obtained from the expression given by NACA which represents the

thickness distribution for an NACA 0012 airfoil. This expression is listed by Abbott and von Doenhoff.[24] The data are plotted in Figure 8. The form of this data resembles that of the velocity distribution data in Figure 7. This prompted the use of the same form for the functional curve fit as given by equation (78). In this case, the following conditions were enforced:

$$\begin{aligned} &\frac{d}{dx/c}(\cos\alpha)\,\Big|_{x=0} = 63.02 \\ &\cos\alpha\,\Big|_{x\to\infty} = -0.014\,x + 1.004 \\ &\frac{d}{dx/c}(\cos\alpha)\,\Big|_{x=.315} = 0 \\ &\cos\alpha\,\Big|_{x=.315} = 1.0 \end{aligned} \tag{81}$$

The coefficients satisfying conditions (81) are as follows:

$$\begin{aligned} A_1 &= -1.406 & \alpha_1 &= 19.91 \\ A_2 &= -0.014 & \alpha_2 &= 64.17 \\ A_3 &= 1.004 \end{aligned} \tag{82}$$

The approximate functional curve fit is also shown in Figure 8. The accuracy of this was found to be within 1 percent of the actual surface data.

With both U and $\cos\alpha$ given in explicit functional forms, the spanwise velocity component was determined by mechanically integrating equation (71). All necessary derivatives of these functions were obtained by differentiation of the approximate expressions.

2.3.5 NACA 0015 at Zero Incidence

Because of the similarity of the NACA 0015 airfoil to the NACA 0012 airfoil, the chordwise potential flow distribution may be approximated by the same functional form that is given by equation (78). The conditions imposed to obtain the coefficients are as

follows:

$$\frac{d}{dx/c}\left(\frac{U}{\Omega z}\right)\Big|_{x=0} = 60.0$$

$$\left(\frac{U}{\Omega z}\right)\Big|_{x\to\infty} = -0.364\ x + 1.323$$

$$\frac{d}{dx/c}\left(\frac{U}{\Omega z}\right)\Big|_{x=.150} = 0 \qquad (83)$$

$$\left(\frac{U}{\Omega z}\right)\Big|_{x=.150} = 1.233$$

With these conditions, the coefficients were calculated and listed as follows:

$$A_1 = 35.71 \qquad \alpha_1 = 31.79$$

$$A_2 = -0.364 \qquad \alpha_2 = 18.35 \qquad (84)$$

$$A_3 = 1.323$$

Once again, both the theoretical data obtained from Abbott and von Doenhoff [24] and the approximate functional curve fit are plotted in Figure 9. The accuracy was found to be within 2 percent over the major portion of the distribution. The functional fit of cosα for the NACA 0015 was forced to satisfy the following conditions:

$$\frac{d}{dx/c}(\cos\alpha)\Big|_{x=0} = 40.4$$

$$\cos\alpha\Big|_{x\to\infty} = -0.021\ x + 1.007$$

$$\frac{d}{dx/c}(\cos\alpha)\Big|_{x=.322} = 0$$

$$\cos\alpha\Big|_{x=.322} = 1.0 \qquad (85)$$

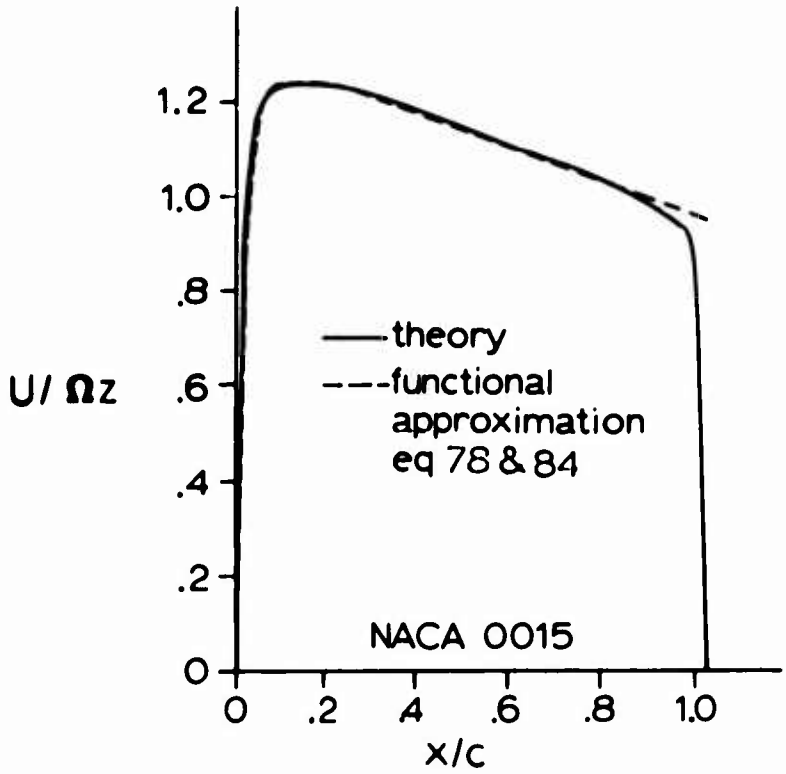

Figure 9. Chordwise Potential Flow for an NACA 0015 Airfoil at Zero Lift.

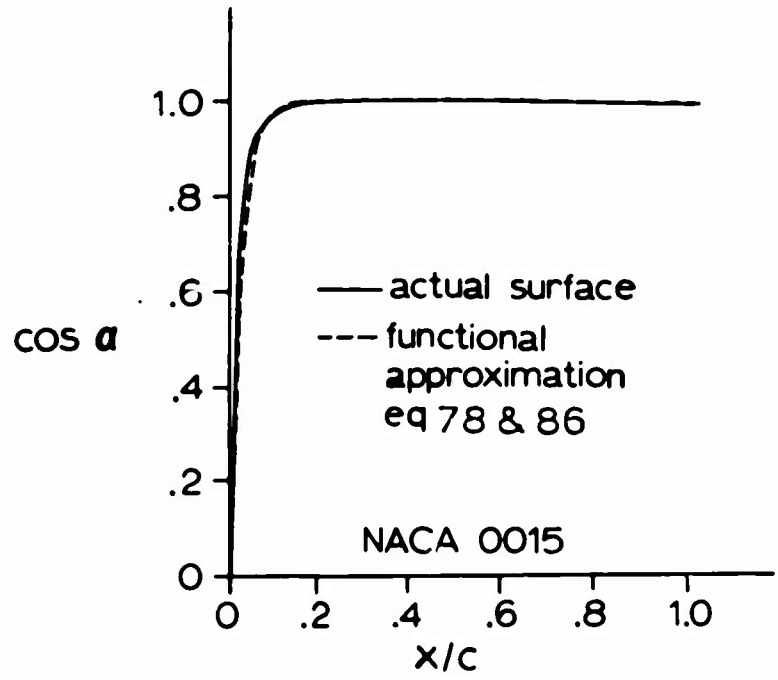

Figure 10. Surface Geometry for an NACA 0015 Airfoil.

The coefficients in equation (78) were obtained from these conditions and are given below:

$$A_1 = -0.201 \qquad \alpha_1 = 8.96$$

$$A_2 = -0.021 \qquad \alpha_2 = 40.32 \tag{86}$$

$$A_3 = 1.007$$

The accuracy of this approximation is approximately 2 percent over the major portion of the curve (see Figure 10).

2.4 BOUNDARY LAYER RESULTS AND DISCUSSION

The analytical boundary layer results are presented in four sections, each representing a different blade shape or potential flow. Reference is made to the analytical calculations of Dwyer and McCroskey[11] as much as possible. Their data were obtained through a combination finite difference-relaxation technique applied directly to the complete Navier-Stokes equations. For this reason, their results do not reflect the assumptions that were necessary in this analysis with regard to the derivation and method of solution of the momentum-integral equations. Therefore, the comparisons with the data of Dwyer and McCroskey[11] may be interpreted as an investigation of the accuracy of the momentum-integral method for three-dimensional rotating boundary layer flows.

2.4.1 Flat Plate, Zero Pressure Gradient

The boundary layer equations for a rotating flat plate exhibit symmetry with respect to the variable x/z. The momentum-integral equations for this case can be reduced to ordinary differential equations for $\Delta(x/z)$ and $\epsilon(x/z)$. Therefore, the numerical differentiation routine discussed in section 2.24 for solving the general partial differential equations is not needed for the rotating flat plate problem. This similarity presents an ideal check on the accuracy of this differentiation routine since the spanwise derivatives can be calculated exactly according to the following expressions:

$$\Delta_z = -\frac{x}{z}\Delta_x \tag{87}$$

$$\epsilon_z = -\frac{x}{z}\epsilon_x \tag{88}$$

The flat plate problem was solved twice. First, similarity was employed and the resulting ordinary differential equations were solved. Second, similarity was ignored and the numerical differentiation technique was used to calculate spanwise derivatives. The results of these two solutions agreed to within less than 1 percent. This accuracy check gives support to the overall technique employed to solve approximately the partial differential equations.

A physical picture of the lines of similarity is shown in Figure 11. Lines of constant x/z are rays emanating from the origin or axis of rotation. All of the results for the flat plate case are presented graphically by plotting each parameter versus x/z. From these plots, the boundary layer data can be examined over the complete blade surface. A small value of x/z could be interpreted as either a position near the leading edge ($x \simeq 0$) or a position at a large distance from the axis of rotation along the span ($z \to \infty$). Likewise, a large value of x/z could mean a large value of x or a small value of z. Thus, Figure 11 must be kept in mind throughout the interpretation of the analytical results.

The variation in the parameters Δ and ϵ over the flat plate surface is shown in Figure 12. The square of the boundary layer thickness is illustrated by the function Δ, while ϵ is related to the ratio of the radial to tangential shear stresses according to equation (89):

$$\epsilon = \frac{\tau_{or}}{\tau_{o\theta}} - \frac{\Delta}{12} \qquad (89)$$

As x/z becomes greater than 1.3, the boundary layer begins to thin instead of the usual steady growth observed in two-dimensional flows. This thinning may be attributed to the strong component of centrifugal force in the x-direction which exerts a strong stabilizing force on the primary flow. Since ϵ is a mixture of physical parameters and the boundary layer thickness parameter, it is difficult to attach a great deal of physical insight to the variation of ϵ.

Figures 13 and 14 present the distributions of the velocity profile parameters over the surface of the flat plate rotor blade. The Pohlhausen parameter in the chordwise velocity profile (Λ_1) is continually increasing. This is indicative of the fact that rotating flows with zero pressure gradient experience an acceleration due to the x-components of centrifugal and Coriolis forces. The value of Λ_2, the Pohlhausen parameter in the spanwise velocity profile, is negative and quite large near the leading edge ($x/z = 0$). This will promote a reverse-flow region in the spanwise profile near the leading edge. Farther aft of the leading edge, Λ_2 decreases in magnitude and this reverse-flow region may disappear. A similar variation is observed for the shear parameters β_1 and β_2; however, the signs are reversed.

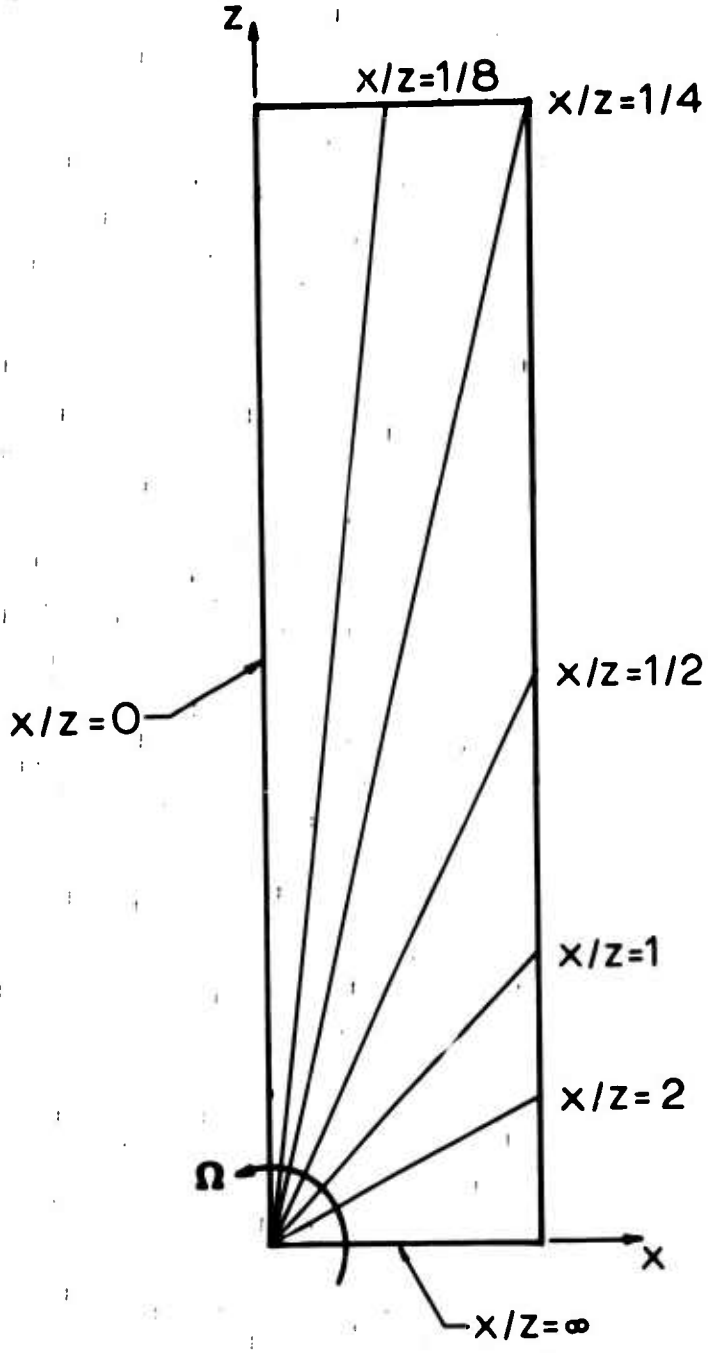

Figure 11. Lines of Similarity for a Rotating Flat Plate.

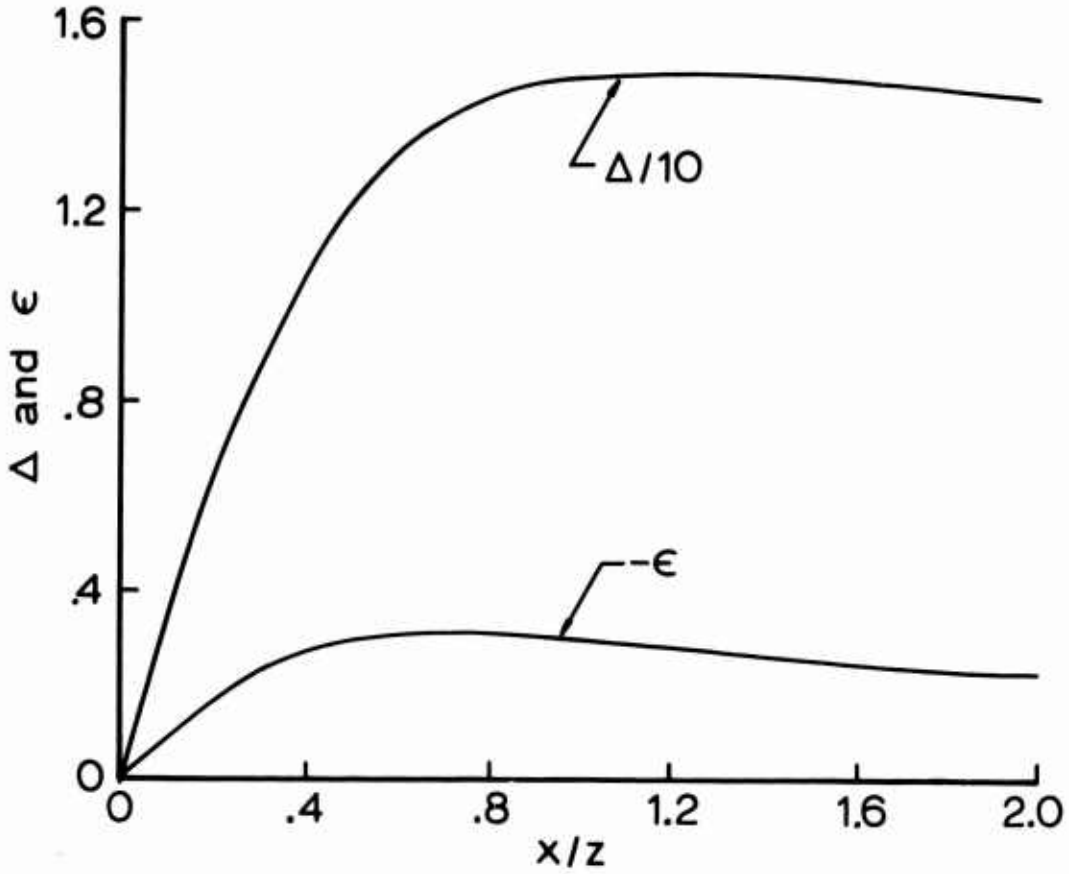

Figure 12. Profile Parameter Variation for a Rotating Flat Plate.

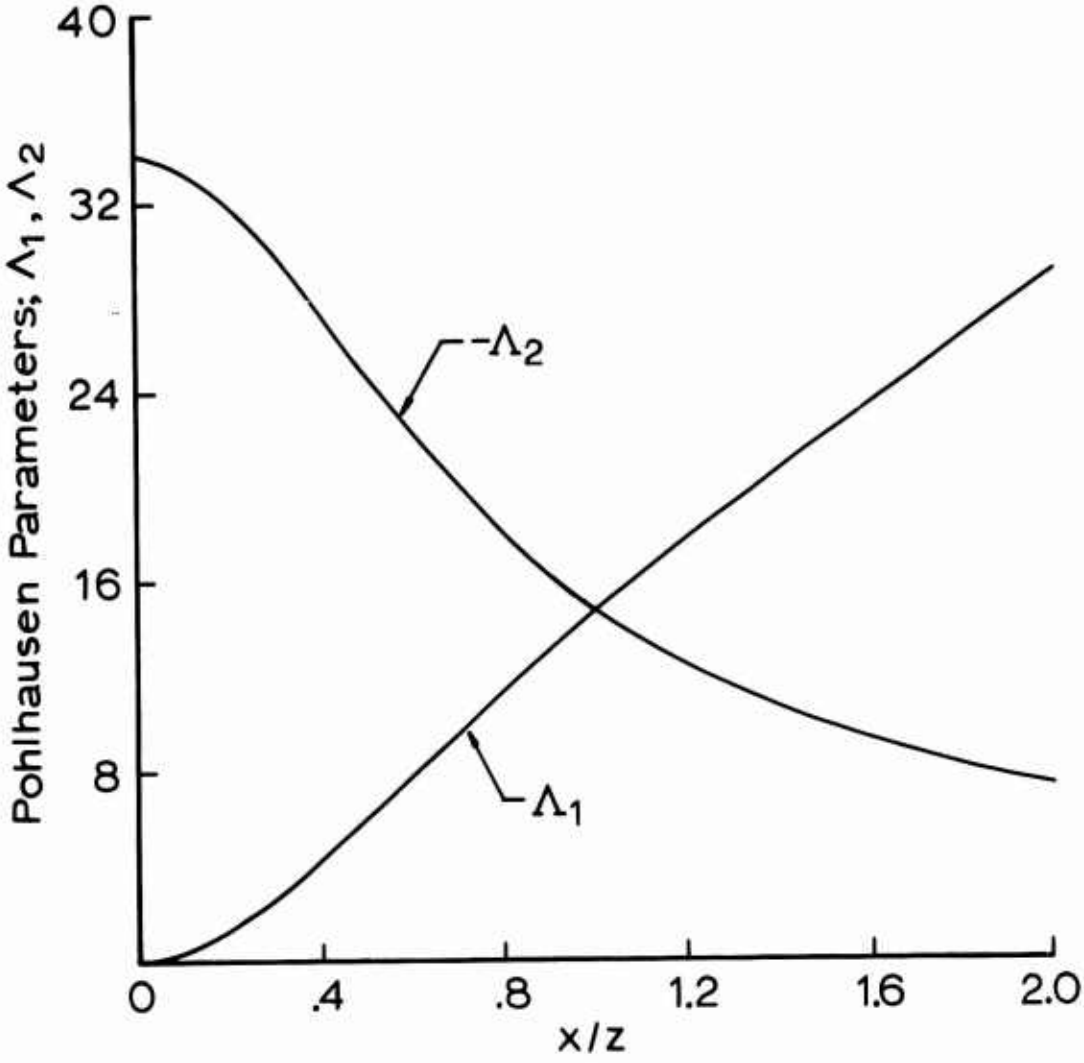

Figure 13. Pohlhausen Parameter Variation for a Rotating Flat Plate.

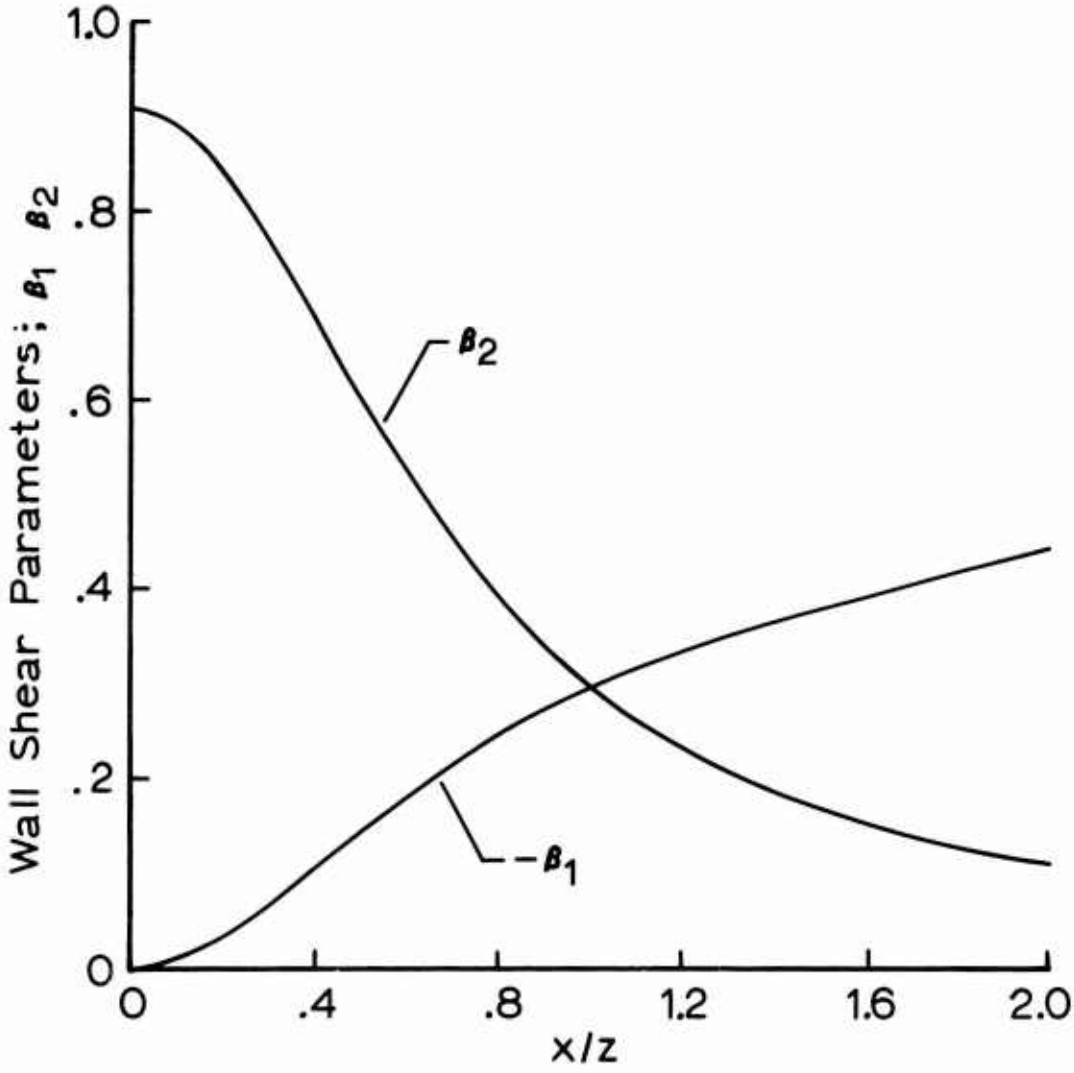

Figure 14. Wall Shear Stress Parameter Variation for a Rotating Flat Plate.

This indicates that β_1 has a decelerating effect on the chordwise flow while β_2 has a stabilizing effect on the spanwise flow. The symmetry of the profile parameter definitions for the flat plate case forces $\Lambda_1 = \Lambda_2$ and $\beta_1 = \beta_2$ at $x/z = 1$.

The total effects of the profile parameters are best observed by examining the chordwise and spanwise velocity profiles at various positions on the blade. Figure 15 illustrates the chordwise velocity profiles for x/z values of 0, 1, and 2. The ordinate used in this figure and in all subsequent velocity profiles is a stretched boundary layer coordinate $y\sqrt{\Omega x/\nu z}$. It is a standard grouping of physical constants that is used for nearly all two-dimensional flat plate analyses.[16] Near the leading edge, the velocity profile is the standard two-dimensional profile. The primary or chordwise profiles show decreased boundary layer thickness or become "fuller" as x/z is increased. This indicates that the fluid in the lower portion of the boundary layer is being accelerated. Again, it is the centrifugal force that promotes this acceleration. The effect is greater for large values of x/z because the x-component of centrifugal force increases with increasing x/z.

The secondary or spanwise profiles in Figure 16 are quite unlike the primary flow profiles, as is expected by the large differences in the values of Λ_1 and Λ_2 near the leading edge. Indeed, the spanwise profile does exhibit a flow reversal near the leading edge. The spanwise velocity is normalized with the absolute value of the potential spanwise velocity. This normalization allows the retention of positive profiles as outlfow and negative profiles as inflow. Near the leading edge, the centrifugal force pumps the lower levels of the boundary layer outward. However, the major portion of the boundary layer is still governed by the potential flow, W, which pulls the spanwise profile inward. As the value of x/z becomes large, the centrifugal force vector shifts to accelerate the chordwise flow and the spanwise outflow is decreased, until the outflow completely disappears. In this region, both the spanwise and chordwise velocity profiles become similar in form and appear to be quite stable.

The velocity profiles on a rotating flat plate are compared with those of Dwyer and McCroskey[11] in Figures 17 and 18 for a position near the leading edge (x/z = 0.0083) and a position considerably aft of the leading edge (x/z = 0.7). The symbols shown represent the analytical solution of Dwyer and McCroskey and are used for ease of comparison. These comparisons represent the first indications that the momentum-integral method is reasonably accurate for predicting the flow over a rotating flat plate. The agreement with Dwyer and McCroskey[11] is good. The profiles match those of the authors with a little better accuracy for x/z = 0.7 than for x/z = 0.0083. This is reasonable since the flow is being accelerated due to rotational effects and the momentum-integral method is known to give better results in two-dimensional accelerated flows.

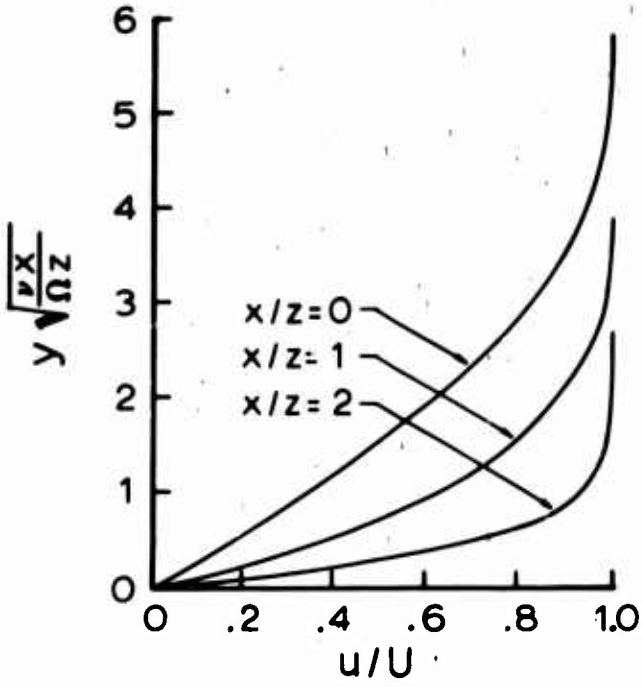

Figure 15. Chordwise Velocity Profiles for a Rotating Flat Plate.

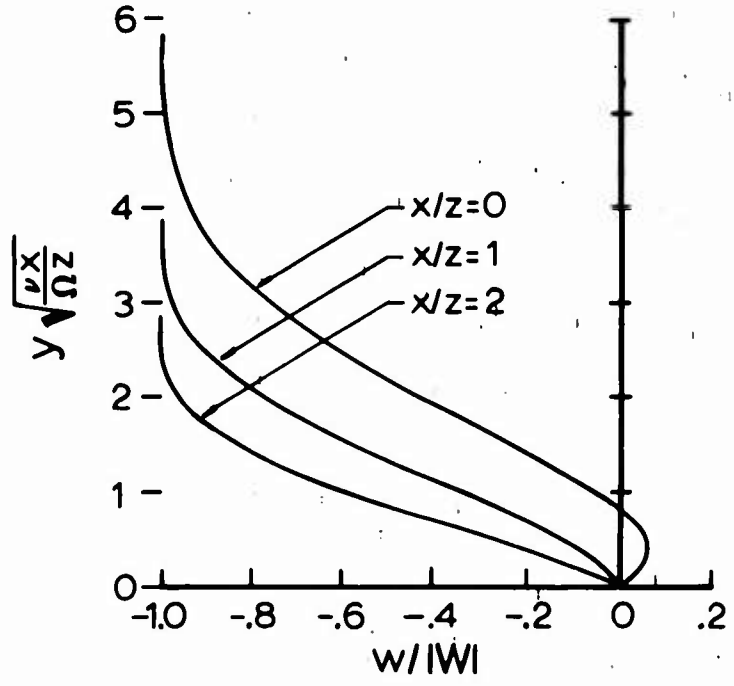

Figure 16. Spanwise Velocity Profiles for a Rotating Flat Plate.

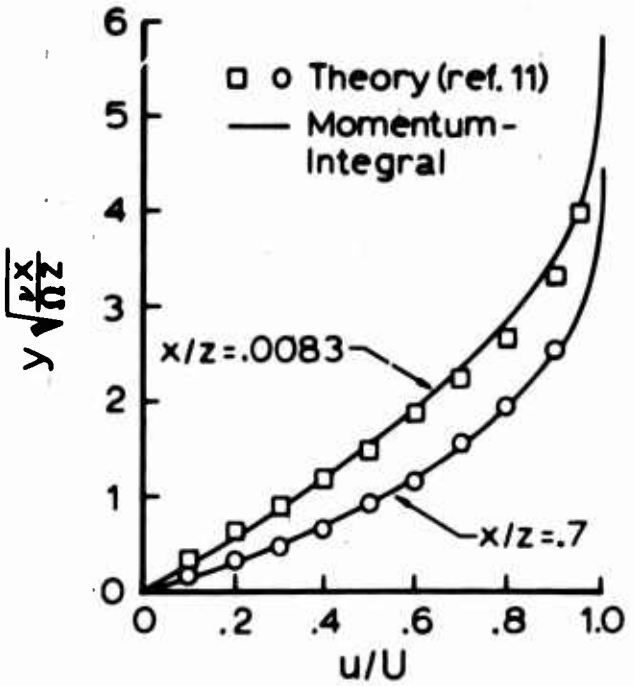

Figure 17. Comparison of Chordwise Profiles With Reference 11 for a Flat Plate.

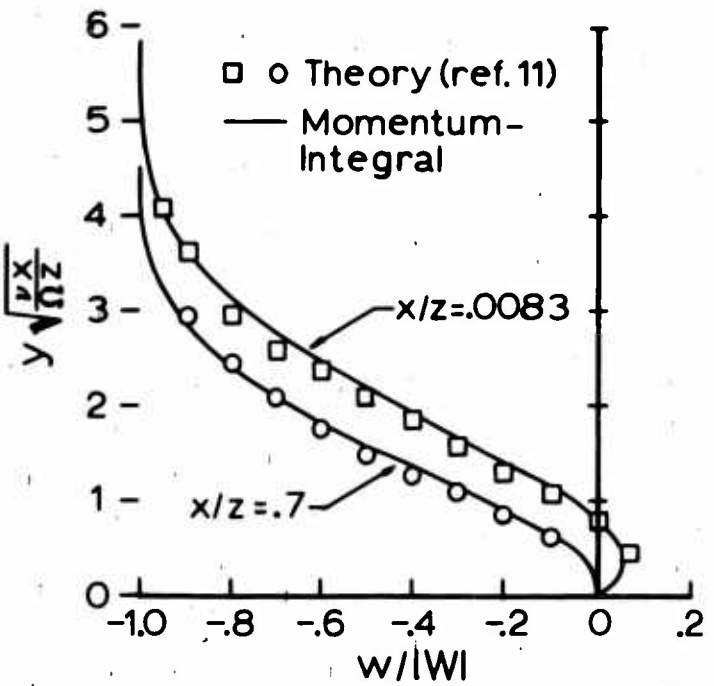

Figure 18. Comparison of Spanwise Profiles With Reference 11 for a Flat Plate.

A second comparison with Dwyer and McCroskey's results for a flat plate is made in Figure 19. In this figure, the ratio of the chordwise shear stress to the equivalent two-dimensional wall shear stress (τ_{ox}/τ_B) is plotted versus x/z. For two-dimensional flow over a flat plate using the momentum-integral method, the shear stress is given by equation (90):

$$\tau_B = \frac{2\mu\Omega z}{\delta_B} \tag{90}$$

Thus, this shear ratio is given by the following equation:

$$\frac{\tau_{ox}}{\tau_B} = \frac{\delta_B}{\delta}\left(1 + \frac{\Lambda_1}{12} + \beta_1\right) \tag{91}$$

where δ_B/δ is the ratio of two-dimensional to three-dimensional boundary layer thickness.

The two methods shown on Figure 19 agree to within 3 percent for $x/z \geq 0.8$. It was shown by Dwyer and McCroskey[11] that a fourth-order perturbation analysis was accurate only for $x/z \leq 0.5$; beyond this value of x/z, the perturbation solution diverged very rapidly. The momentum-integral technique, representing an averaged boundary layer behavior, maintains the correct trend through much larger values of x/z.

The direction of the boundary layer flow near the surface is indicated by the ratio of the spanwise and chordwise wall shear stresses. This ratio is plotted in Figure 20. More accurately, τ_{oz}/τ_{ox} represents the slope of the limiting streamline on the blade surface according to equation (92):

$$\left(\frac{dz}{dx}\right)_s = \lim_{y\to 0}\frac{w}{u} = \frac{\tau_{oz}}{\tau_{ox}} \tag{92}$$

The subscript s is used to indicate that the derivative is taken along a surface streamline. Figure 20 shows that the flow near the surface is outward for $x/z < 0.92$ while for $x/z > 0.92$ this flow is inward. Thus, at $x/z < 0.92$, the spanwise velocity profile is a separation type profile where the velocity gradient at the wall is zero. This does not mean that flow separation occurs in the two-dimensional sense, since τ_{oz} represents only one component of the wall shear stress vector.

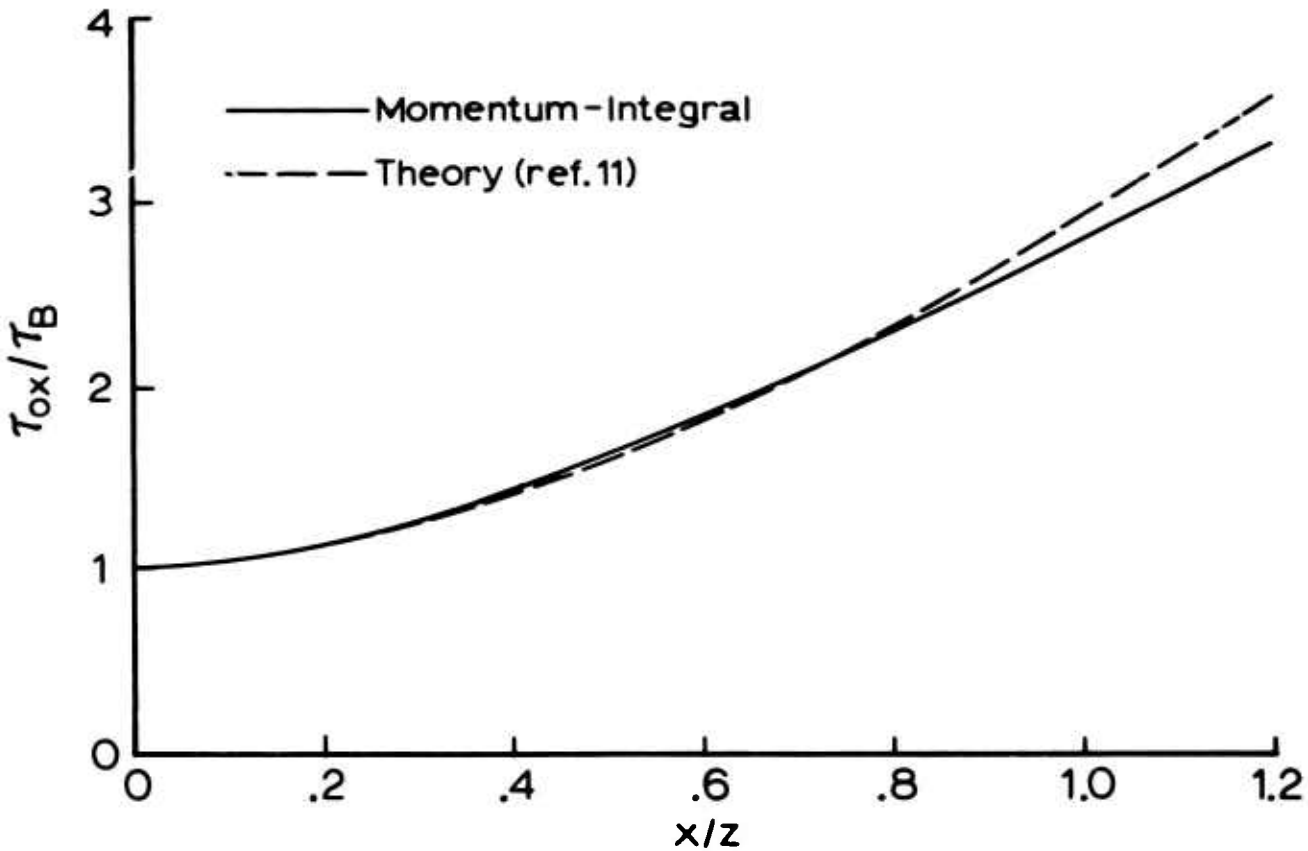

Figure 19. Chordwise Shear Stress Variation for a Rotating Flat Plate.

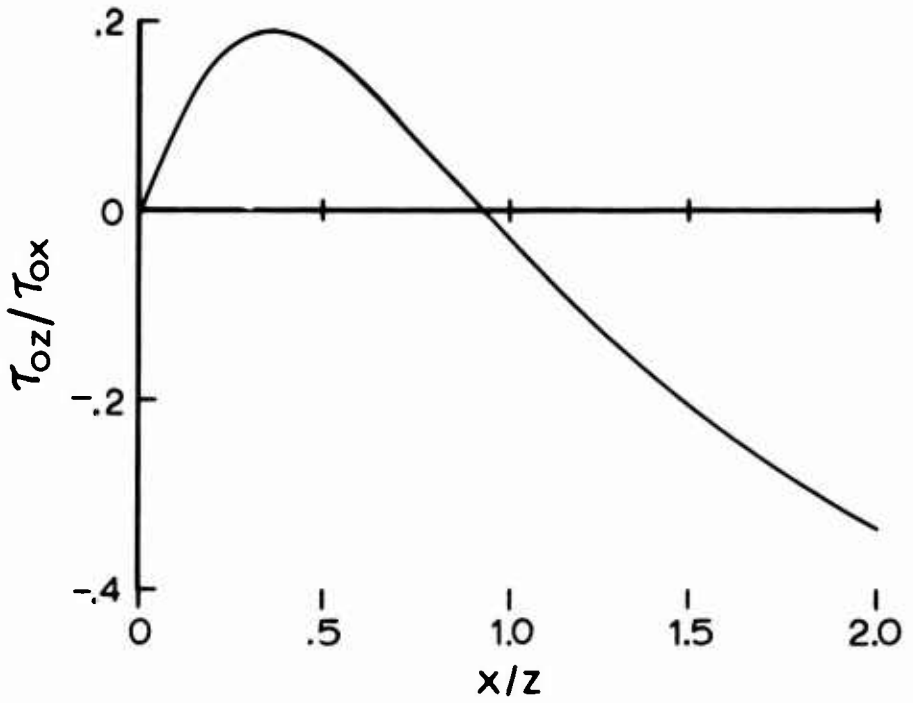

Figure 20. Ratio of Spanwise to Chordwise Wall Shear Stresses for a Rotating Flat Plate.

In general, the rotating flat plate results have shown that the momentum-integral method provides an accurate and stable technique to the solution of the three-dimensional rotating boundary layer problem.

2.4.2 Flat Plate, Adverse Pressure Gradient

The flat plate results are by no means conclusive evidence of the power of the momentum-integral technique. Since most airfoils exhibit an adverse chordwise pressure gradient, a second case is now considered.

This hypothetical potential flow is included in this analysis as a bridge between the simple case of a flat plate airfoil which has zero pressure gradient and the complex case of a real airfoil which has surface curvature and a variable pressure gradient.

In this second case, the airfoil is still assumed to have a sharp leading edge; however, the chordwise potential flow is to be linearly decelerated according to equation (74). The value of k was chosen to give a deceleration similar to that of an NACA 0012 airfoil. Thus, from section 2.3.4, k was chosen to be 0.267.

Figure 21 indicates the location of flow separation on a rotating flat plate airfoil which has a superimposed linearly decelerated potential flow. The stabilizing effects of rotation tend to delay the point of separation from the normal two-dimensional case.

The definition of the point of separation of three-dimensional boundary layer flows has long been a controversial subject. Since universal agreement has not been reached, the definition for separation used throughout this analysis is that point where the chordwise wall shear stress vanishes. This definition is compatible with that used by Dwyer and McCroskey.[11]

For this case, the similarity described by equations (87) and (88) is not applicable. Thus, the numerical differentiation technique described in section 2.2.4 was necessary for the solution presented in Figure 21.

The results of the linearly decelerated flow case are indicative of the results obtained by Banks and Gadd.[9] Their analysis also included a linearly decelerated flow; however, the deceleration was along the tangential, not the chordwise, direction. The tangential component of the potential flow in their analysis is given by equation (93):

$$U = \Omega r(1-k\theta) \tag{93}$$

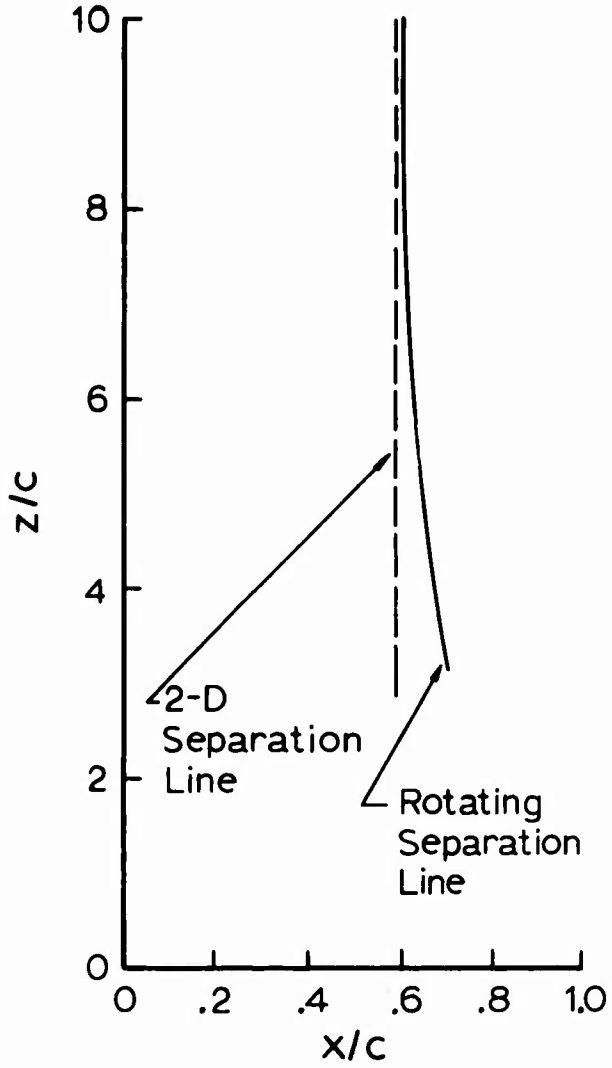

Figure 21. Comparison of Separation Lines for a Linearly Decelerated Flow, Rotating and Nonrotating Cases.

Using equation (93) and assuming that the radial component of potential velocity was zero, similarity with respect to θ is maintained. The results[9] indicate that for values of k less than 0.548, the boundary layer was completely stabilized against separation.

Since $\theta = \tan^{-1}(x/z)$, equation (93) indicates that for a fixed value of x, the adverse pressure gradient effect decreases for increasing values of z. This was a convenient choice since the favorable effects of rotation decrease with increasing values of z. This could explain the complete stabilization of the boundary layer reported by Banks and Gadd.[9] The linear adverse pressure gradient examined in this study does not exhibit this trend as can be observed by the differences in equations (74) and (93).

2.4.3 NACA 0012 at Zero Incidence

The third case considered in this analysis was that of an NACA 0012 airfoil at zero angle of attack. The potential flow for this airfoil was discussed in section 2.3.4. This airfoil shape is used for a number of helicopter rotors and was also used throughout the experimental portion of this study. Only analytical results will be presented here; the experimental comparisons will be discussed later in section IV.

Again, similarity is not present for this case as it was for the flat plate, zero pressure gradient example. The boundary layer solutions for an airfoil with thickness presented the problem of initiating the calculations at the stagnation line along the leading edge. The power series method, coupled with the numerical technique discussed in section 2.2.5, was used to alleviate the singularity problems in this region of the blade.

Chordwise and spanwise velocity profiles are shown in Figures 22 and 23 for a rotating NACA 0012 airfoil. The results of the momentum-integral analysis are plotted as solid lines for a chordwise position $x/c = 0.6$ and spanwise positions of $z/c = 1$ and $z/c = \infty$. This latter spanwise position corresponds to the two-dimensional chordwise flow profile which will be examined first.

The stabilizing effects of rotation are again depicted in the chordwise profiles, since the profile at $z/c = 1$ is considerably "fuller" than the equivalent profile at $z/c = \infty$. The results of the finite difference solution by Dwyer and McCroskey[11] are included for comparison. While their results are for identical spanwise positions, their chordwise position was at $x/c = 0.63$. The comparison is still quite good, especially for the $z/c = 1$ case. It is ironic that the momentum-integral method appears to be more accurate for the three-dimensional rotation case than for the two-dimensional nonrotating case. This can be resolved since the three-dimensional flow has the added stability of the centrifugal and Coriolis accelerations. In fact, the chordwise

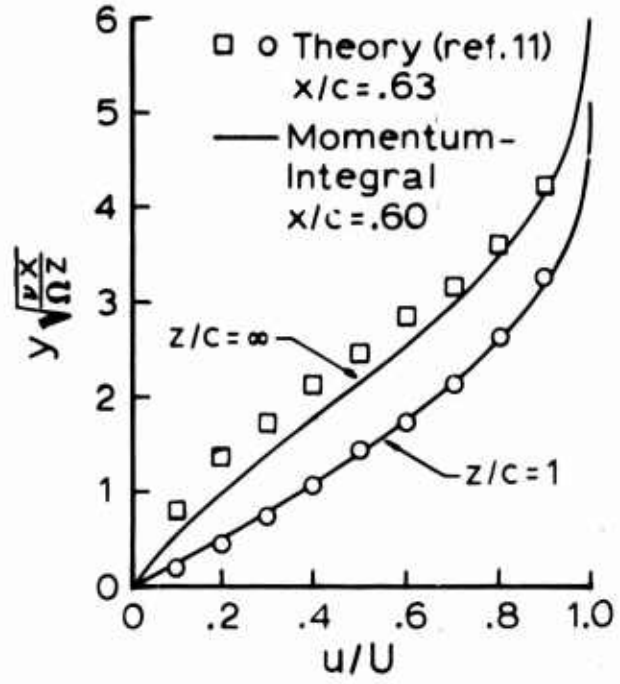

Figure 22. Comparison of Chordwise Velocity Profile With Reference 11 for an NACA 0012 Airfoil.

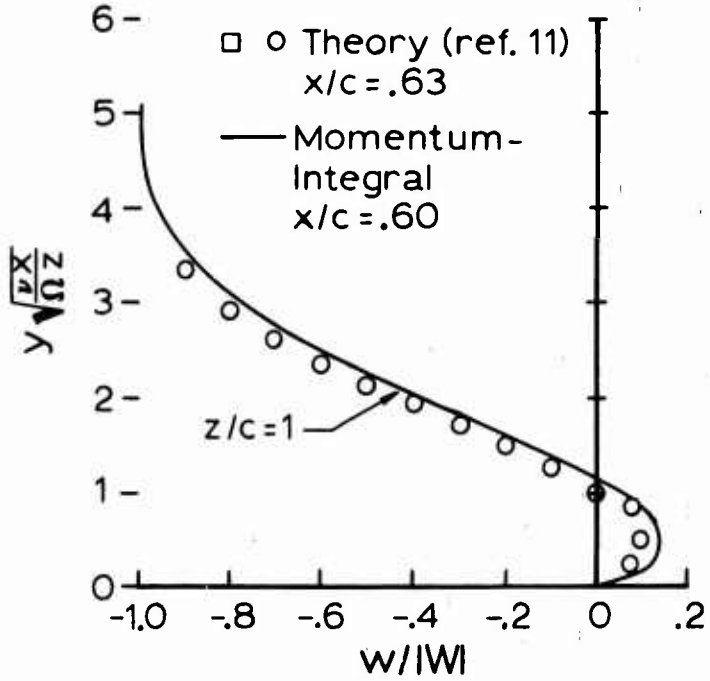

Figure 23. Comparison of Spanwise Velocity Profile With Reference 11 for an NACA 0012 Airfoil.

shear stress was actually increasing at $x/c = 0.6$ and $z/c = 1.0$. Therefore, the two profiles in Figure 22 represent a decelerated flow at $z/c = \infty$ and an accelerated flow at $z/c = 1$.

The spanwise profile at $x/c = 0.6$ and $z/c = 1.0$ is shown in Figure 23. The data from Dwyer and McCroskey[11] are again included for comparison. The spanwise flow exhibits considerably more outflow than was observed in the profiles on a rotating flat plate. This greater outflow can be attributed to the deceleration in the chordwise potential flow. As the chordwise flow slows down, continuity must still be preserved; therefore, the spanwise flow acts as a flow relief and reduces the rate of boundary layer growth.

The separation line determined from the momentum-integral analysis for the 0012 airfoil is illustrated in Figure 24. This is the first real discrepancy between the results of Dwyer and McCroskey[11] and those presented in this study. The two-dimensional asymptote from the momentum-integral analysis occurs at $x/z = 0.77$ while that reported by Dwyer and McCroskey[11] occurs at $x/c \approx 0.70$. The delaying effect of rotation appears to be quite similar for both methods, which indicates that the two-dimensional separation lines are displaced.

The reason for the disagreement in the two-dimensional separation lines is unknown to the authors. The potential flow used by Dwyer and McCroskey[11] was not described in detail, and it is not known how the derivatives of the potential flow components were obtained. To check the capability of the momentum-integral analysis to predict separation, calculations were made for two-dimensional flow over a circular cylinder. The results indicated that laminar separation on the circular cylinder occurs at an angle of 107.5° from the stagnation point. The value reported by Schlichting[16] as a so-called "exact" location of laminar separation is 108.8°. This value was obtained by a power series method which included terms through x^{11}. This example gave strong evidence that the momentum-integral analysis could predict separation to within 1 percent of the "exact" value.

This is not considered to be conclusive evidence that the separation line on an NACA 0012 airfoil is at $x/c = 0.77$. Indeed, there could be some discrepancy in the assumed potential flow for this analysis and that of Dwyer and McCroskey.[11]

Since similarity does not exist on the airfoil, the ratio of the chordwise wall shear stress to the equivalent two-dimensional shear stress must be presented in two separate figures.

In Figure 25, this shear ratio is presented for a fixed chordwise position and a variable spanwise position. The chordwise positions are at $x/c = 0.6$, 0.7, and 0.75 for the momentum-integral analysis while the data from Dwyer and McCroskey[11] are at $x/c = 0.63$. For large values of z, $x/z \rightarrow 0$, this shear ratio approaches unity. As the

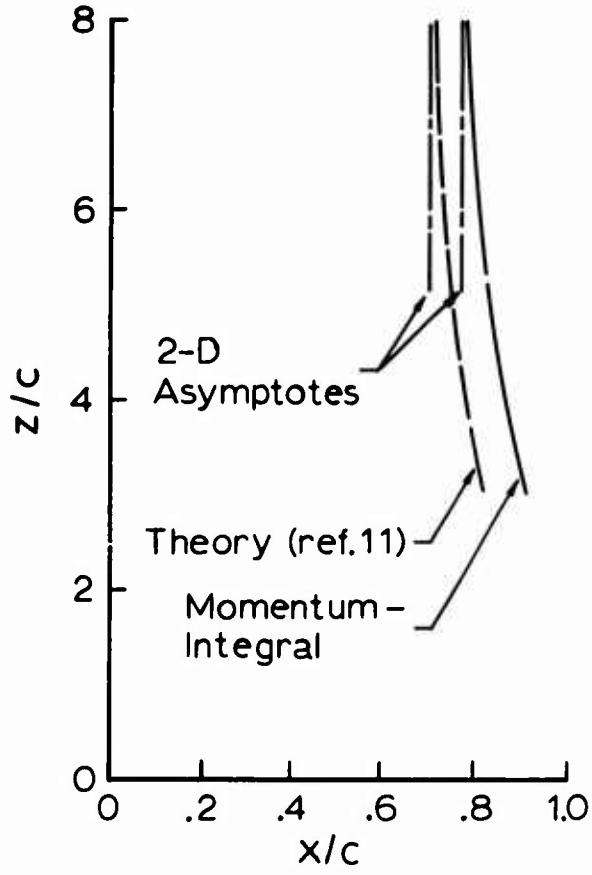

Figure 24. Comparison of Separation Lines With Reference 11 for an NACA 0012 Airfoil.

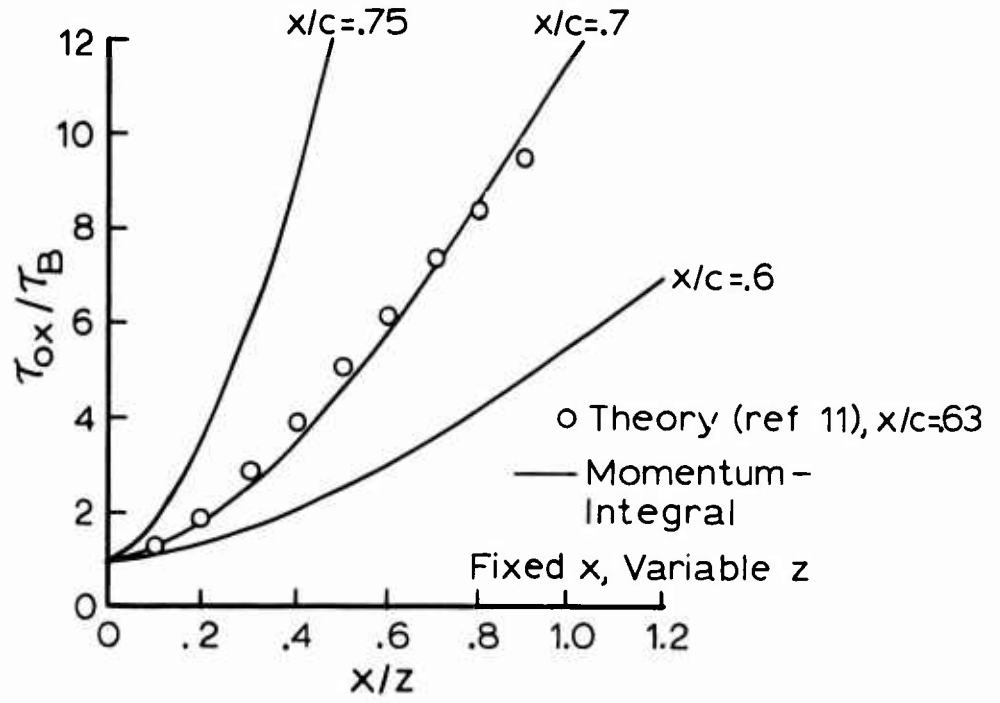

Figure 25. Spanwise Distribution of Chordwise Shear on a Rotating NACA 0012 Airfoil.

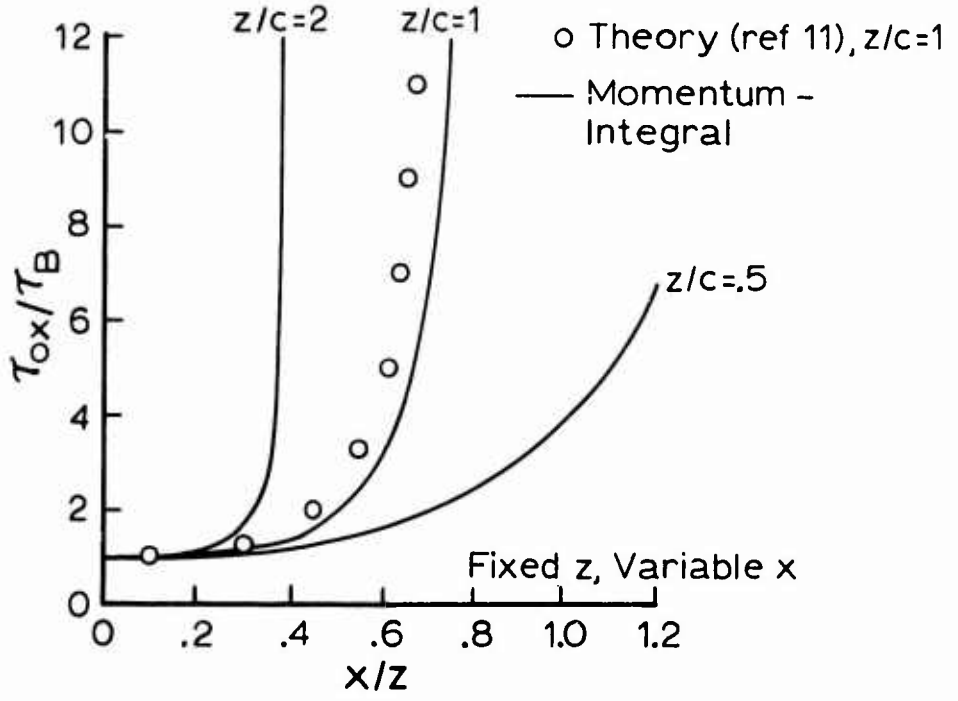

Figure 26. Chordwise Distribution of Chordwise Shear on a Rotating NACA 0012 Airfoil.

spanwise location is decreased, the shear ratio grows, indicating that the rotating flow is not approaching separation as fast as the nonrotating case.

The analytical results of Dwyer and McCroskey[11] at x/c = 0.63 compare quite favorably with the momentum-integral results at x/c = 0.7. This agreement can be explained by examining the separation lines in Figure 24. At x/c = 0.63, the results of Dwyer and McCroskey[11] are within a distance of 0.07 c of the 2-D separation point. At x/c = 0.7, the momentum-integral analysis is also within a distance of 0.07 c of the 2-D predicted separation point. Therefore, it is not unusual that the shear ratios from the two analyses agree at these two different chord positions.

In Figure 26, the shear ratios are plotted for fixed spanwise locations and variable chordwise positions. The discrepancy between the results in this analysis and those of Dwyer and McCroskey[11] at z/c = 1 can again be traced to the difference in the predicted two-dimensional separation points. The rapid rise in the shear ratio for increasing x (for fixed z you move directly along the chord) is indicative of the fact that the two-dimensional chordwise wall shear vanishes at a smaller value of x than the rotating three-dimensional shear.

Aside from the reported displacement of the two-dimensional separation line, the three-dimensional momentum-integral analysis was found to agree quite well with the more complex method of Dwyer and McCroskey[11] for the NACA 0012 rotating boundary layer calculations.

2.4.4 NACA 0015 at Zero Incidence

The final case considered in this analysis is an NACA 0015 airfoil. The momentum-integral technique was proven to be a useful analytical tool by comparing the results of sections 2.4.1 and 2.4.3 with those of Dwyer and McCroskey.[11] Since the NACA 0015 airfoil is also used on a number of helicopter rotors, a small portion of the boundary layer results for this airfoil are included.

The chordwise and spanwise velocity profiles are shown in Figures 27 and 28, respectively. The results are quite similar to those for the 0012 airfoil. The chordwise profile for $z/c = \infty$ and x/c = 0.6 more nearly resembles a separation profile near the blade surface than the corresponding profile in Figure 22. The region of spanwise outflow appears to persist for a greater distance above the surface than for the 0012 airfoil.

The location of the separation line for the 0015 airfoil is presented in Figure 29. The results from the 0012 airfoil are included for comparison. The 0015 airfoil is thicker and has a steeper chordwise pressure gradient, as illustrated by the potential flow calculations in sections 2.3.4 and 2.3.5. Therefore, the boundary layer separates at a smaller value of x/c on the 0015 than on the 0012 airfoil. Since Dwyer and McCroskey did not consider a 0015 airfoil, no comparison can be made with their results for this case.

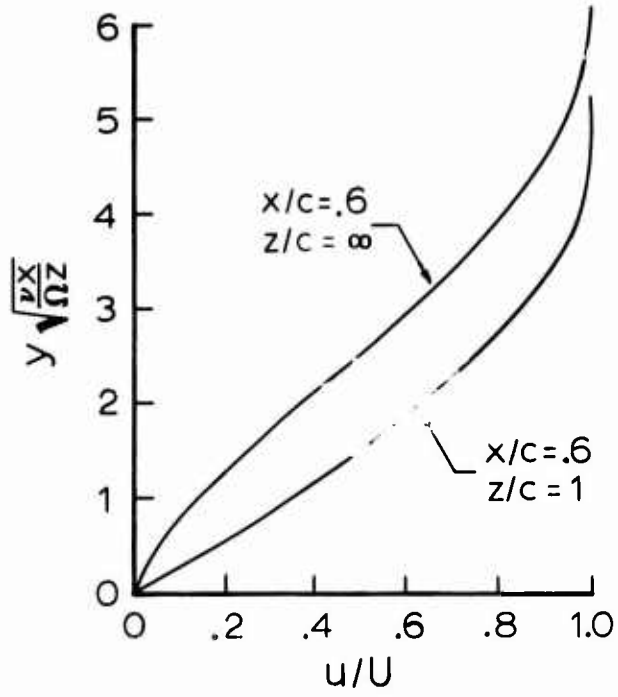

Figure 27. Chordwise Velocity Profiles for an NACA 0015 Airfoil.

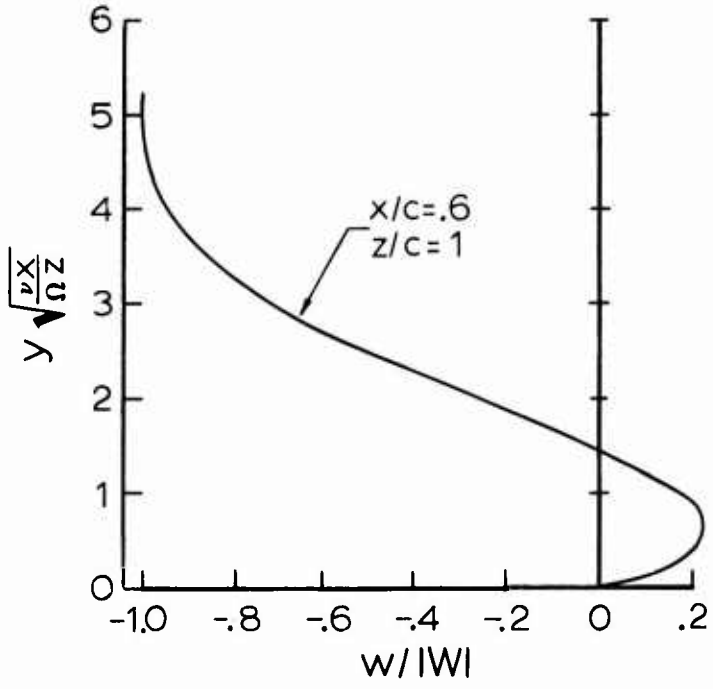

Figure 28. Spanwise Velocity Profile for an NACA 0015 Airfoil.

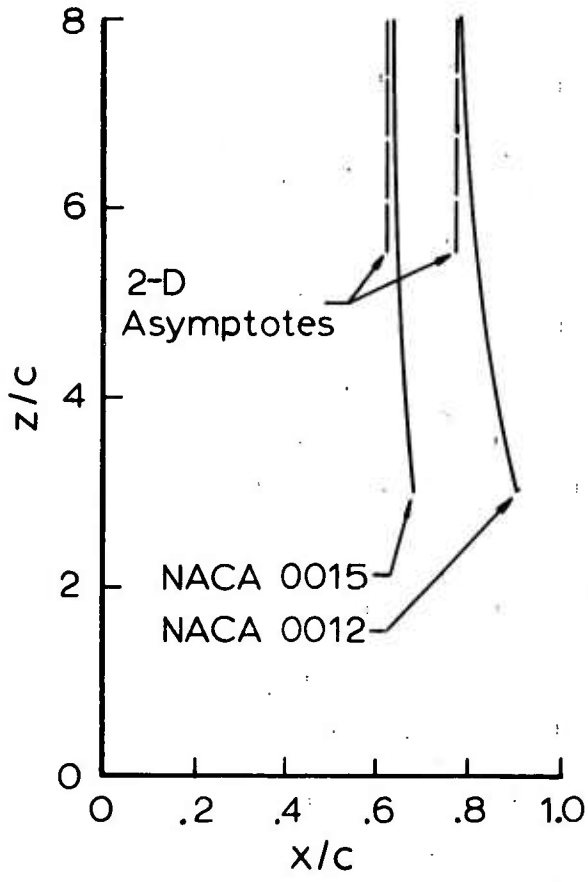

Figure 29. Comparison of Separation Lines for Rotating NACA 0012 and 0015 Airfoils.

III. EXPERIMENTAL STUDIES OF ROTOR BOUNDARY LAYERS--HOVER

The experimental portion of this research was designed to be a preliminary study of the feasibility and usefulness of three experimental techniques for the study of boundary layer behavior tip flow and was not intended to be a conclusive study. The study included flow visualization, surface static pressure data, and boundary layer flow magnitude and direction data.

3.1 TESTING EQUIPMENT

3.1.1 Rotor Stand Test Module

The rotor test stand used to simulate model rotor hover conditions is shown in Figures 30 and 31. A single-blade rotor was used throughout this study. The rotor is powered by two air motors which are connected to a 100-psi supply line through a control valve. The rotor speed is controlled by regulating the air flow rate to these motors. A tachometer is connected to the rotor shaft by a timing belt to prevent slippage errors. A hollow drive shaft permits electronic instrumentation cables to be fed from the rotor hub instrumentation systems to the slip-ring unit at the base of the rotor stand. Cables are attached to the stationary portion of the slip-ring unit and fed through an electrical conduit to the data console located behind the safety wall. The slip-ring unit consists of fifteen rings and uses carbon graphite brushes.

3.1.2 Rotor Blades

All of the rotor blades used had the same construction and were originally the same length. Rotor tests were conducted in a flow channel during latter stages of this study. Because of the limitations of the test section size, a reduction in the length of the rotor blades was necessary.

To minimize the mutual interference between various pieces of instrumentation, three separate blades were fabricated. Each blade was designed to incorporate the instrumentation required to obtain one type of experimental data. The blades were constructed with birch forward sections and balsa trailing sections. The physical data for the three rotor blades are given in the table on page 63.

The flow visualization rotor blade is shown in Figure 32. This blade was constructed for use in a tip flow study.[25] The screws near the tip permit interchangeability of blade tips.

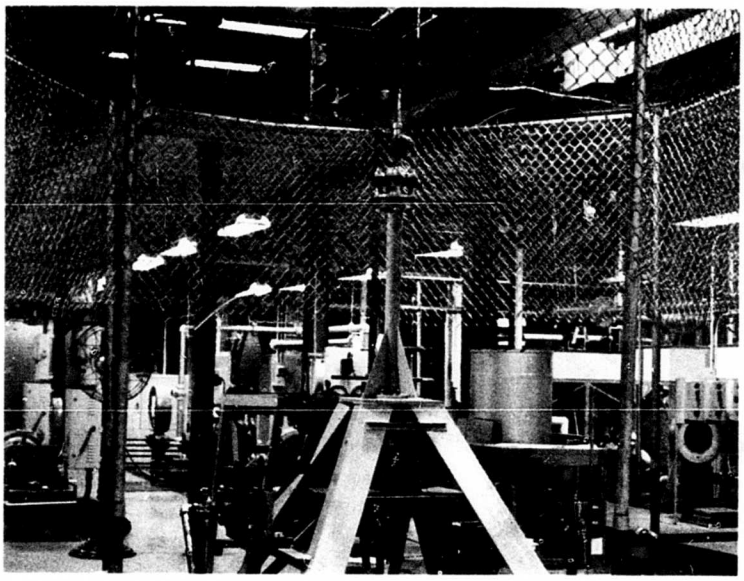

Figure 30. Hover Test Stand.

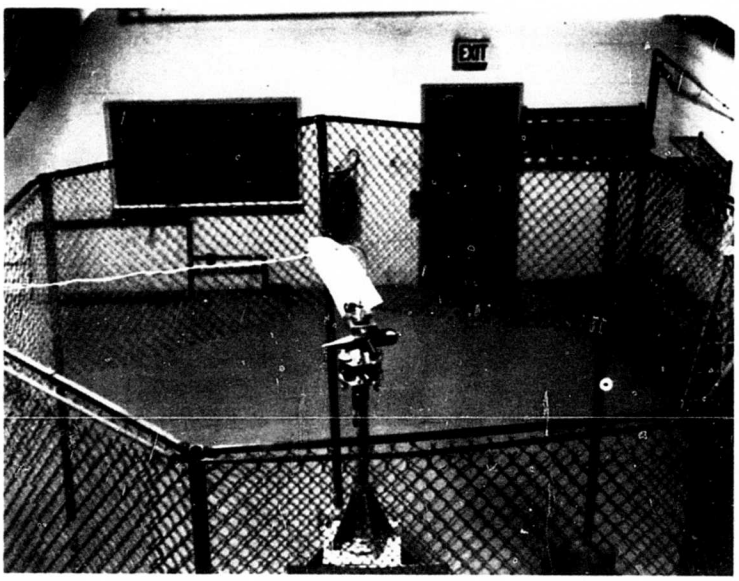

Figure 31. Single-Blade Rotor on Hover Test Stand.

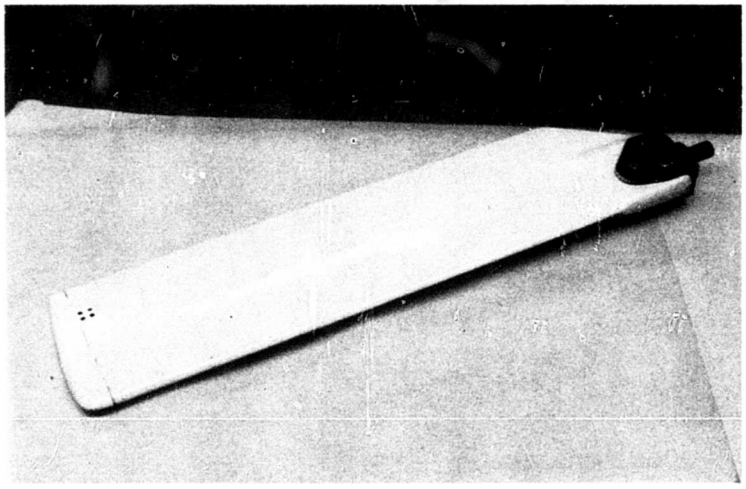

Figure 32. Rotor Blade for Flow Visualization Studies.

PHYSICAL ROTOR DATA

Description	Rotor Blade		
	Visualization	Pressure	Velocity
Airfoil Designation	NACA 0012	NACA 0012	NACA 0012
Span (ft)	4.0	3.50	4.0
Chord (ft)	0.75	0.75	0.75
Twist (deg)	None	None	None
Disk Area (ft^2)	50.2	38.5	50.2
Solidity	0.0596	0.0682	0.0596
Effective Root Cutout (%R)	8.9	9.3	8.9
Lock Number	2.12	1.61	1.82

3.1.3 Pressure Transducers

The pressure transducers utilize semiconductor type strain gages bonded to stainless steel diaphragms and are designed to operate in severe environments. The range of each transducer is 0-25 psia, over which the linearity and hysteresis were quoted at ±0.5 percent of full scale.

In order to remove the pressure transducers after completion of tests, a mounting pad was constructed for each transducer; the typical transducer-pad assembly is shown in Figure 33. The transducers were epoxied onto the pads in such a way that the diaphragm was cantilevered. This prevented the transducer from sensing the strain of the blade. The pad is then attached to the rotor blade with a single screw. In this manner, the transducer was mechanically attached to the rotor blade and could be removed easily.

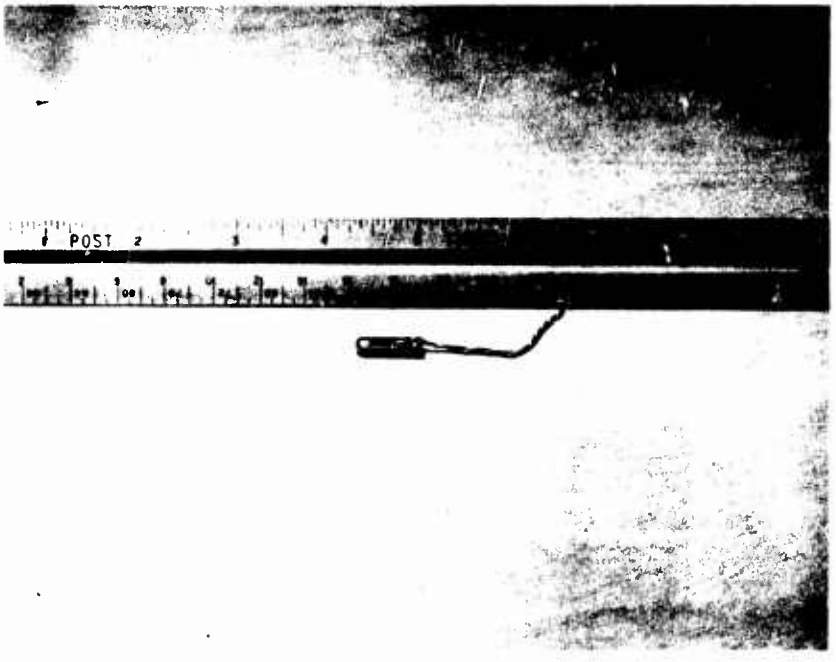

Figure 33. Pressure Transducer and Mounting Pad Assembly.

Figure 34 illustrates the transducers during the mounting process. On the right, the transducers are visible, including the wiring and solder tabs. On the left, the transducers have been covered with thin strips of veneering. Each strip was individually tailored and in each a small hole was drilled prior to attachment with epoxy. After all of the veneering strips were cemented in place, the blade surface was smoothed using very fine sand paper. Finally, the small pressure taps above the transducers were covered and the blade was painted to assure a smooth surface. Although the steps outlined in the mounting procedure were brief, mounting was a very tedious task due to the ease with which the thin diaphragms could be damaged.

The sensitivities of the transducers vary from 1 mV/psi to 2 mV/psi. The output signals that must be transmitted through the slip rings are on the order of 1 mV. Since the available slip-ring unit has a background ring noise of this same order, signal amplification was required. An amplifier package consisting of twelve amplifiers, one for each transducer, and a power regulator for controlling the input transducer power was constructed and is shown in Figure 35. The transducers were paralleled for common power. This amplifier unit was mounted on the rotor hub for signal amplification prior to signal transmission by the slip rings.

3.1.4 Hot-Wire Anemometers

The anemometers used to measure velocities are constant temperature or constant resistance anemometers.

The anemometer probe consists of a fine wire sensor whose resistance is a linear function of temperature. This probe is incorporated as one leg of a Wheatstone bridge network. Let us assume the bridge is balanced. Then, if the sensor temperature changes, the bridge will be unbalanced and a voltage will be present across the output terminals of the bridge. This voltage is amplified by a high-performance d-c differential amplifier. The signal is then fed into a single-ended d-c amplifier for additional gain. This final amplification stage also acts as a d-c level power amplifier since it is placed in a Darlington configuration with a third amplifier. Finally, the current from the output of the Darlington pair is fed to the bridge with a sign to cause the resistance of the probe to change and balance the bridge network. The anemometer output voltage is an indication of the power required to balance the bridge. The value of probe resistance which balances the bridge can be adjusted by varying the value of the potentiometer used as the bridge leg adjacent to the probe. This leg is termed the "overheat" resistor since its value determines the difference between the probe temperature and ambient temperature at zero flow.

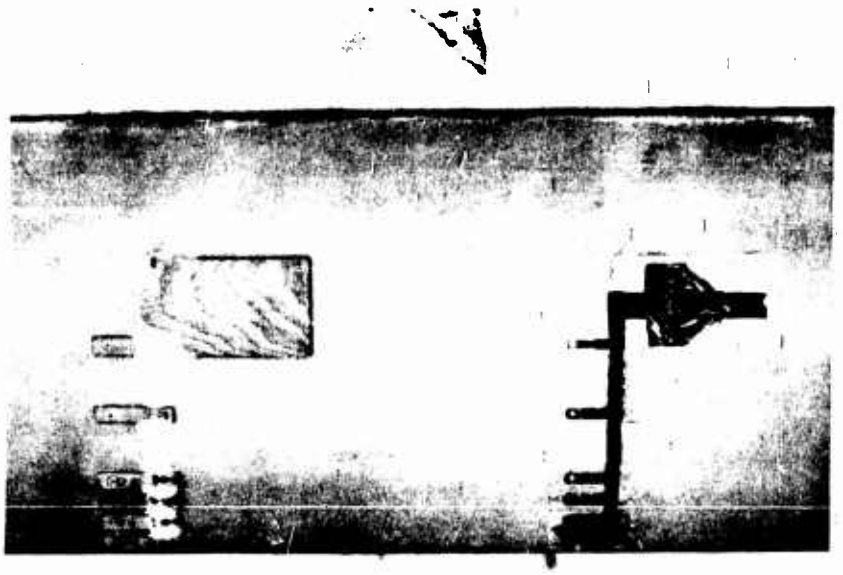

Figure 34. Pressure Blade Showing Transducer Mounting Technique.

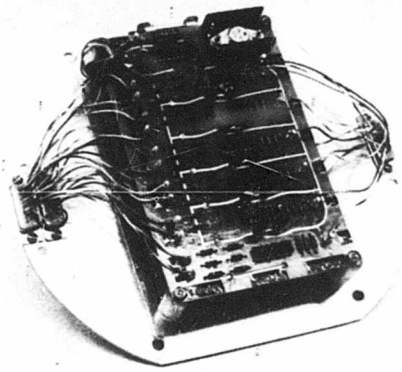

Figure 35. Amplifier Package for Twelve Pressure Transducers.

As was the case with the pressure transducers, the slip-ring noise would mask the anemometer signal unless the aforementioned amplification was mounted on the rotor hub. Thus, only the printed-circuit boards used in the commercial anemometers were purchased. Two of these boards were customized into a dual anemometer package that could be mounted on the rotor hub (see Figure 36). The two boards were mounted vertically facing one another to minimize centrifugal effects.

The operation of the anemometer depends on the heat transfer characteristics between the sensor and the stream being measured. These heat transfer characteristics cause the output voltage to be a nonlinear function of stream velocity at the sensor. As a result, the anemometer is extremely sensitive to low velocities and has a very low sensitivity for high velocities. For boundary layer measurements, a wide range of velocities will be encountered; therefore, linearizers were incorporated to make the sensitivity nearly uniform over the complete velocity range (see Figure 37).

The first hot-wire probe that was used in this study was a boundary layer X-configuration probe. This probe is shown in Figures 38 through 40. The probe was designed to be mounted above the blade surface with the sensors extending into the boundary layer. The X-configuration of the two sensors is clearly defined in Figure 39. This planar orientation of the two sensors is standard for measurement of both flow magnitude and direction except for the vertical spacing between the two wires. Standard probes have a spacing of 0.05 inch while the wires for this probe were placed as close as physically possible and are shown in Figure 40 to be about 0.009 inch. The photographs in Figures 39 and 40 have an amplification of about 40.

This probe was calibrated and tests were initiated on the hover stand. After a few minutes of operation, the sensors were found to be destroyed. New wires were placed on the probe, the probe was recalibrated, hover tests were initiated, and again the sensors were destroyed. After examining the sensors under a microscope, the damage in each case was observed to be a break in the wires at the center of the X. This indicated that either the wires came in physical contact or there was sufficient electronic interference to burn the wires.

To eliminate both of the methods in which the wires were believed to be damaged, a second type probe was ordered. This probe was identical to the first except that the wires were placed in a V-configuration instead of an X-configuration. This permitted the wires to be placed at the same vertical height, which eliminates the measurement error due to the sensors being located at two different boundary layer heights. This V-configuration is shown in Figure 41 with a magnification of about 20. The wire-to-wire interference for this type of probe is considerably reduced. All of the anemometer data reported was obtained from this V-configuration probe. All of the hover data was obtained with a single set of sensors on the V-probe.

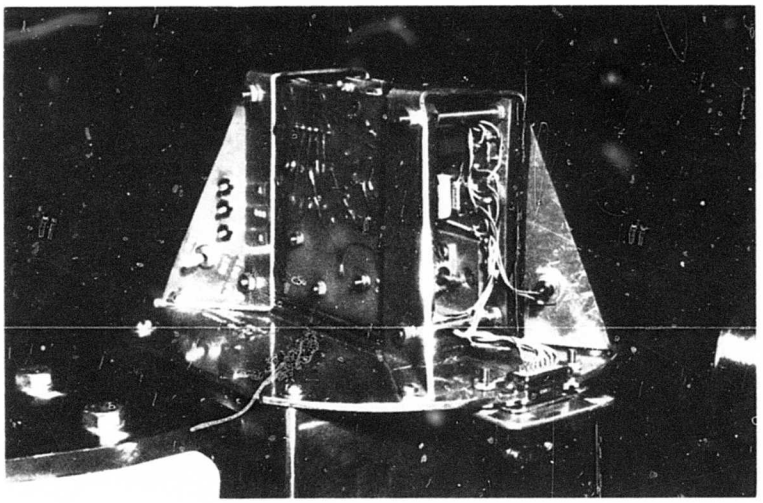

Figure 36. Dual Constant-Temperature Anemometer Package.

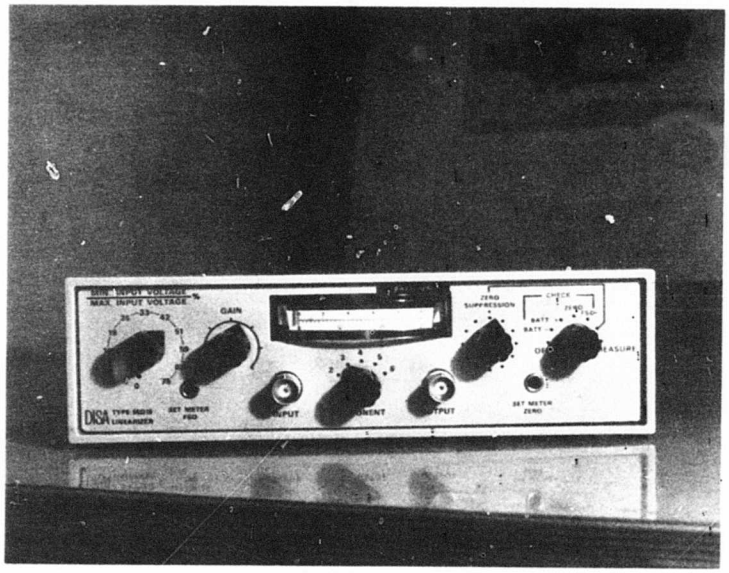

Figure 37. Anemometer Linearizer Unit.

Figure 38. X-Configuration Hot-Wire Boundary Layer Probe.

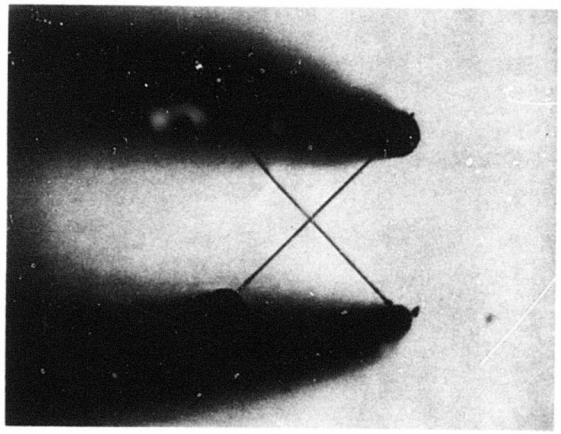

Figure 39. X-Configuration With About 40X Magnification.

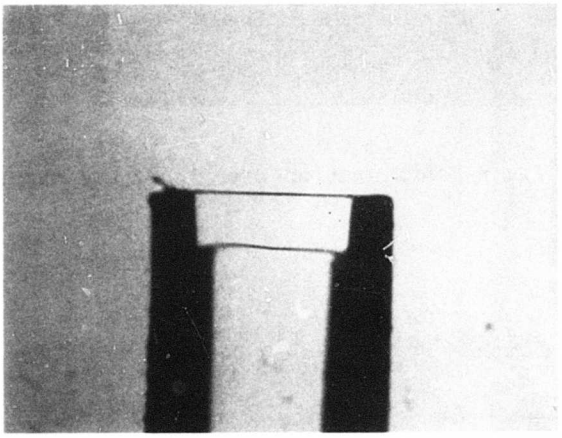

Figure 40. Side View of X-Probe Showing Wire Spacing.

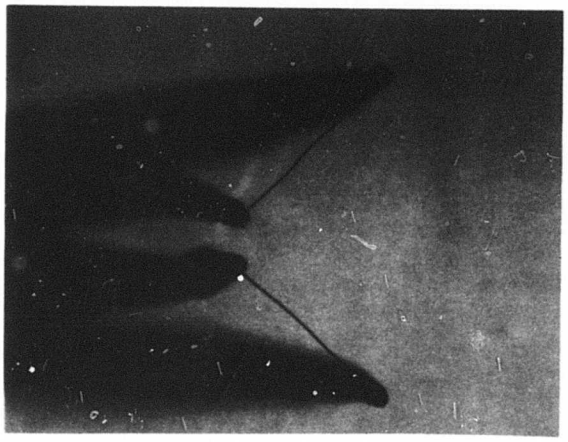

Figure 41. V-Configuration With About 20X Magnification.

3.2 CALIBRATION SYSTEMS

3.2.1 Rotor Stand

The hover stand rotor speed was monitored by a tachometer which was driven by the rotor shaft. The following technique was used to calibrate an accurate scale for the tachometer.

A gear was mounted on the rotor shaft,and a magnetic pickup was rigidly attached to the rotor stand and placed within approximately 1/8 inch of the gear teeth. As the gear teeth pass by the magnetic pickup, they cut magnetic field lines and generate small pulses of electrical current. The frequency of these current, or voltage, pulses can be related directly to the rotor speed.

The pulse frequency could be obtained from an oscilloscope trace of the pulses and a visual count; however, this makes it very difficult to set a desired rotor speed. For this reason, an electronic EPUT (events-per-unit-time) counter was incorporated into the calibration. This meter electronically counts the number of pulses for a preset time period and presents the results on a digital display.

With this technique, the rotor speed was calibrated within an accuracy of 0.5 percent; however, during testing it was not possible to maintain a desired rotor speed more accurately than approximately ±2 percent.

3.2.2 Pressure Transducer

The pressure transducers were calibrated a number of times using three different techniques.

First, the transducers were calibrated by the manufacturer before they were mounted on the specially designed pads. This calibration was performed in a pressurized chamber and was presented as full-scale output millivolts. The calibration was performed at three temperatures from 30°F to 130°F in order to attest the accuracy of the temperature compensation network. Although it varies for each transducer, the maximum sensitivity drift with temperature was only 0.01 mV/°F, while the sensitivity magnitudes varied from 1 mV/psi to 2.5 mV/psi.

A second calibration was performed prior to submerging the transducer-mounting pad assemblies in the rotor blade. The transducers were recalibrated in a pressurized container shown in Figures 42 and 43. The container was sealed by "o-rings" and the cables were removed through a tubing connection in the side. The pressure was controlled by a needle valve while the chamber pressure was recorded by a static pressure port and a mercury or water manometer. A vacuum pump was also used to complete the calibration from -8 psig to +8 psig. The results of this calibration were within 2 percent of the data supplied by the manufacturer.

Because of the complexity of the transducer-mounting and subsequent surface smoothing, a third calibration was performed. This calibration was conducted after the transducers were mounted in the rotor blade surface and surface smoothing was completed. This final calibration technique is depicted in Figure 44, where a tee-connection is shown at the upper part of the drawing. Plastic tubing was connected to each of the upper arms of the tee. One tube led to the manometer and the other tube led to the vacuum supply line. A piece of pliable rubber tubing was placed on the bottom leg of the tee. This rubber tubing could be pressed against the blade surface and a vacuum could be maintained within the tee-connector. Using this device, the transducers could be individually calibrated at any time prior to, or after, the tests.

The results of this final calibration are presented in Figure 45 for a typical transducer. Since all of the transducers were mounted on the upper surface of the blade (the suction side), only negative gage pressures were used during this calibration. The slope of the straight line drawn through the data points was determined by a least square-error method. The data are linear to within 1 percent, and the transducer sensitivities were invariably repeatable to within 2 percent.

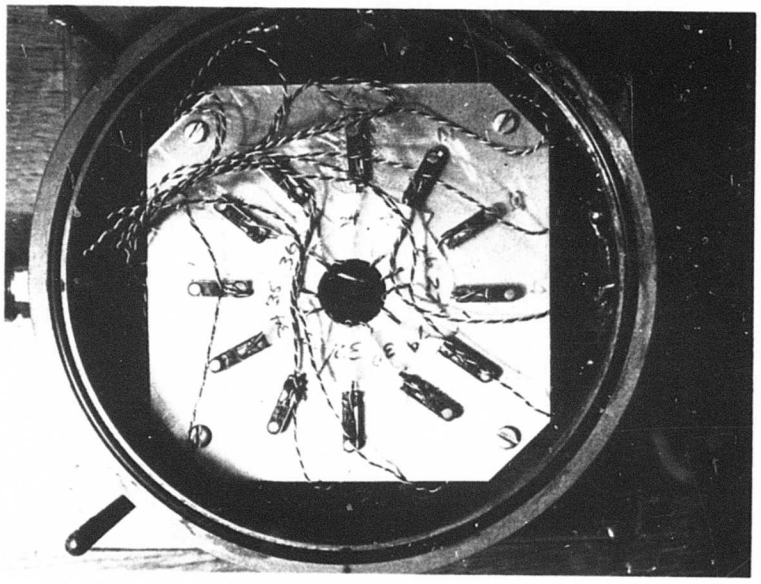

Figure 42. Pressure Transducer Calibration Chamber.

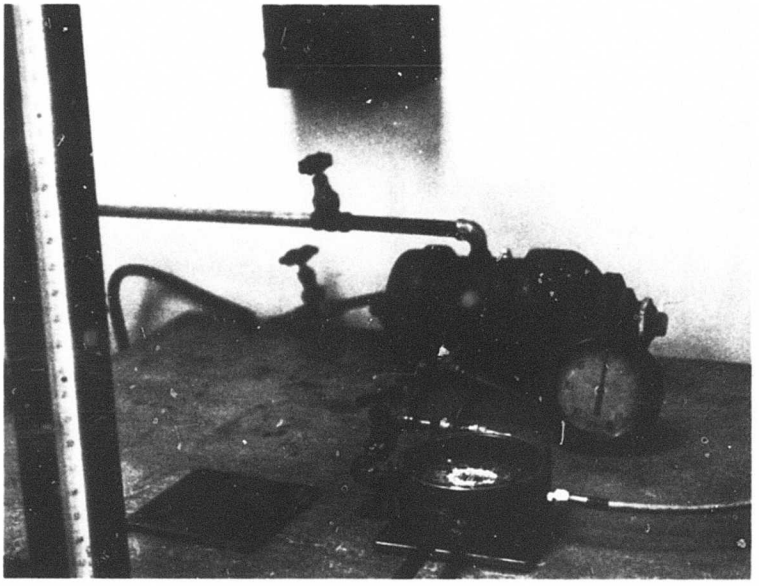

Figure 43. Pressure Transducer Calibration Apparatus.

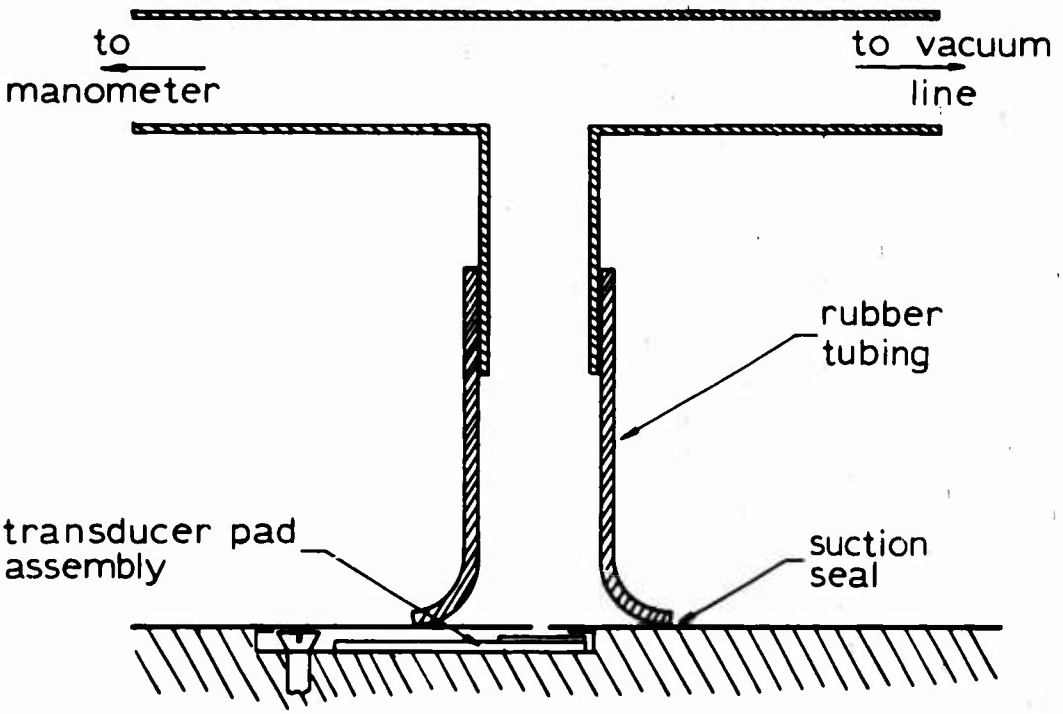

Figure 44. Calibration Device for Pressure Transducers Mounted in Rotor Blade.

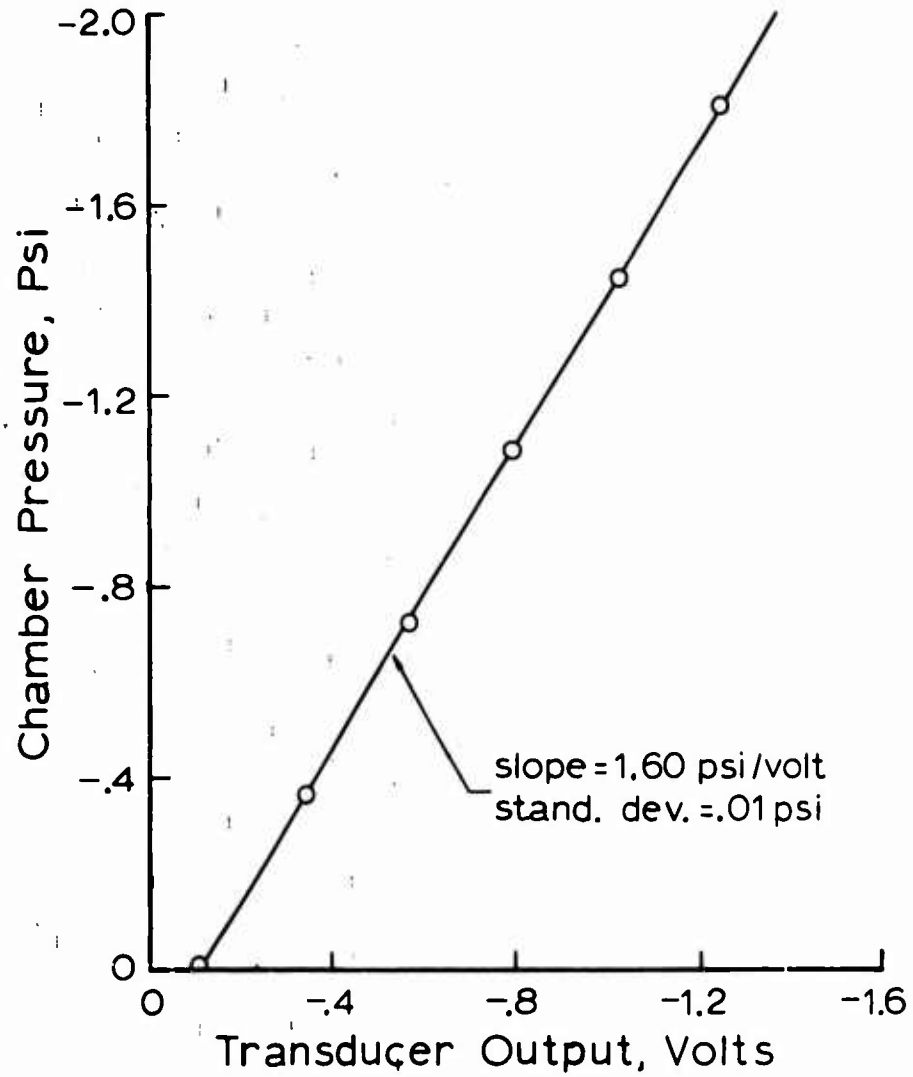

Figure 45. Calibration of a Typical Pressure Transducer.

Finally, the complete transducer electronics system was checked during each calibration.

3.2.3 Hot-Wire Anemometer

In order to calibrate a V-configuration probe which is to be used for measurement of flow magnitude and direction, it is necessary to have a laboratory standard flow with a known magnitude and direction.

To produce such a standard flow, the device shown in Figure 46 was designed, constructed and calibrated. The body consists mainly of a cylindrical chamber made from 4-inch aluminum pipe with a nozzle at one end. The chamber has a vertical plate to deflect the incoming flow, a set of five screens to reduce turbulence, and two ports to measure chamber pressure and temperature. The nozzle is conical with flared inlet and exit regions. The exit diameter is 0.375 inch.

A probe positioning device is shown attached to the top of the nozzle. The V-configuration probe is mounted in the small clamp directly in front of the nozzle. The flow direction relative to the probe body can be adjusted by rotating the probe. A protractor was mounted on the horizontal plate above the positioning device to record the probe's angular position. The speed of the flow at the nozzle exit is controlled by the needle valve located in the 100-psi supply line. An air filter was installed in this supply line to maintain a clean supply of air. Since considerable effort was spent calibrating this nozzle, Appendix I contains a discussion of the method and results of this calibration.

The V-configuration probe calibration was performed by setting a nozzle exit velocity and recording the output voltages of each anemometer at probe angular positions from -45° to +45' in increments of 5°. A complete calibration involved repetition of this process for a number of exit velocities to cover the range expected during testing.

An attempt was made to correlate the results of this calibration with the "cosine" law used by Champagne, Sleicher and Wehrmann[26] with a single wire probe. After many unsuccessful attempts of correlation with this simple law, it was concluded that another method must be used to maintain the accuracy of the calibration. A numerical technique was developed to correlate the calibration data.

Figure 47 illustrates the V-configuration denoting the left sensor as B and the right sensor as A. The stream velocity is of magnitude V and approaches the probe with an outflow angle γ. The components of velocity normal to sensors A and B are denoted by V_A and V_B, respectively. These velocities may be related to the flow magnitude V and direction γ by equations (94) and (95):

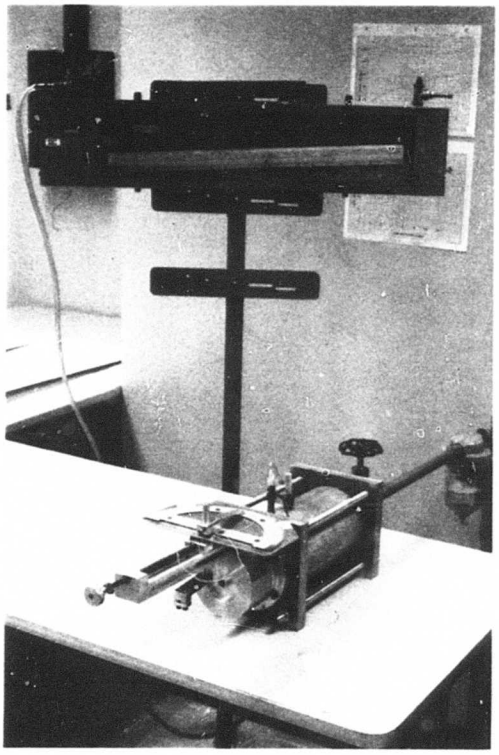

Figure 46. Hot-Wire Calibration Device.

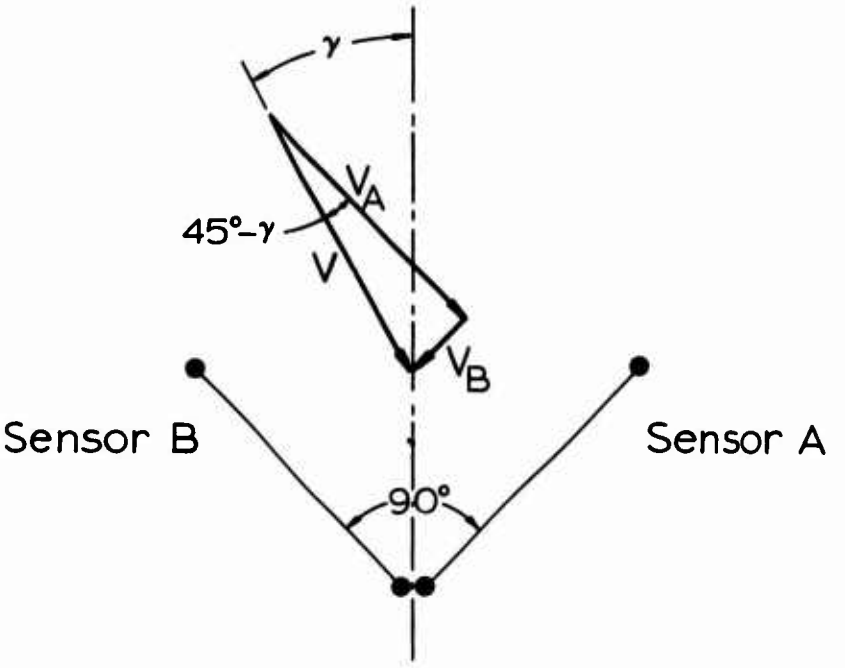

Figure 47. V-Configuration Hot-Wire Probe Geometry.

$$V_A = V \cos(45°-\gamma)$$

$$= \frac{V}{\sqrt{2}} (\cos\gamma + \sin\gamma) \tag{94}$$

$$V_B = V \sin(45°-\gamma)$$

$$= \frac{V}{\sqrt{2}} (\cos\gamma - \sin\gamma) \tag{95}$$

Rearranging these expressions yields

$$V \sin\gamma = \frac{V_A - V_B}{\sqrt{2}} \tag{96}$$

$$V \cos\gamma = \frac{V_A + V_B}{\sqrt{2}} \tag{97}$$

which can be solved directly for the flow magnitude and direction in the form given by equations (98) and (99):

$$V = \left[\left(\frac{V_A - V_B}{\sqrt{2}} \right)^2 + \left(\frac{V_A + V_B}{\sqrt{2}} \right)^2 \right]^{1/2} \tag{98}$$

$$\tan\gamma = \frac{V_A - V_B}{V_A + V_B} \tag{99}$$

Since linearizers were incorporated into the calibration, the components of velocity V_A and V_B are approximately proportional to the output voltages of anemometers A and B. With this in mind, the output voltages were grouped according to equations (98) and (99) and the following definitions were made:

$$\text{V-MAGNITUDE} = \left[\left(\frac{v_A - v_B}{\sqrt{2}}\right)^2 + \left(\frac{v_A + v_B}{\sqrt{2}}\right)^2\right]^{1/2} \tag{98}$$

$$\text{V-DIRECTION} = \frac{v_A - v_B}{v_A + v_B} \tag{99}$$

where v_A and v_B are the output voltages of anemometers A and B, respectively.

Calibration produces a data array of voltages v_A and v_B for various values of flow magnitude V and flow direction γ. To correlate these results, the voltage parameters V-MAGNITUDE and V-DIRECTION were calculated according to equations (98) and (99). Also, the flow magnitude was dimensionalized into the wire Reynolds number defined by

$$Re_w = \frac{Vd}{\nu} \tag{100}$$

where d is the wire diameter.

A computer program was devised to automatically perform a complete correlation of the resulting calibration data. This includes a regression analysis for subsequent data interpolation and computerized plotting of the data to show "goodness of fit". These plots are included in Figures 48 through 52. The solid lines in these figures represent the regression curve-fit, while the symbols are the calibration data.

Figure 48 illustrates the variation of these voltage parameters with wire Reynolds numbers and flow direction. During calibration, the flow direction is fixed and the probe is rotated; therefore, Figures 48 through 52 refer to γ as the probe body angle.

Figure 49 illustrates the variation of V-MAGNITUDE with wire Reynolds number. The variation of these data about a single straight line indicates that V-MAGNITUDE, while primarily a linear function of Re_w, has a slight variation with the probe body angle.

Figure 50 illustrates the variation of V-DIRECTION with the probe body angle. Again, V-DIRECTION is primarily a function of probe body angle; however, the data scatter indicate a slight variation with wire Reynolds number. If each wire identically obeyed the "cosine" law, V-DIRECTION could be represented as the tangent of the probe body

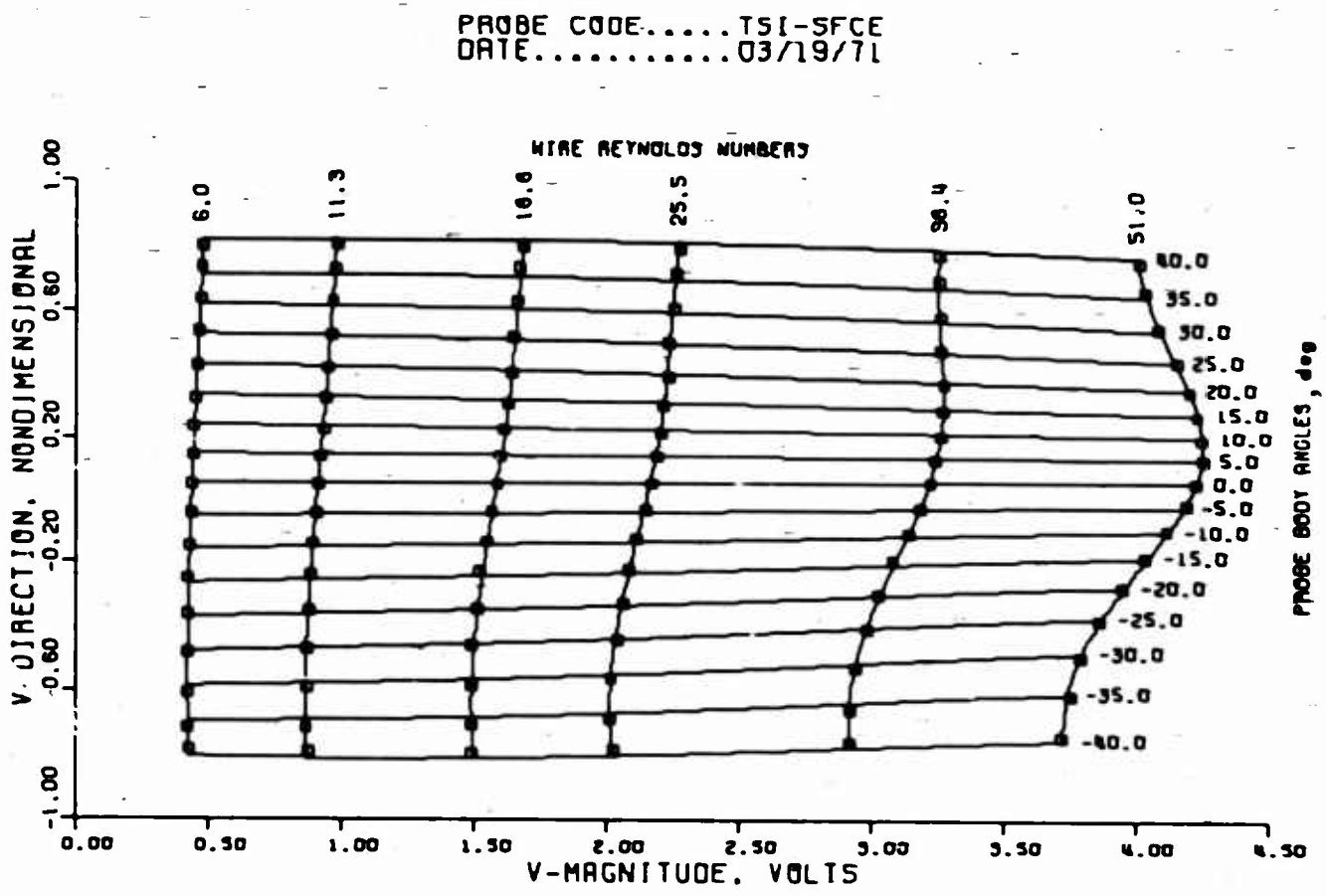

Figure 48. V-DIRECTION Versus V-MAGNITUDE.

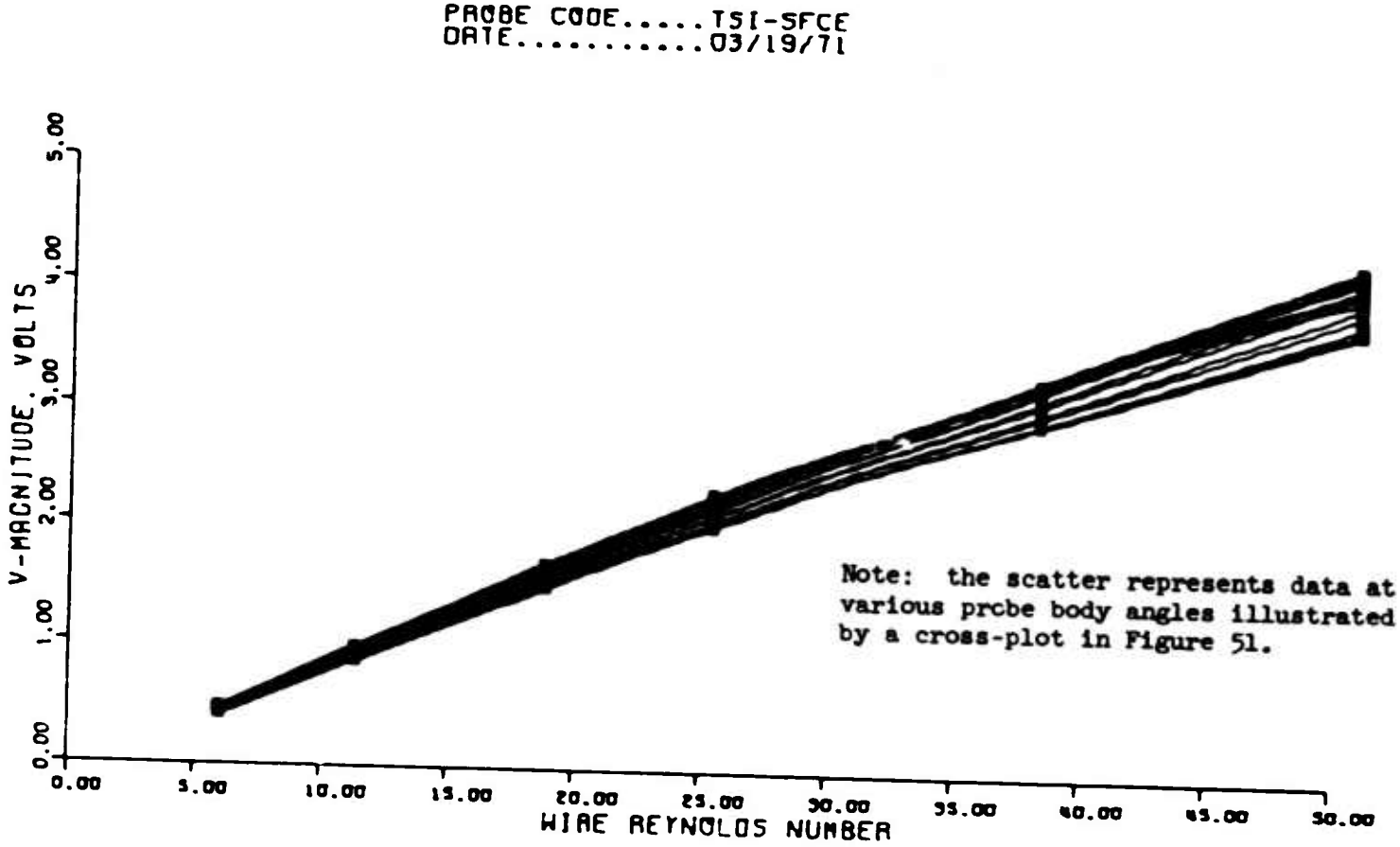

Figure 49. V-MAGNITUDE Versus Wire Reynolds Number.

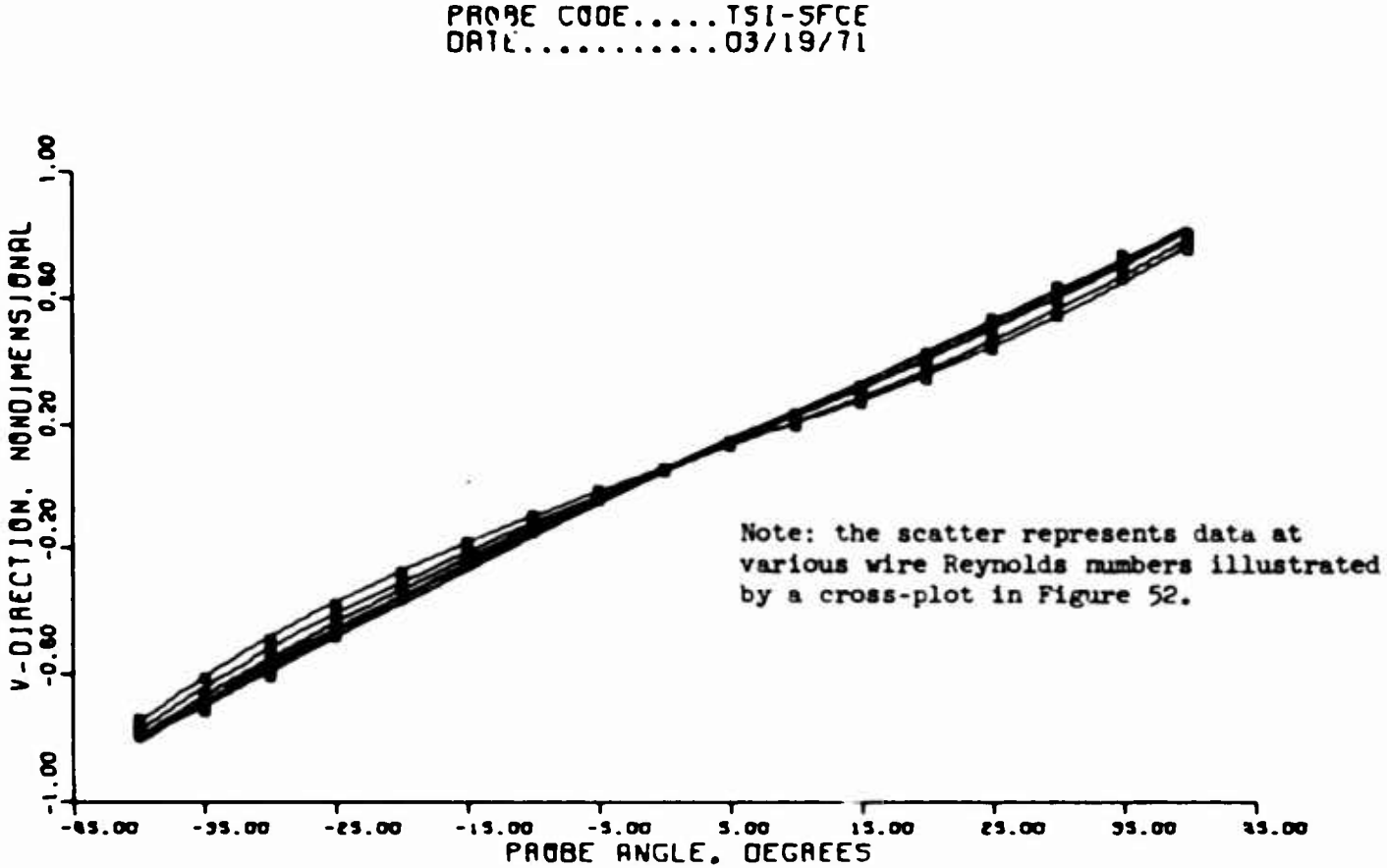

Figure 50. V-DIRECTION Versus Probe Body Angle.

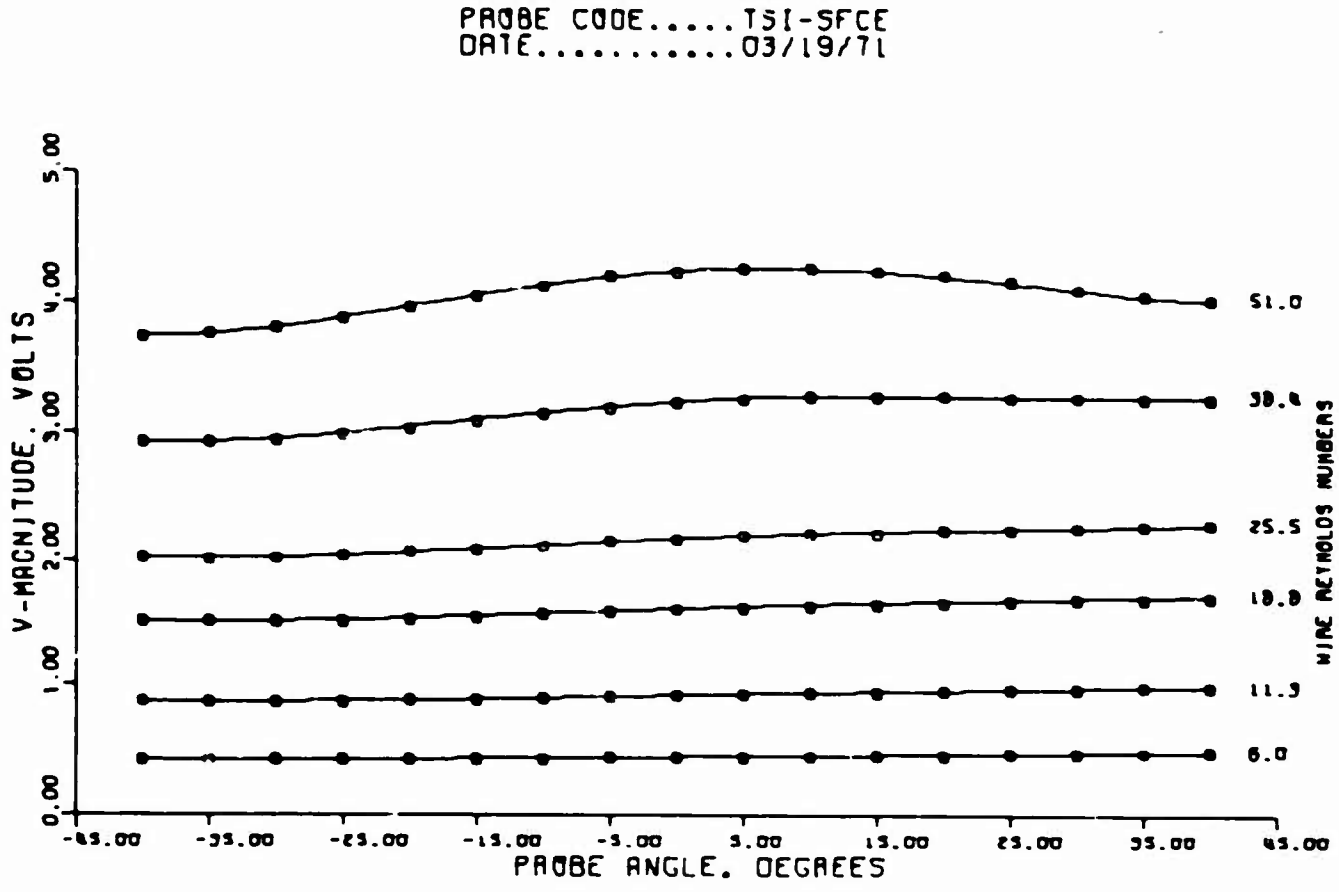

Figure 51. V-MAGNITUDE Versus Probe Body Angle.

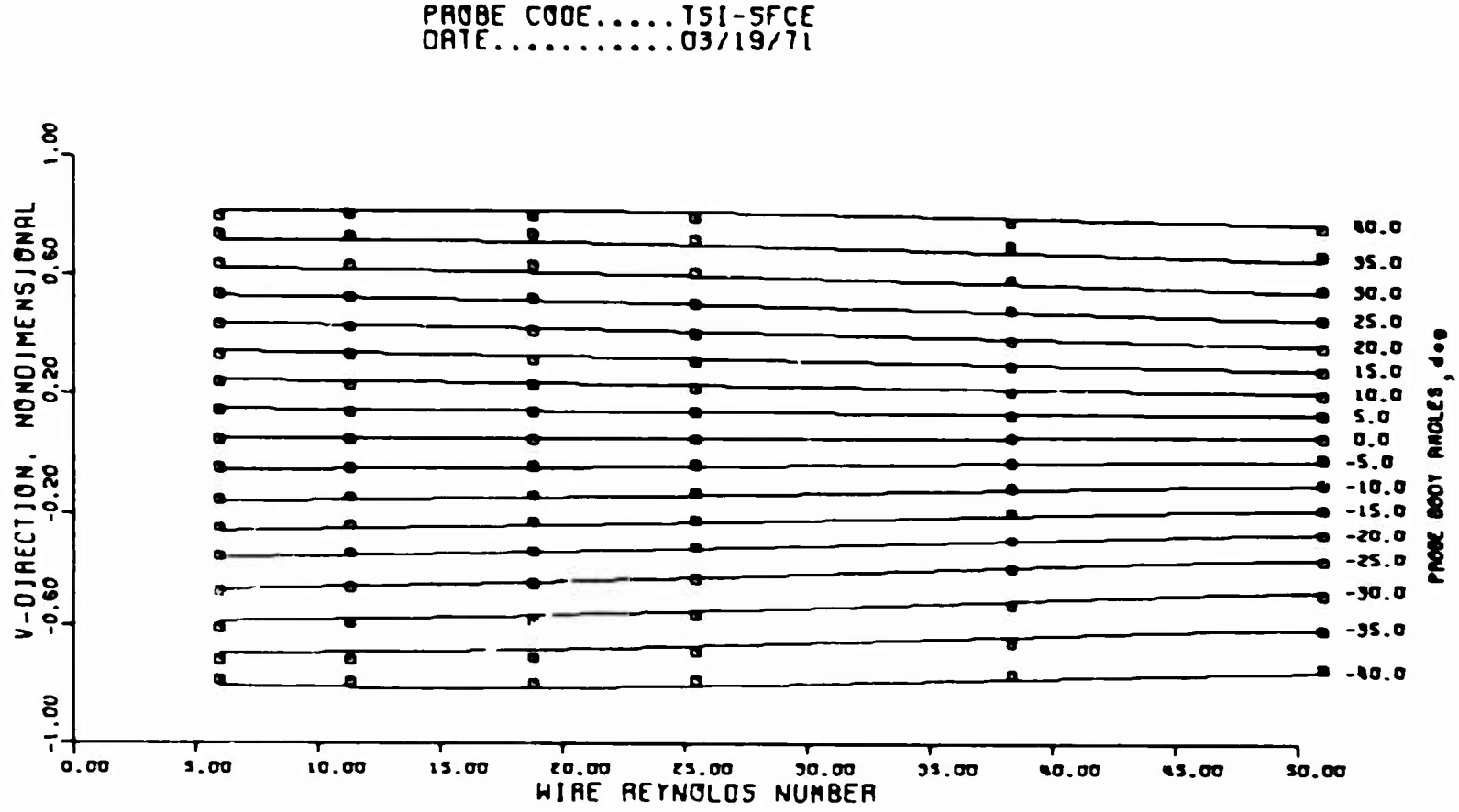

Figure 52. V-DIRECTION Versus Wire Reynolds Number.

angle. Therefore, Figure 50 would be a unique tangent curve, not a band of curves as were obtained in the actual calibration.

Figures 51 and 52 are cross-plots of Figures 49 and 50. They represent the secondary variations of V-MAGNITUDE and V-DIRECTION. These two figures best illustrate the accuracy of the regression analysis.

During data reduction, the regression analysis was solved in reverse. That is, the numerical curve-fit equations were solved for values of Re_w and γ when given the voltages V_A and V_B.

3.3 TESTING PROCEDURES

3.3.1 Visualization Tests

The ammonia feed apparatus used for the visualization tests is shown in Figure 53. The pressurized tank of gaseous ammonia was bubbled through a liquid ammonia solution and then fed to the top of the rotor stand shown in Figure 31. The ammonia then passed through a transfer ring, through a tube inserted in the rotor blade, and out the small orifices in the blade surface.

The technique used in these tests is almost identical to that described by Velkoff, Blaser and Jones.[27] The only difference is that the tests in this study incorporated a revolute film while those of Velkoff, Blaser and Jones[27] used regular ozalid paper. The revolute film comes in a variety of colors, has a more uniform coating of diazo dye, is more easily attached and removed from the blade, and gives a more permanent trace than the ozalid paper.

The surface traces are obtained by bringing the rotor to the desired hover condition and forcing ammonia to flow into the rotating boundary layer by opening the valve on the tank of gaseous ammonia. After the trace is formed, the valve is closed, the rotor is stopped, and the plastic revolute film is removed. This film represents a permanent surface trace for the set rotor conditions of the test.

3.3.2 Pressure Measurements

Each pressure transducer has a nonzero output voltage at atmospheric pressure condition. This offset voltage can vary from test date to test date due to barometric pressure variations. To account for this possible variation, the offset voltages were determined prior to testing and were checked during the conduct of any series of tests. During the actual testing, the offset voltages were found to remain constant. The values of this voltage were subtracted from the pressure transducer outputs to represent surface pressures above the barometric ambient pressure.

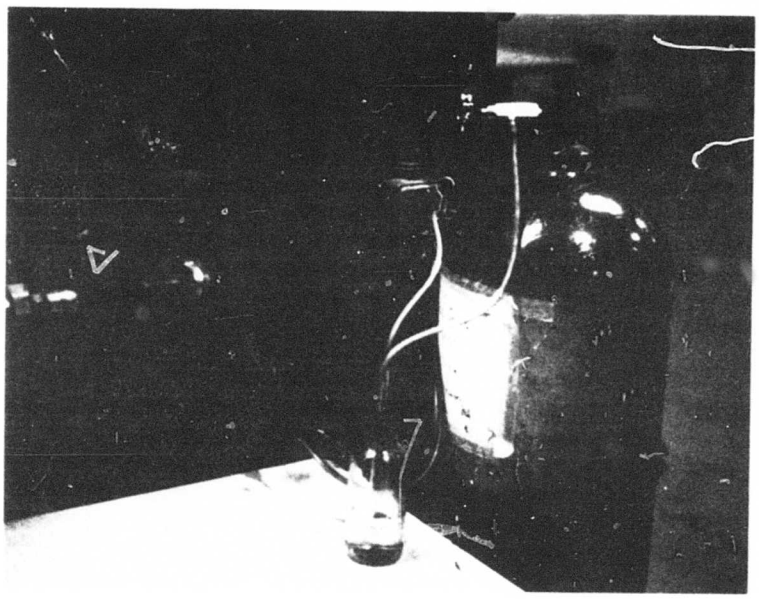

Figure 53. Ammonia Feed Apparatus for Visualization Tests.

The ambient temperature, barometric pressure, and wet-bulb temperature were recorded during each test to determine the local air density. The air density was used to calculate the local free-stream dynamic pressure and subsequently dimensionalize the data into pressure coefficient form.

All of the pressure data were obtained at 800 rpm and consisted of three consecutive independent tests.

3.3.3 Velocity Measurements

The velocity measurements represent the most significant experimental contribution of this study; thus, the anemometer testing procedure will be examined in detail.

The V-configuration probe was mounted above the blade surface and oriented as shown in Figures 54 and 55. Figure 54 illustrates the probe as it is viewed from the rotor blade tip. The anemometer amplifier package can be seen in the background. Figure 55 shows the probe as seen from the blade leading edge. The plane of the V-configuration sensors is set parallel to the blade surface by the apparatus pictured in Figure 56. It consists of a traversing microscope and associated mechanism to attach the microscope rigidly to the blade. By viewing the probe and probe surface simultaneously through the 100X lens of the microscope, the probe could be aligned accurately.

The vertical position of the probe is adjusted by rotating a nut attached on the bottom surface of the blade. A lock nut was used to maintain a fixed probe position during the tests. After the probe was locked in the desired position, the traversing microscope was used to measure the perpendicular distance from the blade surface to the sensor plane. This traversing mechanism permitted a readability to the nearest 0.0001 inch. Measurements were made from 0.1 inch to 0.002 inch to cover the complete boundary layer flow.

The tests were conducted in the following sequence. The chordwise and spanwise positions were chosen and the probe was aligned at this surface position by the technique just described. The probe was set at a position near 0.1 inch to represent a condition outside the boundary layer. At this probe position, tests were conducted at four rotor speeds (100, 200, 300, and 400 rpm) and four pitch angles (0°, 5°, 10°, and 15°). The probe was then lowered and tests were repeated until data was obtained across the entire boundary layer. This sequence of tests required the fewest adjustments of the probe and minimized the possibility of accidental probe damage from contact with the sensors.

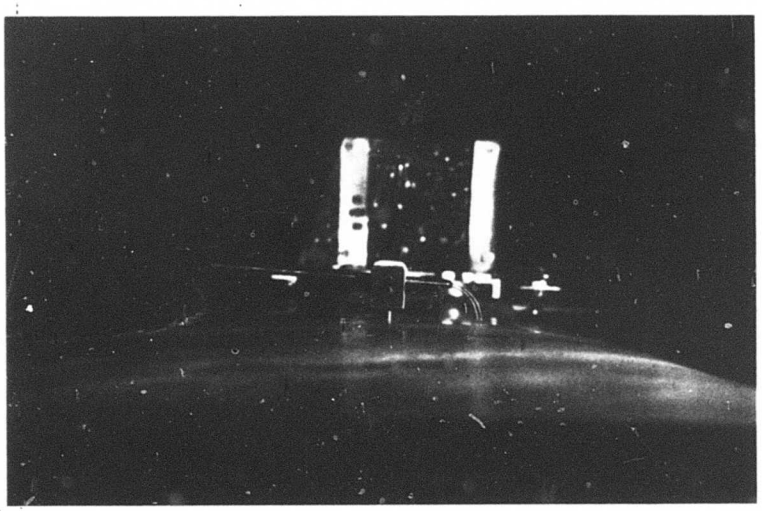

Figure 54. Hot-Wire Probe Mounted on Rotor Blade as Viewed From the Blade Tip.

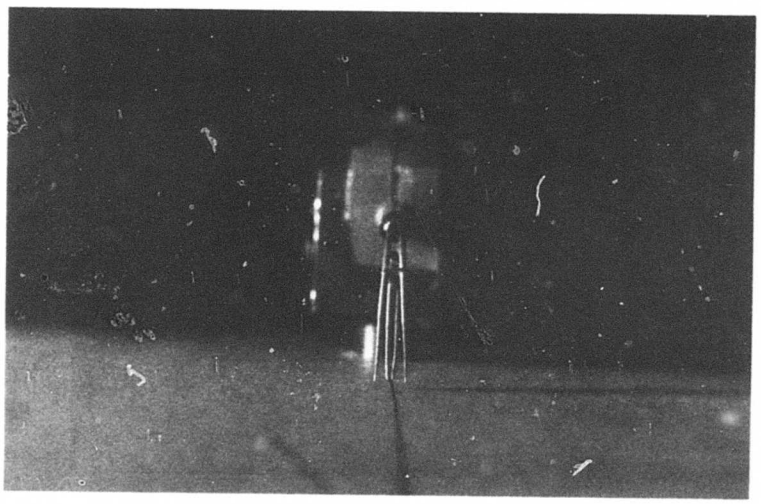

Figure 55. Hot-Wire Probe Mounted on Rotor Blade as Viewed From the Leading Edge.

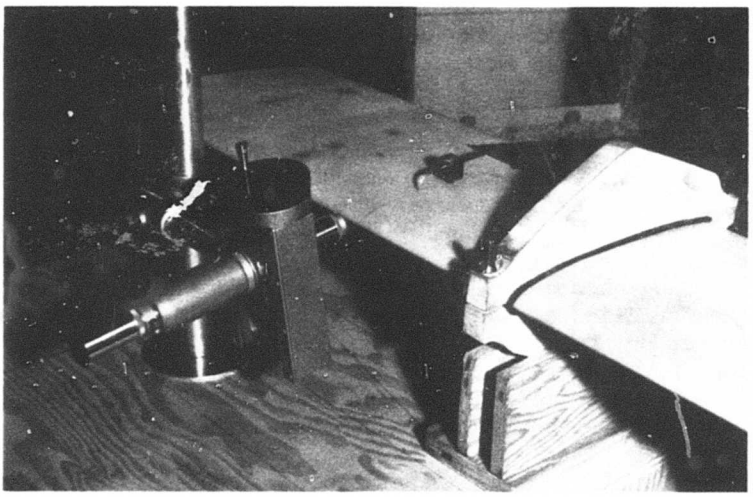

Figure 56. Traversing Microscope Attached to Rotor Blade During Probe Height Measurement.

3.4 TEST RESULTS AND DISCUSSION

3.4.1 Ammonia Surface Traces

The ammonia visualization traces give an indication of the flow direction in the lower portion of the boundary layer. The traces are shown in Figures 57 through 59. The data in these figures were obtained at a pitch angle of 12° and rotor speeds of 250, 700, and 990 rpm, respectively. Data at pitch angles of 13.5° and 15° are presented in Appendix II; however, these data only serve to confirm the results of the data in Figures 57 through 59.

The leading and trailing edges are marked in each figure. Orifices were located at chordwise positions of 0, 5, 10, 15, 20, 25, 30, 35, 40, 50, 60, and 75 percent chord (at spanwise positions of 50, 60, 70, 80, 90, and 99 percent radius.) In some of the data, traces were not formed at the orifices near the trailing edge. Because of the large negative pressures on the upper surface near the leading edge, most of the ammonia would escape in this region.

The 250 rpm data at 50 percent radius indicate a region of outflow from 5 to 10 percent chord. This action is similar to that reported by Velkoff, Blaser and Jones,[27] in which flow discontinuities were hypothesized to be standing laminar separation bubbles. No discontinuities can be observed at any of the other radial positions for any of the rpm conditions tested. Since the discontinuity is believed to be a laminar flow phenomenon, it disappears when the flow transitions prior to the formation of the separation bubble. The tip Reynolds numbers corresponding to 250, 700, and 990 rpm are 0.66, 1.83, and 2.59 million, respectively. This indicates that the local free-stream Reynolds number at the location of the discontinuity was 0.33 million. All other data have higher Reynolds numbers.

The traces at 60 and 70 percent radius at all of the rpm conditions indicate a small amount of outflow in the region prior to the 25 percent chord position. The flow appears to be very stable over the complete blade. Even the flow following the discontinuity is well behaved and appears to be strongly attached to the airfoil.

The flow near the tip has a strong tendency to flow inward. This action is caused by the motion of the tip vortex. This tip vortex is created by unequal pressures on the upper and lower surfaces which cause a net flow around the tip from lower to upper surface. The effect of this spanwise tip flow is not evident at the 99 percent radius trace until about the 20 percent chord positions. This could indicate that the tip vortex is being formed in the first 20 percent chord.[25]

In summary, the ammonia trace visualization data only indicate the overall gross flow effects. At Reynolds numbers below 0.33 million,

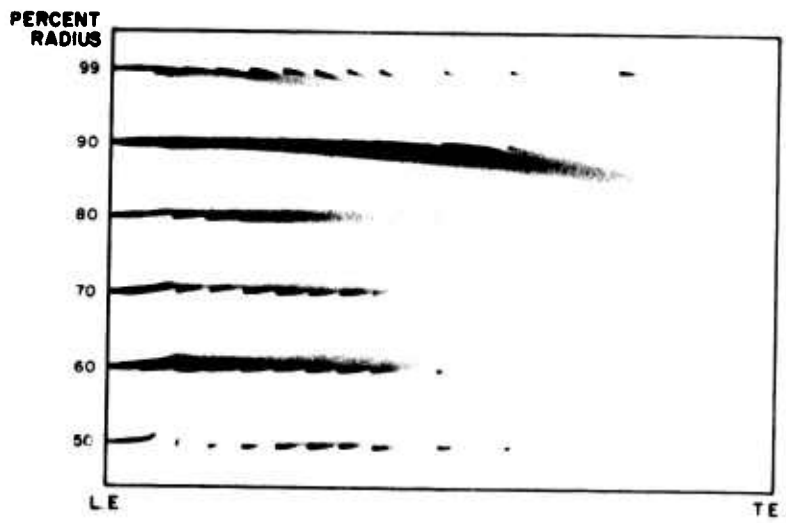

Figure 57. Ammonia Trace Data; θ = 12°, 250 rpm.

Figure 58. Ammonia Trace Data; θ = 12°, 700 rpm.

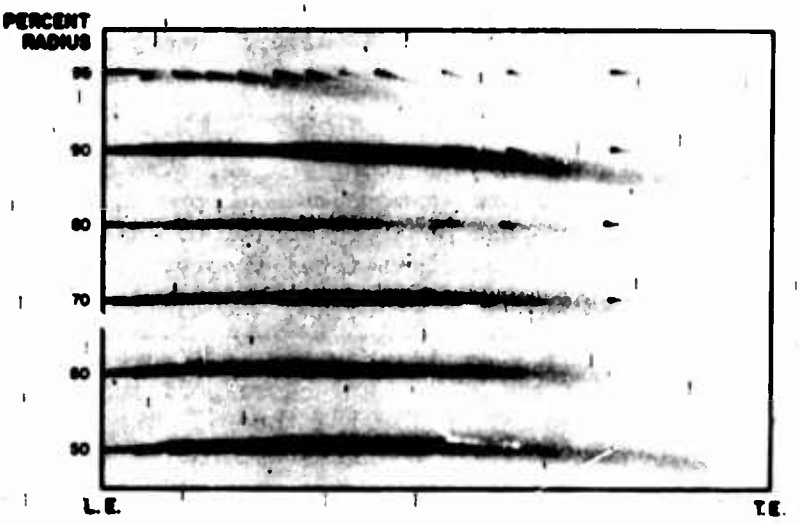

Figure 59. Ammonia Trace Data; $\theta = 12^{o}$, 990 rpm.

these data indicate the occurrence of standing laminar separation bubbles. It is hoped that this flow phenomenon can be examined using the hot-wire technique.

3.4.2 Surface Static Pressures

The surface static pressure data are shown in Figures 60 and 61. These data were obtained at 800 rpm and pitch angles of 0, ±5°, ±10°, and ±15°. The pressure transducers were located at 5, 10, 15, 20, 35, and 50 percent chord stations at both 70 and 93 percent radius positions on the blade. Since transducers were located only on the upper surface, the negative pitch angles were used to indicate the pressure on the lower surface of the blade. The data are presented in pressure coefficient form.

The solid curves are theoretical two-dimensional pressure distributions. In order to calculate this two-dimensional distribution, the local angle of attack for each hover condition had to be estimated. This estimation was made using simple blade element theory as described by Gessow and Myers,[28] and does not include the three-dimensional effects of the rotating case.

Figure 60 presents the data at 70 percent radius. The pressure coefficients are greater than the two-dimensional theory in the region from the leading edge to the 25 percent chord position. Aft of this position the data fall below the two-dimensional theory. This same trend occurs on both upper and lower surfaces.

The data at 93 percent radius are illustrated in Figure 61. At this location, the data aft of the 25 percent chord position on the upper surface of the blade also fall below the theory. The pressure coefficients near the leading edge are not greatly underestimated by the two-dimensional theory. The effects of tip proximity could be evident in the 93 percent radius pressure data.

The number of transducers used greatly limited the usefulness of the results. With only six transducers per spanwise position, it was difficult to accurately define the chordwise pressure distributions. Data were taken only on the forward half of the airfoil since it was felt this was the most important region. However, the data in Figures 60 and 61 indicate the same trends as the two-dimensional theory. Again, it is not known how accurate this comparison should be since the accuracy of the theory is questionable.

3.4.3 Boundary Layer Velocity Data

Velocity data were obtained with the hot wires for spanwise stations of 72 and 92 percent radial stations. Rotor speeds of 100 and 400 rpm were run. Tests run at the 72% radius station included pitch angles of 0, 5, 10, 15 degrees, and at chordwise locations of 10, 15,

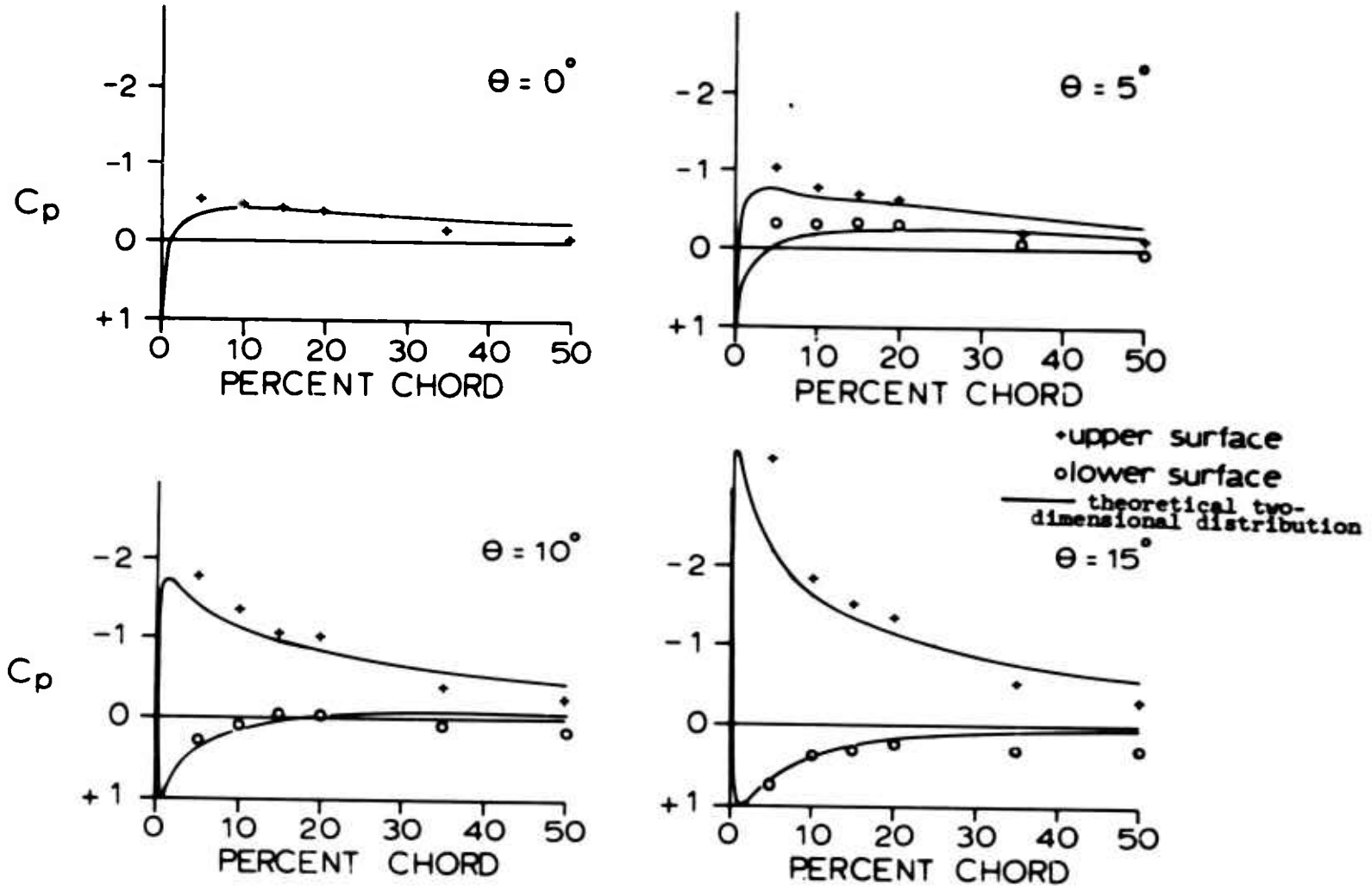

Figure 60. Surface Static Pressure Data at 70% Radius.

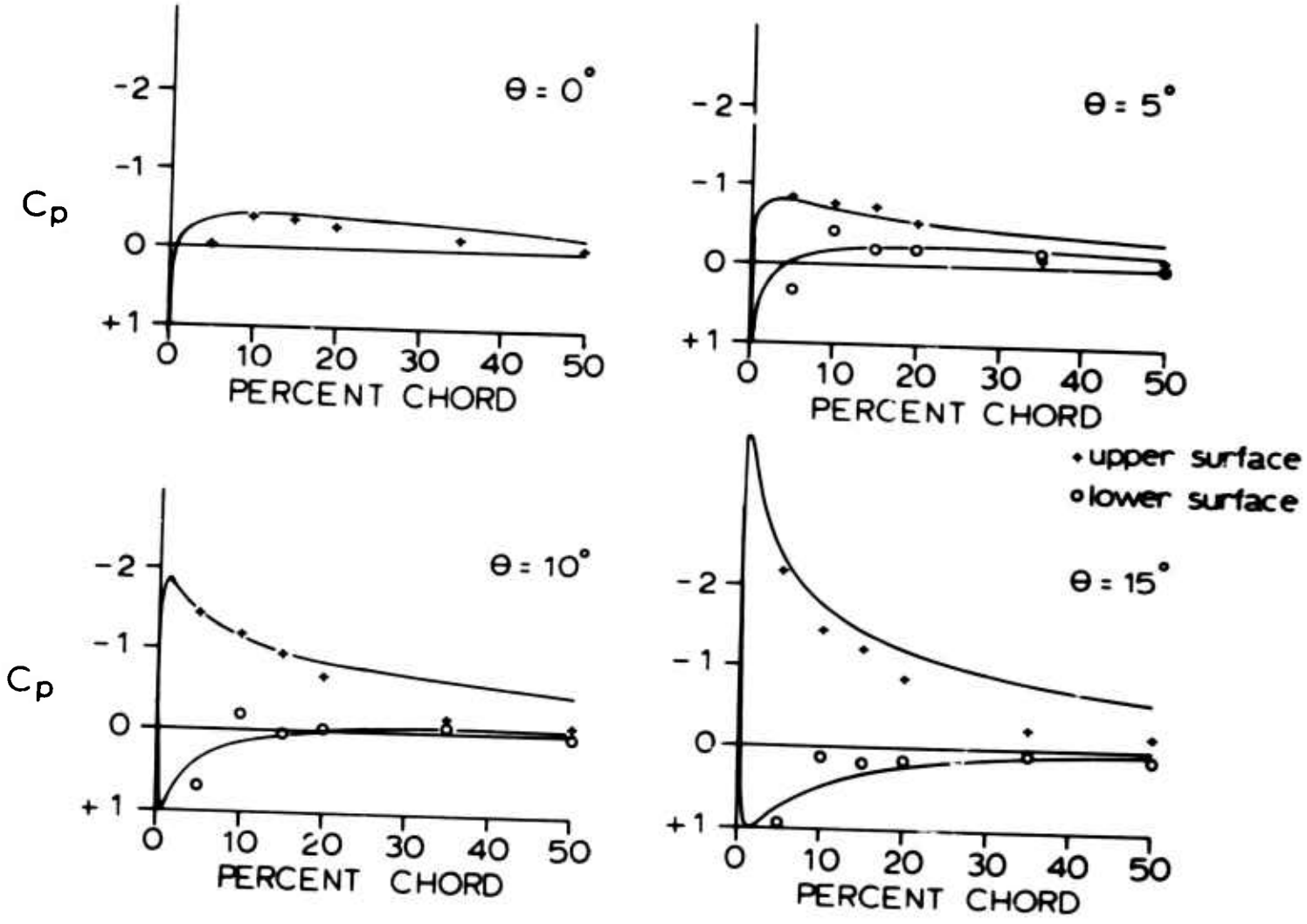

Figure 61. Surface Static Pressure Data at 93% Radius.

20, 25 percent chord. Tests run at 92% radius included pitch angles of 0 and 5 degrees and chordwise locations at 15 and 25 percent. Typical data obtained are shown in Figures 62 and 63 and are discussed extensively in this section. Added velocity data may be found in Appendix IV.

Figures 62 and 63 represent boundary layer velocity data at a fixed spanwise position of 72 percent radius, fixed pitch angle of 10°, and rotor speeds of 100 and 400 rpm. The graphs from left to right represent increasing chordwise positions of 10, 15, 20 and 25 percent chord. The top row of graphs are chordwise velocity profiles, the middle row are spanwise velocity profiles, and the bottom row are outflow angles. Since all of the measured velocities are nondimensionalized by their corresponding experimental potential flow component, the experimental values of the chordwise potential flow U and the spanwise potential flow W are also listed at each position. The data are all plotted versus actual vertical distance above the blade surface.

First, the data at 100 rpm will be examined. At 10 percent chord, the chordwise profile exhibits a linear region near the surface and then rapidly approaches the potential flow value. The spanwise flow exhibits a slight overshoot type of profile. The outflow angle varies from a small value at the outer edge of the boundary layer to a relatively large value near the surface. This large outflow may be attributed to the centrifugal pumping action which occurs as the air particles become trapped in the boundary layer.

The top row of graphs depicts the development of the chordwise boundary layer. The profile becomes less and less "full" as the chordwise position is increased from 10 to 20 percent chord. At 25 percent chord, the chordwise profile seems to have inherited a new shape. This chordwise boundary layer development can be explained as follows.

It appears that a laminar separation bubble is standing on the rotor blade in the vicinity of 20 to 25 percent chord for the hover conditions in Figure 62. The best indications of the existence of a separation bubble are the separation profile shape at 20 percent chord and the much "fuller" profile that occurs just 5 percent chord downstream. These data indicate that a very abrupt change occurred between 20 and 25 percent chord.

The hypothesis for explaining the data in Figure 62 follows. The chordwise flow is laminar at 10 percent chord; however, the steep adverse chordwise pressure gradients observed in Figures 60 and 61 are decelerating this flow. By the time the flow reaches the 20 percent chord position, the chordwise component of the wall shear stress has almost vanished. A laminar separation takes place shortly after the 20 percent chord position is passed. When the flow separates, it gains momentum from the free stream and reattaches as a turbulent boundary layer. Therefore, the chordwise profile observed at 25 percent chord is a turbulent flow profile.

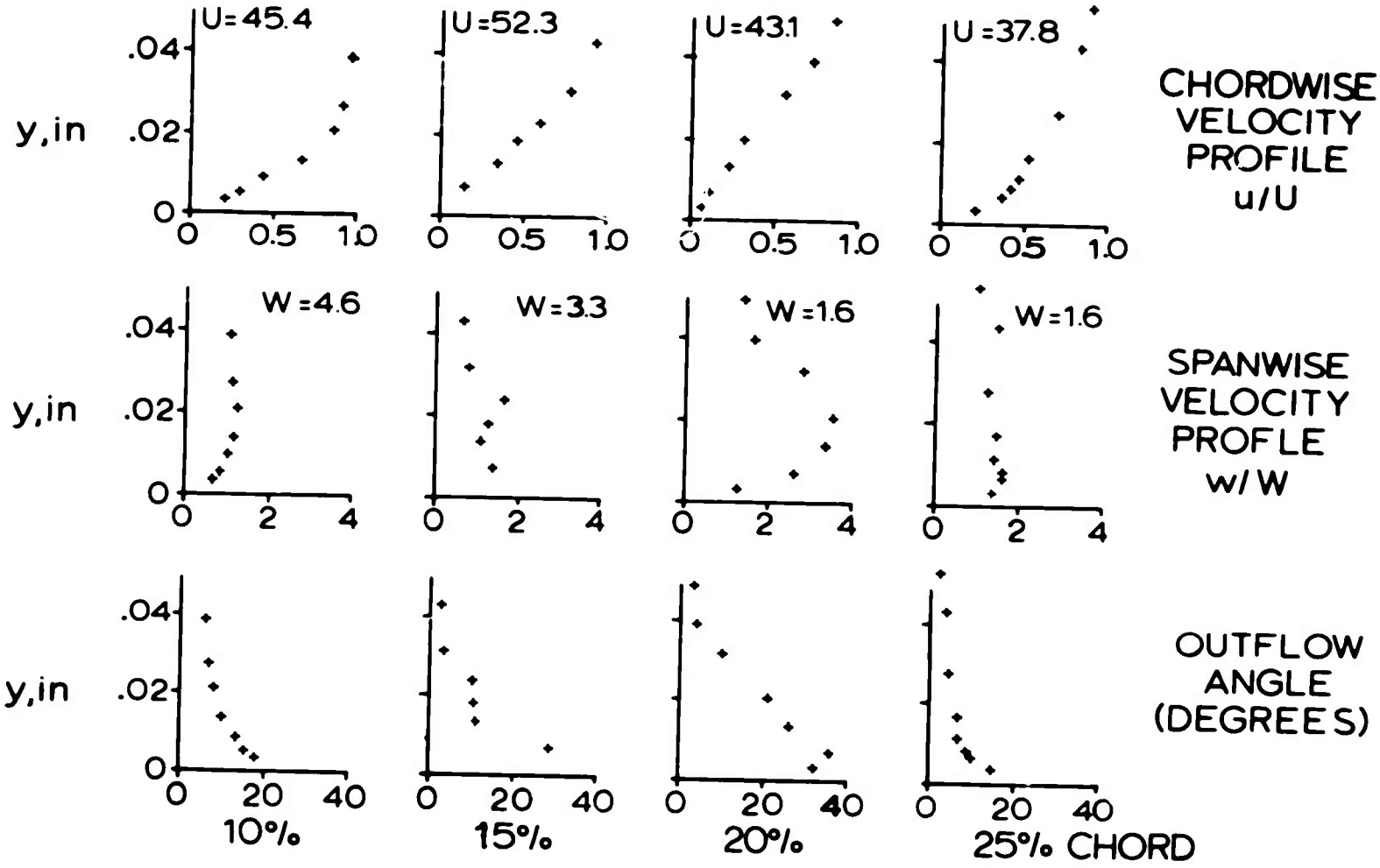

Figure 62. Velocity Data at 72% Radius, $\theta = 10^{\circ}$, and 100 rpm.

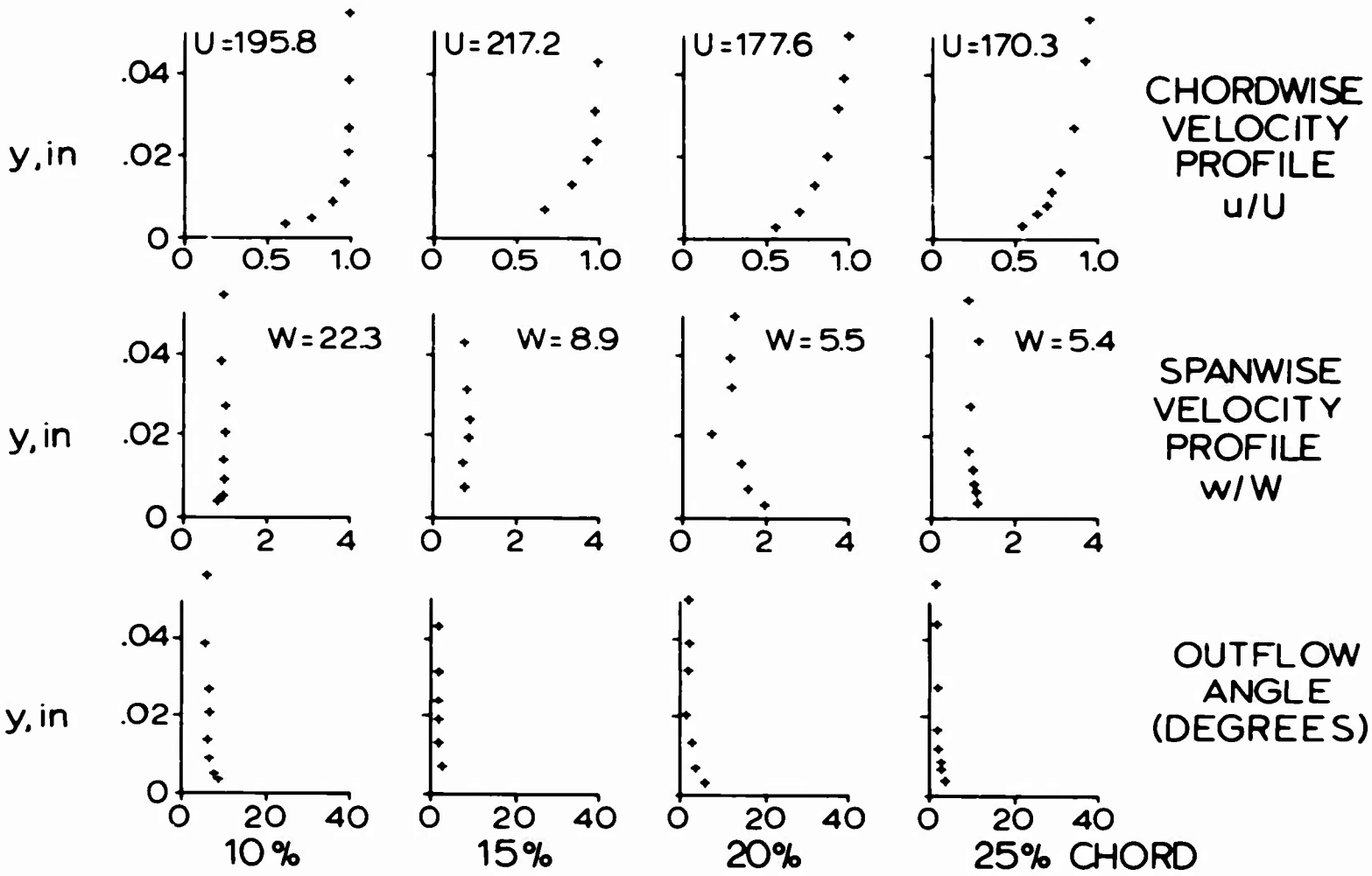

Figure 63. Velocity Data at 72% Radius, θ = 10°, and 400 rpm.

Next, the spanwise profile development can be observed as the flow progresses along the chord from 10 percent to 25 percent. In the reduction of the data, all velocity measurements are normalized by dividing by the free-stream velocity. The free-stream velocity is shown with each curve. In the case of the spanwise data, the magnitude of this velocity is very small and difficult to measure. Consequently, scatter in the data may be present when the value of W is quite small. The spanwise profile at 10 percent chord indicates a very small amount of overshoot, prior to approaching zero near the surface. As the flow progresses to 15 percent chord, this profile shape becomes rather "jagged", which may be due to experimental error. However, at 20 percent chord, the data indicate an extremely smooth profile which exhibits a large amount of overshoot. This illustrates that as the chordwise flow approaches a separation profile, the spanwise flow is greatly accelerated to maintain continuity within the boundary layer. This spanwise relief permits the rotating boundary layer to remain thinner than the associated two-dimensional boundary layer. At 25 percent the spanwise velocity profile shows a little overshoot very near the wall.

The ammonia trace data of Figure 57, and the vast amount of similar data reported by Velkoff, Blaser and Jones,[27] was interpreted only after the hypothesis of the existence of laminar separation bubbles on the rotating airfoils. Although this hypothesis was consistent with every trend that was illustrated by the ammonia data, it was still not a proven fact. The data of Figure 62 present a significant contribution to the support of the laminar separation bubble hypothesis. First, the chordwise profiles indicate laminar separation and turbulent reattachment, which was discussed at length by Velkoff, Blaser and Jones.[27] Next, the almost instantaneous increase in the spanwise outflow at 20 percent chord (the vicinity of vanishing chordwise wall shear) is very reminiscent of the ammonia discontinuities.

The ammonia trace "surface streamlines" actually turn sharply outward away from the potential streamlines at the discontinuities. The outflow angles in Figure 62 also corroborate this trend in the ammonia data. The outflow angle is actually a measure of the angle between the chord line and the streamline at a given boundary layer height. For example, in Figure 62 at 20 percent chord, the outflow angle reaches a peak value of about 36° at approximately 0.007 inch from the blade surface, while the outflow angle is only about 3° at 0.050 inch from the blade surface. Again, this large outflow in the boundary layer is indicative of the ammonia trace discontinuities.

Figure 63 presents data at the same θ as Figure 62, but at 400 rpm. At this speed, the boundary layer thickness is considerably smaller; therefore, fewer data points were obtained within the boundary layer. The results at 400 rpm do not indicate the existence of a laminar separation bubble. This increase in Reynolds number has probably initiated transition prior to laminar separation, as was observed with the ammonia traces. The rather rapid growth in the boundary layer thickness can still be observed in the chordwise velocity profiles.

When using a hot wire for velocity measurements close to a solid boundary, errors may be introduced if the effect of the boundary on the rate of heat loss from the wire is ignored. To account for this heat loss, the experimental data of Wills[29] were used. Wills obtained experimental data on various diameter wires in a known boundary layer flow. His data were then used to calculate correction factors for heat losses to the surface. For constant-temperature wires, this correction factor was found to be a function of the ratio of distance from the surface to the wire radius. This correction factor was lifted from Wills[29] and was incorporated into the hot-wire data reduction scheme to account for wall proximity heat losses and associated velocity measurement errors.

IV. COMPARISON OF ANALYSIS AND EXPERIMENTS--HOVER

This section compares the analytical and experimental portions of the study for which calculations and measurements were made for a rotating NACA 0012 airfoil at zero lift.

The experimental hot-wire data at $\theta = 0°$ (zero lift condition) were obtained at spanwise locations of $z/c = 3.87$ and $z/c = 4.92$. The chordwise locations at which velocity profiles were obtained are indicated in Figure 64. The relationships between z/c and percent radius are shown along with the relationships between x/c and percent chord. At $z/c = 3.87$, the Reynolds numbers based on the blade chord are 0.158, 0.316, 0.474, and 0.632 million, which correspond to rotor speeds of 100, 200, 300, and 400 rpm, respectively. At these rotor speeds, the Reynolds numbers at $z/c = 4.92$ are 0.185, 0.369, 0.554, and 0.739 million, respectively.

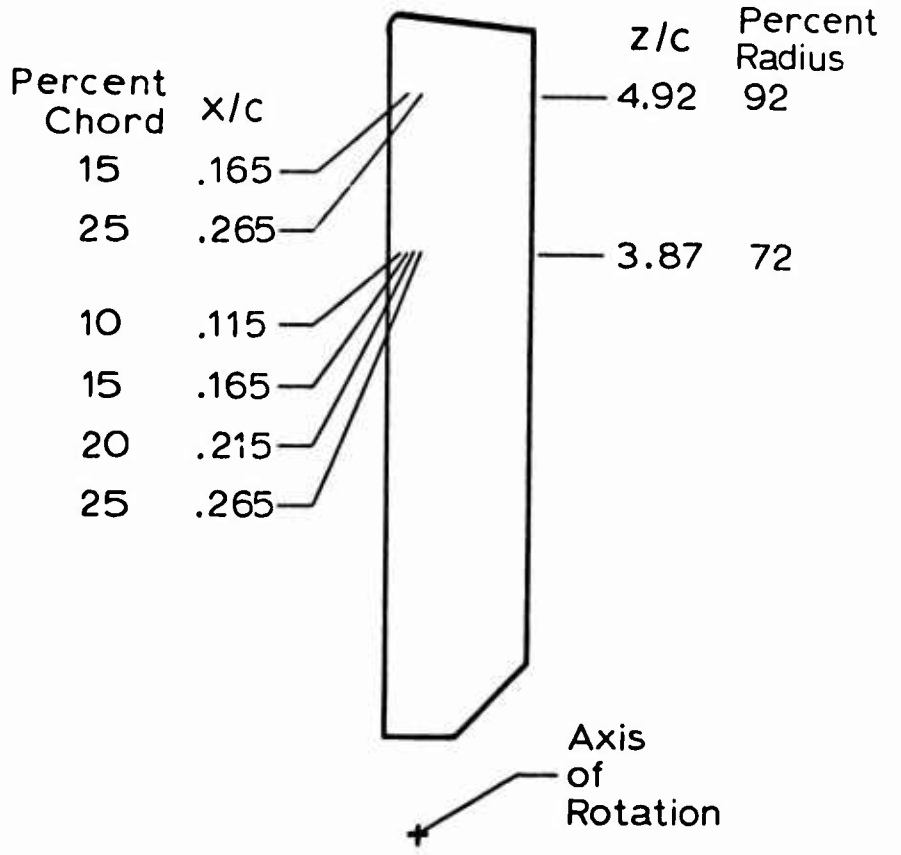

Figure 64. Location of Hot-Wire Data on Rotor Blade.

Figures 65 through 70 present chordwise velocity profiles on a rotating NACA 0012 airfoil at zero lift. By plotting versus the "stretched" boundary layer coordinate, $y\sqrt{(\Omega z)/(\nu x)}$, used in the analytical study, the data at different rotor speeds or Reynolds numbers can be combined into a single graph. The solid line in each of these figures indicates the velocity profile predicted by the momentum-integral analysis.

At each location on the blade, the experimental data indicate a "fuller" profile than the analytical calculations. The analytical calculations assumed that the flow was laminar. Due to variations in the blade surface roughness, the actual flow may be transitioning, or even turbulent. If this were the case, the profiles within the boundary layer would be "fuller" than the corresponding laminar flow profiles.

Another point must be made regarding the limitations of the analytical solutions. One of the major controlling factors in making boundary layer calculations is the potential or inviscid flow. This region dictates whether a flow even occurs; however, its most important contribution is the acceleration or deceleration of the boundary layer flow. Throughout all of the analytical calculations, this potential flow was obtained from theoretical, two-dimensional calculations. Any inaccuracies occurring in the potential flow would alter the displacement thickness and ultimately the wall shear stress distribution. The disagreement between theory and experiment in Figures 65 through 70 could indicate an inaccuracy in the assumed potential flow.

Except for Figure 66, the experimental chordwise velocity data congregate quite well for the range of Reynolds numbers presented. Figure 66 indicates a considerable amount of data scatter. The data presented in this figure represent the very first rotor hot-wire data obtained in this study. Since the probe was positioned by visually viewing the probe through the microscope, the consistency of the data depended greatly on the technique used while adjusting the probe height. After this first profile was completed, the consistency of the data appears to be much improved, as indicated by Figures 65, 67, 68, 69, and 70.

The spanwise profiles are compared in Figure 71 for a chordwise position $x/c = 0.115$ and a spanwise position $z/c = 3.87$. The results indicate that no comparison can be made between experimental and theoretical spanwise profiles. Very near the blade surface, the theoretical profile is moving toward the experimental data; however, it soon reverses its direction. The theoretical profile is primarily inflow while all of the experimental data indicate outflow.

The inconsistencies of Figure 71 can be explained by examining the location of the axis of rotation in each case. Throughout the analytical study, the axis of rotation was placed at the blade leading

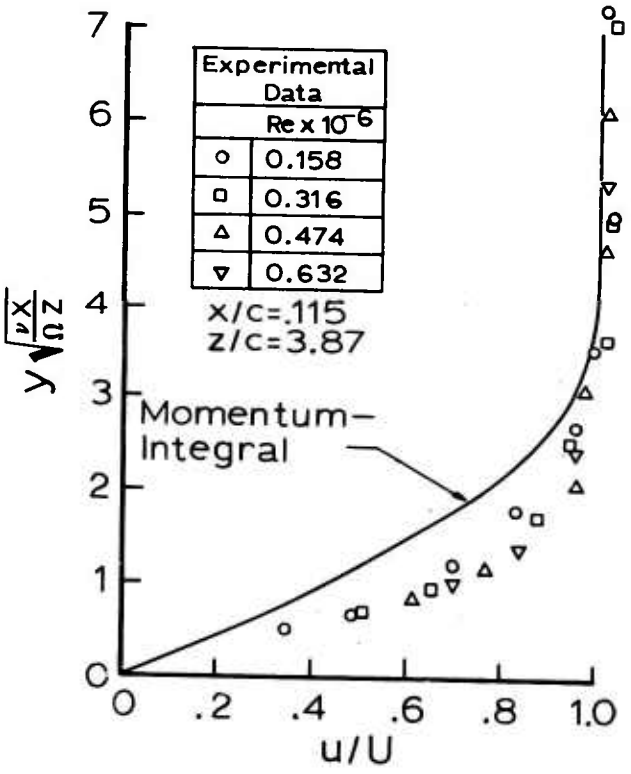

Figure 65. Chordwise Profiles on an NACA 0012 at x/c = 0.115 and z/c = 3.87.

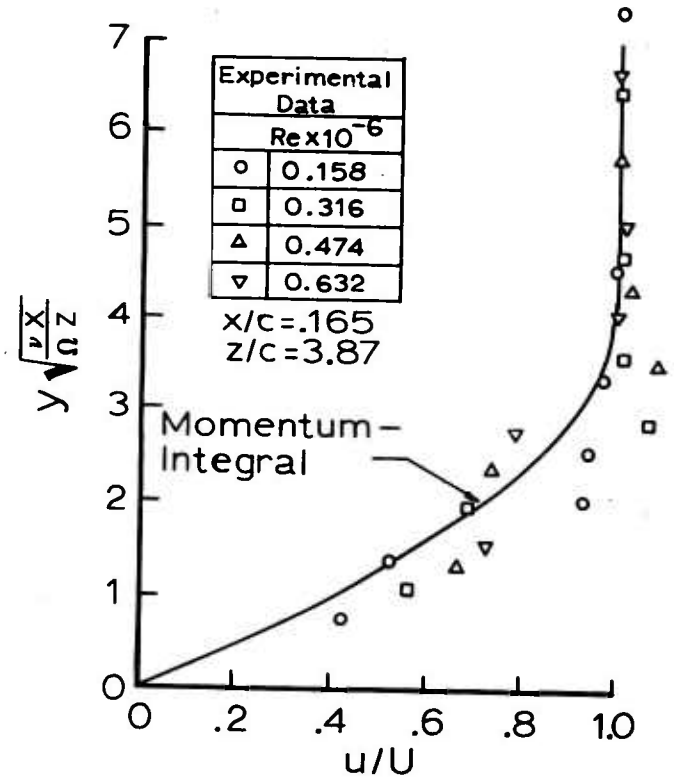

Figure 66. Chordwise Profiles on an NACA 0012 at x/c = 0.165 and z/c = 3.87.

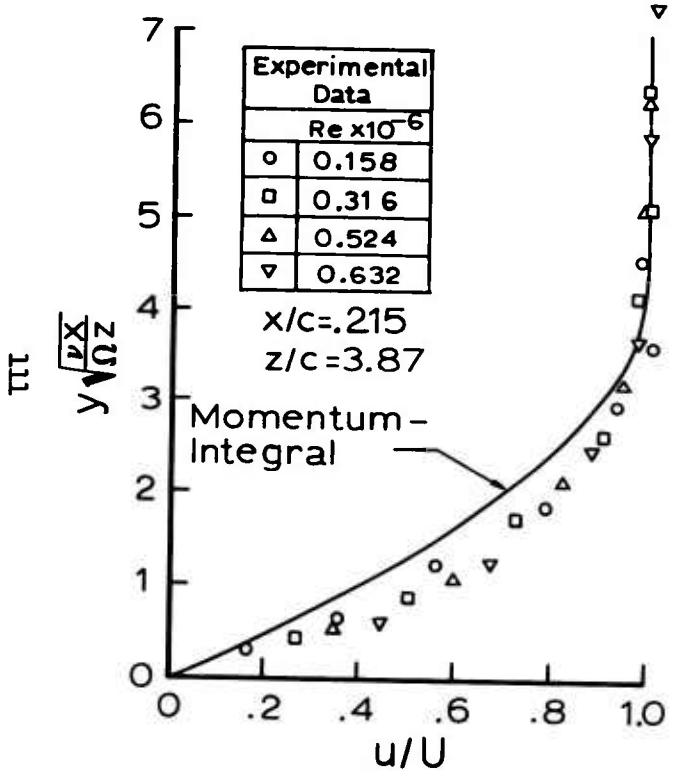

Figure 67. Chordwise Profiles on an NACA 0012 at x/c = 0.215 and z/c = 3.87.

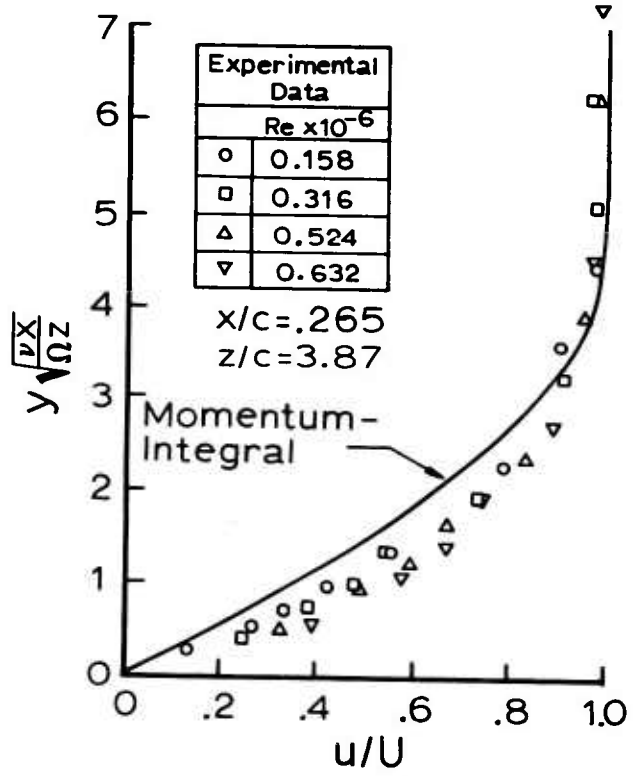

Figure 68. Chordwise Profiles on an NACA 0012 at x/c = 0.265 and z/c = 3.87.

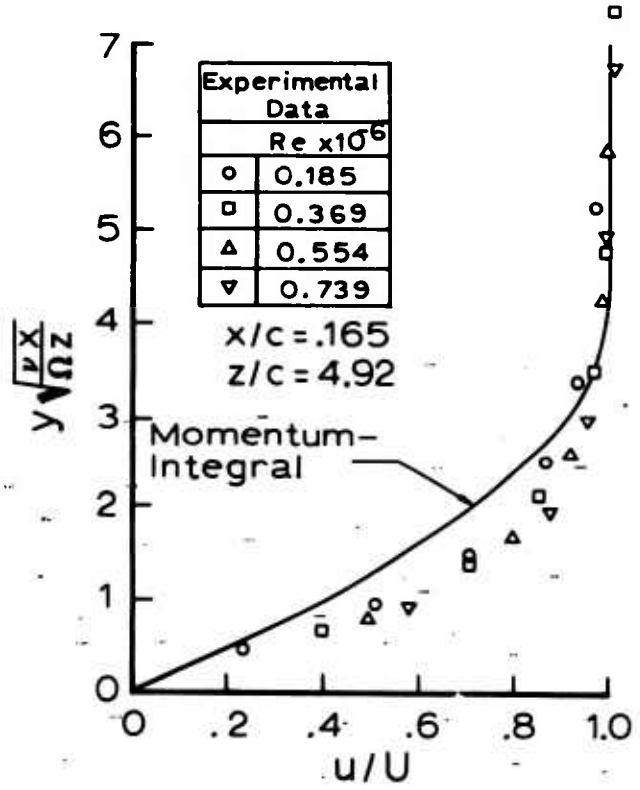

Figure 69. Chordwise Profiles on an NACA 0012 at x/c = 0.165 and z/c = 4.92.

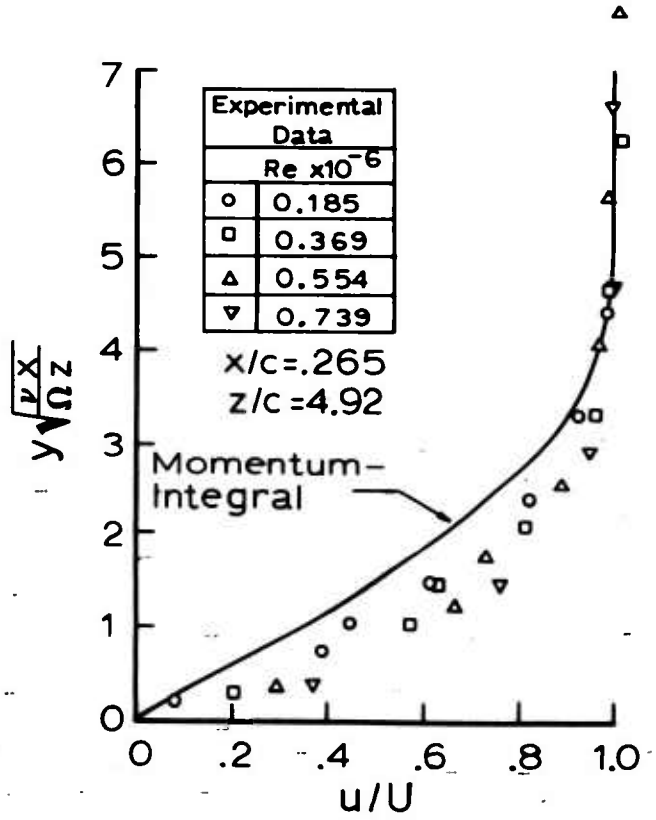

Figure 70. Chordwise Profiles on an NACA 0012 at x/c = 0.265 and z/c = 4.92.

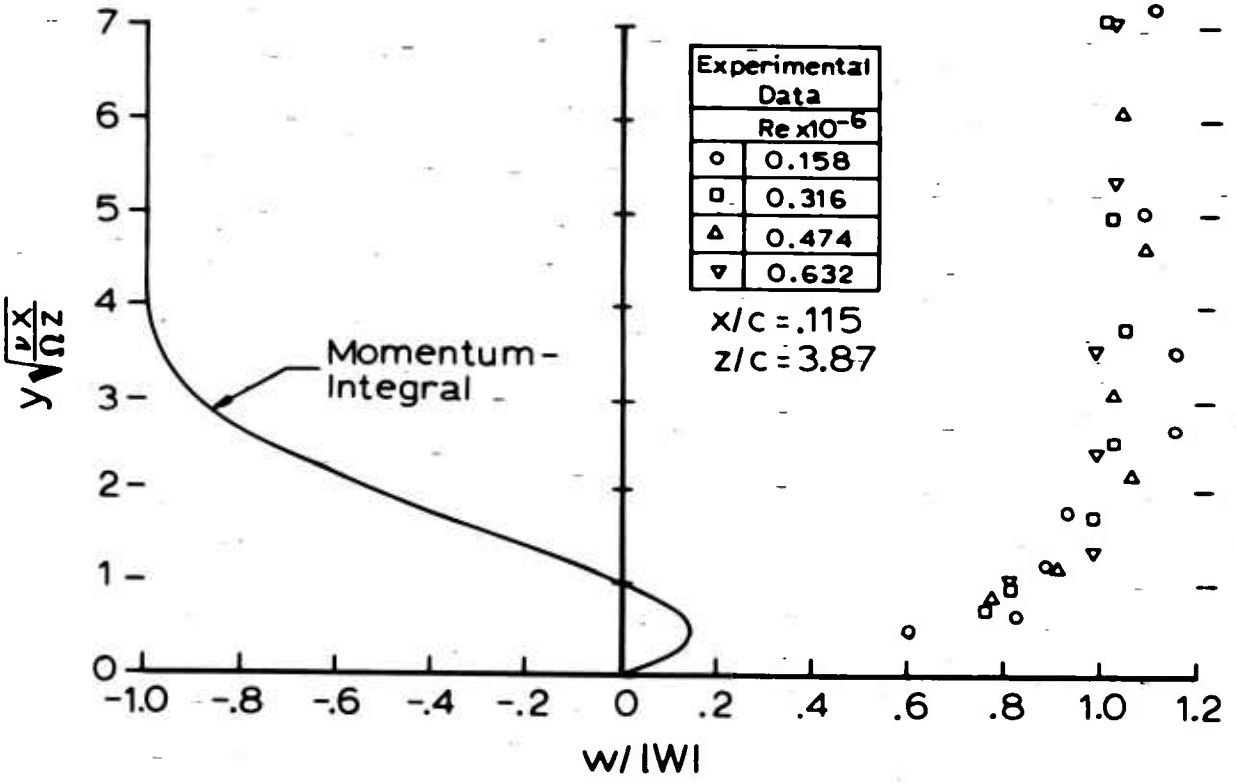

Figure 71. Spanwise Profiles on an NACA 0012 at x/c = 0.115 and z/c = 3.87.

edge, as shown in Figure 1, to simplify the mathematics and to compare results with other investigators. The rotor blades used in the experimental portion of this study were rotated about their quarter-chord positions. This seems like a very minor point; however, the spanwise flow is less than 10 percent of the total flow in the positions near the leading edge where measurements were made. For this reason, the direction of this spanwise flow is very sensitive to small changes in the geometry.

For example, the potential streamlines of an NACA 0012 airfoil can be closely approximated by circular arcs near the leading edge of the blade, as shown in Figure 72. Since all of the experimental data was obtained in the region in front of the quarter chord, the experimental spanwise potential flow is outward while the analytical spanwise potential flow is inward. This explains why the momentum-integral profile shown in Figure 71 reverses its direction. The lower portion of the boundary layer is still pumped outward due to the large component of centrifugal force; however, the upper portion of the boundary layer is governed principally by the inward potential flow. This analytical curve in Figure 71 would be greatly changed if the direction of the spanwise potential flow were reversed.

A possible explanation for the differences in the analytical and experimental chordwise profiles can be deduced with the aid of Figure 71. The experimental spanwise flow is outward as indicated in Figure 71. Outflow in a rotating system creates an equivalent favorable pressure gradient. All but the bottom level of the analytical profile is inflow as indicated in Figure 71, and inflow in a rotating system creates an equivalent adverse pressure gradient. These effective favorable and adverse pressure gradients, due to the Coriolis forces, could tend to create the differences in the chordwise profiles that were indicated in Figures 65 through 70.

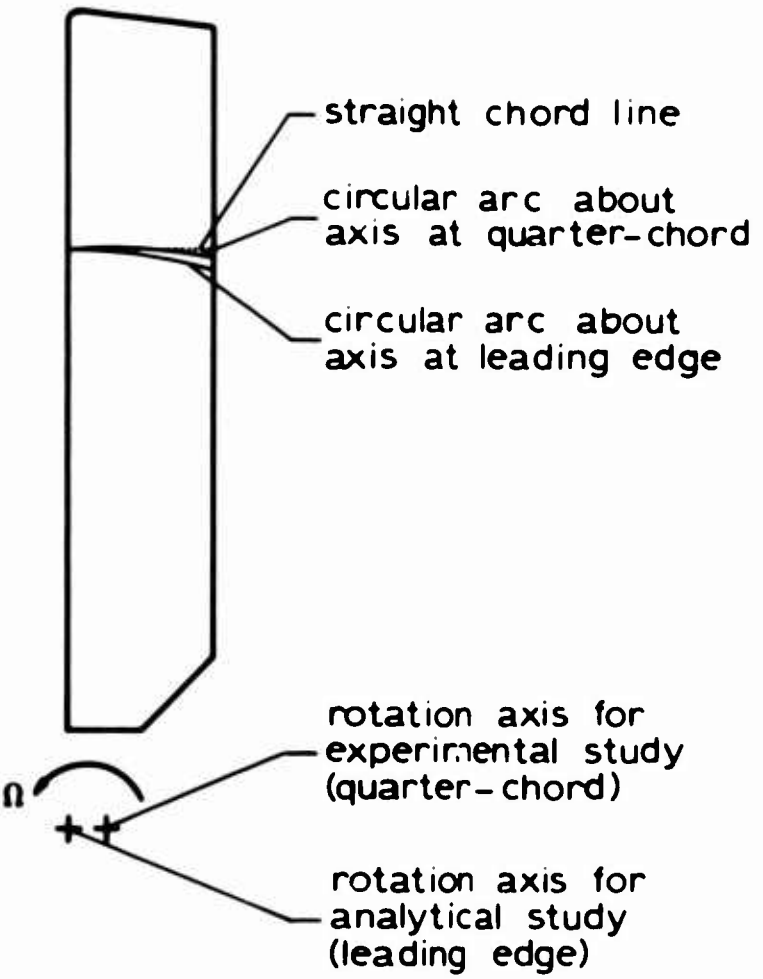

Figure 72. Approximate Potential Streamlines on a Rotating NACA 0012 Airfoil Near the Leading Edge.

V. TIP FLOW STUDY--HOVER

5.1 BACKGROUND

5.1.1 Flow Over Tips

The flow over the tips of a wing of finite span leads to the formation of tip vortices.[30,31] Similar vortices spring from the tips of helicopter rotor blades. The interaction of this tip vortex flow with the boundary layer near a blade tip forms the basis for the study presented in this section.

5.1.2 Previous Experimental Studies

Several experimental studies have been conducted in recent years to investigate the nature of the flow over the tips of helicopter blades (or fixed-wing airfoils) and the influence of tip design on rotor performance.

A report published in 1968 by Richard F. Spivey[32] discusses the results of two- and three-dimensional wind tunnel tests and flight tests conducted on helicopter rotor tips at Bell Helicopter Company. The report discusses the effects of profile, camber and planform on lift, drag, noise, etc. Pressure distribution data were obtained on a square-tip stationary airfoil at different yawed positions in a wind tunnel. Smoke flow tests were also conducted in hovering, and it was found that the tip vortex was in the same position on the upper surface of the tip as indicated by the pressure distribution data in the wind tunnel. Surface oil flow tests were also conducted on full-scale helicopter rotors, and results were consistent with the previous tests. The results of these tests show that the vortex is not moved outward by centrifugal force or pressure gradients on a rotating blade in hover, but remains in the same relative position as in nonrotating blade wind tunnel tests. The surface oil flow tests may not be conclusive because of the vast difference in the density and viscosity of the oil and the air flowing over the oil.

Spivey[32] also describes studies made with modified tip shapes including swept-forward, swept-aft, and others. Pressure distribution data were obtained in stationary wind tunnel tests; also, surface oil flow tests were conducted. The swept-aft tip was considered to be advantageous because it provides compressibility relief similar to a swept-wing aircraft. Finally, flight tests were performed, based on the results of the wind tunnel tests, using a 70° swept-aft tip, and it was found that a 3-percent decrease in power was required in forward flight. Most of the emphasis[32] was on the effects of tip design on rotor performance. While some pressure distribution data were obtained, very little information on the flow direction at various points on the tip was presented.

Another report on the subject of the flow over wing tips was published by Piziali and Trenka in January 1970 at Cornell Aeronautical Laboratory.[33] They describe two-dimensional wind tunnel tests performed on an NACA 0012 airfoil with six different tips. The primary source of data was smoke flow which was allowed to pass over the blade tip and was photographed. Oil flow on the surface was also used. The greatest contribution of this report[33] is the set of photographs showing the air flow pattern over the tips and vortex formation. These photos show that the most severe tip vortex is generated with the square tip. The oil flow tests were used to show flow patterns on the airfoil surface, and to some extent, this objective was achieved. The greatest restriction on the results of this report is that the tests were nonrotational. The behavior of the flow over the tips during rotation will differ to some extent due to the three-dimensional effects and centrifugal forces.

A third recent report on the subject of flow over tips was published in June 1970 by W. A. Spivey of Bell Helicopter Company and G. G. Morehouse of NASA Ames.[34] This report describes tests performed on three tip shapes in a wind tunnel and on the tail rotor of a helicopter. Acenaphthene flow visualization was used in the tests. Pressure distribution data and lift-drag data were also obtained. Full-scale tests were also conducted on the main rotor of a helicopter. The acenaphthene sublimed from the tip surface according to the amount of local skin friction present. In this manner, regions of separation, laminar boundary layer, etc., could be observed. However, local flow direction at various points on the tip could not be seen from this test procedure.

Some of the conclusions reached in this report were: (1) at low Mach number and low C_L, the swept-tip rotors perform better than square-tip rotors; (2) at low Mach number and high C_L, the square-tip rotor is superior; and (3) at high Mach numbers and high C_L, swept-tip rotors are better than the square-tip rotor.

While all of the above reports contribute something to the knowledge of the flow over the tips of airfoils and the effect of tip shape in rotor performance, none of them clearly shows the direction of the air flow at various points on the tip during rotation. Piziali and Trenka[33] give the best information regarding the flow over the tip, but it primarily shows the air flow pattern after the flow has left the tip. The oil streak flow technique used by previous experimenters to show the flow direction on the tip surface may be questionable in rotation where centrifugal effects play a large part.

5.2 EXPERIMENTAL PROGRAM

5.2.1 Test Facility and Instrumentation

All tests were conducted on the rotor test stand located at The Ohio State University (see section 3.1.1). For the tip study, the following additional information is pertinent.

Power to drive the rotor was supplied by two Gast air motors and transmitted through two V-belts from each motor to pulleys at the bottom of the shaft (Fig. 73). A small cantilever beam arrangement was employed to transmit the torque from the pulleys to the shaft. This was done to provide a convenient place to locate a strain gage for torque measurement (Fig. 74).

Thrust measurement was obtained through SR-4 strain gages mounted on steel hoops which were stretched by the thrust force. The steel hoops were mounted between two plates at the top of the mast; the top plate was free to move vertically, and was constrained only by the two steel hoops (Figs. 75 and 76). The thrust force pulled upward on the top plate, thereby stretching the hoops and generating a strain gage voltage. The thrust and torque voltages were transmitted to the control panel through electrical slip rings located at the very bottom of the shaft. A digital voltmeter (DVM) was used to display the voltage. All strain gages required a 20-volt input and contained four 350-ohm resistance elements. The output of the strain gages was on the order of 0 to 30 millivolt.

The ammonia azo system used for the tip flow visualization, described in section 3.3.1, is similar to that used previously.[36] The ammonia transfer ring used in all ammonia tests is mounted on top of the hub and is shown in Figure 77.

Rotor speed was obtained from a tachometer. A notched belt connected to the rotor shaft drove an electrical generating device which was wired to the tachometer to indicate the rotor speed (Fig. 73).

5.2.2 Rotor Tip Design and Fabrication

Five tip designs were selected for study. Each tip had a 9-inch chord and was designed to be interchangeable with a 9-inch chord model blade with an NACA 0012 profile. The blade was 38-13/16 inches long from the center of rotation to the interface between the blade and the tip. Figure 78 shows the end of the blade without a tip.

Tip No. 1 is a square tip as shown in Figure 79. It is formed by simply cutting off the blade in a plane perpendicular to the radius.

Tip No. 2, shown in Figure 81, is defined by rotating the blade cross section about the chord and thereby sweeping out at the body of revolution. This tip forms a reference for comparison with other tips.

A swept-aft tip was selected for the design of Tip No. 3 shown in Figure 83. Its shape is formed by extending the leading edge of the airfoil rearward at a 45° angle to intersect the trailing edge. This tip has been studied previously and is known to produce high and uneven pressure concentrations.[35]

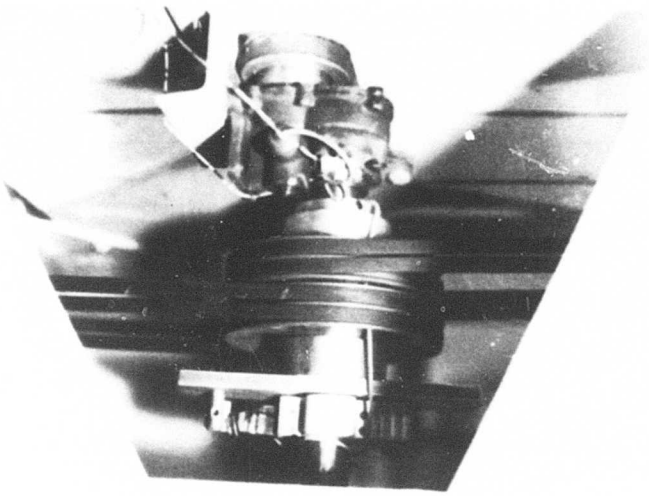

Figure 73. Pulleys and Belts at Base of Rotor Shaft.

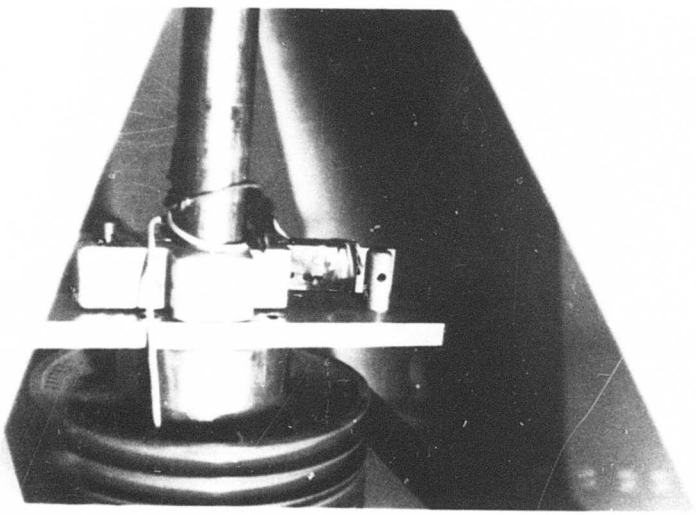

Figure 74. Torque Measuring Device.

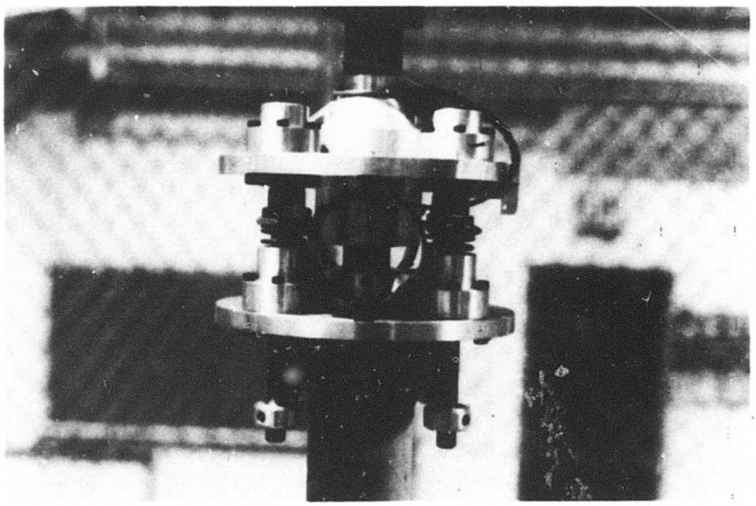

Figure 75. Thrust Measuring Device.

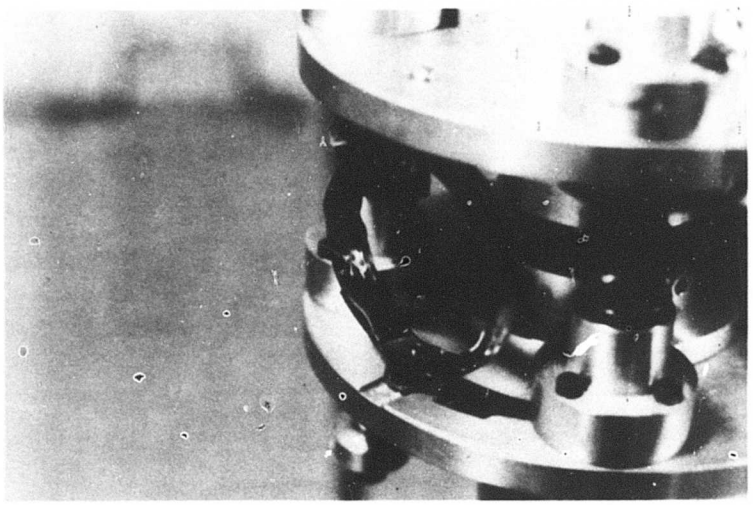

Figure 76. Thrust Ring and Strain Gages.

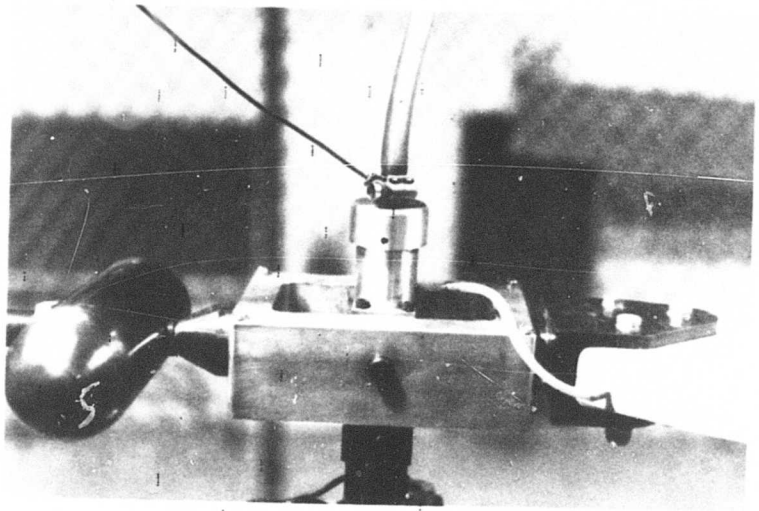

Figure 77. Ammonia Transfer Ring.

Figure 78. Blade With Tip Removed.

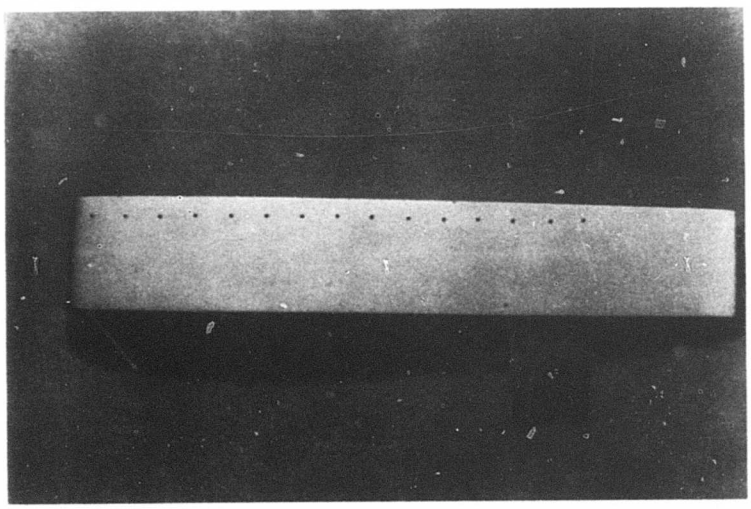

Figure 79. Top View of Square Tip (No. 1).

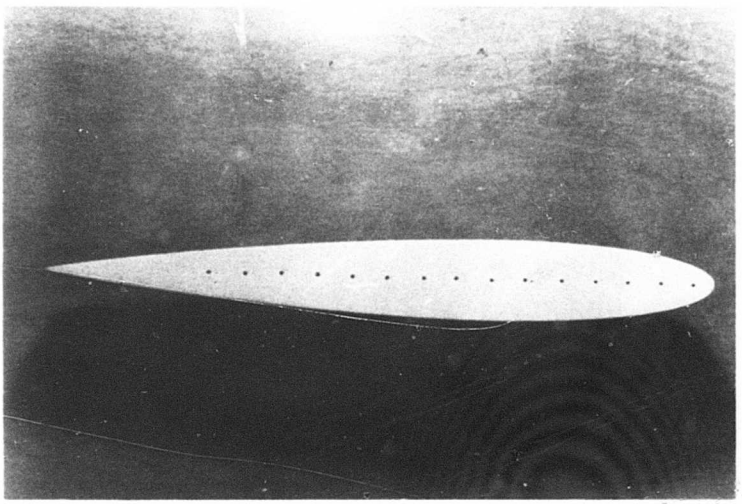

Figure 80. End View of Square Tip (No. 1).

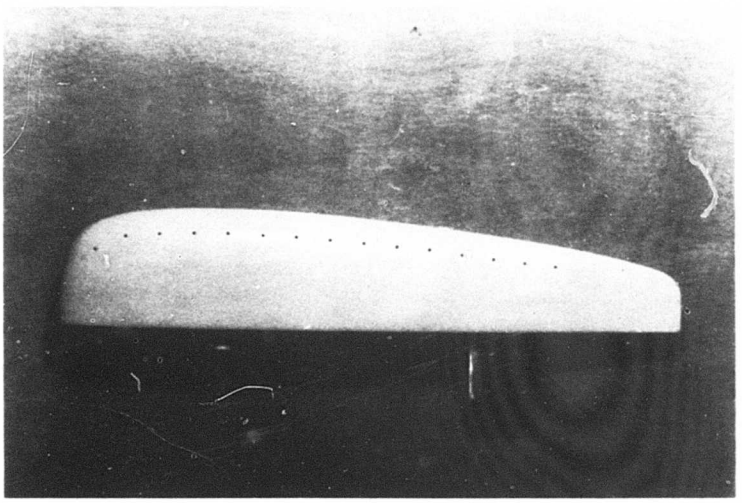

Figure 81. Top View of Standard Tip (No. 2).

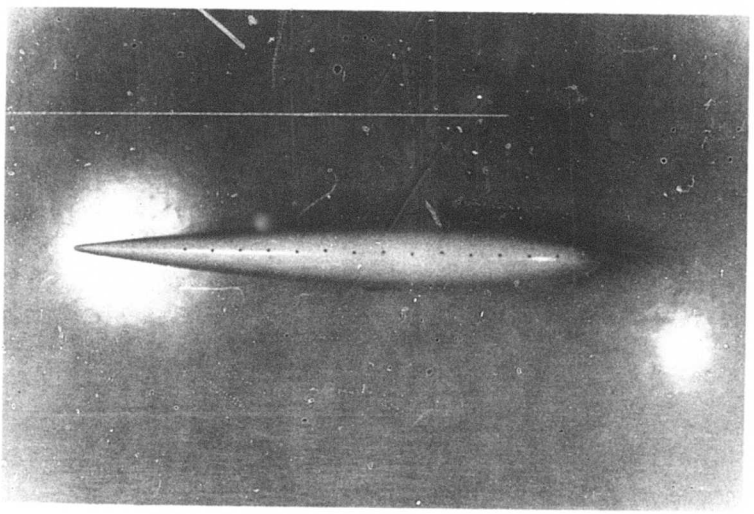

Figure 82. End View of Standard Tip (No. 2).

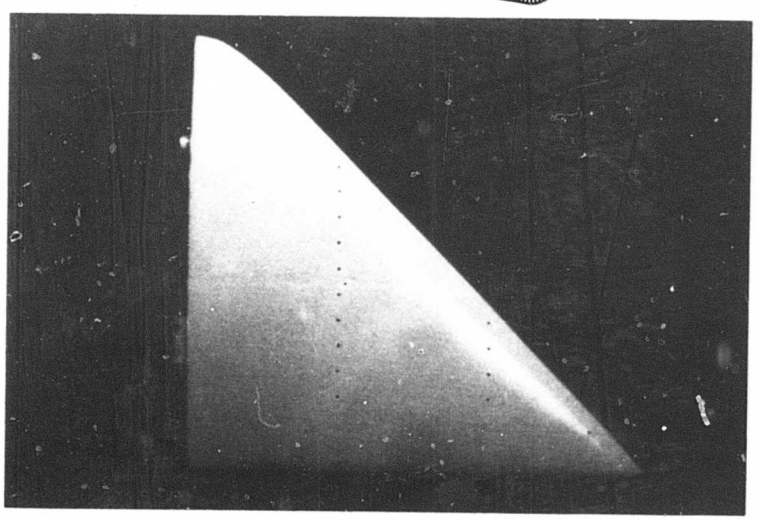

Figure 83. Top View of Swept-Aft Tip (No. 3).

Tip No. 4 is trapezoidal in shape and is shown in Figure 84. It was chosen because it approaches the idealized elliptical tip shape but is much easier to fabricate.

Tip No. 5, Figure 85, known as the cusp tip, was chosen because there had been some encouraging results from previous tests.

A second blade with a 7-inch chord containing a standard tip was also investigated. The tip on this blade was not removable.

Tips 1 and 2 were cut from blocks of sugar pine. A groove approximately 3/16 inch wide and 1/8 inch deep was milled inside these two tips near the outer edge. Small holes (~0.04 in.) were drilled approximately 1/2 inch apart on the top, end, and bottom of each tip so that each hole intersected the groove. A larger hole (3/16 in.) was drilled from the interface of each tip into the groove. This hole aligned with the aluminum tube in the blade to provide a flow path for the ammonia into the tip. A short piece of "Tygon" tubing was inserted between the hole in the tip and hole in the blade to prevent ammonia from leaking to the surface through the blade-tip interface. A piece of aluminum 1/8 inch by 1 inch was epoxied into the rear of each tip to provide for the tongue of the tongue-in-groove joint previously described. Another piece of aluminum was epoxied into the front of each tip to provide for a groove portion of the forward joint.

Tips 3, 4, and 5 were cut from balsa wood. Aluminum inserts were epoxied into these tips to provide for joints in the same manner as for tips 1 and 2. To provide for added strength, tips 3 and 4 were covered with aircraft quality cloth. Tip No. 5 was covered with fiberglass cloth. All tips were finished with white lacquer and sprayed with a clear polystyrene Q-dope. The Q-dope was used to protect the paint from the methyl alcohol used to remove the diazo sensitizing solution applied prior to each test. Without the Q-dope, the alcohol was found to remove the lacquer after repeated applications.

To provide for a good seal between the tips and the blade, a silicone sealant was applied to the mating wood surfaces and around the Tygon tubing before each tip was fastened to the blade.

5.2.3 Description of Tests

5.2.3.1 Flow Visualization. Flow visualization tests were conducted with each tip to provide a visual indication of the flow direction of the boundary layer at various points on the tips. The procedure consisted of injecting small amounts of ammonia gas into the boundary layer through many tiny holes in the tip. Before each test, the tip was sprayed with a solution containing diazonium salts, which, when exposed to ammonia, changed color from yellow to black or dark blue. After the desired pitch angle was set and the rotor brought up to speed,

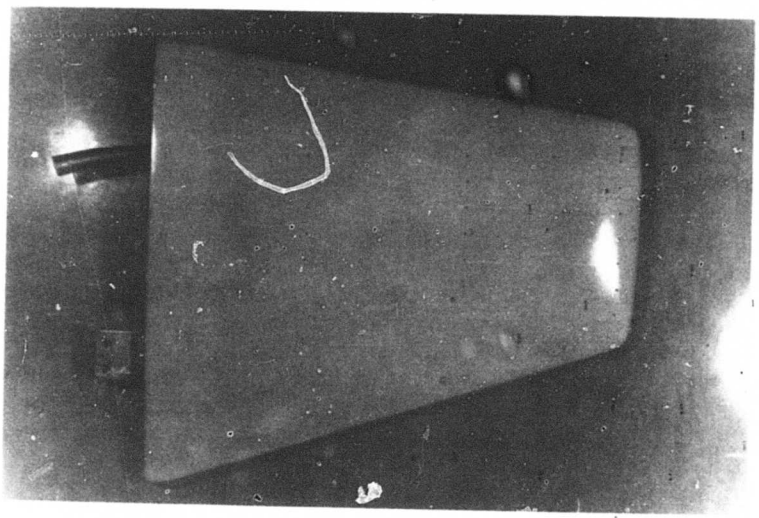

Figure 84. Top View of Trapezoidal Tip (No. 4).

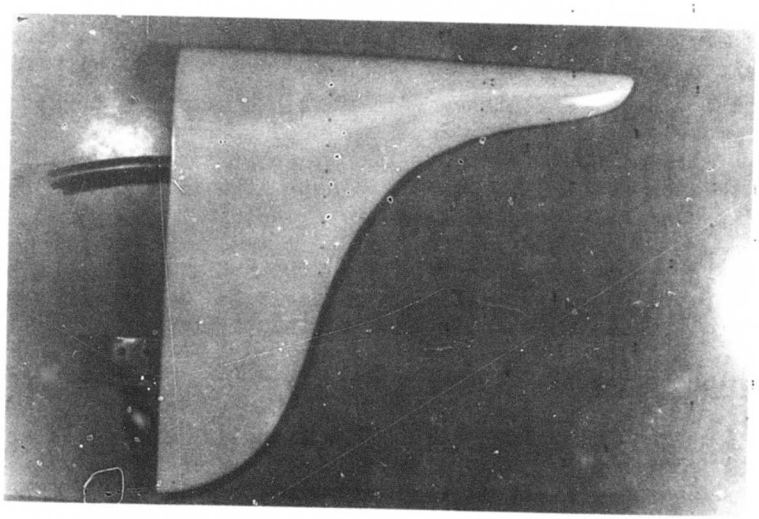

Figure 85. Top View of Cusp Tip (No. 5).

a pulse of ammonia was released and expelled through the holes. The ammonia vapor from each hole left a distince trail or trace on the surface of the tip. Upon examination of these traces, one could get a good indication of the direction of the flow in the boundary layer all over the tip. Experience was required to know how long to pulse the ammonia to get good traces. Too short pulses left too faint traces; too long pulses made traces run into each other. Therefore, considerable variation in the quality of the traces was realized in the test series, as will be seen upon examination of the photographs.

The ingredients for the sensitizing solution consisted of a vehicle (similar to clear shellac), citric acid, coupling component, and diazonium salt. The following arounts of each were mixed in making a batch of solution for a test series:

Vehicle	100 cc
Citric Acid	2 grams
Coupling Component	1/2 gram
Diazonium Salt	2 grams

The vehicle made the chemicals stick to the tips. The diazonium salt and coupling component (napthol) formed the dark-colored azo dye upon exposure to ammonia. The purpose of the citric acid was to prevent the diazo and coupling component from forming the dye prematurely. Good results were obtained using the above combination of ingredients; however, it was not necessary to have precisely those amounts for good results. After the sensitizing solution was prepared, it was applied to the tip prior to each test using a small hand-held sprayer.

Photographs were taken of the traces following each test. Usually, two photos were taken per test, one showing the upper surface and end and the other showing the lower surface and end. The traces were then removed from the tip by wiping with a cloth containing methyl alcohol.

The camera used to photograph the traces was a 35-mm single-lens reflex camera with a built-in "spot and average" light meter. Kodak Tri-X film with an ASA rating of 400 was used. Lighting was provided by two 150-watt flood lights located approximately 45° in front of and behind the tip at a distance of approximately 2 feet. The camera was hand held. The minimum distance between camera and tip was 18 inches due to focusing limitation of the camera lens (50 mm f/2). However, in photographing the larger tips, the camera was held farther away (20 to 24 in.) to capture the entire tip.

5.2.3.2 Thrust and Torque. In obtaining thrust and torque data, the bridge outputs were first zeroed at 0 rpm. The rotor was then brought up to the desired rpm and thrust and torque outputs were recorded. Problems with thrust zero shift were encountered during testing caused by mechanical "hang-up" in the bearings. Zero shifts were found to occur when running tests with increasing rpm followed by decreasing

rpm. The "hang-up" or hysteresis occurred only when the thrust load changed from increasing values to decreasing values. Consequently, all data were run with increasing rpm only for all the tips tested. Therefore, the thrust data can be considered to be useful for comparing the effects on thrust of changes in tip shape. The absolute values of thrust, however, may be of limited usefulness. The thrust values, including the effects of hysteresis, are within ±5% over the entire range. The thrust values for pitch ranges from 8 to 16° pitch are within ±3% including hysteresis. The thrust values for increasing measurements only are considered to be within ±2% when used for comparison. The torque values when corrected for the influence of torque-thrust coupling are considered to be accurate to within ±2%.

The torque-thrust coupling was caused by the transmittal of torque through the thrust rings from the bottom plate to the upper plate. The thrust device was designed so that the torque would be transmitted by the four rods between the two plates (Fig. 75). Nevertheless, the torque exerted a twisting effect on the rings which produced an apparent thrust output which increased with torque. This coupling effect was measured by applying known torques to the rotor and recording the thrust reading and used to correct for the torque effect before the thrust coefficients were calculated. The magnitude of the torque-induced thrust output was at most 2.4 pounds of thrust out of 81.1 pounds, or less than 3 percent.

5.3 RESULTS

5.3.1 Flow Visualization

In general, good results were obtained using the flow visualization technique previously described. The flow traces were usually sharp and well defined. However, under certain conditions, the traces sometimes became fuzzy and poorly defined. The biggest problem encountered in obtaining good traces was getting the ammonia to flow through all the holes in the tip simultaneously. Due to the pressure difference between upper and lower surfaces at high pitch angles, the ammonia tended to flow out through the holes in the upper surfaces, and not out the holes in the lower surface. If the ammonia pressure were increased to the point where flow was obtained through the holes in the lower surface, excessive amounts of ammonia would be expelled from the holes in the upper surface, thereby ruining the traces on the upper surface. This problem was solved by inserting small tips of wooden toothpicks into the holes in the upper surface after satisfactory traces were obtained on the upper surface. The ammonia was again pulsed and thereby forced to flow out of the holes in the lower surface. This procedure was repeated as many times as necessary until good traces were obtained from all the holes in the tip. Usually, two or three runs were required at high pitch angles (above 8°) to obtain the desired traces. The question of what effect the toothpick tips had on the flow field around the tip should be considered. Actually, the answer to this question was provided by the traces themselves. Only when a trace was so long that it ran into the

following hole which contained a toothpick tip could any effect be observed. (For example, see Fig. 89.) The traces from the lower surface wrapped around the tip and impinged on the toothpick tips (now removed) which were inserted into the holes on the tip and left a flow pattern similar to the classic flow over a cylinder. The traces which did not reach the toothpick tips exhibited no abnormalities, so it is assumed that the portion of the traces which did not impinge on the toothpick tips are unaffected by the tips and would appear the same if no toothpicks were present.

5.3.1.1 Square Tip. The first series of flow visualization tests was performed with the square tip. Tests were conducted at 400 rpm and pitch angles from 0 to 16° in 2° increments to define the effect of pitch angle on the flow over the tip. The photographs obtained from this test series are shown in Figures 86a through 86r. Pictures of both upper and lower surfaces are presented. The lower surface pictures may be interpreted as results for negative pitch angles. The figures show that relatively little change in the flow pattern occurs for 2° changes in pitch angle. Therefore, all subsequent tests were conducted in 4° increments, namely, 0, 4, 8, 12 and 16°.

The photos at 0° pitch angle reveal that the flow pattern is virtually the same on the upper and lower surfaces, as would be expected. The traces on the end of the tip flow almost straight back. The direction of the traces on the upper surface is interesting to study as the pitch angle is changed from zero. The first two or three traces flow somewhat outward; the next four flow inward slightly; the next five flow almost straight back; and the last three show a tendency to flow outward. Figure 86g (6° pitch) shows the drastic change in flow direction between the seventh and eighth hole on the upper surface. The traces in front of the eighth hole flow gently inward, but the traces in the following holes showed a marked tendency to flow outward. The point where the flow changes direction from inward to outward on the upper surface is clearly a function of the pitch angle. For example, Figure 86o (14° pitch) shows the break point to be between the fifth and sixth holes. Following is a summary of this trend.

Pitch Angle, Degrees	First Hole on Upper Surface To Exhibit Outward Flow
0	13th
2	10th
4	8th
6	8th
8	7th
10	7th
12	6th
14	5th
16	5th

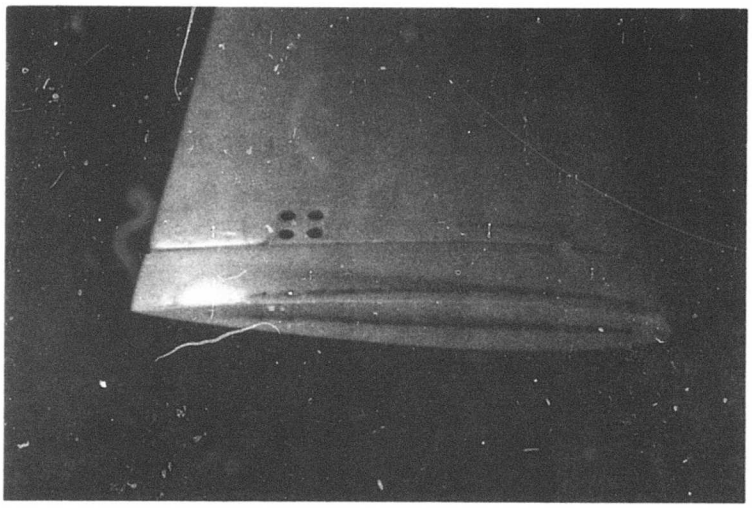

Figure 86a. Top View of Square Tip at 400 rpm and 0° Pitch Angle.

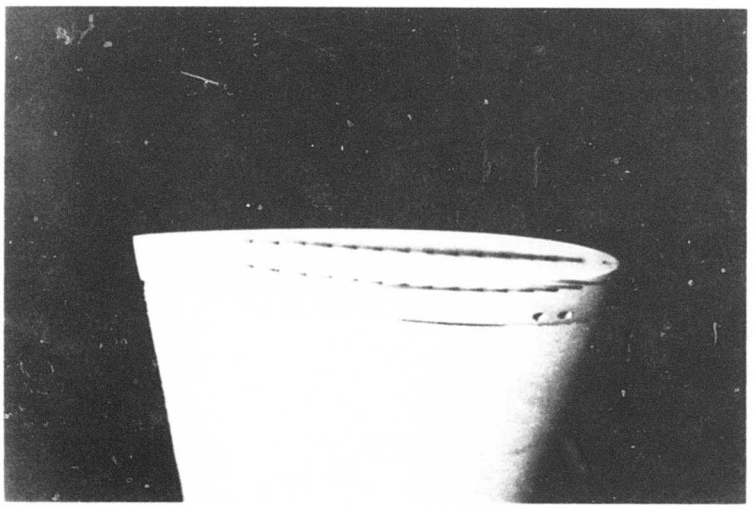

Figure 86b. Bottom View of Square Tip at 400 rpm and 0° Pitch Angle.

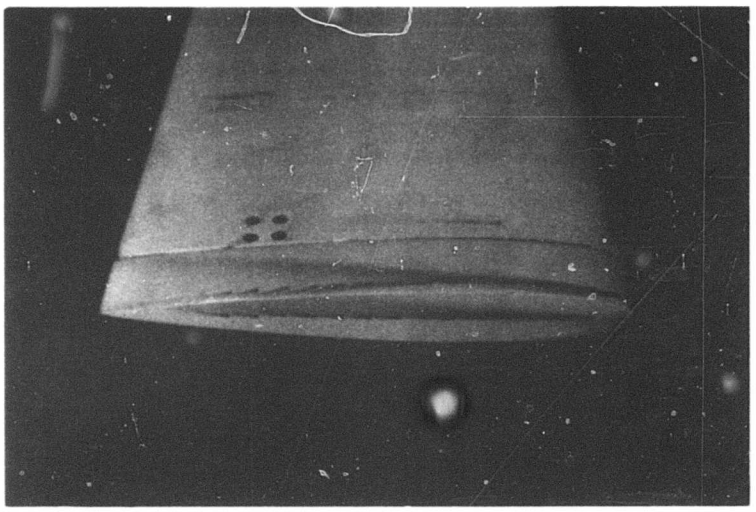

Figure 86c. Top View of Square Tip at 400 rpm and 2° Pitch Angle.

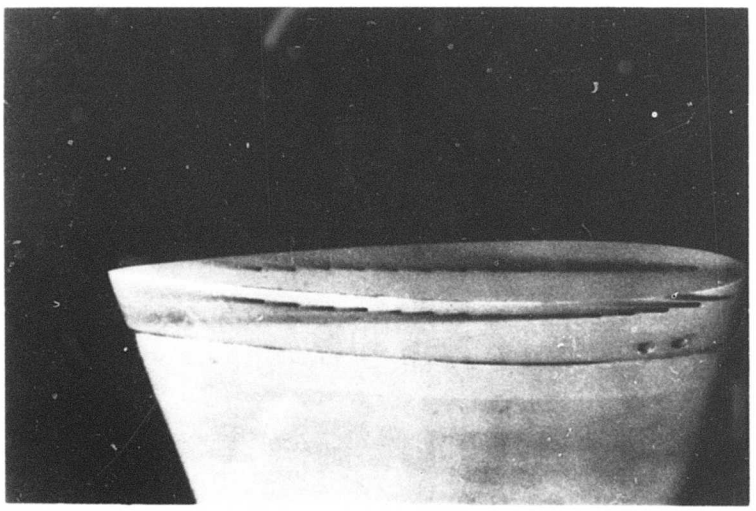

Figure 86d. Bottom View of Square Tip at 400 rpm and 2° Pitch Angle.

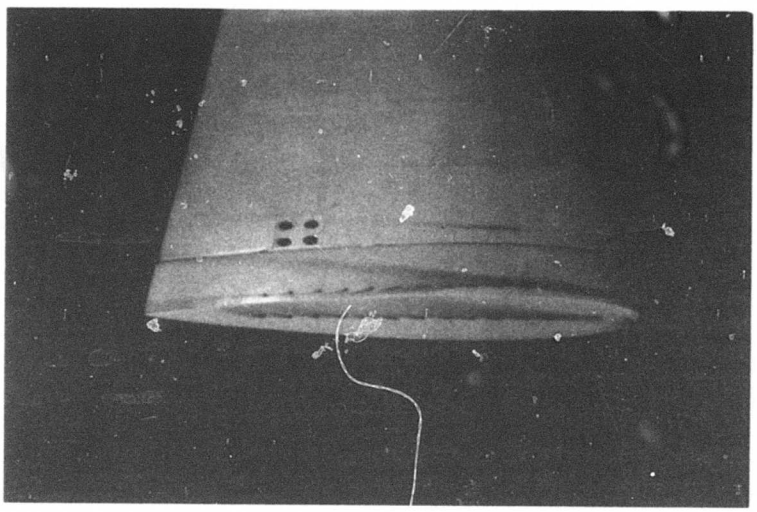

Figure 86e. Top View of Square Tip at 400 rpm and 4° Pitch Angle.

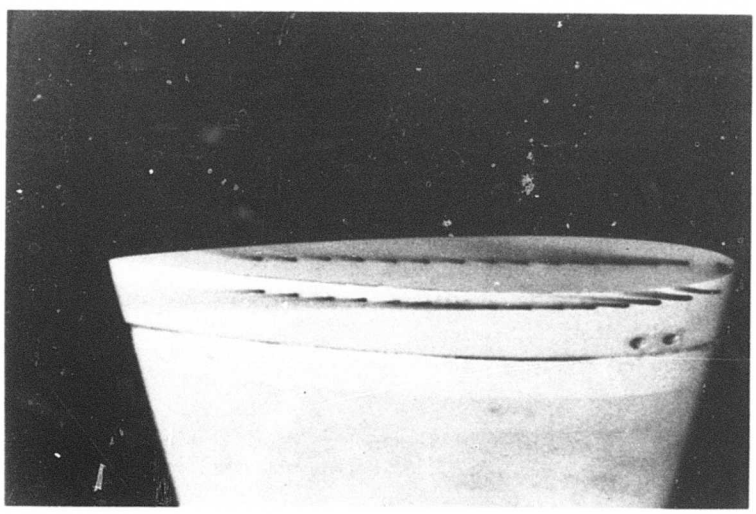

Figure 86f. Bottom View of Square Tip at 400 rpm and 4° Pitch Angle.

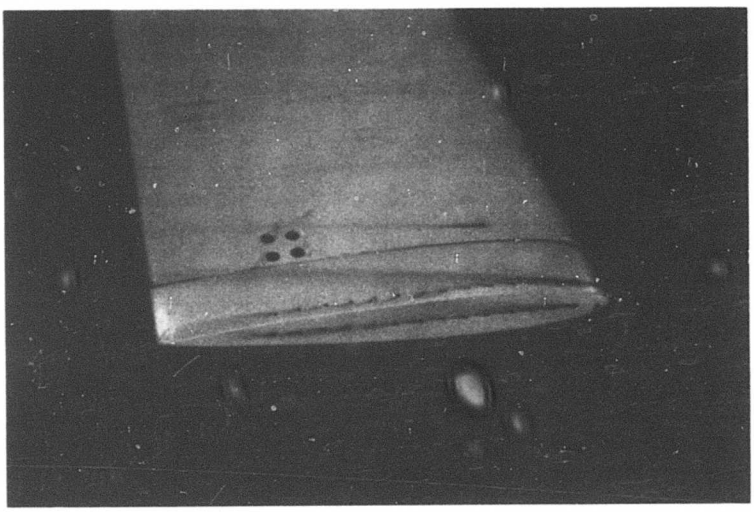

Figure 86g. Top View of Square Tip at 400 rpm and 6° Pitch Angle.

Figure 86h. Bottom View of Square Tip at 400 rpm and 6° Pitch Angle.

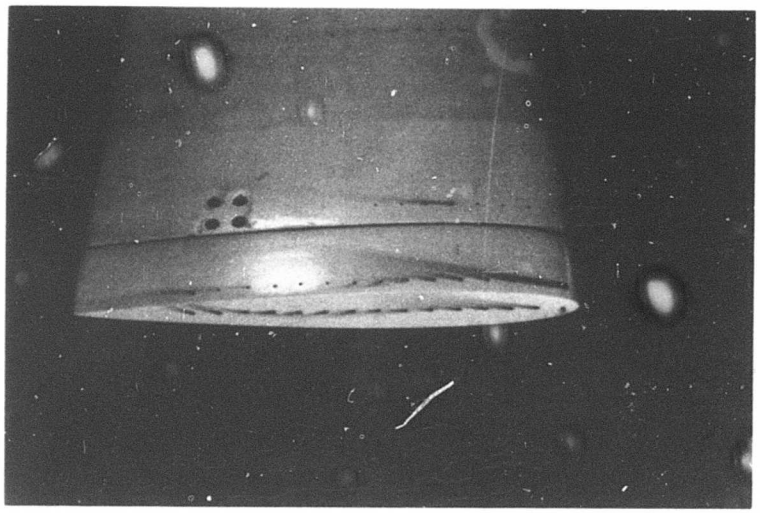

Figure 86i. Top View of Square Tip at 400 rpm and 8° Pitch Angle.

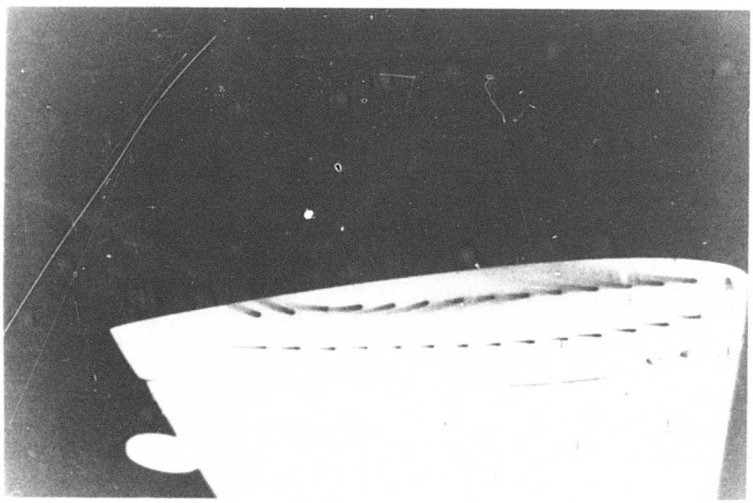

Figure 86j. Bottom View of Square Tip at 400 rpm and 8° Pitch Angle.

Figure 86k. Top View of Square Tip at 400 rpm and 10° Pitch Angle.

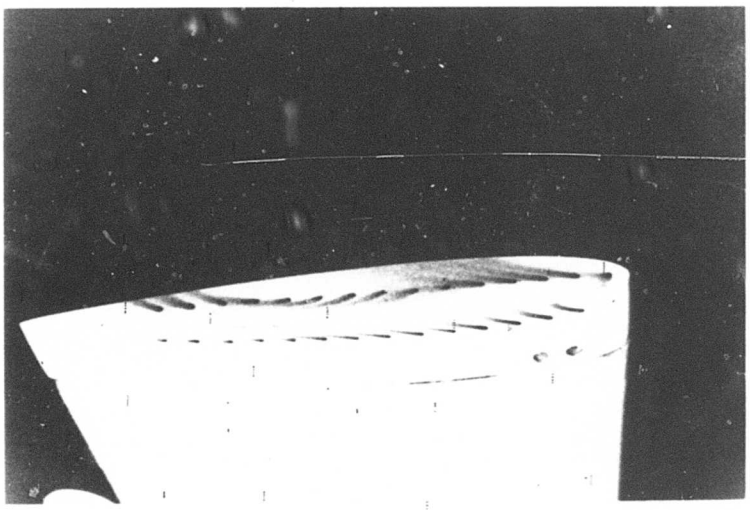

Figure 86ℓ. Bottom View of Square Tip at 400 rpm and 10° Pitch Angle.

Figure 86m. Top View of Square Tip at 400 rpm and 12° Pitch Angle.

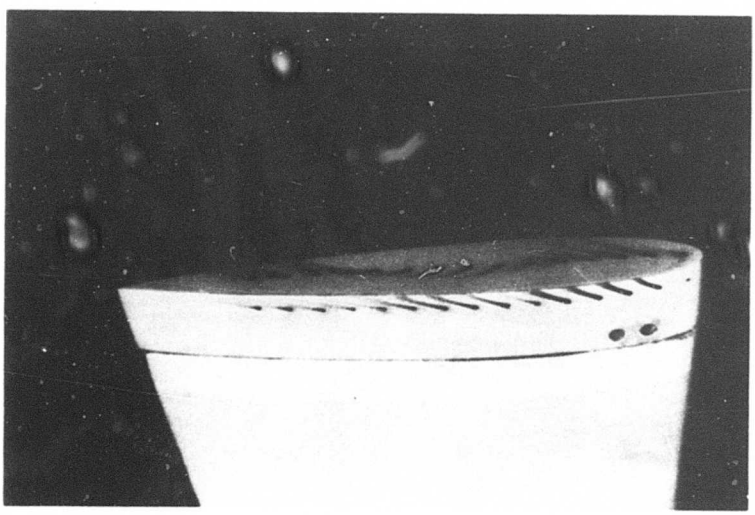

Figure 86n. Bottom View of Square Tip at 400 rpm and 12° Pitch Angle.

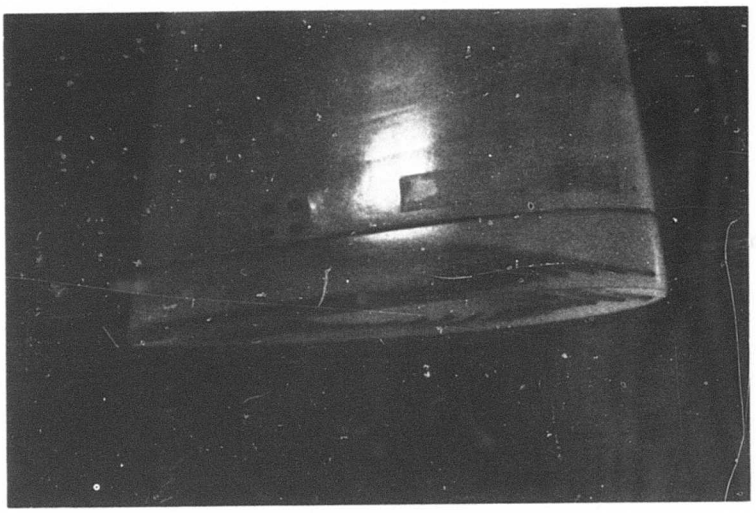

Figure 86o. Top View of Square Tip at 400 rpm and 14° Pitch Angle.

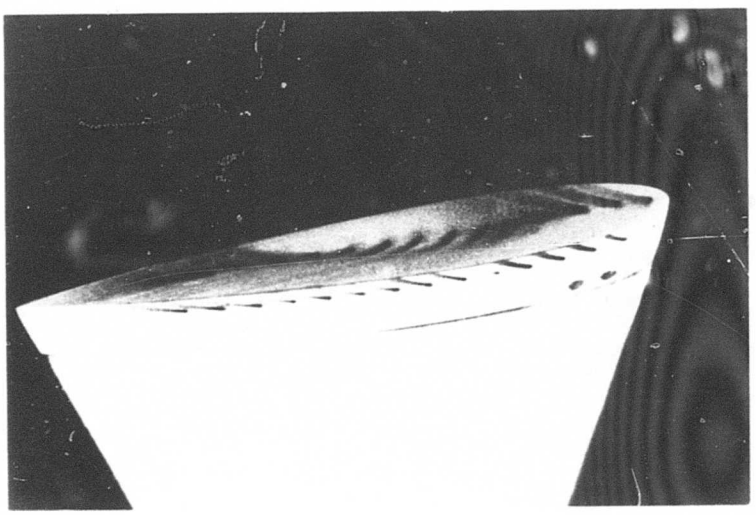

Figure 86p. Bottom View of Square Tip at 400 rpm and 14° Pitch Angle.

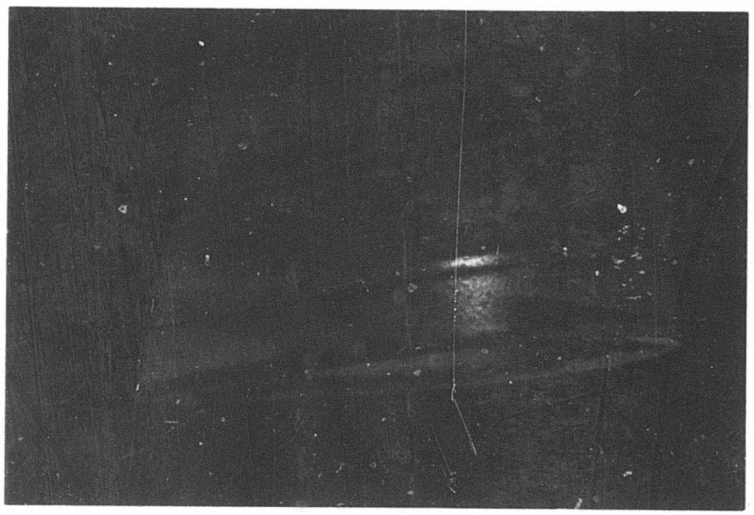

Figure 86q. Top View of Square Tip at 400 rpm and 16° Pitch Angle.

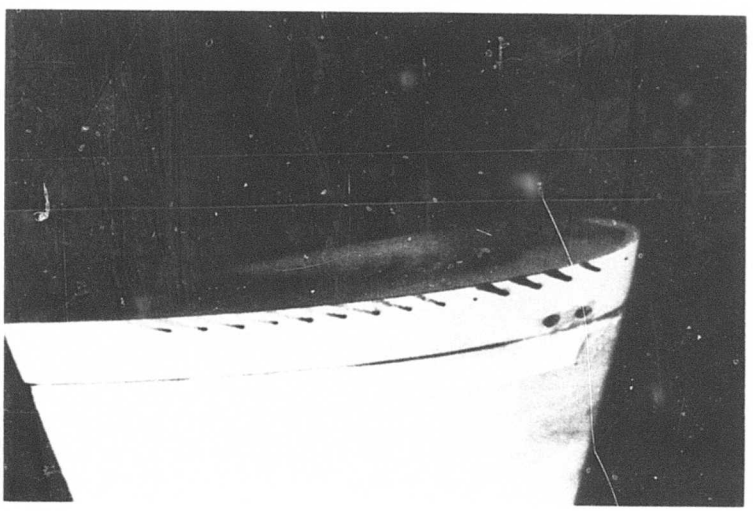

Figure 86r. Bottom View of Square Tip at 400 rpm and 16° Pitch Angle.

The break-point position was plotted as a function of pitch angle in Figure 87. This plot clearly shows the influence of pitch angle on break-point position.

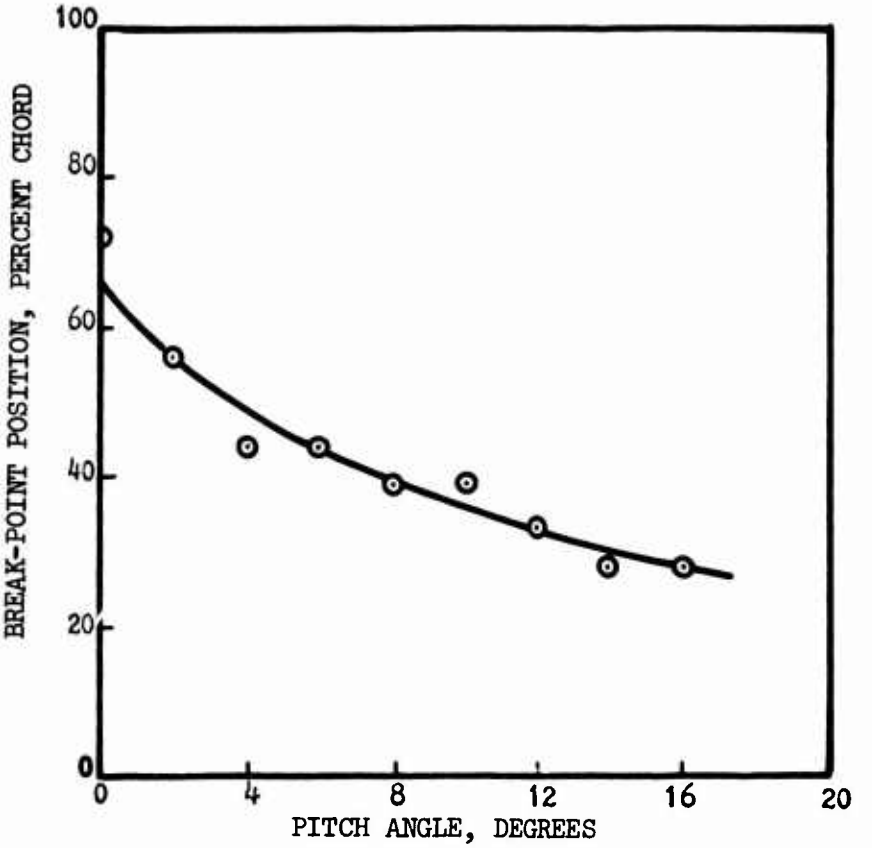

Figure 87. Point at Which Traces Change Direction From Inward to Outward on Upper Surface of Square Tip Versus Pitch Angle.

The traces on the underside of the tip do not exhibit the same trends as those on the upper surface. The flow traces on the lower surface at angles of attack of 0, 2, 4, and 6° exhibit essentially the same flow pattern. The first four traces show slight outflow; the flow then turns and proceeds chordwise, and finally starts turning inward. As pitch angle increases, the degree of outflow on the lower surface

increases, as observed by comparing Figure 86b with 86r. Almost all the traces at pitch angles from 10 to 16° show outflow on the lower surface. The explanation for the reversal of the flow direction from inward to outward on the lower surface between low and high pitch angles can be found by considering the relative magnitudes of pressure gradient (lower to upper surface) and free-stream (dynamic) pressure. As pitch angle increased, the pressure gradient from lower to upper surface increased to the point where it overcame the free-stream dynamic pressure, and thereby dictated the flow direction.

The final, and perhaps most interesting, trend in these photos is the pattern of the traces on the end of the tip. At 0' pitch the traces flow straight back; at slightly positive pitch angles (2, 4, 6°), the traces flow slightly upward, as would be expected due to the pressure difference between upper and lower surface. However, at pitch angles of 8° and above, a surprising flow pattern is revealed. The flow starts upward as before; but at the same distance back from the leading edge that the flow on the upper surface turned outward, the traces on the end of the tip suddenly turn downward. Then, the traces again turn upward farther downstream. The point where the flow turns from upward to downward is essentially the same function of pitch angle that was observed in the flow on the upper surface. The physical explanation for the flow pattern will be discussed in a subsequent section.

Additional tests were conducted with the square tip at rotor speeds of 500 and 600 rpm to determine the effect of Reynolds number on the flow pattern over the tip. Figures 86m, 88a, and 88b show the flow pattern at 400, 500, and 600 rpm at the 12° pitch angle. The three photos show that the point at which the flow on the upper surface turns outward and the flow on the end turns downward is at the same location for the three different speeds; namely, at the sixth hole from the leading edge. Comparison of individual traces from photo to photo reveals that they are virtually identical. The only difference is a subtle change in the angle of the traces on the end of the tip, which can be seen from careful comparison of Figure 86m and 88b. One interesting point is that the sixth hole from the leading edge does not exhibit any significant trace, whereas the holes in front of and in back of this hole show good traces. This may indicate that the boundary layer is separated from the surface momentarily at the point where the flow changes direction. This will be discussed further in a subsequent section. Since these tests demonstrated that rotational speed over the range 400 to 600 rpm had no significant effect on the flow pattern, most of the tests on the subsequent tips were conducted at 500 rpm.

5.3.1.2 Standard Tip. The next tip tested was the so-called standard tip. The tests were conducted at 0, 4, 8, 12, 16 and 18° and 500 rpm. Results of these tests are presented in Figures 89a through 89m. At 0° pitch angle (Figs. 89a and 89b), the traces flow

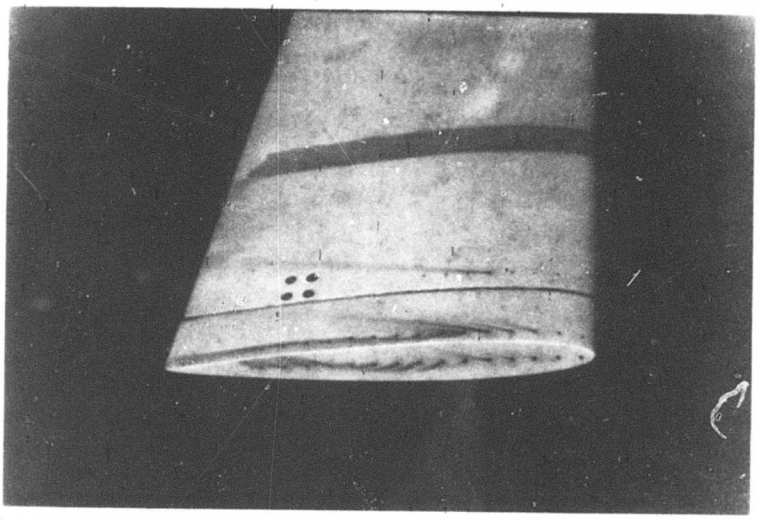

Figure 88a. Top View of Square Tip at 500 rpm and 12° Pitch Angle.

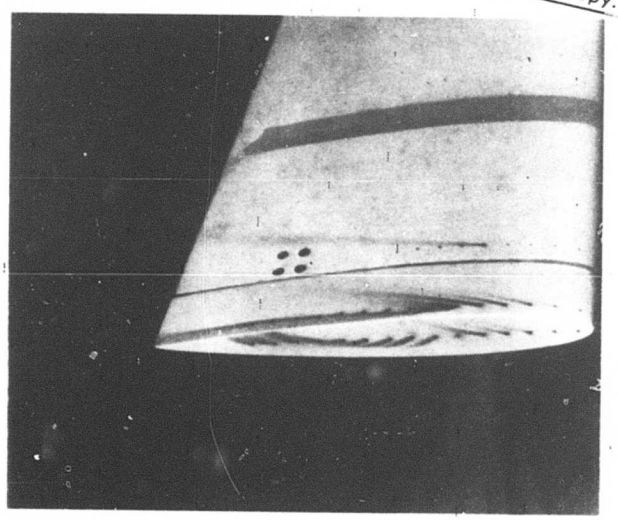

Figure 88b. Top View of Square Tip at 600 rpm and 12° Pitch Angle.

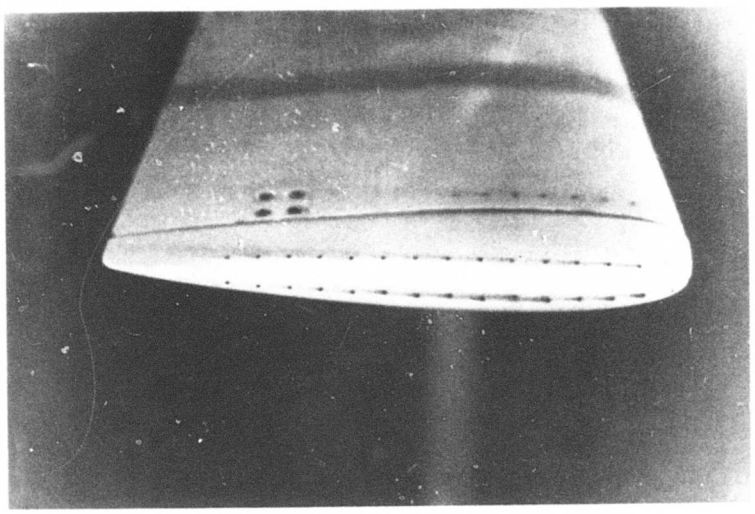

Figure 89a. Top View of Standard Tip at 500 rpm and 0° Pitch Angle.

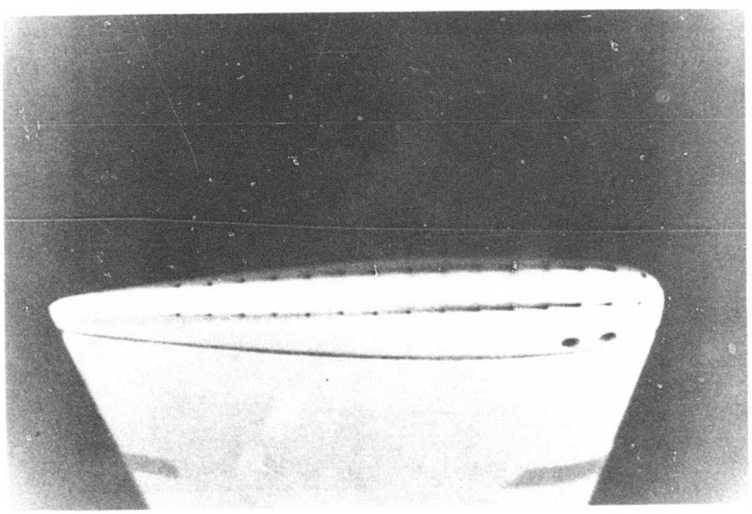

Figure 89b. Bottom View of Standard Tip at 500 rpm and 0° Pitch Angle.

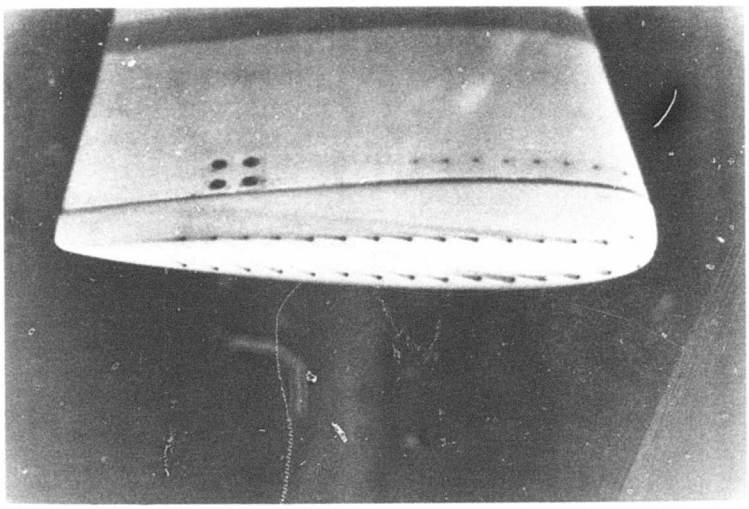

Figure 89c. Top View of Standard Tip at 500 rpm and 4° Pitch Angle.

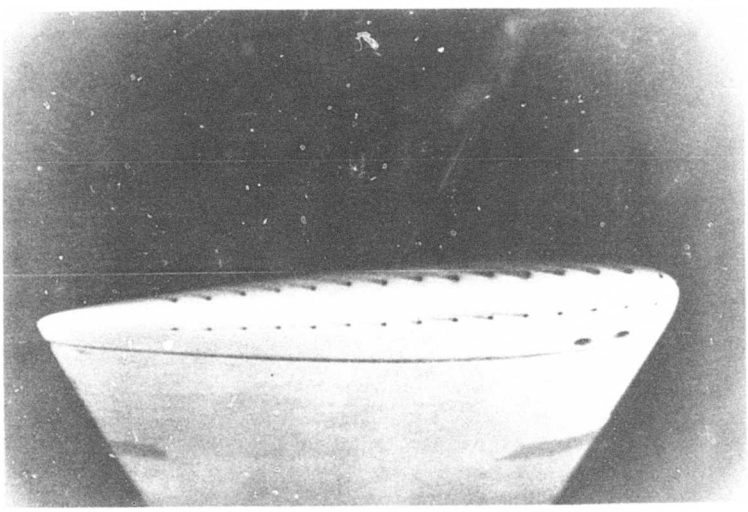

Figure 89d. Bottom View of Standard Tip at 500 rpm and 4° Pitch Angle.

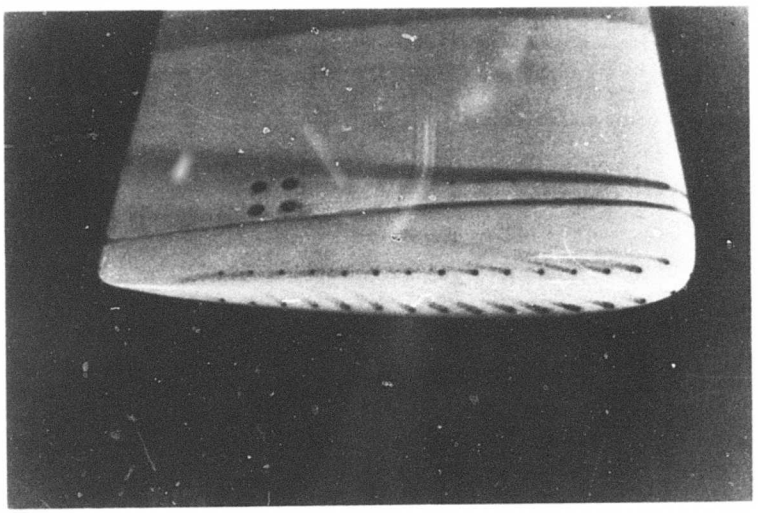

Figure 89e. Top View of Standard Tip at 500 rpm and 8° Pitch Angle.

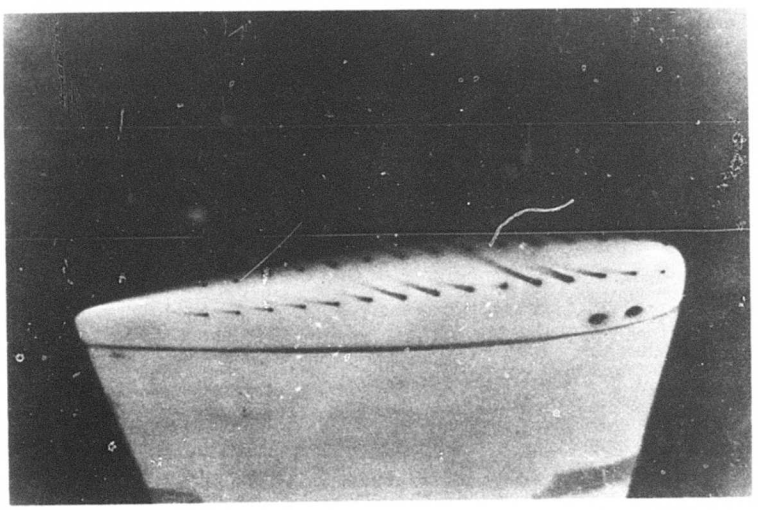

Figure 89f. Bottom View of Standard Tip at 500 rpm and 8° Pitch Angle.

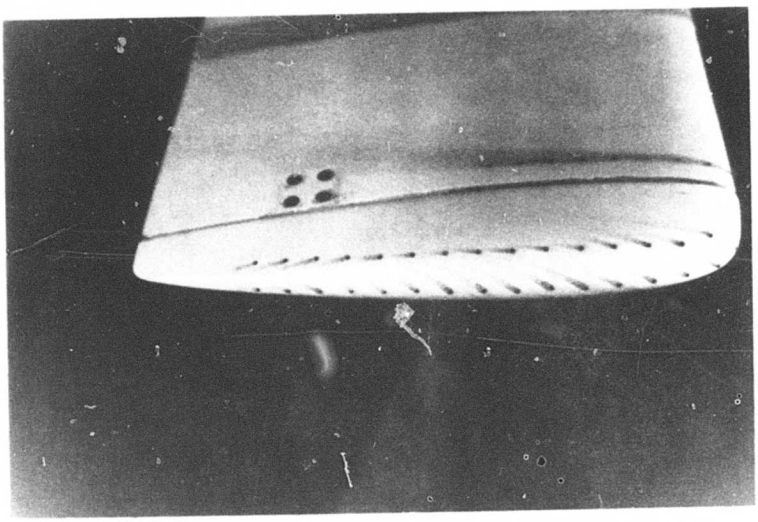

Figure 89g. Top View of Standard Tip at 500 rpm and 12° Pitch Angle.

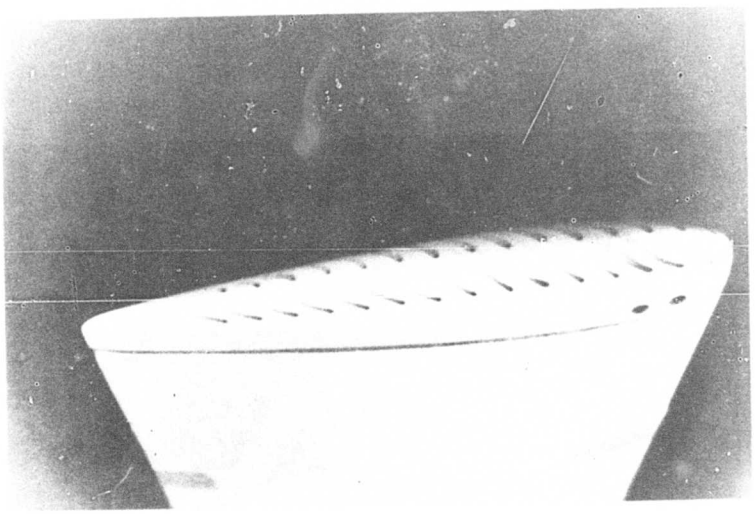

Figure 89h. Bottom View of Standard Tip at 500 rpm and 12° Pitch Angle.

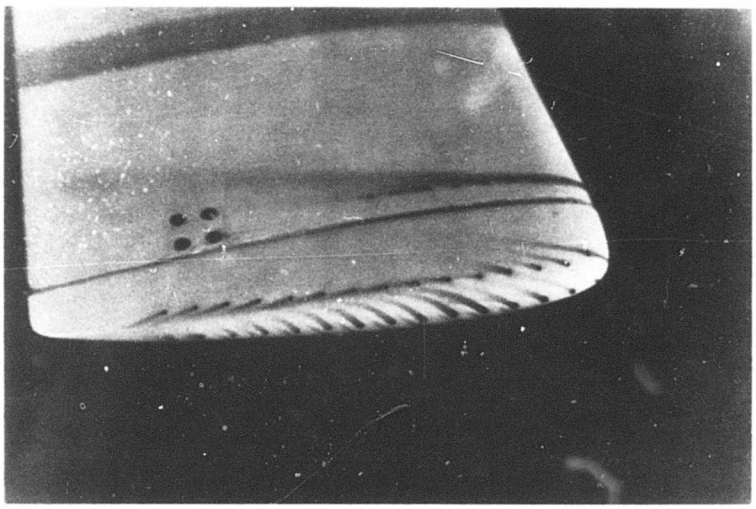

Figure 89i. Top View of Standard Tip at 500 rpm and 16° Pitch Angle.

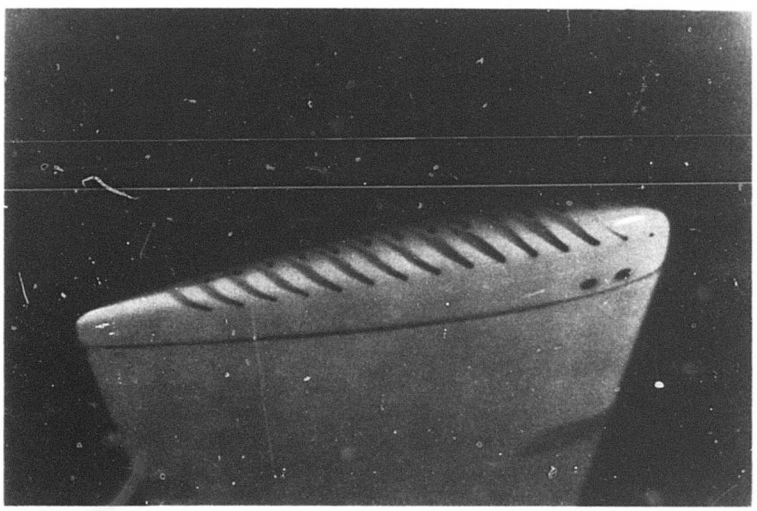

Figure 89j. Bottom View of Standard Tip at 500 rpm and 16° Pitch Angle.

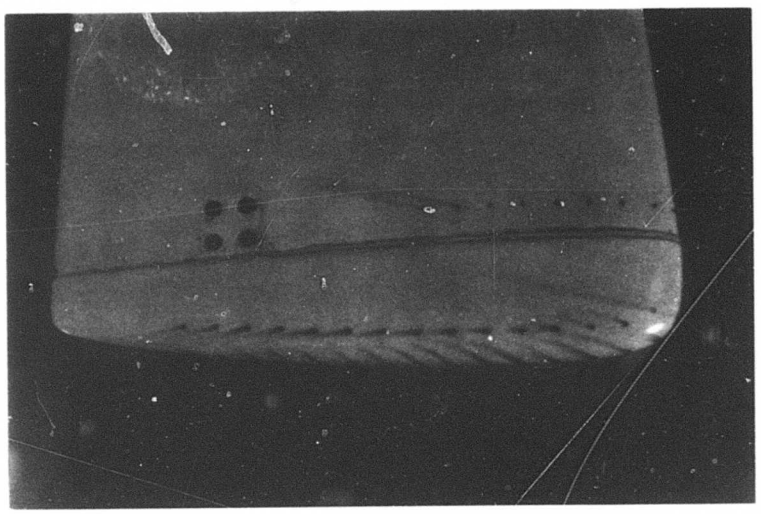

Figure 89k. Top View of Standard Tip at 500 rpm and 18° Pitch Angle.

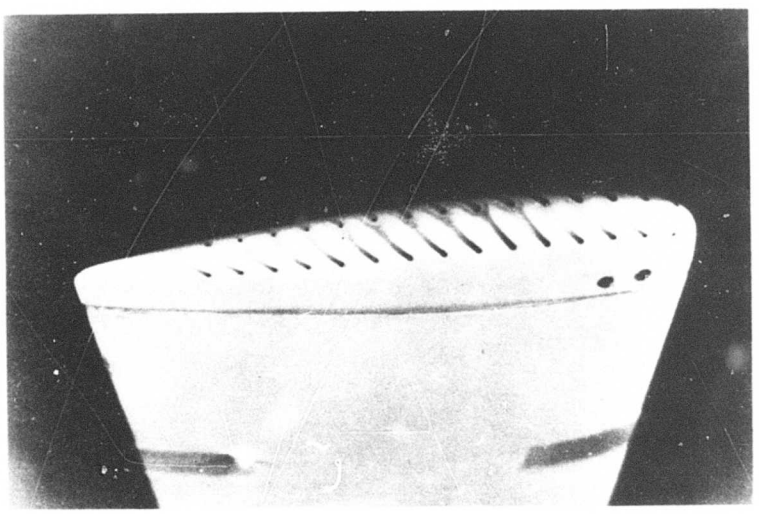

Figure 89ℓ. Bottom View of Standard Tip at 500 rpm and 18° Pitch Angle.

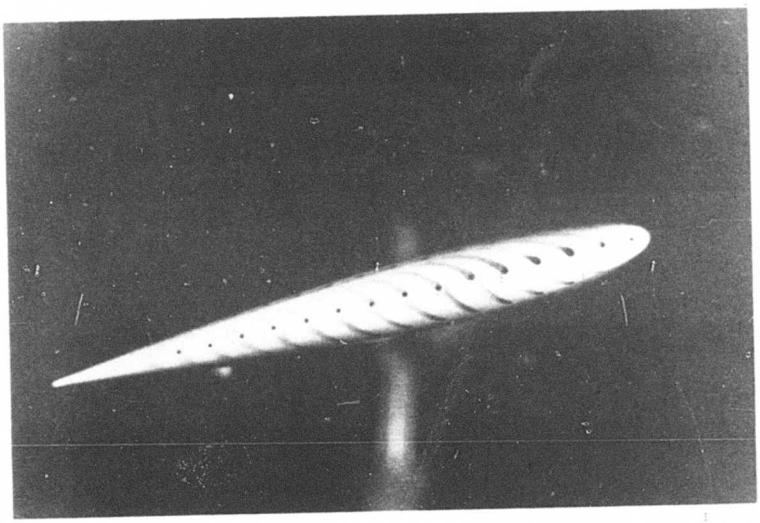

Figure 89m. End View of Standard Tip at 500 rpm and 18° Pitch Angle.

almost straight back and do not exhibit any anomalies. The traces on the end of the tip show a slight tendency to flow upward; this is most likely due to a small error in setting the pitch angle slightly above 0°. For pitch angles from 4 to 18°, the traces reveal flow patterns of a similar nature. Figure 89c shows the upward flow on the end of the tip; this becomes more and more pronounced at higher pitch angles (as shown in Figs. 89i and 89m) due to the increasing pressure gradient from the lower to upper surfaces. Figure 89j clearly shows the flow pattern from the bottom surface around the underside of the tip. (Note the effect of the toothpick tips on some of the traces at the outer row of holes.) The traces reveal a definite "roll-up" of the lower surface boundary layer around the tip. This roll-up begins very near the leading edge at high pitch angles (above 8°). Figure 89m shows that the flow over the tip is in the form of a spiral, and the traces from the lower surfaces are almost continuous with those emanating from the end of the tip.

The flow pattern on the upper surface of the tip is shown in Figure 89i. The traces from the first four or five holes flow inward; the traces then change direction and flow almost straight back as they did in the case of the square tip; finally, the last five or six holes exhibit outward flow. The change in flow direction on the upper surface becomes more discernible at higher pitch angles, and is only slightly evident in Figure 89c (4° pitch angle). Again, as in the case of the square tip, there is a tendency for the change in flow direction to move toward the leading edge with higher pitch angle, although it is not as pronounced as for the square tip.

Figures 89f and 89h show flow traces on the underside of the tip at 8° and 12° pitch angle. There is an apparent change in the flow direction at or near the sixth hole from the leading edge in Figure 89f. The flow ahead of this point appears to go in a more outward direction than the traces following this hole. This same effect is observable from Figure 89h. Note that the trace from the sixth hole is definitely not parallel to the traces emanating from the hole in front of and in back of it. Moreover, at the ninth hole there is another clear change in the direction of the flow, and the traces following the ninth hole are all essentially parallel. The explanation for these apparent changes in flow direction is not known at this time.

Another series of tests was conducted with the standard tip at 1000 rpm and pitch angles of 0, 4, 8, 12 and 16°. The results of these tests are presented in Figures 90a through 90j and show essentially the same flow patterns as those for the tests conducted at 500 rpm. This supports the earlier statement that Reynolds number has relatively little effect on the flow pattern. One difference noted between the traces at 500 and 1000 rpm can be seen by comparing Figures 89h and 90h. The lower surface traces reveal a change in flow direction at the eighth hole in Figure 90h (1000 rpm), whereas this change took place at the sixth and ninth holes in Figure 89h (500 rpm). The traces in Figures 90j, k and ℓ are smeared somewhat due to the diazonium salt solution's "running" during rotation.

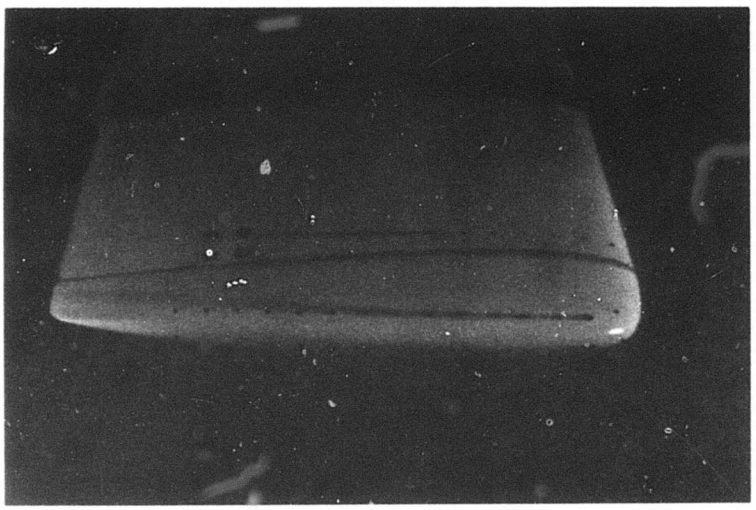

Figure 90a. Top View of Standard Tip at 1000 rpm and 0° Pitch Angle.

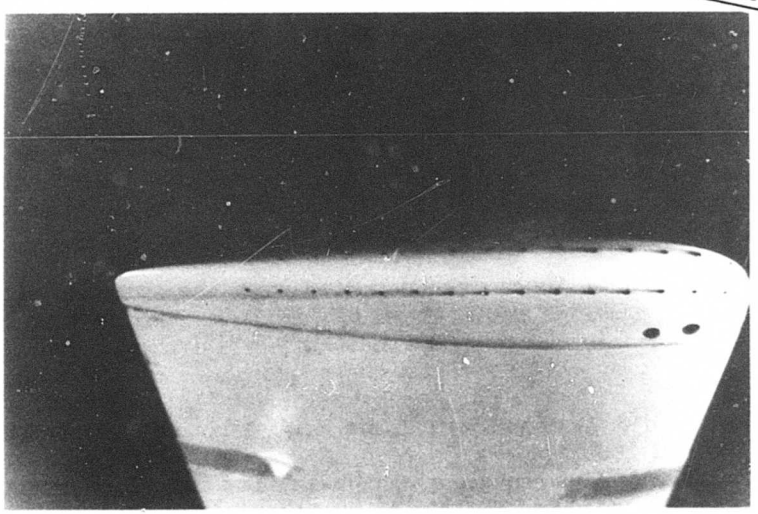

Figure 90b. Bottom View of Standard Tip at 1000 rpm and 0° Pitch Angle.

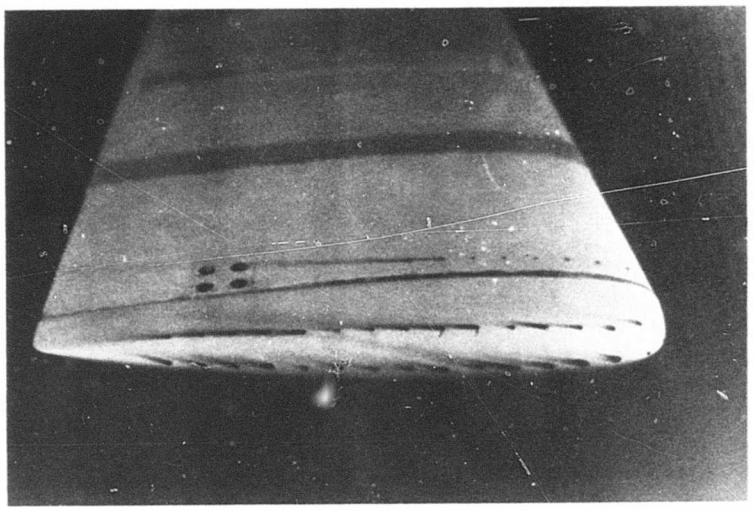

Figure 90c. Top View of Standard Tip at 1000 rpm and 4° Pitch Angle.

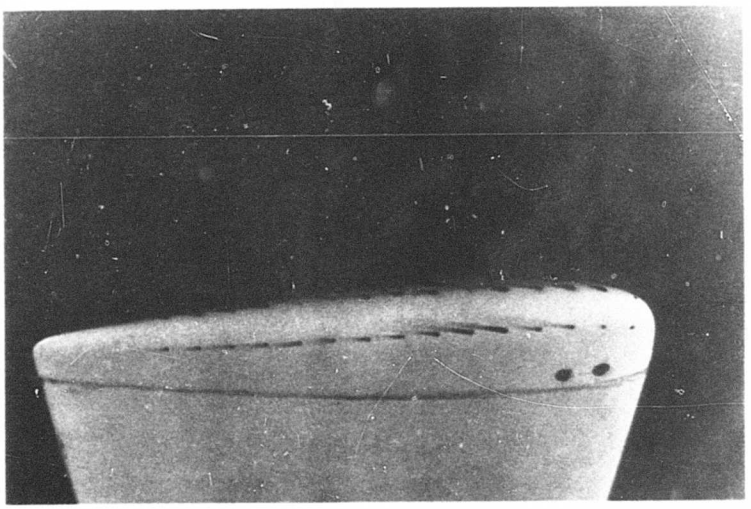

Figure 90d. Bottom View of Standard Tip at 1000 rpm and 4° Pitch Angle.

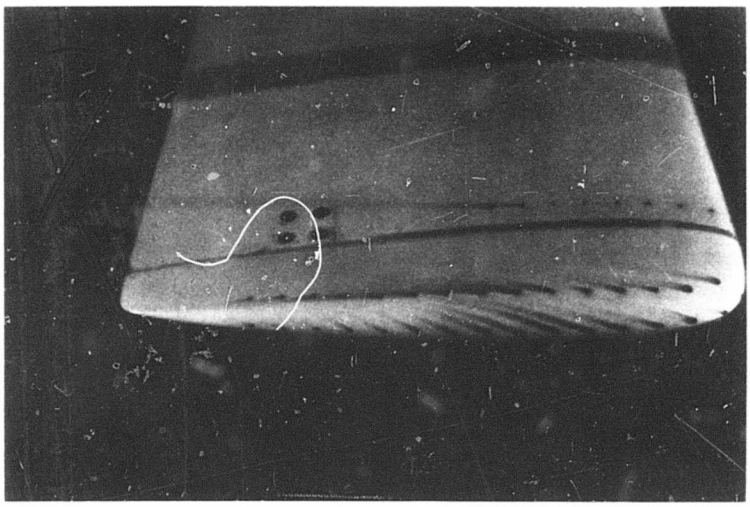

Figure 90e. Top View of Standard Tip at 1000 rpm and 8° Pitch Angle.

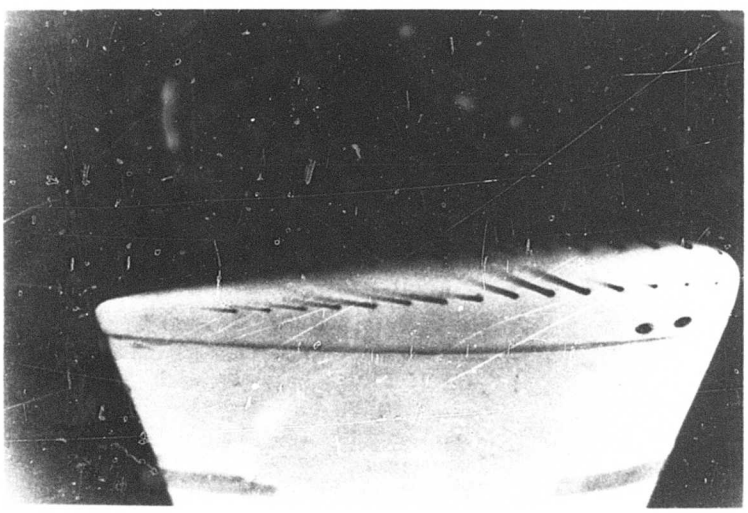

Figure 90f. Bottom View of Standard Tip at 1000 rpm and 8° Pitch Angle.

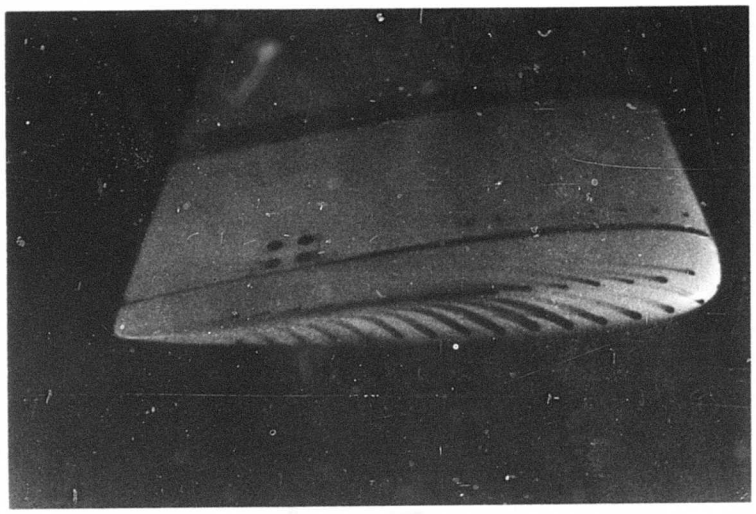

Figure 90g. Top View of Standard Tip at 1000 rpm and 12° Pitch Angle.

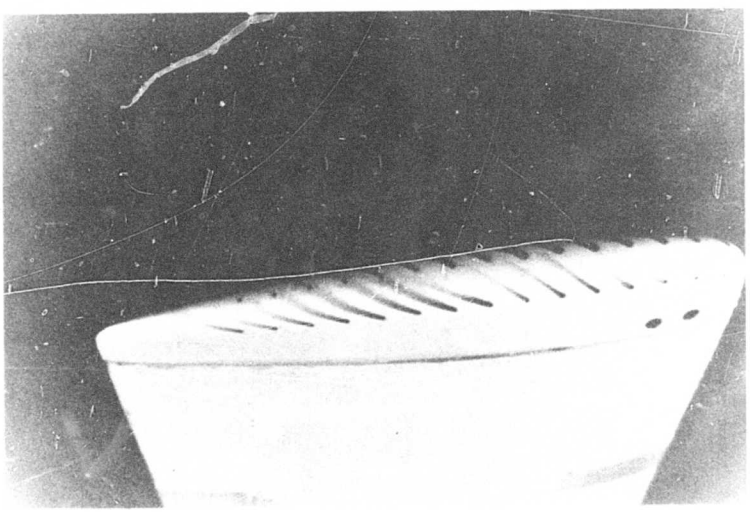

Figure 90h. Bottom View of Standard Tip at 1000 rpm and 12° Pitch Angle.

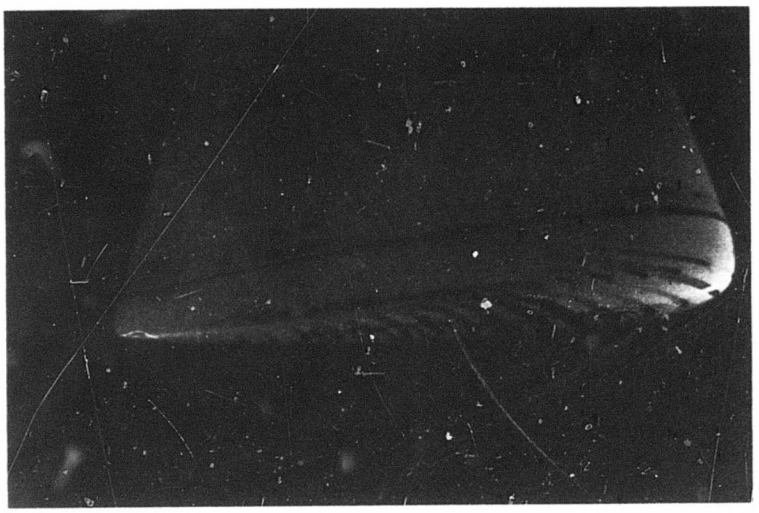

Figure 90i. Top View of Standard Tip at 1000 rpm and 16° Pitch Angle.

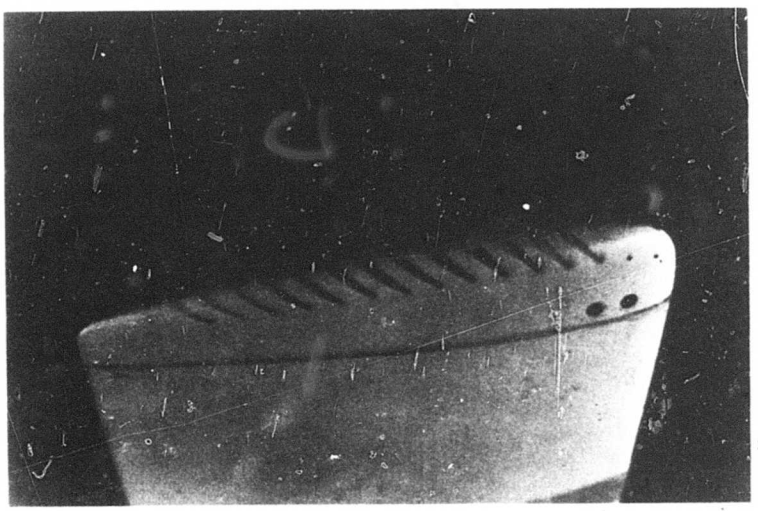

Figure 90j. Bottom View of Standard Tip at 1000 rpm and 16° Pitch Angle.

5.3.1.3 Swept-Aft Tip. The next tip tested was the swept-aft tip. A series of tests was conducted at 500 rpm and pitch angles of 0, 4, 8, 12 and 16°. Again, the traces on the lower surface may be interpreted as those for negative angles of attack. Figures 91a through 91j present the results of these tests. These photos show evidence of inflow in almost every case, both on the upper surface and lower surface. The inflow appears greatest near the leading edge and near the end of the tip. Pitch angle has a much smaller effect on the flow pattern than for the two previous tips. For example, compare Figure 91a with 91g. There is some tendency for greater inflow on the upper surface with increasing pitch angles, and for a lesser inflow on the lower surface with higher pitch angles. This is consistent with the previous statement that the pressure gradient increases the tendency for flow from the lower surface to the upper surface. The traces on the lower surface are sharp and clear, whereas the traces on the upper surface are fuzzy and more diffuse, especially at high pitch angles. This result is indicative of the nature of the flow in these regions, i.e., the flow on the upper surface is probably separated and highly turbulent (see Fig. 91i) while the boundary layer is probably well attached on the lower surface due to the high pressure in this region. It is interesting to note the flow pattern in Figure 91g near the first holes following the leading edge. There are faint traces which show that some "spanwise" flow is occurring near the leading edge.

5.3.1.4 Trapezoidal Tip. The fourth tip tested was the trapezoidal tip. A test series was conducted at 500 rpm and pitch angles of 0, 4, 8, 12 and 16°. Photographs of these tests are presented in Figures 92a through 92j. Figures 92a, c, e, g, and i, which show the upper surface at each pitch angle, reveal inflow which increases near the end of the tip. No unusual flow patterns are evident from these photos. The last two traces in the outermost row in Figure 92i start to turn slightly outward near the trailing edge. The traces from the inner two rows of holes on the lower surface flow virtually straight back in all cases, and show essentially no effects due to the tip. The traces emanating from the outer row of holes on the lower surface exhibit essentially the same flow pattern that was observed from the standard tip; namely, a rolling-up effect which increases greatly with pitch angle. This result is reasonable since the end of the trapezoidal tip is very similar to the standard tip.

5.3.1.5 Cusp Tip. The fifth tip configuration which was investigated was the cusp tip. Again, a series of tests was conducted at 500 rpm and pitch angles of 0, 4, 8, 12 and 16°. Photographs of these test results are presented in Figures 93a through 93j. The traces on the upper surface (Figs. 93a, c, e, g, i) show that the flow direction changes from straight back or slightly outward to inward at the point where the length of the tip decreases sharply (near the seventh hole from the leading edge). The traces over the outer row of holes on the upper surface reveal flow separation at the 12 and 16° pitch angles. The traces on the lower surface are somewhat

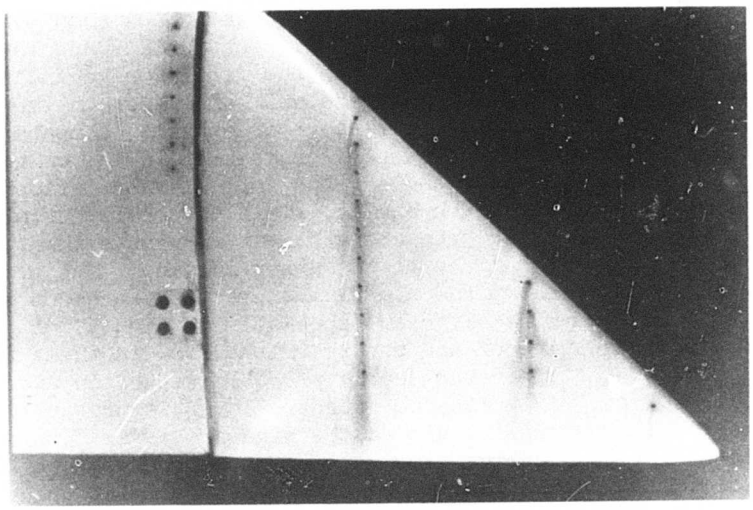

Figure 91a. Top View of Swept-Aft Tip at 500 rpm and 0° Pitch Angle.

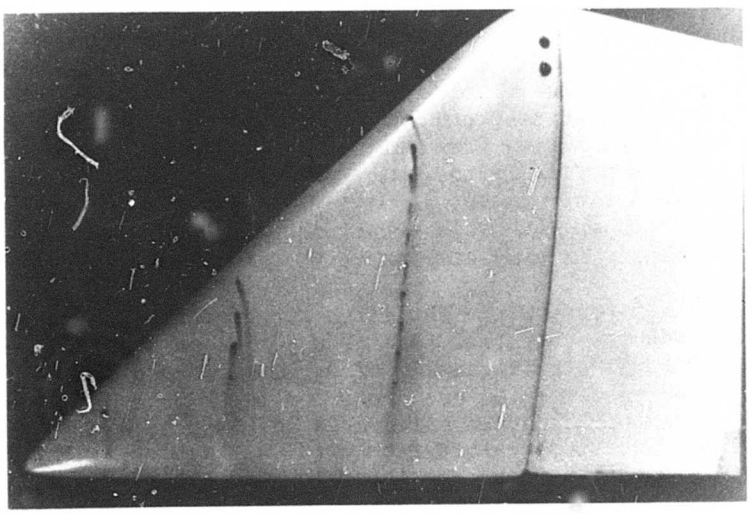

Figure 91b. Bottom View of Swept-Aft Tip at 500 rpm and 0° Pitch Angle.

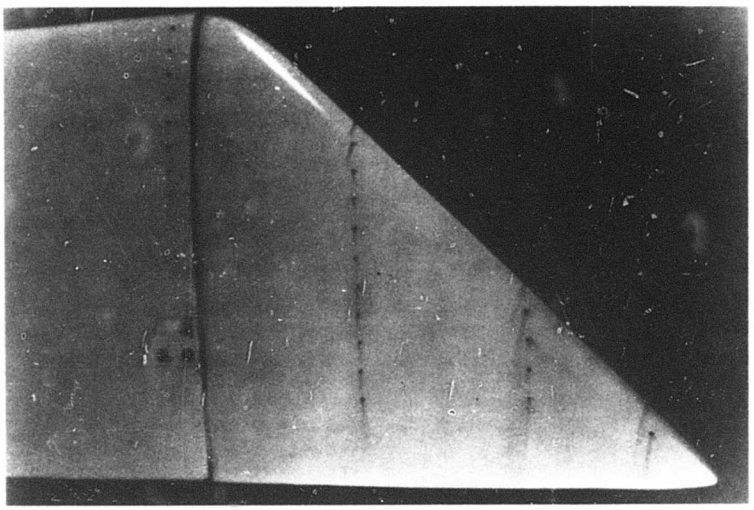

Figure 91c. Top View of Swept-Aft Tip at 500 rpm and 4° Pitch Angle.

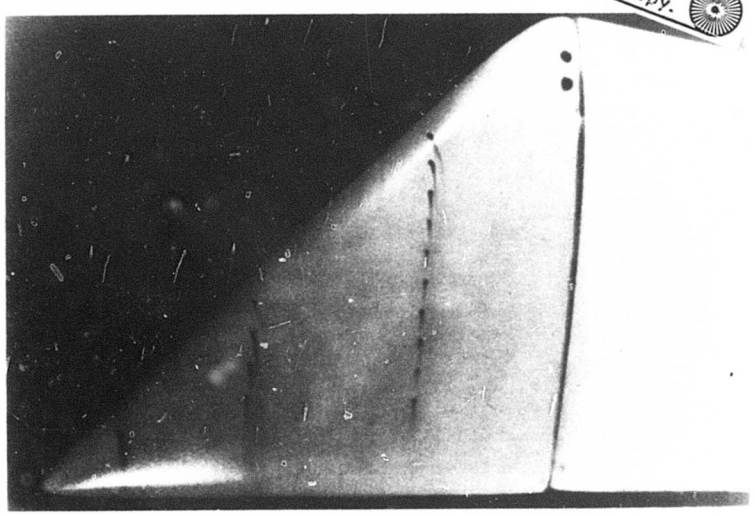

Figure 91d. Bottom View of Swept-Aft Tip at 500 rpm and 4° Pitch Angle.

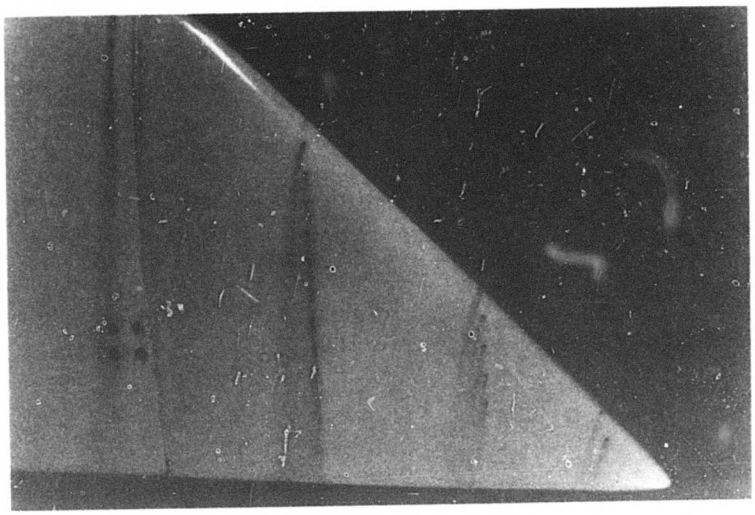

Figure 91e. Top View of Swept-Aft Tip at 500 rpm and 8° Pitch Angle.

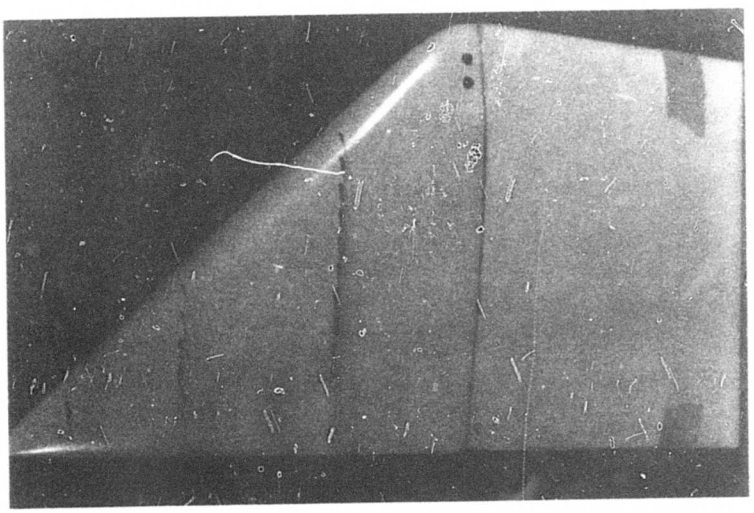

Figure 91f. Bottom View of Swept-Aft Tip at 500 rpm and 8° Pitch Angle.

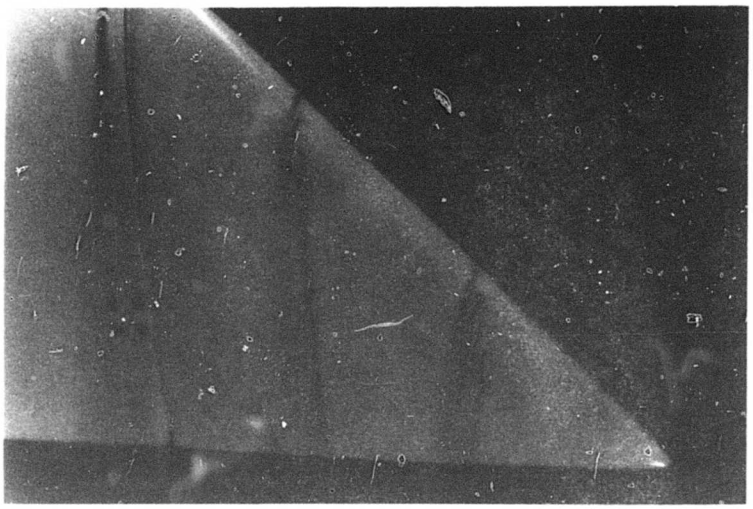

Figure 91g. Top View of Swept-Aft Tip at 500 rpm and 12° Pitch Angle.

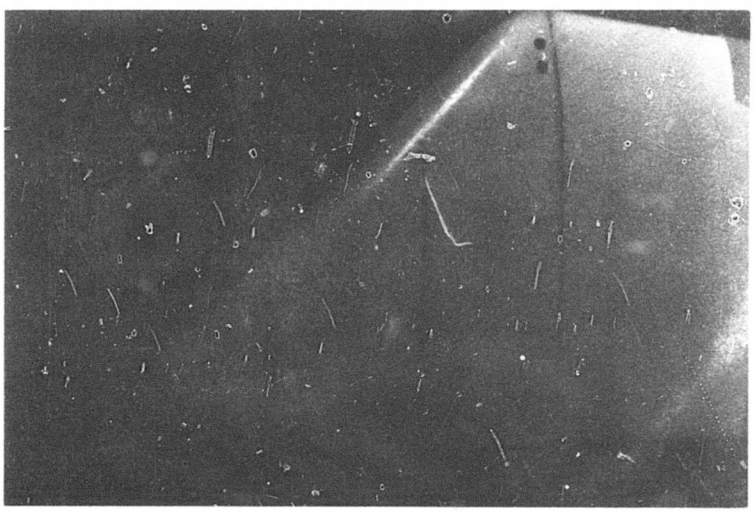

Figure 91h. Bottom View of Swept-Aft Tip at 500 rpm and 12° Pitch Angle.

Figure 91i. Top View of Swept-Aft Tip at 500 rpm and 16° Pitch Angle.

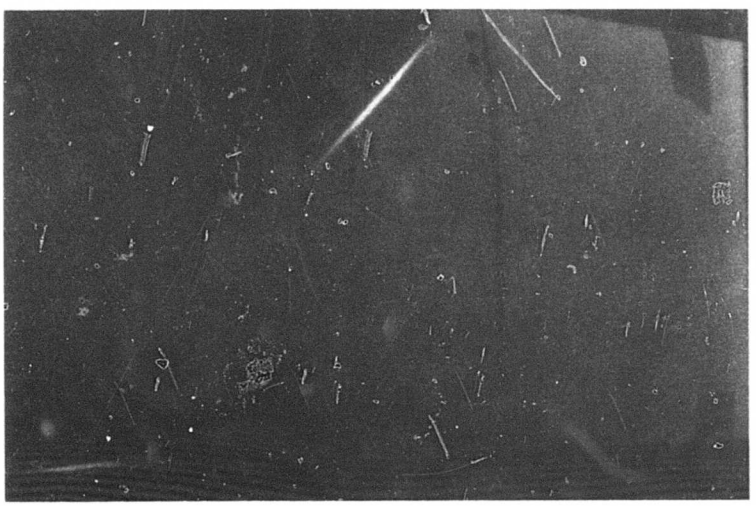

Figure 91j. Bottom View of Swept-Aft Tip at 500 rpm and 16° Pitch Angle.

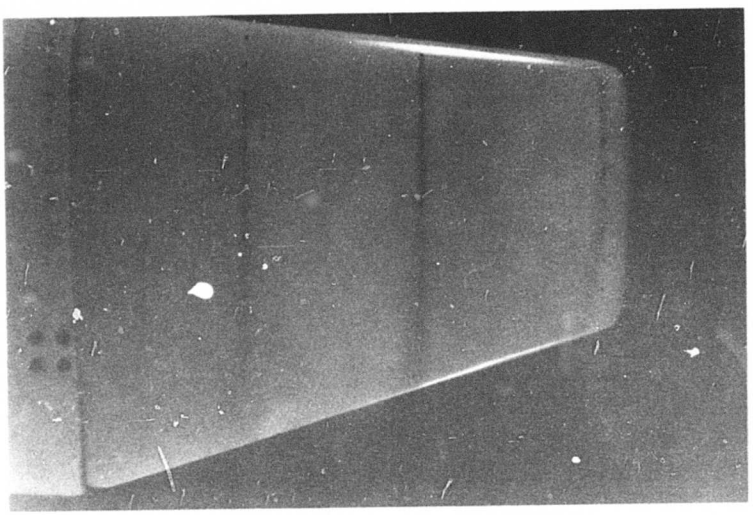

Figure 92a. Top View of Trapezoidal Tip at 500 rpm and 0° Pitch Angle.

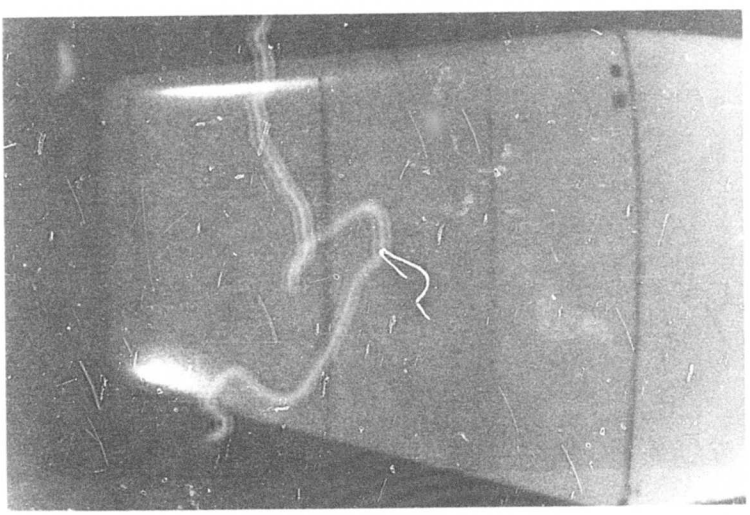

Figure 92b. Bottom View of Trapezoidal Tip at 500 rpm and 0° Pitch Angle.

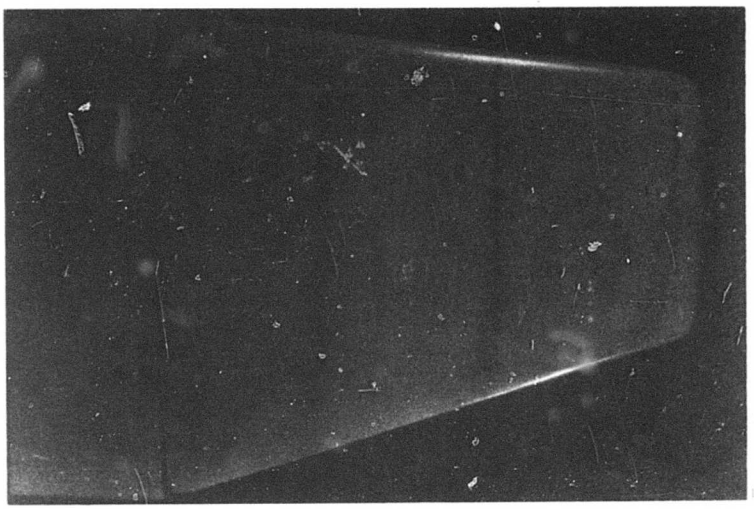

Figure 92c. Top View of Trapezoidal Tip at 500 rpm and 4° Pitch Angle.

Figure 92d. Bottom View of Trapezoidal Tip at 500 rpm and 4° Pitch Angle.

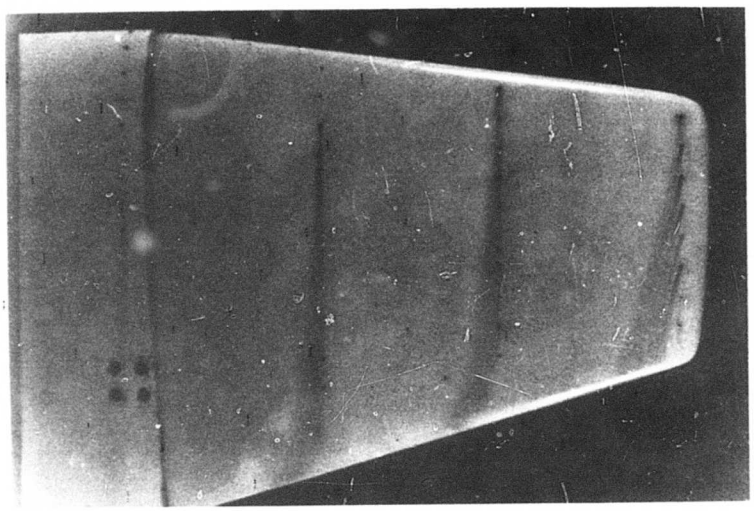

Figure 92e. Top View of Trapezoidal Tip at 500 rpm and 8° Pitch Angle.

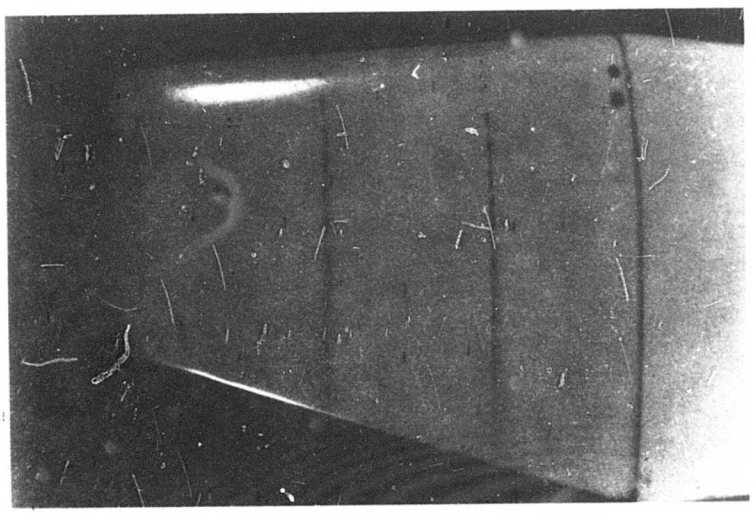

Figure 92f. Bottom View of Trapezoidal Tip at 500 rpm and 8° Pitch Angle.

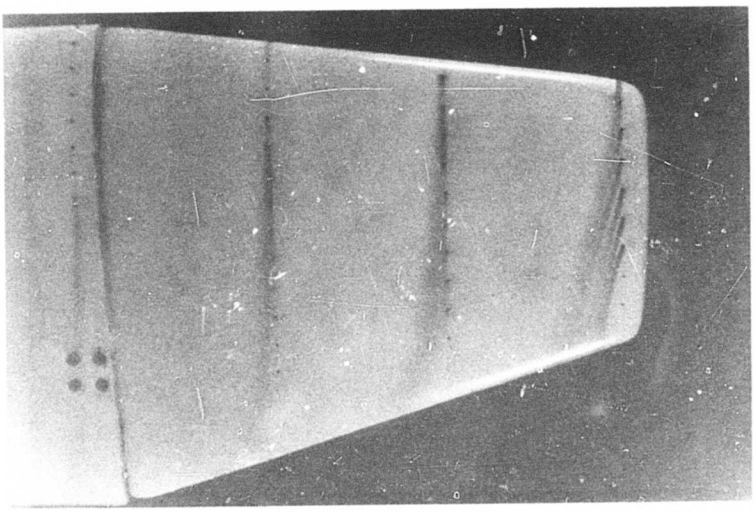

Figure 92g. Top View of Trapezoidal Tip at 500 rpm and 12° Pitch Angle.

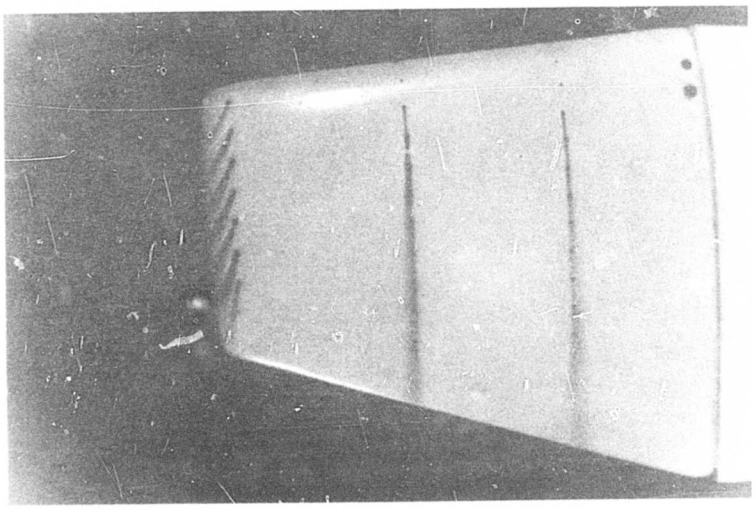

Figure 92h. Bottom View of Trapezoidal Tip at 500 rpm and 12° Pitch Angle.

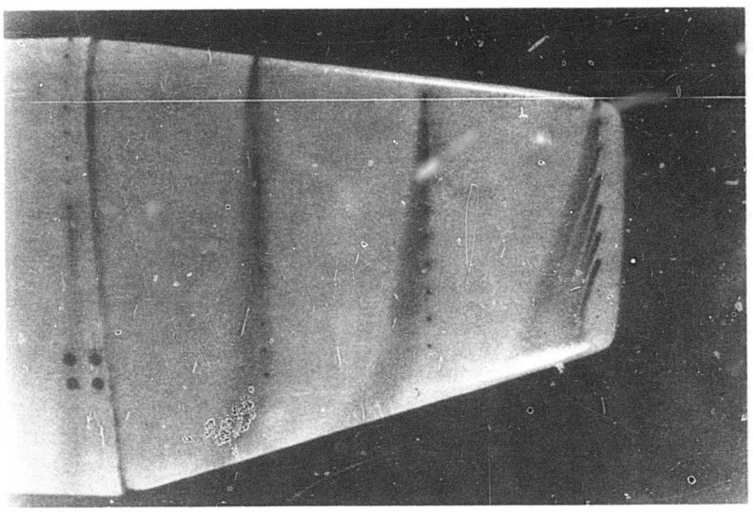

Figure 92i. Top View of Trapezoidal Tip at 500 rpm and 16° Pitch Angle.

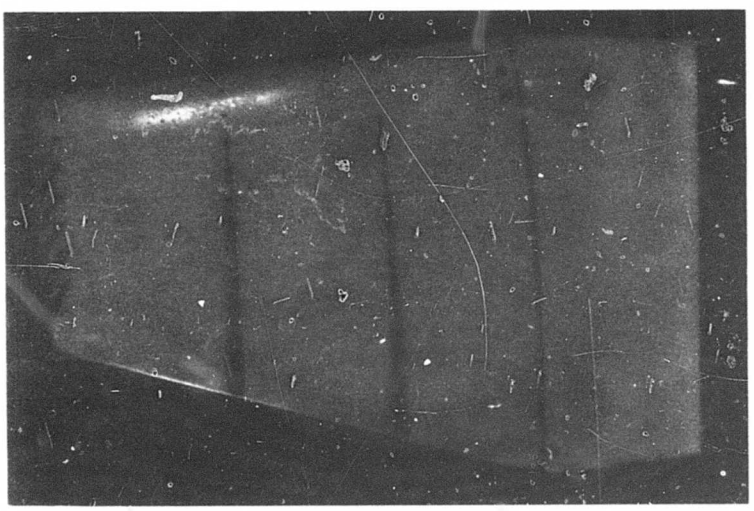

Figure 92j. Bottom View of Trapezoidal Tip at 500 rpm and 16° Pitch Angle.

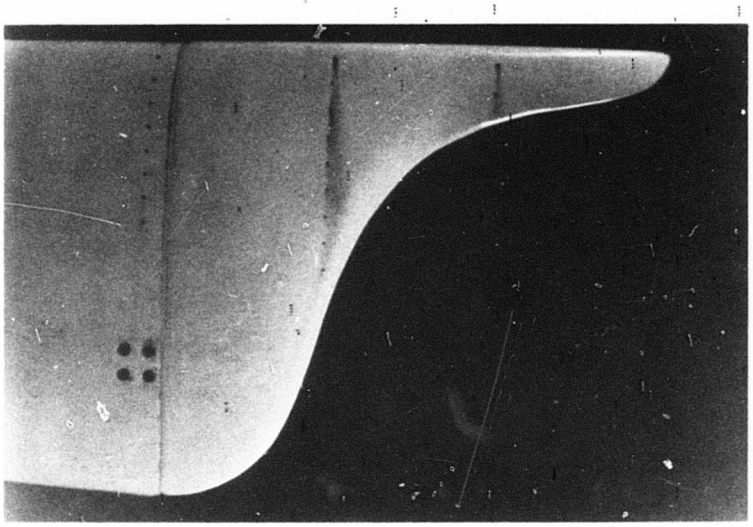

Figure 93a. Top View of Cusp Tip at 500 rpm and 0° Pitch Angle.

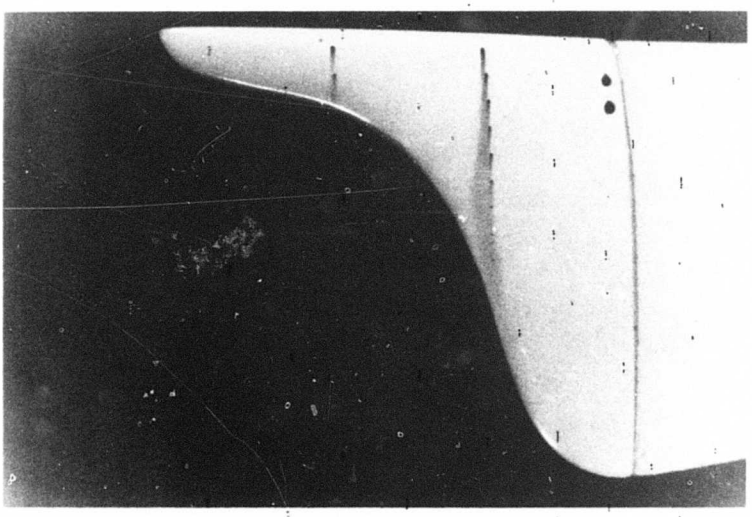

Figure 93b. Bottom View of Cusp Tip at 500 rpm and 0° Pitch Angle.

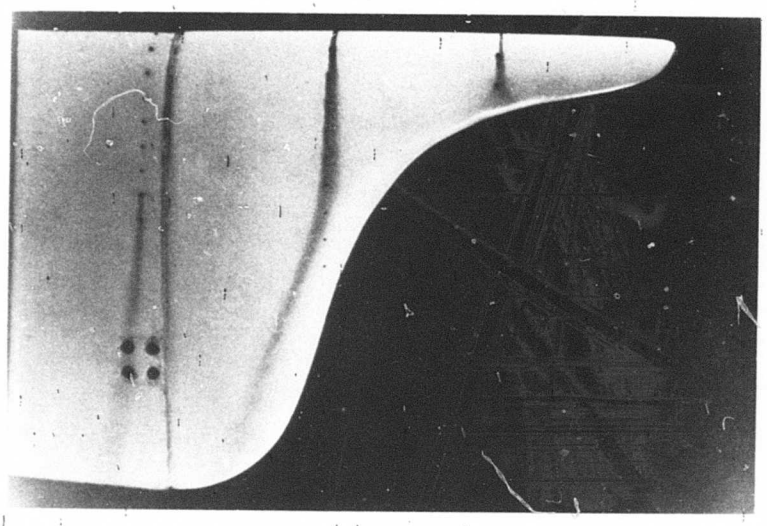

Figure 93c. Top View of Cusp Tip at 500 rpm and 4° Pitch Angle.

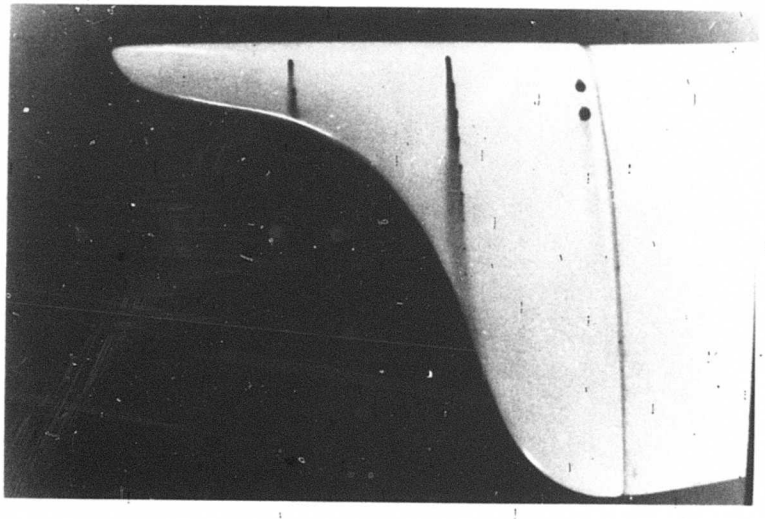

Figure 93d. Bottom View of Cusp Tip at 500 rpm and 4° Pitch Angle.

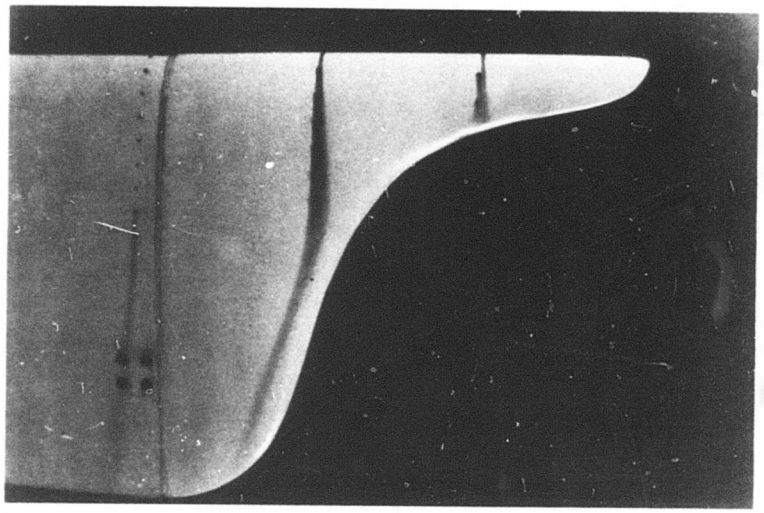

Figure 93e. Top View of Cusp Tip at 500 rpm and 8° Pitch Angle.

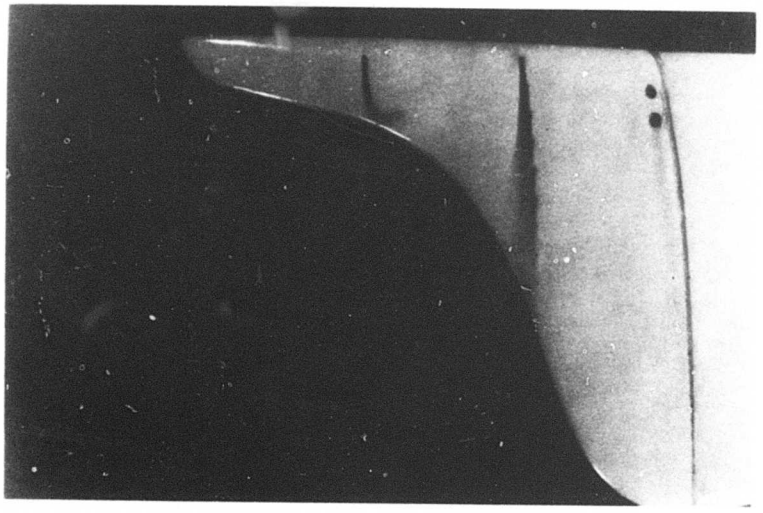

Figure 93f. Bottom View of Cusp Tip at 500 rpm and 8° Pitch Angle.

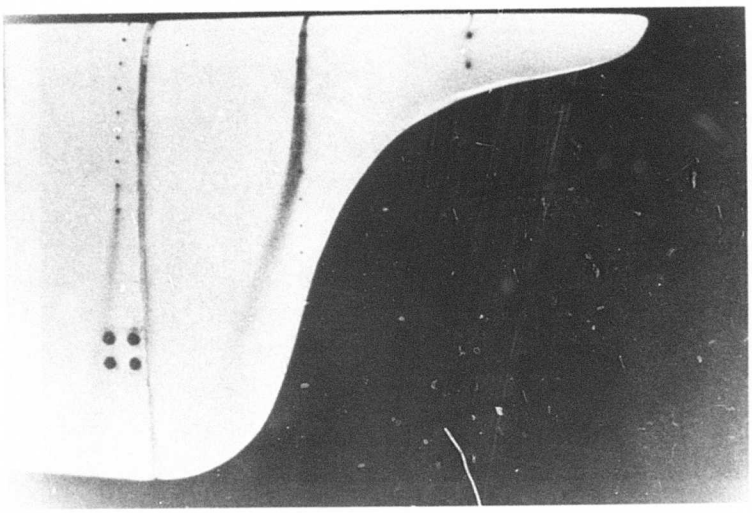

Figure 93g. Top View of Cusp Tip at 500 rpm and 12° Pitch Angle.

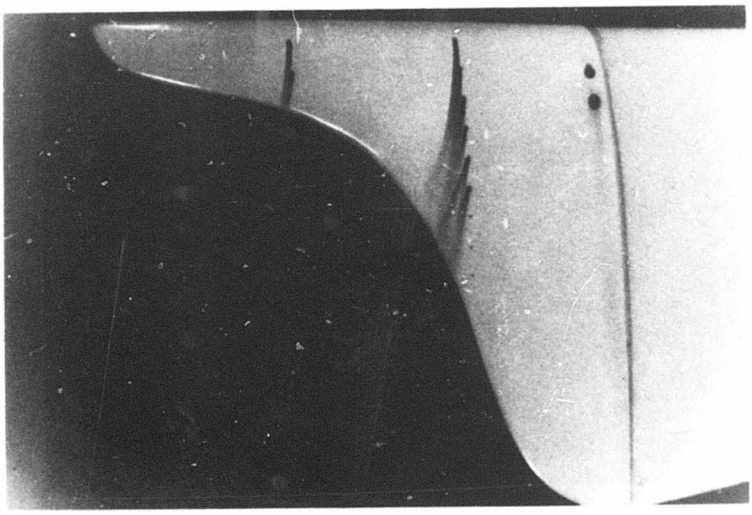

Figure 93h. Bottom View of Cusp Tip at 500 rpm and 12° Pitch Angle.

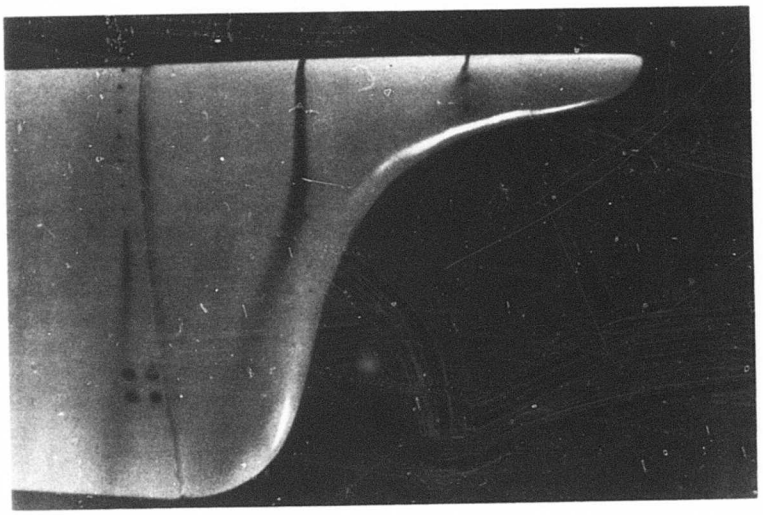

Figure 93i. Top View of Cusp Tip at 500 rpm and 16° Pitch Angle.

Figure 93j. Bottom View of Cusp Tip at 500 rpm and 16° Pitch Angle.

more clearly defined. The inner row reveals outflow which increases significantly with higher pitch angles. (Unfortunately, the last three or four holes in the inner row did not function.)

In general, little additional information is revealed about the nature of the flow around the tip in these photographs. The effects of the lower-to-upper surface pressure gradient are evident as seen by the inflow and outflow.

5.3.1.6 Seven-Inch-Chord Standard Tip. The last tip investigated was another standard tip; instead of a 9-inch chord, this blade and tip had a 7-inch chord. Figures 94a to 94j present the traces obtained from tests conducted at 500 rpm and pitch angles of 0, 4, 8, 12 and 16°. In general, the flow patterns are similar to those of the 9-inch-chord tip. However, the holes on the upper and lower surfaces of the 7-inch tip are not as close to the end of the tip as in the case of the 9-inch tip. Therefore, the flow patterns are not as similar as might be expected. For example, the outflow on the underside of the tip does not appear as pronounced for the 7-inch tip. Only at 12 and 16° pitch angles does the roll-up process become evident. The flow patterns on the upper surfaces are quite striking at 12 and 16° pitch angles. The change from inflow to outflow is clearly evident at the ninth hole from the leading edge. When the traces at 12° pitch obtained from the 9-inch tip are compared with those from the 7-inch tip, it appears that the change from inflow to outflow occurs over a shorter length, and the region of straight-back flow is not evident. Again, caution must be used before drawing any conclusions from the comparison because the holes on the 7-inch tip were not as close to the end of the tip as those on the 9-inch tip. The flow patterns may actually be more similar than indicated due to the disparity in hole location.

5.3.2 Thrust and Torque

The thrust and torque data were converted to coefficient form, and C_T vs C_Q curves were plotted from these data for each tip. The following equations were used to calculate C_T and C_Q:

$$C_T = \frac{T}{\rho\pi R^2(\Omega R)^2} \tag{101}$$

$$C_Q = \frac{Q}{\rho\pi R^2(\Omega R)^2 R} \tag{102}$$

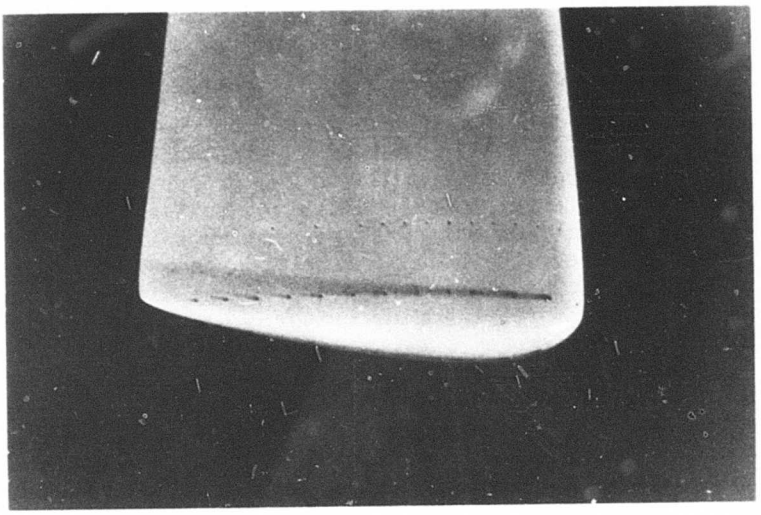

Figure 94a. Top View of 7-Inch-Chord Standard Tip at 500 rpm and 0° Pitch Angle.

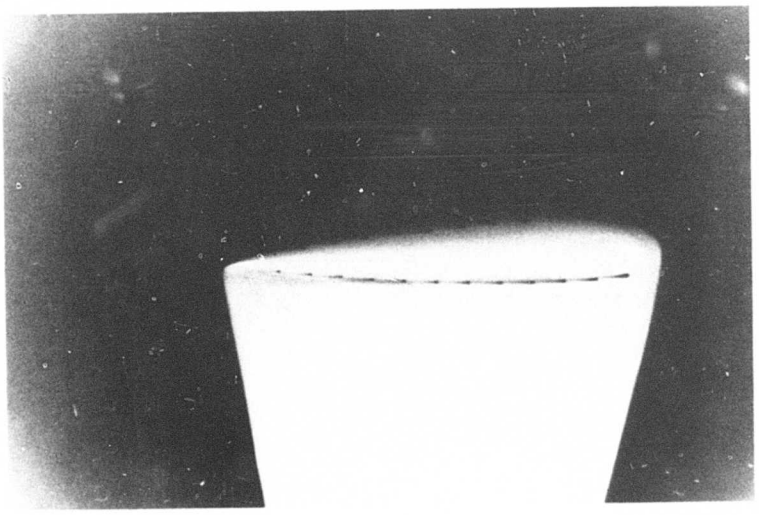

Figure 94b. Bottom View of 7-Inch-Chord Standard Tip at 500 rpm and 0° Pitch Angle.

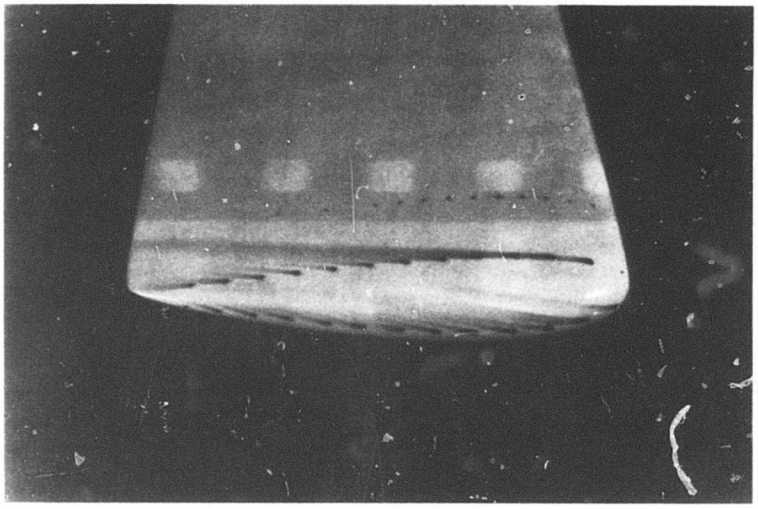

Figure 94c. Top View of 7-Inch-Chord Standard Tip at 500 rpm and 4° Pitch Angle.

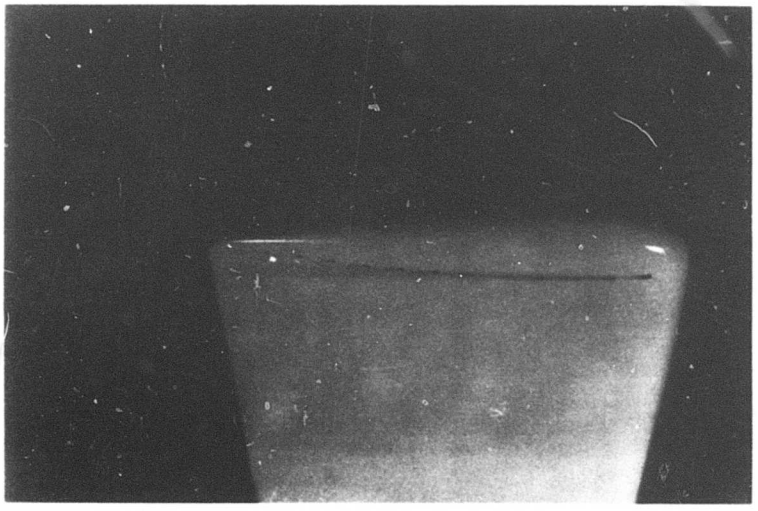

Figure 94d. Bottom View of 7-Inch-Chord Standard Tip at 500 rpm and 4° Pitch Angle.

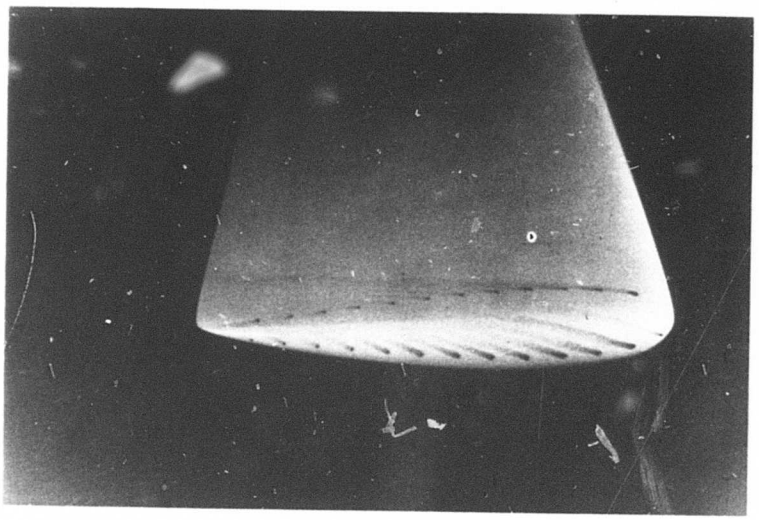

Figure 94e. Top View of 7-Inch-Chord Standard Tip at 500 rpm and 8° Pitch Angle.

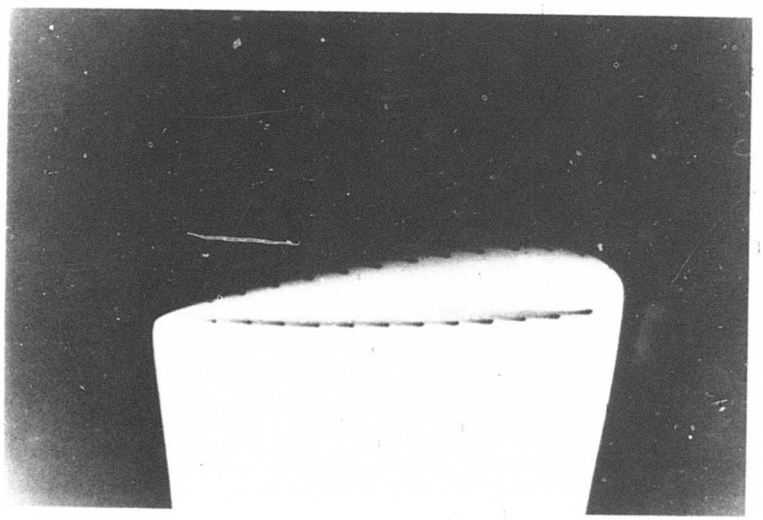

Figure 94f. Bottom View of 7-Inch-Chord Standard Tip at 500 rpm and 8° Pitch Angle.

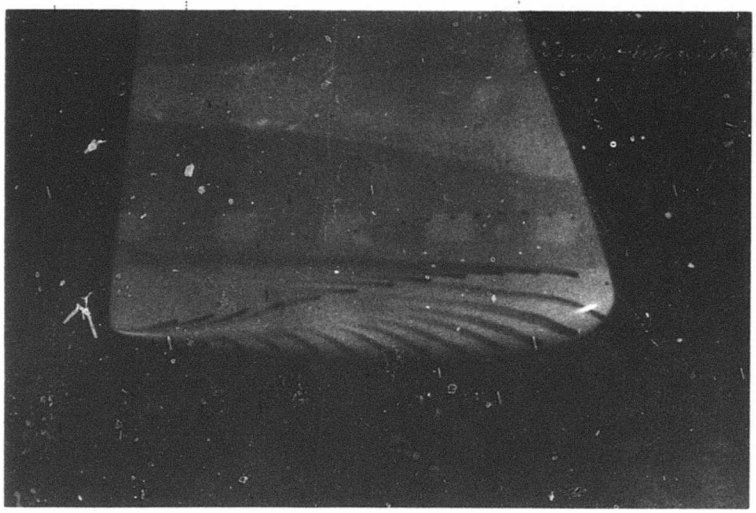

Figure 94g. Top View of 7-Inch-Chord Standard Tip at 500 rpm and 12° Pitch Angle.

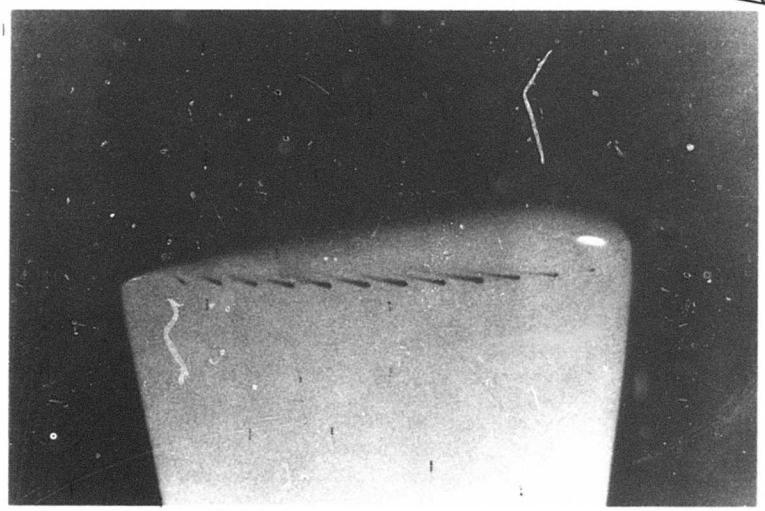

Figure 94h. Bottom View of 7-Inch-Chord Standard Tip at 500 rpm and 12° Pitch Angle.

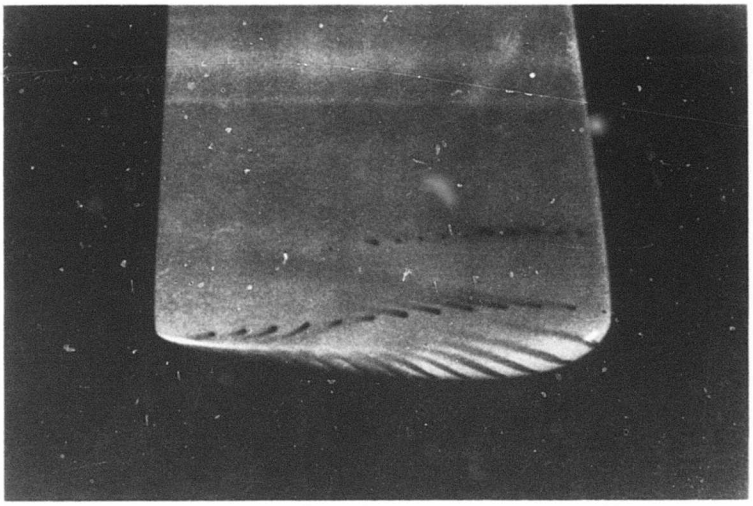

Figure 94i. Top View of 7-Inch-Chord Standard Tip at 500 rpm and 16° Pitch Angle.

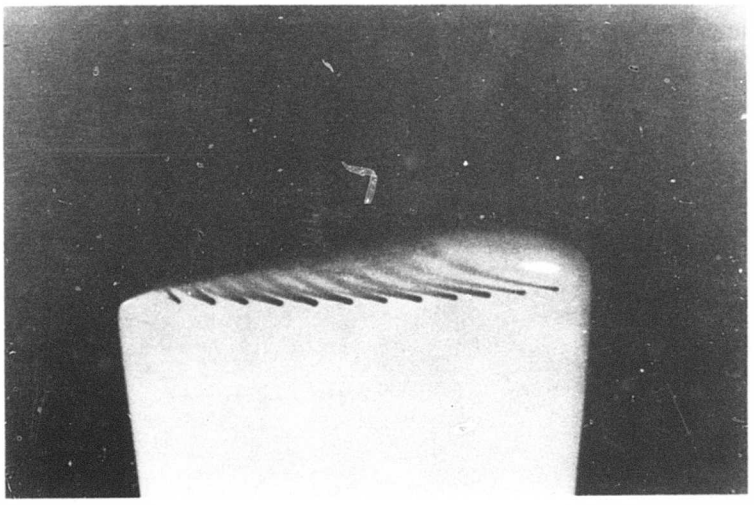

Figure 94j. Bottom View of 7-Inch-Chord Standard Tip at 500 rpm and 16° Pitch Angle.

Figures 95a through 95e show the C_T vs C_Q data. The symbols represent the actual data and the curves represent least-squares best fit of the function $C_Q = b + mC_T^{3/2}$.

The coefficients m and b represent the slope and intercept of the straight line of C_Q vs $C_T^{3/2}$. After obtaining m and b, the curves of C_Q vs C_T were constructed from the above equation. The form of the function $C_Q = b + mC_T^{3/2}$ is based on simple blade-element theory as derived by Gessow and Myers.[28] The assumptions in this theory include ideal blade twist and a constant profile drag coefficient. All of the fitted curves had correlation coefficients of better than 0.99 with respect to the actual data. These curves will be discussed further in a subsequent section.

5.4 DISCUSSION OF RESULTS OF TIP STUDY

5.4.1 Flow Visualization

Figures 86k and 86ℓ show typical flow patterns on the square tip. Three different flow regions are discernible; namely, the region from the leading edge to approximately 30 percent chord, another region from 30 percent chord to about 70 percent chord, and finally, the last 30 percent chord. In the first region the flow on the upper surface exhibits inflow, the lower surface outflow, and the traces on the end of the tip reveal upward flow. These traces indicate a general flow from the lower to the upper surface, or in other words, a tendency for the air on the lower surface to roll up around the tip and spill over onto the upper surface. This phenomenon is due to the pressure gradient which exists between the upper and lower surfaces.

In the second region, the flow on the upper and end surfaces reverses direction while the flow on the lower surface does not change significantly. A possible explanation of this is that a spiral-shaped vortex is generated on the tip and starting to peel away from the tip at the beginning of the second region. The vortex turns in a counterclockwise direction as viewed from the rear. Hence, by the time the vortex is in the second region, the flow adjacent to the upper and end surfaces is outward and downward, as indicated by the traces.

Figure 96 is an attempt to depict the nature of the flow over the square tip in the three regions discussed above. A section view is shown for each region. Section A-A shows that the air flows relatively continuously from lower to upper surfaces. In the second region (Section B-B), vortices are being generated and are creating outward and downward flow adjacent to the upper and end surfaces, respectively.

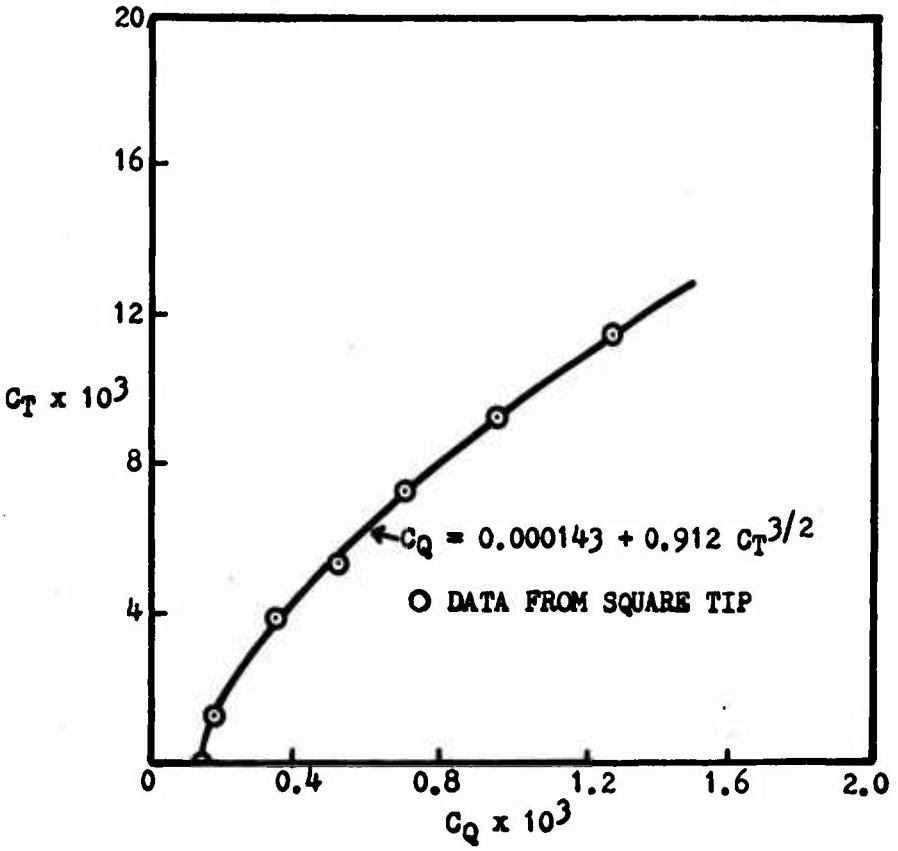

Figure 95a. C_T Versus C_Q for Square Tip.

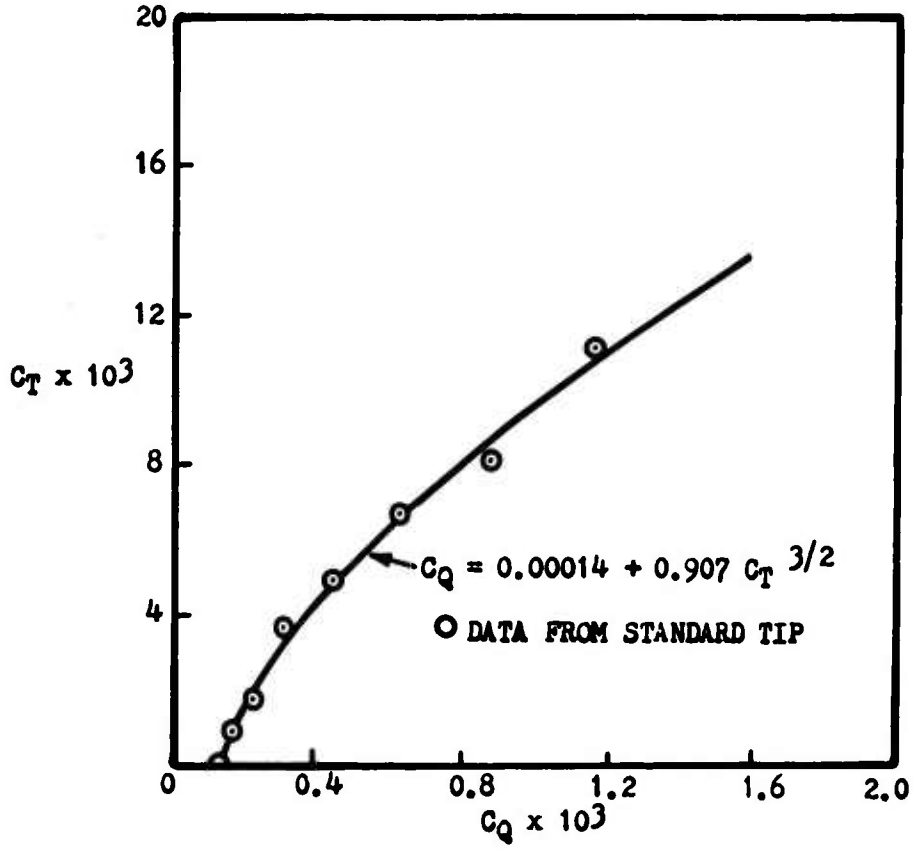

Figure 95b. C_T Versus C_Q for Standard Tip.

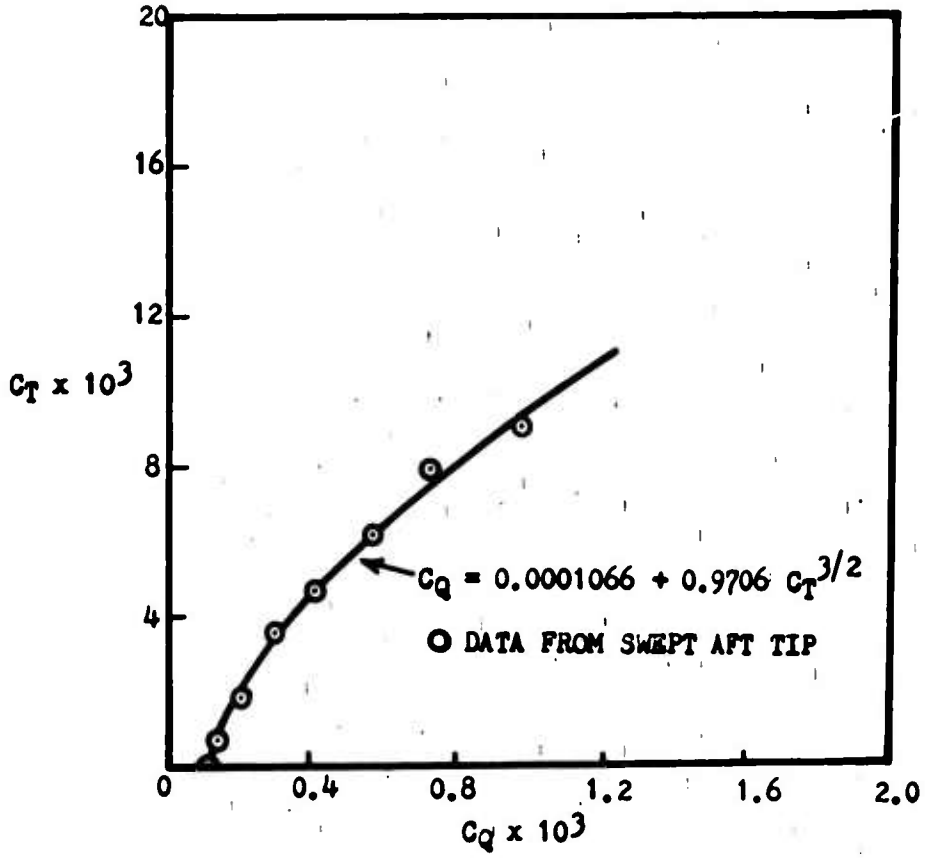

Figure 95c. C_T Versus C_Q for Swept-Aft Tip.

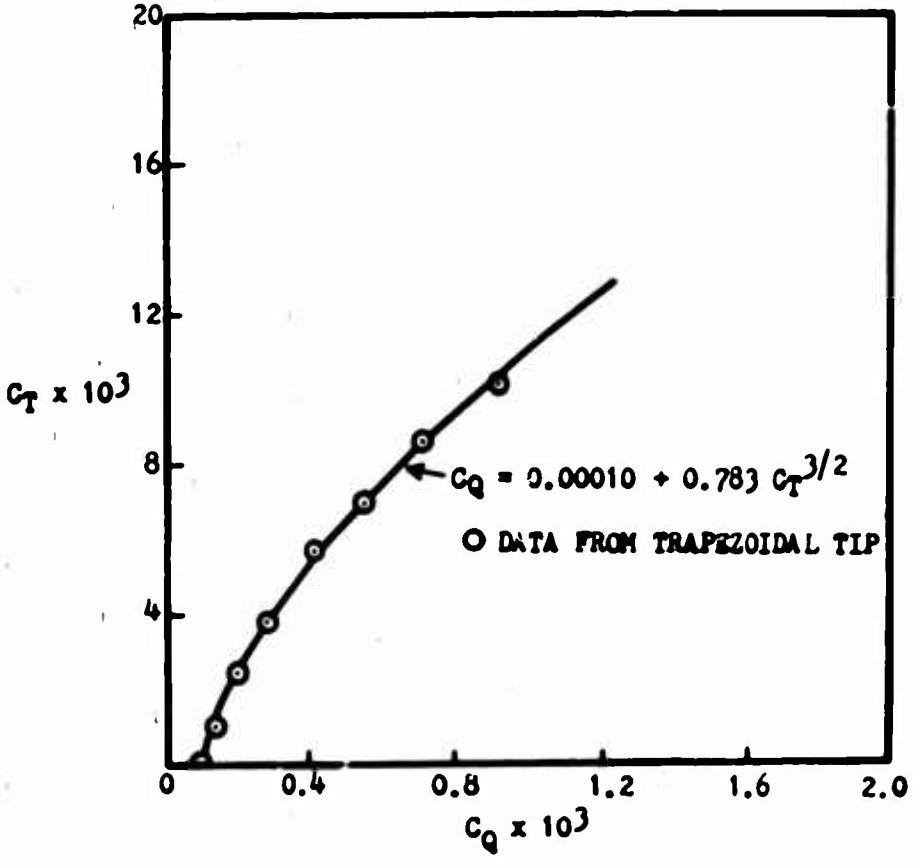

Figure 95d. C_T Versus C_Q for Trapezoidal Tip.

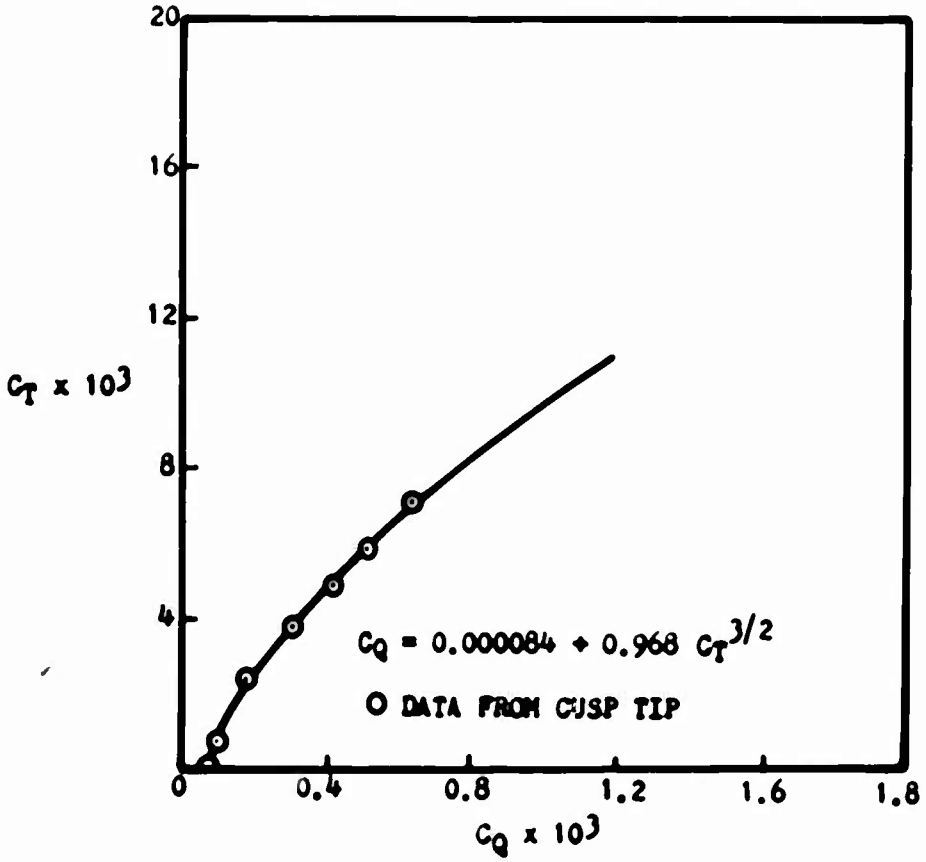

Figure 95e. C_T Versus C_Q for Cusp Tip.

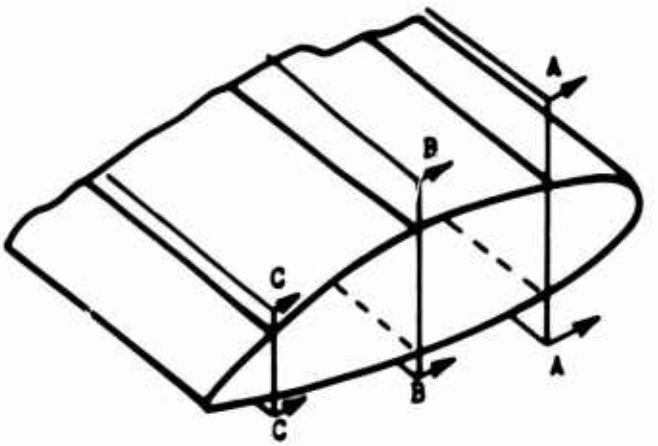

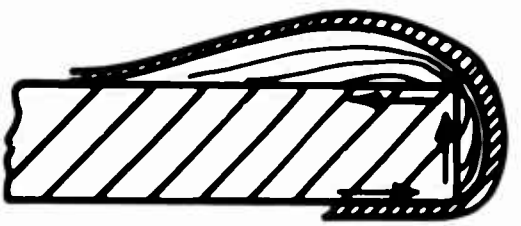

SECTION
A - A

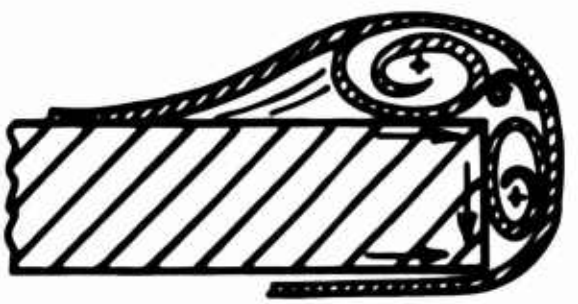

SECTION
B - B

SECTION
C - C

Figure 96. Sketch of Typical Flow Patterns Around Square Tip.

An envelope of air surrounding the vortices is also shown. Finally, in Section C-C, the outflow and inflow on the lower and upper surfaces are very small; how ver, some upward flow persists on the end of the tip.

Figures 89g and 89h show a typical flow pattern observed with the standard tip. The greatest difference between the traces observed with this tip and the square tip is that this tip does not exhibit any change in flow direction on the end surface. The traces emanating from the lower surface and end flow smoothly and continuously over the tip. The only flow direction changes appear on the upper surface.

Figure 97 shows two section views of the standard tip in an attempt to depict the nature of the flow pattern. Section A-A shows a section prior to flow reversal on the upper surface. The boundary layer flow is continuous from lower to upper surfaces. In Section B-B, however, which is in the region of outward flow on the upper surface, a vortex is generated on the upper surface and results in outward flow adjacent to the upper surface.

Thus, the primary difference between the flow over the square tip and that over the standard tip is the nature of the flow field near the end of the tip. The square tip generates a vortex on the end (at moderately high pitch angles), whereas the standard tip does not produce this vortex. Both tips show vortices on the upper surface at moderately high pitch angles.

5.4.2 Thrust and Torque

Referring again to Figures 95a through 95e, since the C_T vs C_Q curves fall so closely together, it is difficult to determine which tips are better than others by trying to compare curves. However, an indication of the relative performance of the tips is provided by the factor m calculated previously. The m represents the slope of the C_Q vs $C_T^{3/2}$ curve. Therefore, the higher the m, the more torque required for a given thrust. The lower the m, the better the aerodynamic performance. The tips are listed according to the value m as follows:

Tip No.	Shape	m
4	Trapezoidal	0.783
2	Standard	0.907
1	Square	0.912
5	Cusp	0.968
3	Swept-Aft	0.971

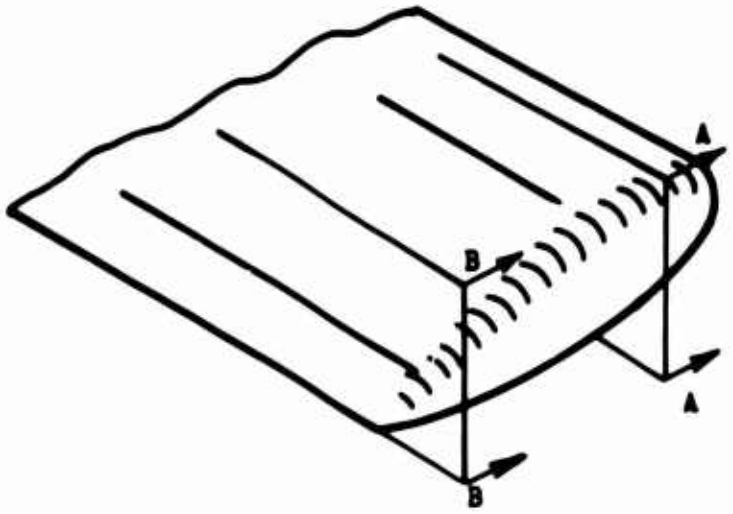

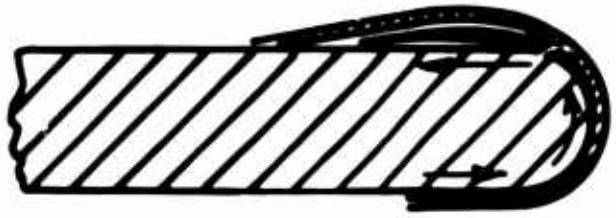

SECTION
A - A

SECTION
B - B

Figure 97. Sketch of Typical Flow Patterns Around Standard Tip.

The m of the trapezoidal tip is much lower than for the other four tips; the square and standard tips are nearly equal, as are the cusp and swept-aft tips. These results are most likely due, in part, because in calculating C_T and C_Q, the radius of the blade was taken from the center of rotation to the very tip of the tip. Tips 1 and 2 were nearly the same length, and Tips 3, 4, and 5 were all the same length. However, most of Tip 5 and much of Tip 3 did not extend to this maximum radius, but were swept back or cut away. Tip 4, on the other hand, had a relatively small amount of tip cut away.

VI. EXPERIMENTAL BOUNDARY LAYER STUDY--FORWARD FLIGHT

The experimental forward flight studies include flow visualization, surface pressure, and velocity measurements. Since the boundary layer velocity data obtained in the hover mode provided the most significant boundary layer information, the primary effort throughout this portion of the study was concentrated on the use of the hot-wire technique in making forward flight velocity measurements.

6.1 TESTING EQUIPMENT

The testing equipment used for the forward flight measurements include a flow channel, a rotor drive system, and a pulse valve. All instrumentation used for the hover tests was simply transferred to the flow channel area for these measurements. All rotor blades were cut back to 3.5-foot radius for the forward flight tests due to limited size of flow channel.

6.1.1 Flow Channel and Rotor Drive System

The flow channel used throughout this portion of the study is shown in Figure 98. The test section is 4 feet high, 8 feet wide and 8 feet long. The channel test section velocity range is 0-100 fps. The rotor drive system is mounted beneath the test section, and the rotor shaft extends into the center of the test section. A thorough description of this flow channel and rotor stand is presented by Velkoff, et al.[36]

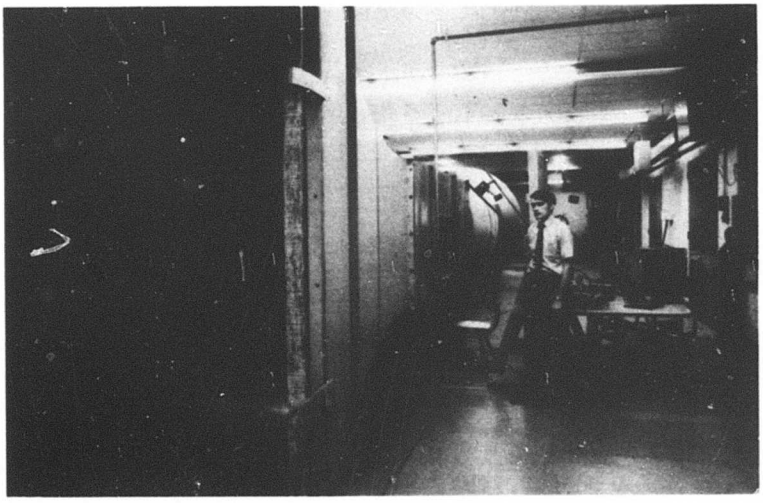

Figure 98. Flow Channel Used for Forward Flight Simulation Tests.

The electronic cables were fed through the hollow rotor shaft just as they were for the hover stand. A slip-ring unit was used to transmit the electronic signals to the stationary data recorders.

6.1.2 Ammonia Pulse Valve

The visualization tests in the forward flight rotor conditions require that the ammonia be injected into the boundary layer at a specified azimuth position. A pulse valve was constructed for this specific purpose and is shown in Figure 99. The valve consists of two circular disks, one which rotates and one which remains stationary. A small hole was drilled in each disk at positions such that the holes will align once per revolution of the moving disk. A Teflon ring was inserted between the rotating disks to allow pressure sealing without excessive wearing of the disks.

6.2 CALIBRATION SYSTEMS

6.2.1 Flow Channel and Rotor Drive System

The airspeed at the flow channel test section was measured with a standard Pitot-static probe.

The rotor speed was monitored by the method that was used to calibrate the hover stand tachometer as discussed in section 3.2.1. In this manner, no calibration, as such, was required, since this method of measuring rotor speed is accurate to within 0.5 percent. The inability to maintain a given rotor speed during the test resulted in a net rotor speed measurement error of approximately ±1 percent.

6.2.2 Ammonia Pulse Valve

The pulse valve used for the forward flight ammonia visualization studies must produce a pulse of extremely short duration. For example, at a rotor speed of 400 rpm, the rotor makes one revolution during a time period of only 150 milliseconds. Therefore, if the ammonia is to be injected into the boundary layer during a blade rotation of 15° azimuth, the pulse must have a duration of only 6.3 milliseconds, which is a very stringent requirement for a mechanical valve.

The pulse valve, shown in Figure 99, was calibrated by fixing the lower disk, rotating the upper disk and supplying air to the rotating portion by a transfer ring. The valve exit line was connected to the flow visualization rotor blade. A hot wire was positioned above a typical orifice, and the upper disk of the valve was rotated by an electric motor and a belt drive.

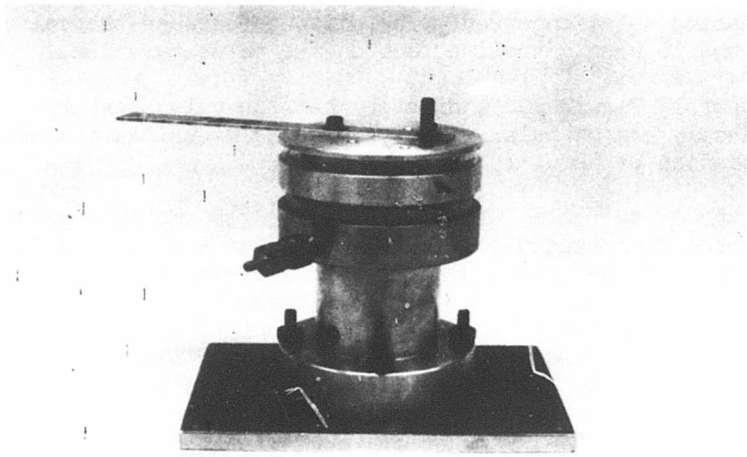

Figure 99. Ammonia Pulse Valve Used in Forward Flight Visualization Tests.

The controlled variables of this calibration were the rotation speed, the line pressure supplied to the valve, and the distance between the valve and the orifice under investigation.

Figure 100 illustrates the pulse duration versus supply pressure. Data are presented at distances from valve to orifice of 32 inches and 44 inches and rotation speeds of 500 rpm and 1000 rpm. At supply pressures of about 2 inches of mercury, the pulse durations vary from about 2.5 milliseconds to 4.5 milliseconds to 6 milliseconds. The general trend indicates that the pulse duration increases with increasing supply pressure. As would be expected, the pulse duration also decreases with increasing rotation speed. The distance between the valve and the orifice seems to have a small effect on the pulse duration.

In general, Figure 100 indicates that the valve can produce pulses of sufficiently narrow pulse width to produce visualization data within a blade rotation of about 15° azimuth.

Even though the pulse width is sufficiently small, a second question was posed with regard to the useability of the pulse valve. This question involved the measurement of the time required for the pulse to travel from the valve to the orifice, which is termed the delay time of the pulse. Figure 101 illustrates the variation of the delay time of the pulse versus distance from valve to the orifice in question. The data were taken at a valve rotation speed of 500 rpm and supply pressures of 10 and 20 inches of mercury. Considerable data scatter is present; however, the trend of increasing pulse delay time with increasing distance is evident. The dashed line illustrates the calculated delay time based on the assumption that the pulse is travelling at the local sonic velocity. The experimental data indicate longer delay times than the sonic theory. This could be due to the fact that the pulses are not travelling at exactly sonic velocity and must move around corners in the tubing within the blade.

A typical pulse is shown in Figure 102. This pulse was recorded with the air supply reservoir set at 2 inches of mercury gage pressure, a rotation speed of 500 rpm, and a distance of 32 inches from the valve. The pulse is shown on the upper beam while the lower beam illustrates the time at which the valve was first opened. The peak volocity of the pulse is about 1.0 fps. For this pulse, the delay time is 4.6 milliseconds while the pulse duration is about 4 milliseconds.

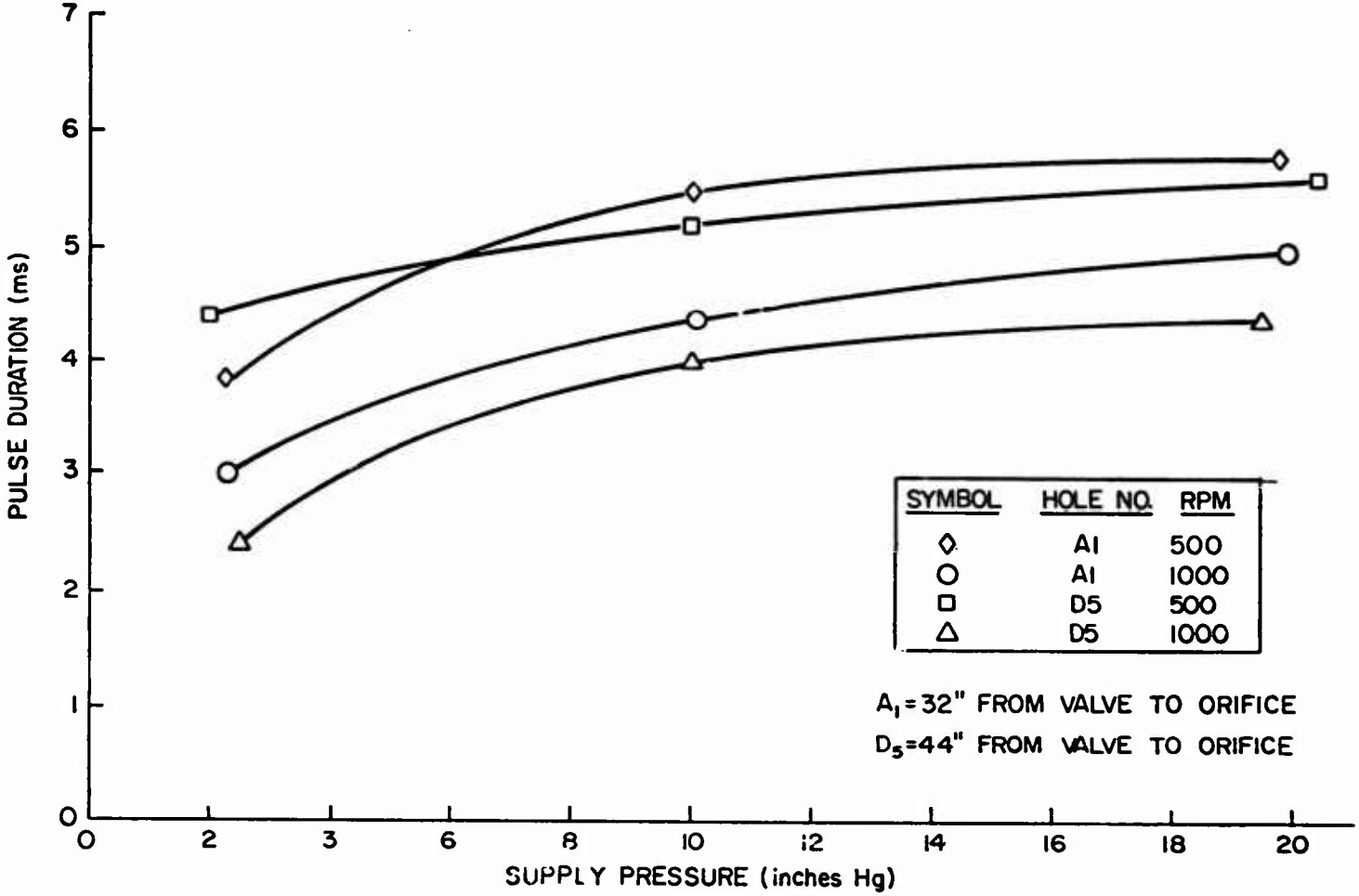

Figure 100. Pulse Duration Versus Supply Pressure.

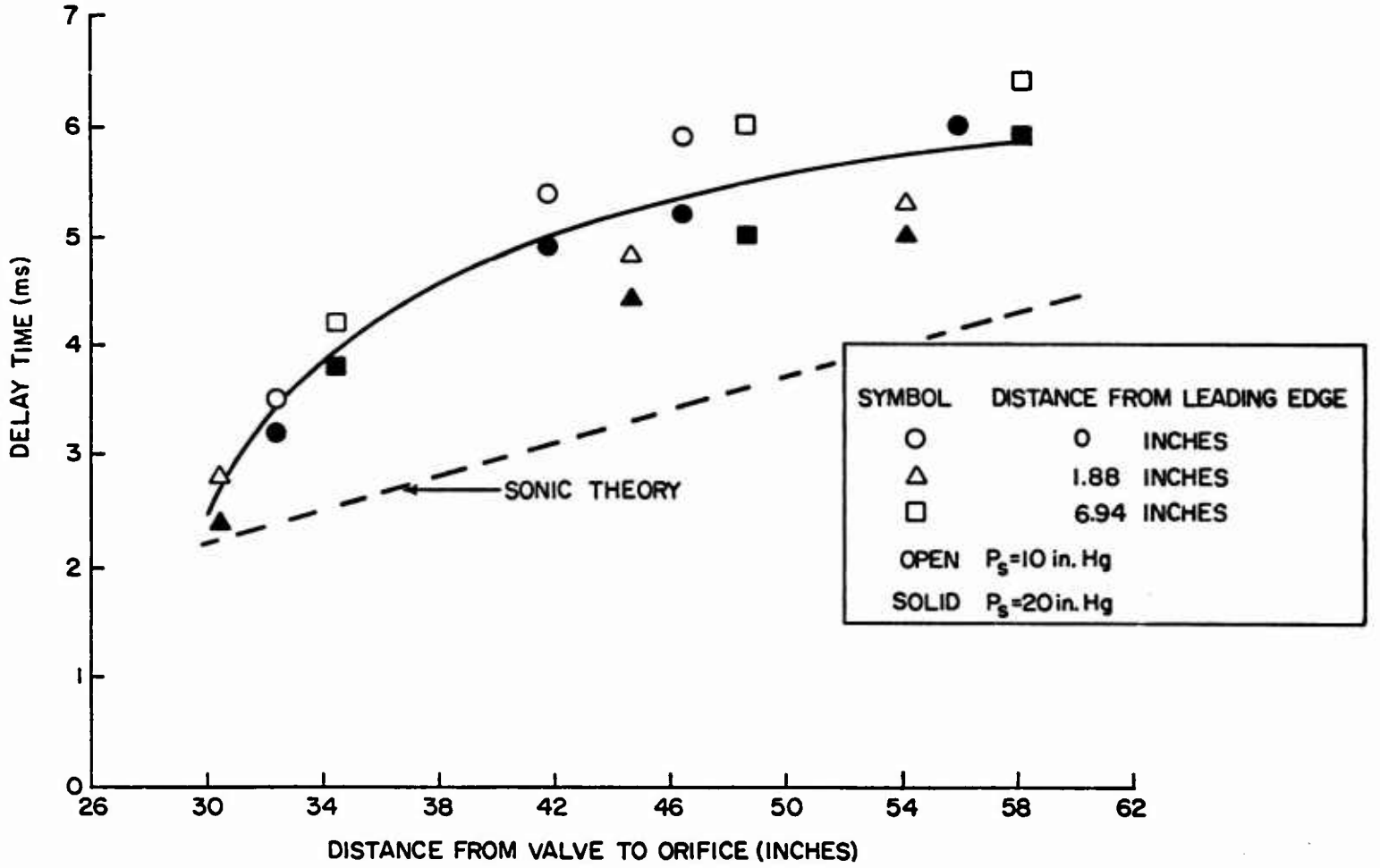

Figure 101. Delay Time Versus Distance From Valve to Hole

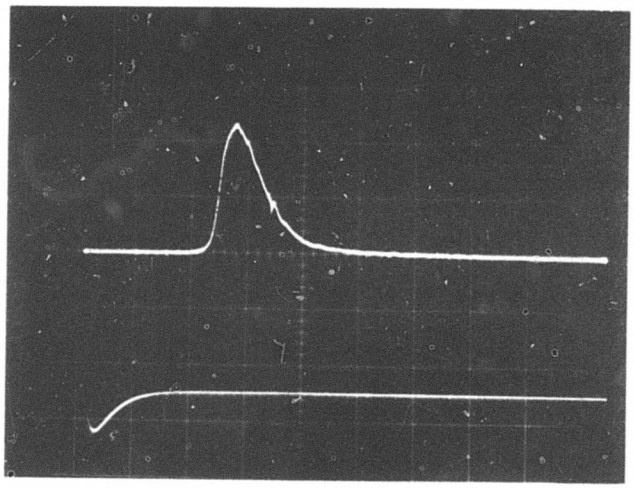

Figure 102. Typical Shape of the Pulse During Calibration.

6.3 TESTING PROCEDURE

The flow channel tests were conducted in the manner discussed by Velkoff, et al.[36] First, a flight condition was selected. A computer program for various rotor thrust loadings and gross weights indicated the necessary values of blade pitch angle and shaft tilt angle. The rotor was then brought up to speed, the wind tunnel was started, and the test section velocity was set at the desired value. At this point, the tunnel simulation of the desired forward flight condition was completed and one of the three types of boundary layer tests could be initiated.

6.3.1 Visualization

The ammonia pulse valve was mounted on the rotor hub. The ammonia was fed through the top of the flow channel test section to the port on the top disk of the valve which was held stationary during the tests; however, it was rotated between tests to allow investigations at various azimuth positions. The ammonia would then pass through the valve as a pulse once every revolution of the blade at the desired azimuth position. Throughout these tests, the revolute film was used to record the surface traces. Since the ammonia is pulsed for very short time periods in the forward flight tests, the length of time required for the formation of a dark trace was considerably longer than for the hover tests where the ammonia was released continuously.

6.3.2 Pressure Measurements

The forward flight pressure measurement procedure is similar to the hover test procedure except that the data had to be continuously recorded. Thus, a light beam oscillograph was used in place of a digital dc voltmeter. The oscillograph was calibrated before each sequence of tests with a standard supply voltage.

In addition to continuous recording of the pressure data, a time marker was needed to indicate the position of the blade. A magnetic pickup was positioned near a small screw on the rotor shaft. This pickup produced a small once-per-revolution voltage pulse. This pulse was used to operate a reed relay which was placed in series with one of the transducer outputs. Therefore, whenever the blade passed a certain azimuth, a break could be observed in the output of this transducer. This method was used because there were no spare light beams specifically for time markers.

6.3.3 Boundary Layer Velocity Measurements

The forward flight velocity measurement procedure is similar to the hover test procedure. Once again, the data had to be recorded continuously on the light beam oscillograph. For these tests, only two channels of the oscillograph were in use. This allowed the use of

a separate channel to record the blade position marker. Throughout these tests, the direct output of the magnetic pickup was used for this indicator.

All of the forward flight velocity data were obtained at a mean rotor lift coefficient of C.5 and advance ratios of 0.2, 0.25, and 0.3. The rotor speed was fixed at 400 rpm and the tunnel airspeed was monitored to vary the advance ratio. Data were obtained in the following sequence.

The blade position was chosen at which a velocity profile was desired. The probe was located at this position by viewing the sensors through the traversing microscope mechanism discussed in the hover test procedure. The forward flight condition was chosen and the tunnel-rotor combination was started. When the systems reached equilibrium, the data were recorded on the oscillograph. This process was repeated until all of the desired flight conditions were completed. Then, the probe was lowered and these flight conditions were repeated. In this manner, the probe adjustments were kept to a minimum. Data obtained in this manner may exhibit a slight scatter due to inaccuracies in reproducing the flight conditions; however, this was not considered to be as important as maintaining sensors on the hot-wire probe.

The test equipment used in the forward flight velocity measurements is shown in Figure 103.

6.4 TEST RESULTS AND DISCUSSION

6.4.1 Ammonia Surface Traces

Several runs were made in forward flight using the ammonia trace technique. In order to secure traces, run time with ammonia flowing was varied from a few seconds up to 3 minutes duration. No visible traces were found for the shorter run times. A typical trace that was obtained with the pulse valve system is shown in Figure 104. This trace is for the condition of 400 rpm, $\mu = 0.3$, $C_{L_\alpha} = 0.5$, and $\Psi = 180°$. At this azimuth one would expect the ammonia traces to form as single lines moving inboard from each hole or to form two distinct traces as shown for $\Psi = 180°$ in Figure 41 (Ref. 36). Figure 104, however, reveals a fan-shaped trace with no clear indication of a preferred direction of flow. All other traces taken with the pulse valve at various azimuth positions revealed similar fan-shaped traces emanating from each chordwise orifice. Although tests were repeated with various run times and ammonia supply pressures, the results were unchanged.

Since all the traces obtained were fan-shaped independent of the azimuth position, the ammonia trace data were not considered to be usable. It appears that the ammonia gas remaining in the lines from the pulse valve to the orifice could have issued from the orifice

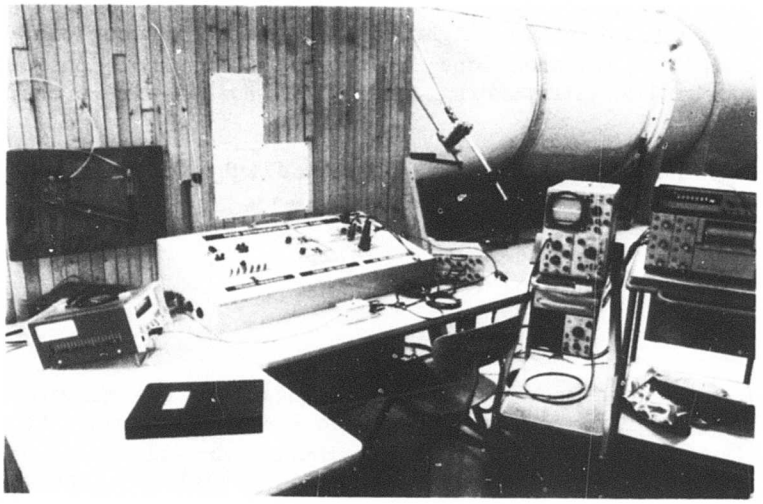

Figure 103. Test Equipment Used During the Forward Flight Hot-Wire Velocity Measurements.

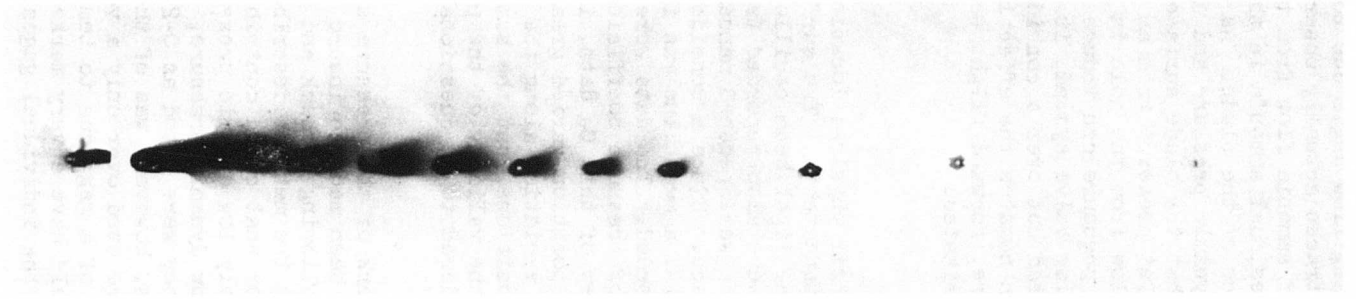

Figure 104. Ammonia Traces at 400 rpm, $\mu = 0.3$, $C\ell_m = 0.5$, and $\psi = 180°$.

over a much greater azimuth than had been predicted from the extensive pulse width calibration tests. If the ammonia left the orifice for a longer duration, then the changing flow angle due to forward flight would result in the fan-shaped traces actually observed. A possible reason for the increased time of ammonia flow from the orifice is believed to be the existence of residual ammonia in the line and the varying pressure field on the surface of the blade. As the blade rotates around the azimuth, the local dynamic pressure and angle of attack vary considerably, with the result that the blade surface pressure varies periodically. In turn, the outlet pressure from an orifice varies; this can cause the ammonia to flow from the hole in response to that pressure. Regions of low blade pressure can induce added emission of the ammonia. Thus, with the pulse valve system, it is possible for the effective pulse width to be spread out over a considerable azimuth of a rotor revolution. This action negates the effectiveness of the pulse valve approach. As a consequence, forward flight testing with the ammonia trace technique was terminated.

6.4.2 Surface Static Pressures

The pressure pickups and their physical locations on the blade were unchanged from the hover stand tests. The surface static pressures were recorded continuously on the light beam oscillograph. The mean values of the surface pressure were also recorded from a digital voltmeter. The surface pressure data were reduced manually by reading data points from the oscillograph trace. Since a considerable amount of oscillation was found in the data, a mean line was faired through the data and the mean value was recorded. The data were then processed to obtain the results in the form of pressure coefficient, C_p, at various chordwise positions. Upon review of this C_p data, it became evident that C_p at any selected azimuth position varied greatly and did not represent the expected pressure variation along the chord. Data were examined at several azimuthal positions, but the same irregularities were found. As a consequence, the validity of the pressure data in the forward flight regime was considered to be questionable, and no data are presented.

Prior to test, careful rework of the pressure sensing elements and of the entire blade surface had been made to insure that the entire system was working properly. Following recheck and rework, each pressure gage was recalibrated using the methods described on the hovering pressure data. A possible factor that could contribute to the erratic results obtained is the relatively low dynamic pressures involved in these particular tests. With low dynamic pressure, the gages used are relatively insensitive, since they were rated as 0-25 psia gages. The range of pressures on the blades, however, was of the order of 14 psia to 15 psia. Thus, the gages were used over only a very small portion of their range. Any zero shift of a gage due to temperature, mounting or centrifugal field effects could have a very marked influence on the absolute values of pressures of the individual gages, and this factor

could contribute to the erratic results found. The more satisfactory operation of these gages in hovering than in forward flight can be explained by the fact that to get good pressure data, high hover rpm values were used. In the tunnel tests, such higher rotor speeds were difficult to use at high advance ratios.

6.4.3 Boundary Layer Velocity Data

The hot-wire data obtained during the simulated forward flight rotor conditions were recorded on light-sensitive paper. The traces represented output voltages of the two anemometers. These traces were examined and a typical cycle was chosen. This cycle was divided into a number of equally spaced sections at which the voltages were determined. These voltages were converted to velocity magnitude and direction in the hover hot-wire data. This data reduction scheme required many man-hours; therefore, only a limited amount of data are presented in a continuous azimuth form; but considerable data are given at specified azimuth positions.

The continuous data are illustrated in Figures 105 and 106. These data were obtained at a blade surface position of 15 percent chord and 63 percent radius. The rotor speed was 400 rpm and the flow channel air velocity was 28 fps. The advance ratio for these data was $\mu = 0.2$.

Figure 105 illustrates the variation in the magnitude of the local velocity vector versus azimuth position of the blade. Data are presented at two heights above the blade surface. The data at $y = 0.0918$ inch is indicative of the potential flow outside of the boundary layer, while the data at $y = 0.0108$ inch is indicative of the flow near the center of the boundary layer. The solid curve was calculated from the theoretical chordwise and spanwise components of the free-stream velocity given by equations (103) and (104):

$$\frac{U_\infty}{\Omega R} = r/R + \mu \sin \psi \qquad (103)$$

$$\frac{W_\infty}{\Omega R} = \mu \cos \psi + \lambda\beta \qquad (104)$$

The subscript ∞ refers to the free-stream conditions, λ is the inflow ratio, and β is the flapping angle. The inflow ratio and the flapping angle were determined from a uniform downwash, first harmonic blade element analysis.

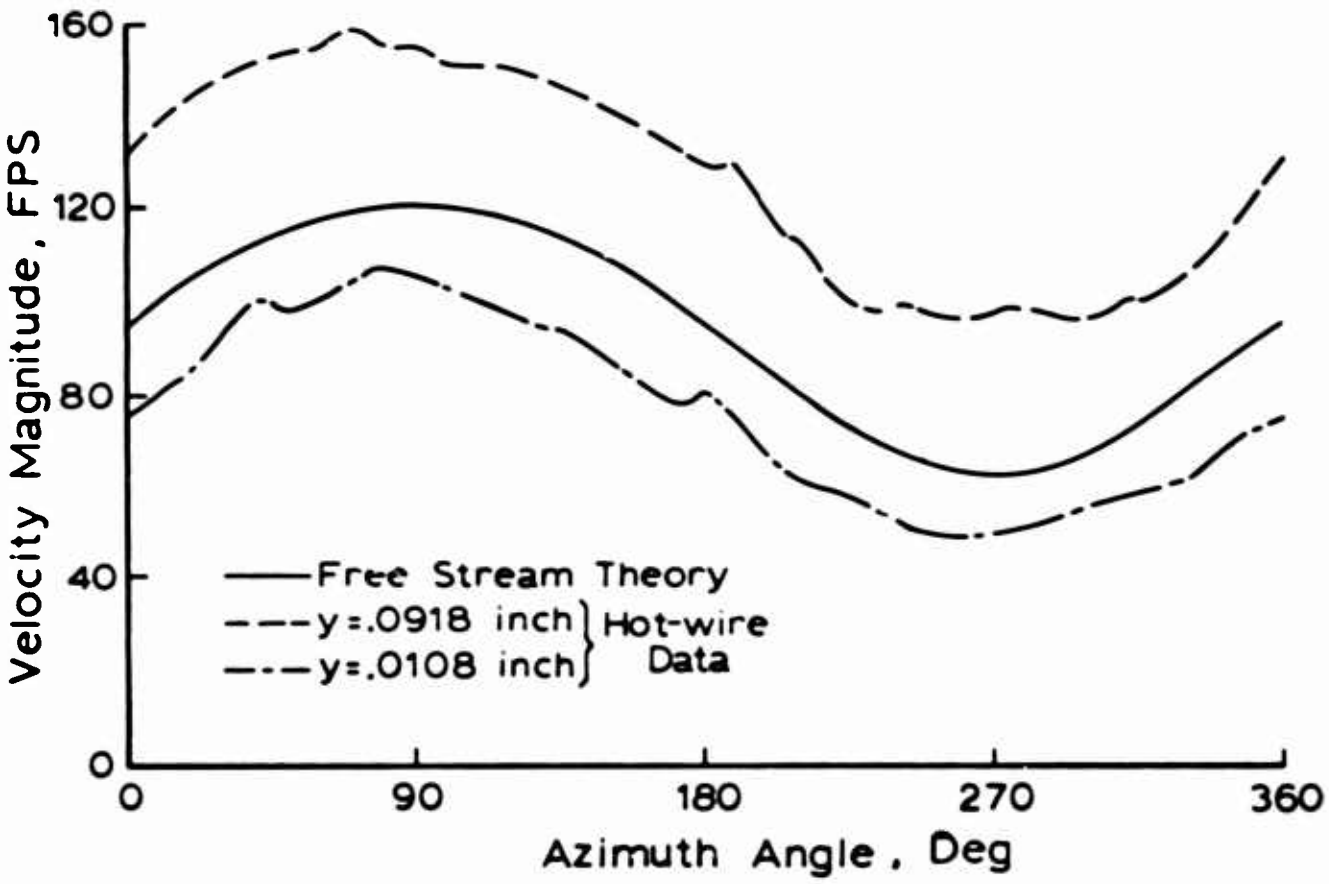

Figure 105. Velocity Magnitude Versus Azimuth for 15% Chord, 63% Radius, and $\mu = 0.2$; Rotor Shaft Angle = -5.6° (forward tilt), Blade Pitch = 7.5°.

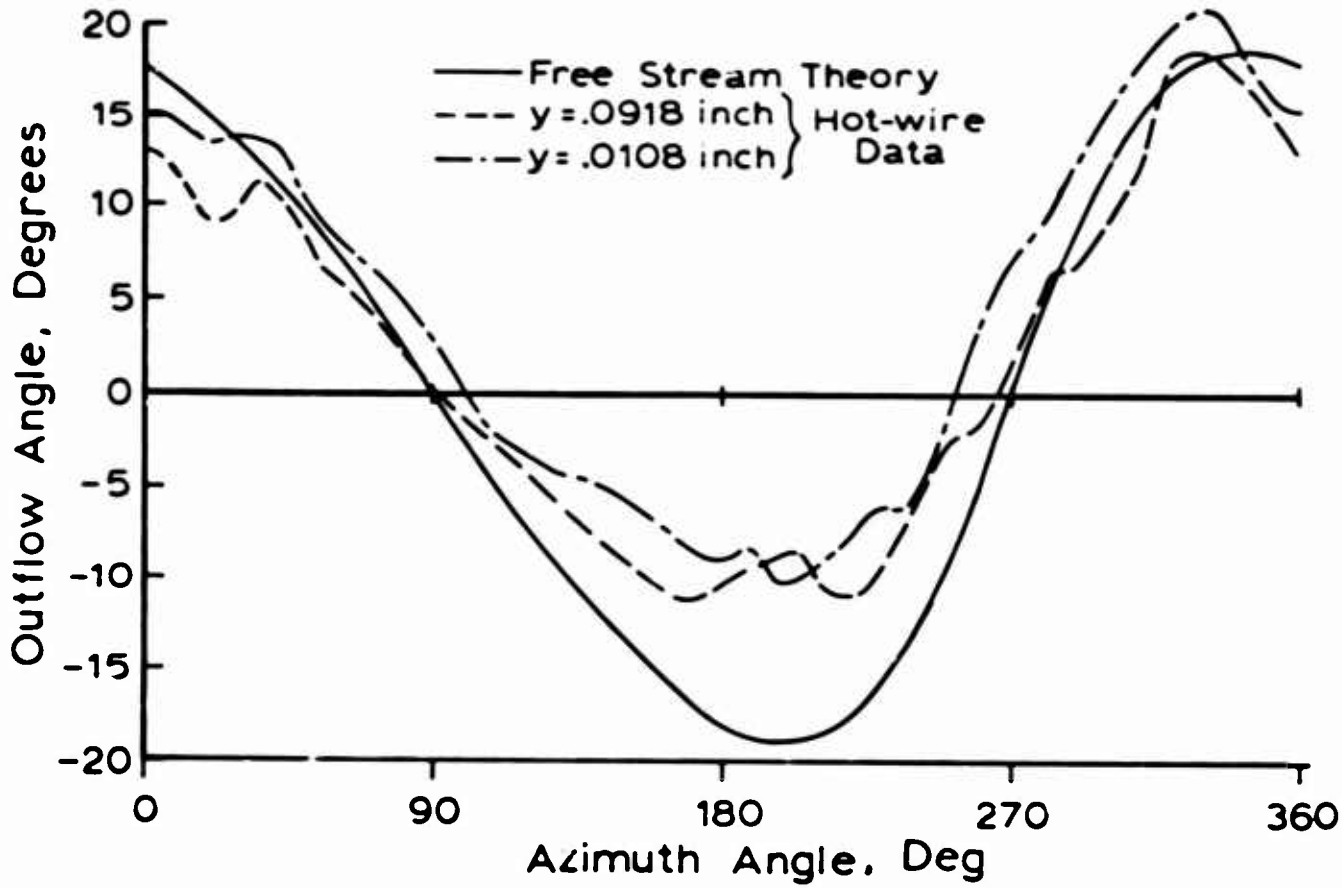

Figure 106. Outflow Angle Versus Azimuth for 15% Chord, 63% Radius, and $\mu = 0.2$; Rotor Shaft Angle = -5.6° (forward tilt), Blade Pitch = 7.5°.

The general shapes of both curves representing experimental data are very similar to the free-stream theoretical curve. The mean velocities of the three curves are approximately 132, 96, and 76 fps, respectively, from highest to lowest curves. The potential flow data have a larger mean value due to the acceleration of the flow across the upper surface of the airfoil at an angle of attack. At y = 0.0108 inch above the surface, the probe was deep enough in the boundary layer to indicate a mean velocity lower than the free stream.

The local flow direction, or outflow angle, is shown in Figure 106 versus azimuth angle. Again the data are presented for y = 0.0918 inch and y = 0.0108 inch to indicate the flow outside and inside the boundary layer. The theoretical free-stream outflow angle was also calculated from equations (103) and (104) and is included in this figure. The experimental data again follow the same trend as the free-stream theory; however, a number of additional effects are evident. First note that the peak outflow angle, as illustrated by the experimental data, occurs at about 300° azimuth while theory predicts the outflow to peak at 360° or downwind. This effect could be because the flow at the downwind position has passed through the hub region where the instrumentation unit has added to the usual flow interference. At ψ = 180°, the data tend to indicate a smaller inflow angle than free-stream theory. Since this position is upstream of the rotor hub region, there is no interference; however, since the rotor plane is tilted, this could indicate that the streamlines curve to flow down through the rotor disk.

Examining the experimental data of Figure 106 from a boundary layer view reveals that the flow within the boundary layer exhibits an outflow angle which is generally larger than the corresponding angle outside the boundary layer. This action is forcing the boundary layer flow outward with respect to the local free-stream flow.

Additional hot-wire data obtained in the flow channel are presented in Figures 107 through 115 at azimuth positions of 0, 90, 180, and 270°. All data were obtained at 63 percent radius; chordwise positions of 15, 20, and 25 percent; and advance ratios of μ = 0.2, 0.25, and 0.3. These data are presented in a form similar to the hover data.

Aside from a few data points, the chordwise velocity profiles are reasonably smooth. The spanwise profiles are very erratic at the conditions where the potential spanwise component, W, is small. This may be attributed to the fact that the data were made dimensionless by dividing by this potential component which tends to amplify the experimental data scatter. The scale for the outflow angle is negative for ψ = 180°, since the flow is inward in this region.

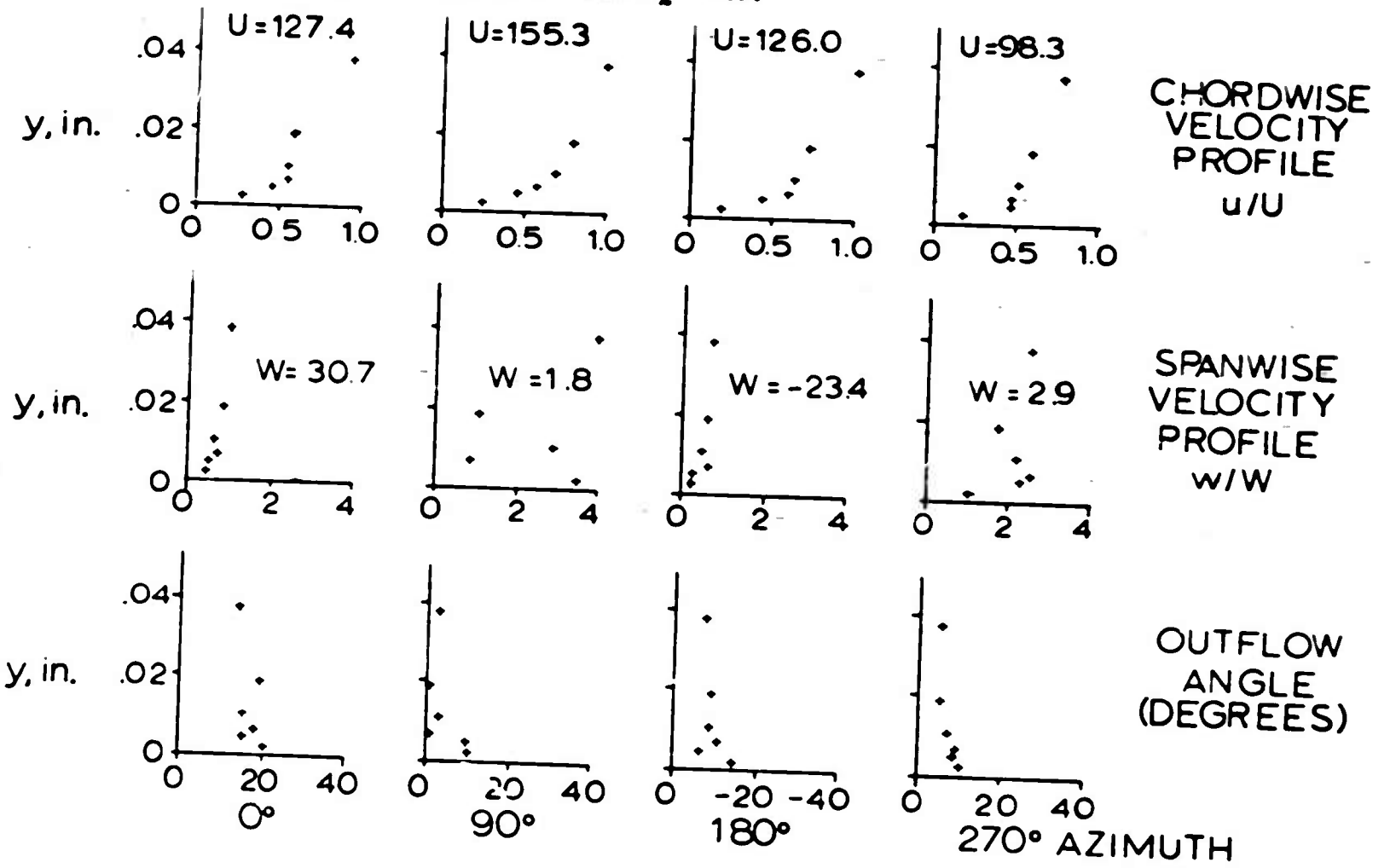

Figure 107. Velocity Data at 63% Radius, 15% Chord, and μ = 0.2.

Rotor Shaft Angle = -5.6°. Blade Pitch = 7.5°. Rotor Speed = 400 rpm. Mean C_ℓ = 0.5.

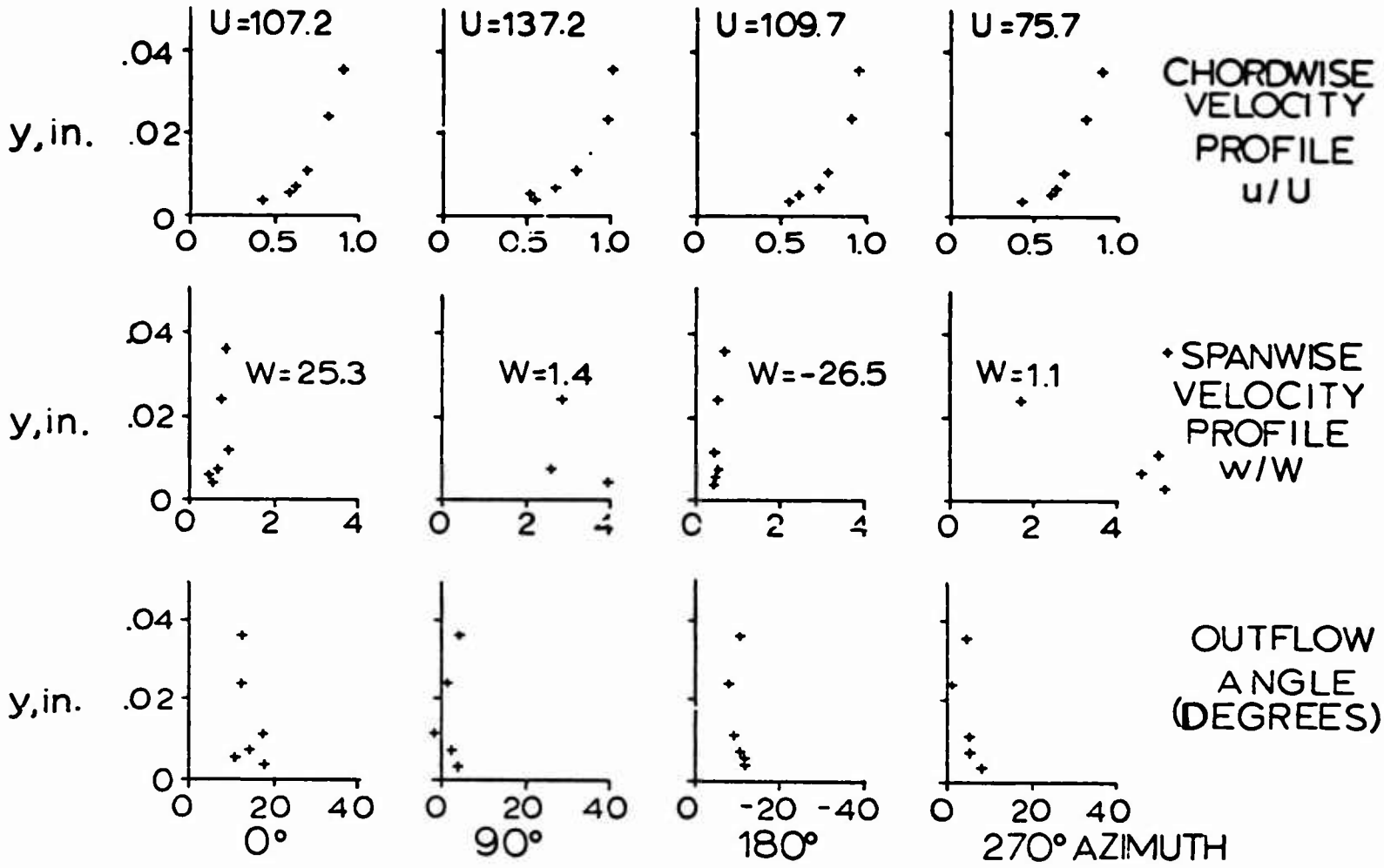

Figure 108. Velocity Data at 63% Radius, 20% Chord, and μ = 0.2.

Rotor Shaft Angle = -5.6°. Blade Pitch = 7.5°. Rotor Speed = 400 rpm. Mean C_ℓ = 0.5.

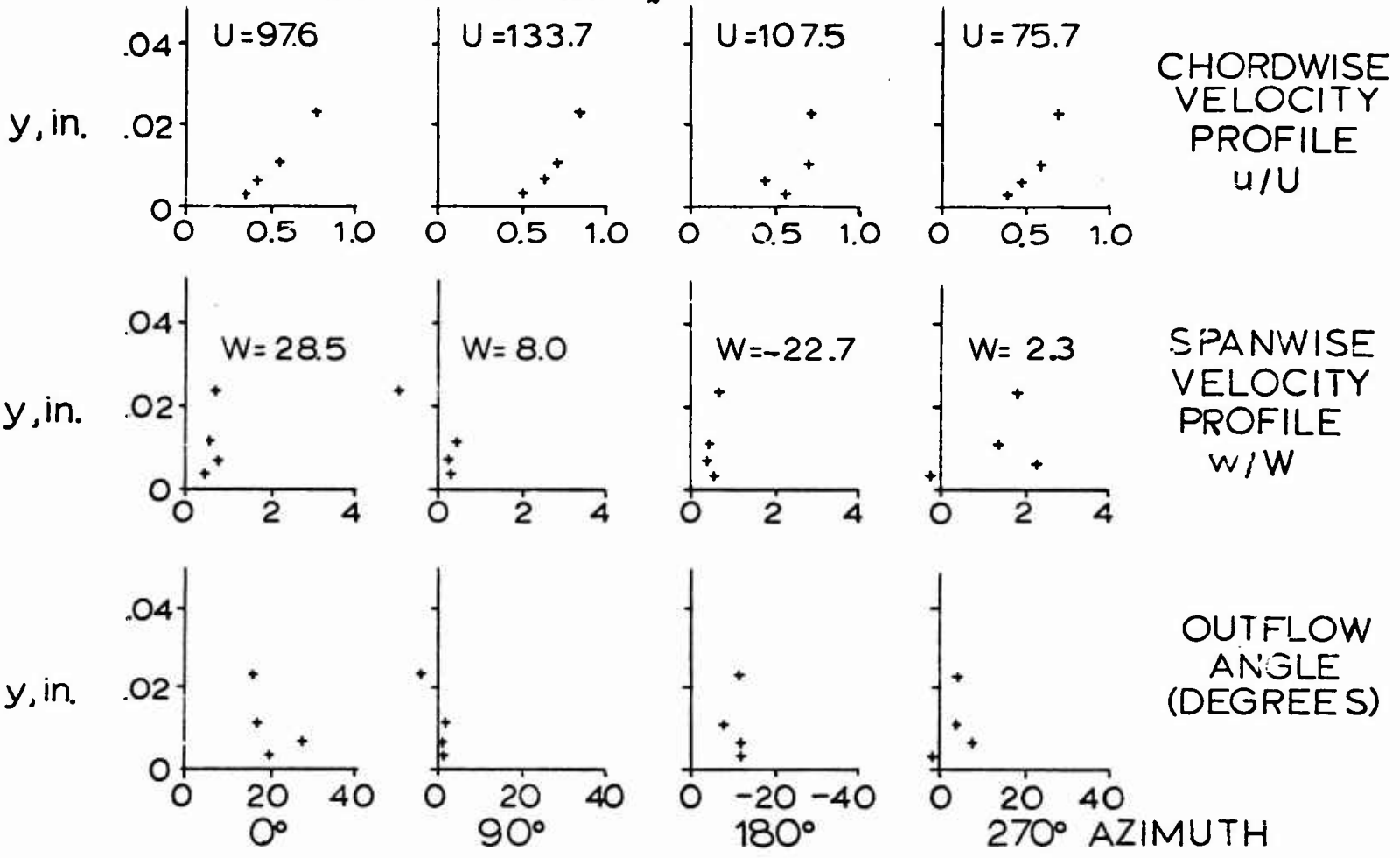

Figure 109. Velocity Data at 63% Radius, 25% Chord, and μ = 0.2.

Rotor Shaft Angle = -7.8°. Blade Pitch = 8.2°. Rotor Speed = 400 rpm. Mean C_ℓ = 0.5.

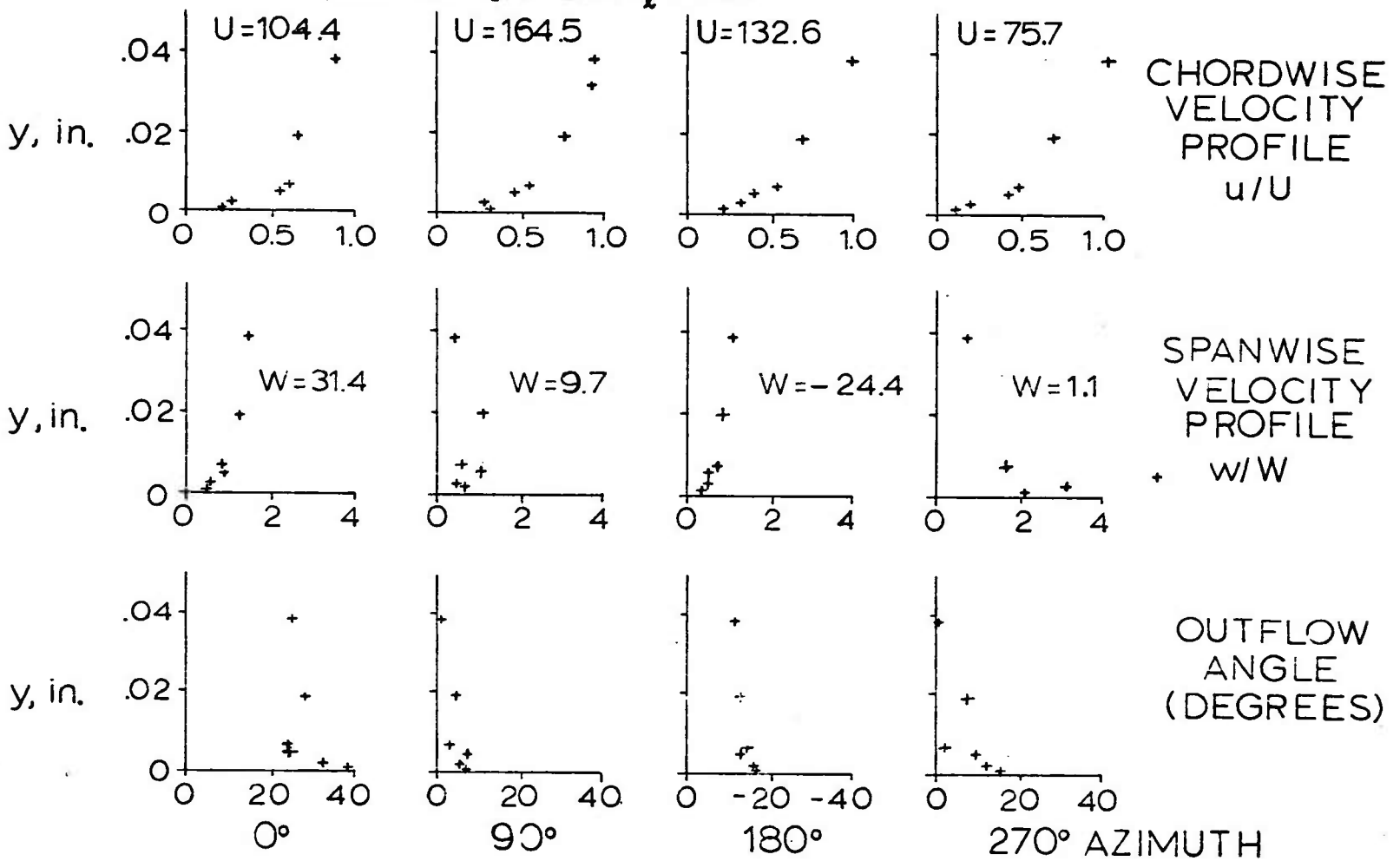

Figure 110. Velocity Data at 63% Radius, 15% Chord, and μ = 0.25.

Rotor Shaft Angle = -7.8°. Blade Pitch = 8.2°. Rotor Speed = 400 rpm. Mean C_ℓ = 0.5.

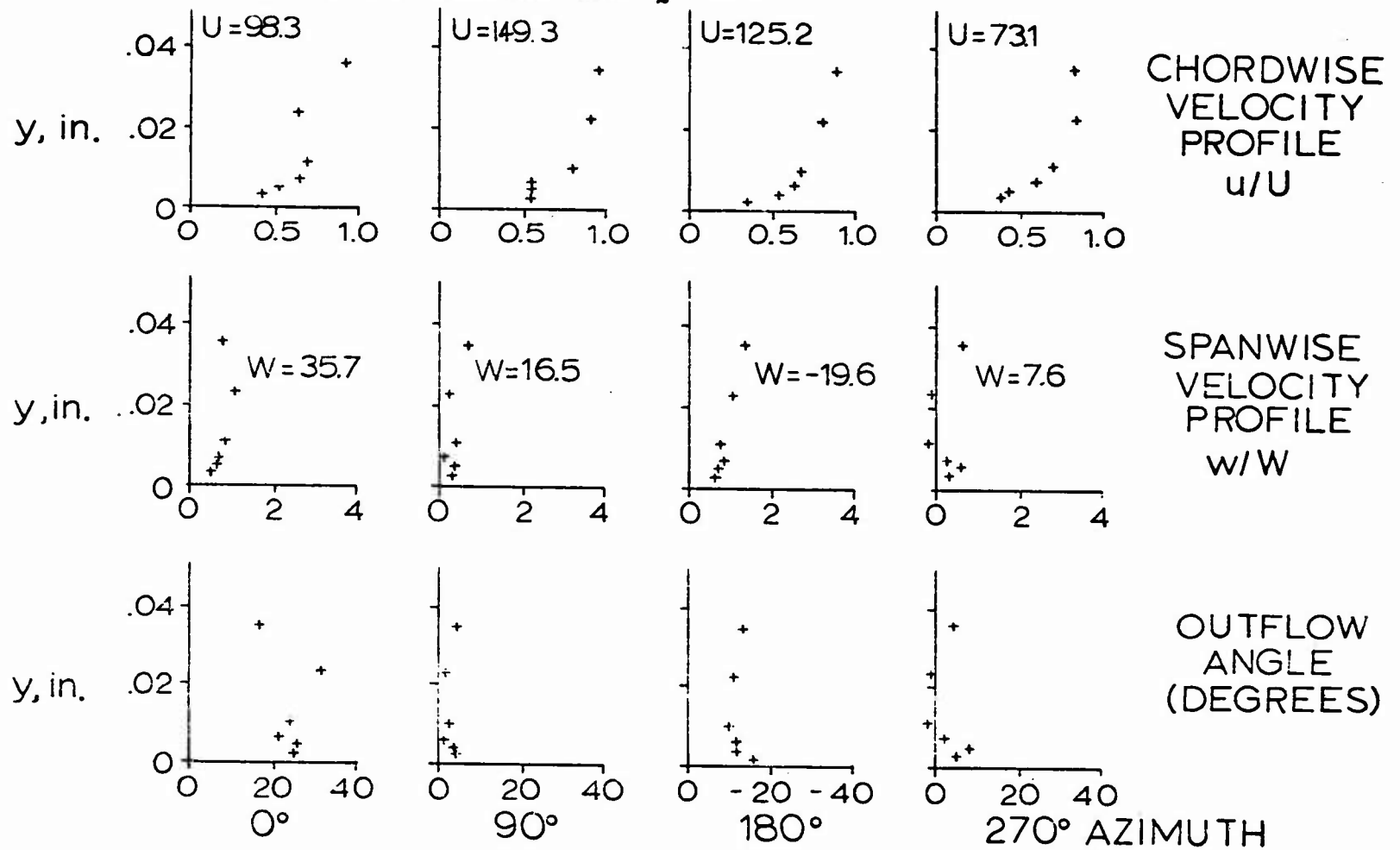

Figure 111. Velocity Data at 63% Radius, 20% Chord, and μ = 0.25.

Rotor Shaft Angle = -7.8°. Blade Pitch = 8.2°. Rotor Speed = 400 rpm. Mean C_ℓ = 0.5.

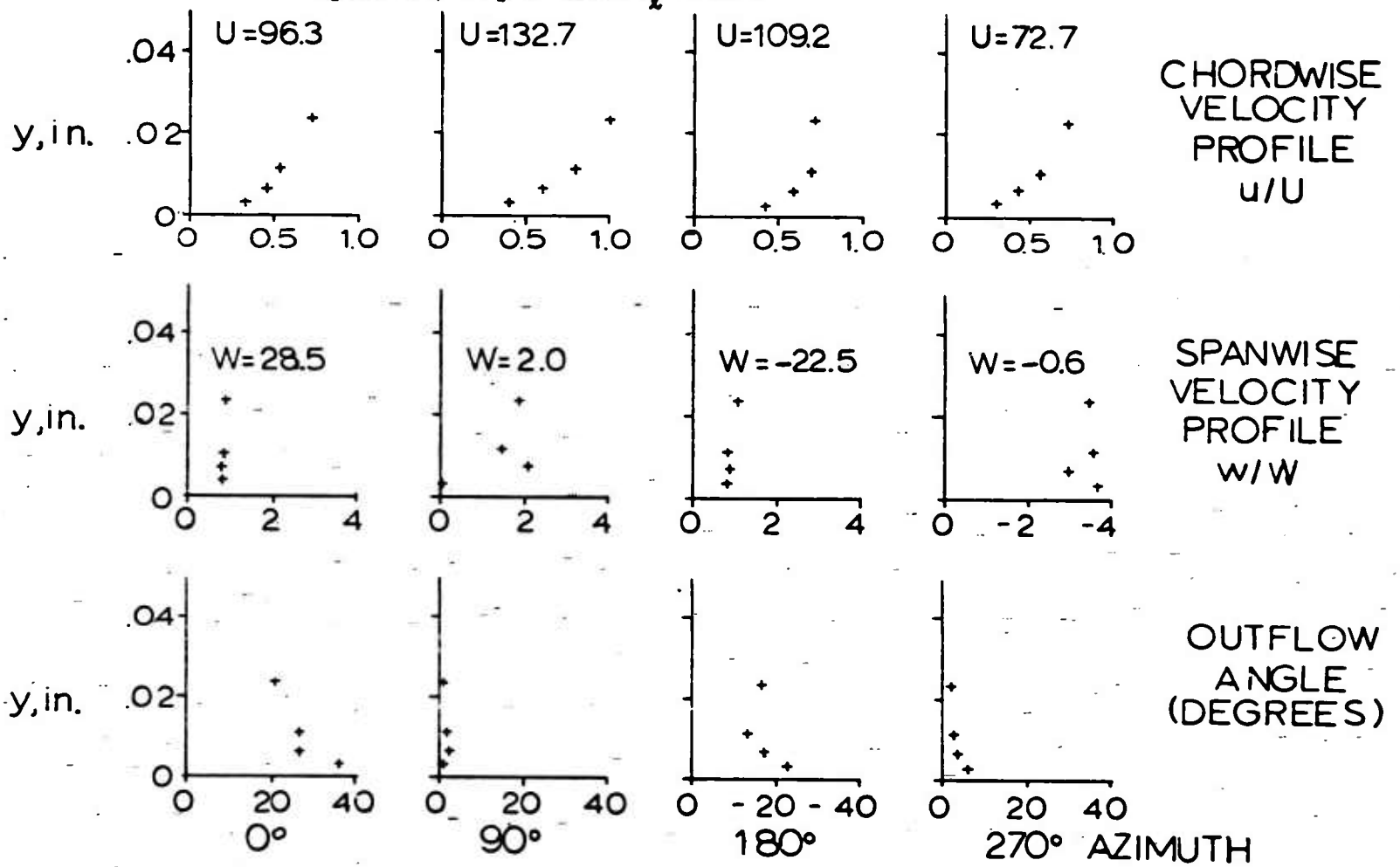

Figure 112. Velocity Data at 63% Radius, 25% Chord, and μ = 0.25.

Rotor Shaft Angle = -10.4°. Blade Pitch = 9.4°. Rotor Speed = 400 rpm. Mean C_ℓ = 0.5.

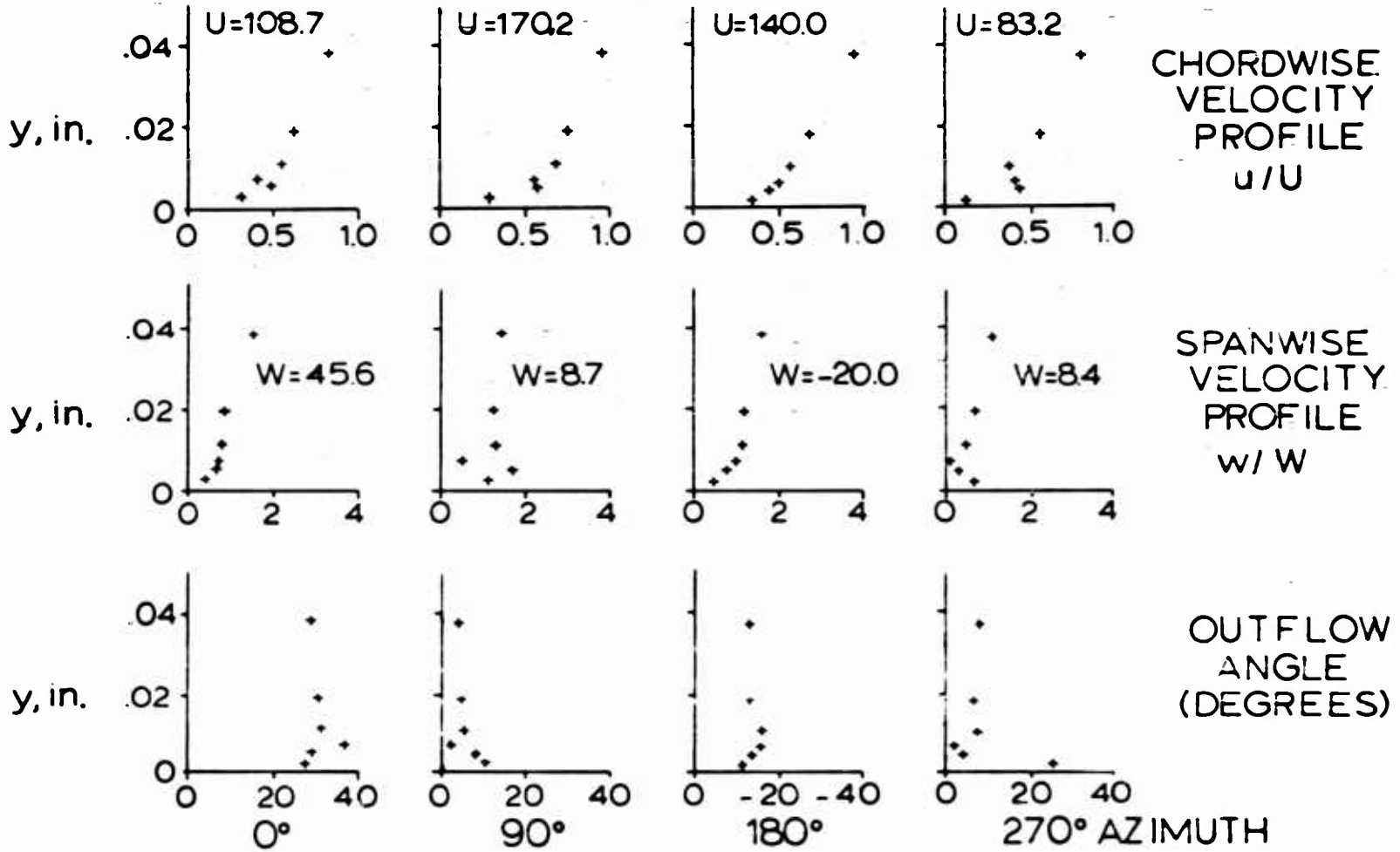

Figure 113. Velocity Data at 63% Radius, 15% Chord, and μ = 0.3.

Rotor Shaft Angle = -10.4°. Blade Pitch = 9.4°. Rotor Speed = 400 rpm. Mean C_L = 0.5.

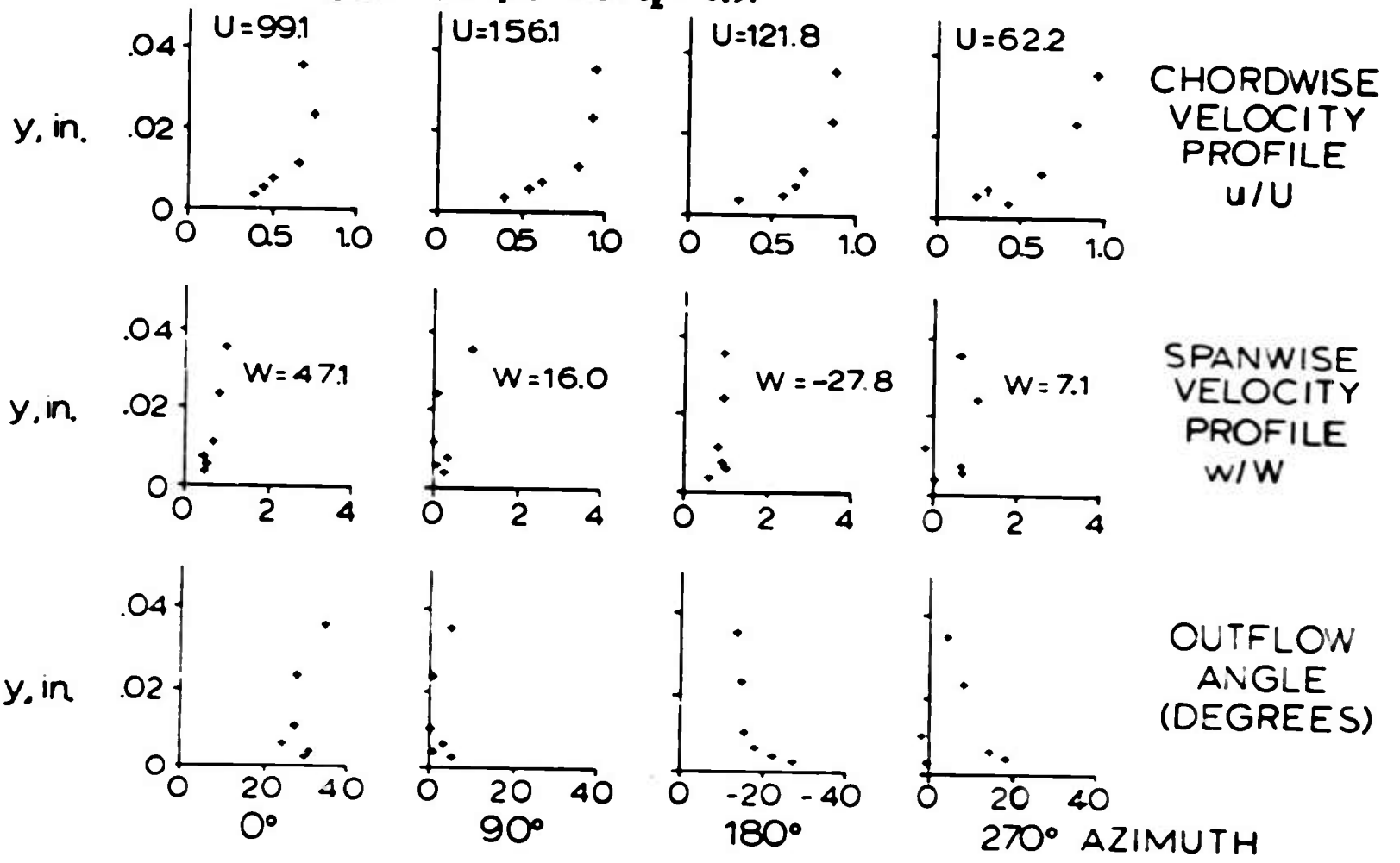

Figure 114. Velocity Data at 63% Radius, 20% Chord, and μ = 0.3.

Rotor Shaft Angle = -10.4°. Blade Pitch = 9.4°. Rotor Speed = 400 rpm. Mean C_{ℓ} = 0.5.

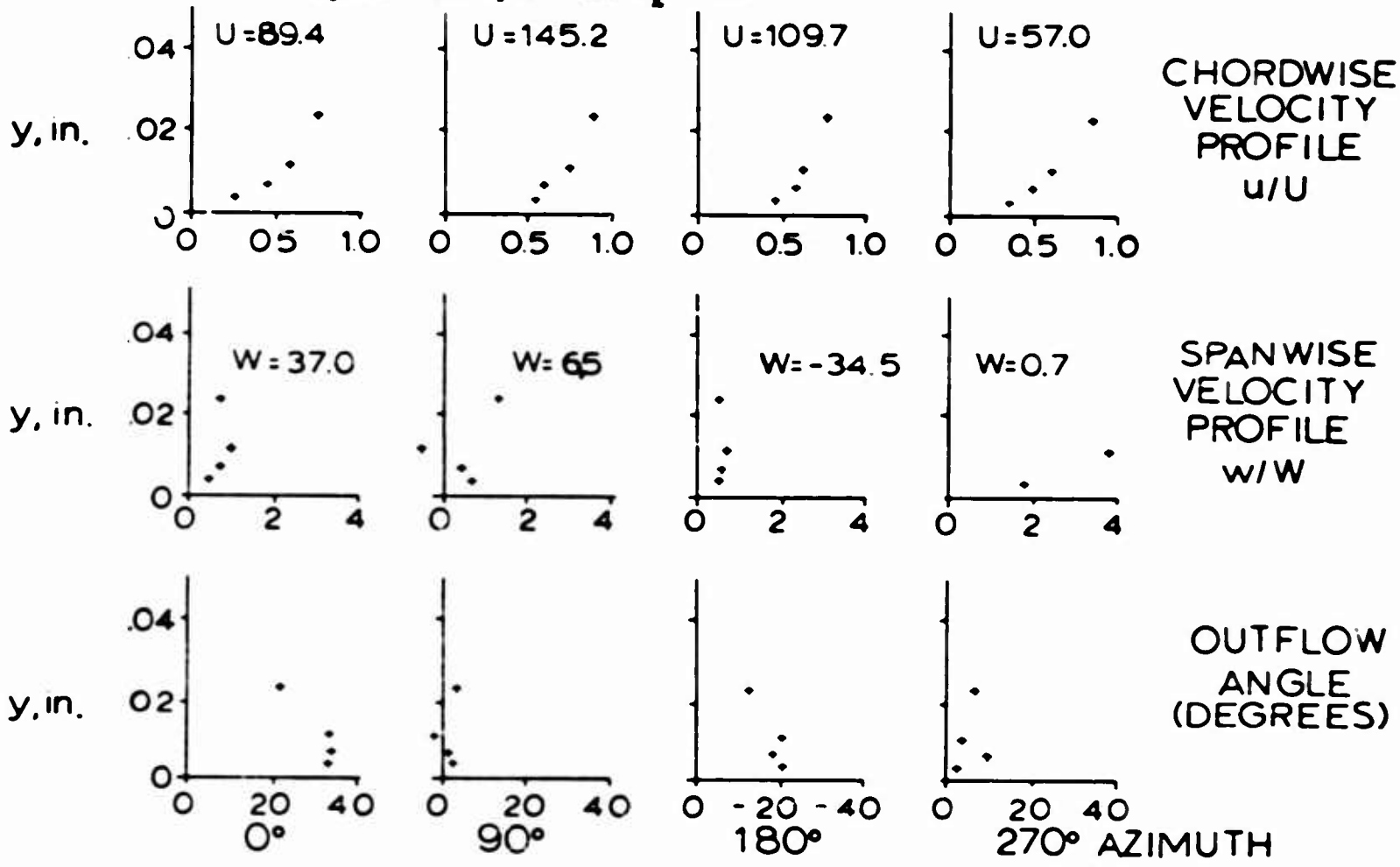

Figure 115. Velocity Data at 63% Radius, 25% Chord, and μ = 0.3.

The chordwise profiles tend to exhibit the usual boundary layer behavior. One point illustrated in the outflow angles is that the flow exhibits a greater outflow at $\phi = 0°$ than the corresponding inflow at $\phi = 180°$. Again, this indicates that the aggregate effects of rotation tend to force the boundary layer flow outward. This outward acceleration tends to increase the outflow angle at $\phi = 0°$ and decrease the inflow angle at $\phi = 180°$.

VII. CONCLUSIONS AND RECOMMENDATIONS

7.1 CONCLUSIONS

1. The hot-wire anemometer instrumentation provided the most significant results of this study. It is believed that data on boundary layer profiles provided by this portion of the study will serve as a foundation for future analytical and experimental research and provide a better base for airfoil design especially suited for rotors. It is believed that over most of the velocity profiles the magnitudes of the velocity were determined to within ± 2% and the flow angles to within ± 2°.

2. The velocity data obtained at a Reynolds number of 158,000 and 10° pitch indicate the presence of a laminar separation and a turbulent reattachment between 20 and 25 percent chord on an NACA 0012 airfoil.

3. The results of the hot-wire study have served to verify the hypothesis of the existence of laminar separation bubbles on rotors. Therefore, these results provide positive substantiation to the conclusions drawn from the ammonia trace studies of this research and those of Velkoff, Blaser, and Jones.[27]

4. The momentum-integral method, combined with the numerical solution technique, provided an accurate engineering approach to three-rotating boundary layer calculations. The comparisons with the so-called "exact" solutions[11] provided sound evidence of the accuracy of this momentum-integral technique.

5. The ammonia flow visualization technique using the revolute film produces higher quality traces than did the oxalid paper used.[22] The ammonia traces can only be used to indicate an averaged boundary layer flow direction; however, the in-hover technique is so simple and inexpensive that the results obtained per time and money spent greatly outweigh the limitations.

6. Pressure data obtained during hover conditions require a larger number of transducers per spanwise location in order to be data worthy of detailed interpretation. Although the simple blade element theory[28] is useful for beginning analyses, it will not predict local angles of attack with sufficient accuracy to calculate two-dimensional pressure distributions.

7. The measurements of the flow around the square tip revealed the presence of a vortex at the end face of the blade, in addition to the expected primary vortex which rolls up at the tip of the blade.

8. The point of inception of the primary tip vortex is a function of the pitch angle, and varies from approximately 30 percent chord at 16° pitch angle to 70 percent chord at 0° pitch angle for the square tip.

9. The magnitude of the boundary layer velocity around the azimuth in forward flight seems to exhibit a consistent behavior when compared to the flow measured just outside the boundary layer. In general, the angle of flow within the boundary layer is always more outward than the external flow, indicating an influence of the centrifugal force within the boundary layer.

10. Analysis of the ammonia traces in forward flight revealed that the use of a hub-located pulse valve did not provide well-defined traces indicating flow direction. It is concluded that the line length and residual ammonia could have contributed to the poor traces obtained.

7.2 RECOMMENDATIONS

1. A number of extensions could be made to the momentum-integral analysis. Among these are the application of this method to rotors with lift, the modification of the theory to allow the axis of rotation to be spaced an arbitrary distance from the blade leading edge, and the addition of a turbulent shear stress variation to more accurately predict the boundary layer trends in real flows.

2. It is recommended that any experimental attempt to measure surface pressures on a rotating airfoil include a minimum of 10 transducers, densely spaced near the leading edge at each spanwise blade position.

3. Since only a small region of the blade was investigated in hovering using the hot-wire probe, it is recommended that the experimental procedures developed during this study be used to provide a complete set of boundary layer information over an entire blade. This investigation should include data in the blade tip region to provide information relative to the formation of the tip vortex. It should include data taken near the root of the blade to attempt to verify the theoretical conclusion that the most significant effects of rotation exist near the center of rotation. Since only a limited number of azimuth positions in forward flight could be reduced and studied in the present study, it is recommended that a much wider range of azimuth positions and radial stations be studied in subsequent research, with particular emphasis given to the retreating blade stall regime.

4. In order to obtain more consistent data in forward flight, it is considered essential to attempt to develop a means whereby the probe height may be adjusted while the flight conditions are maintained.

5. New hot-wire sensors have been released by anemometer manufacturers. These sensors employ gold plating of the wires in the vicinity of the support needles to lessen the adverse heat transfer gradients in this region. The use of these new sensors on the V-configuration probe may allow the application of the "cosine" law during calibration and greatly reduce the vast amount of calibration data. It is hoped that further studies will investigate the improvements offered by this new sensor.

LITERATURE CITED

1. Sears, W. R., POTENTIAL FLOW AROUND A ROTATING CYLINDRICAL BLADE, J. Aero. Sci., Vol. 17, No. 3, 1950, p. 183.

2. Fogarty, L. E.,and Sears, W. R., POTENTIAL FLOW AROUND A ROTATING ADVANCING CYLINDRICAL BLADE, J. Aero. Sci., Vol. 17, No. 9, 1950, p. 599.

3. McCroskey, W. J.,and Yaggy, P. F., LAMINAR BOUNDARY LAYERS ON HELICOPTER ROTORS IN FORWARD FLIGHT, AIAA J., Vol. 6, No. 10, 1968, pp. 1919-1926.

4. Fogarty, L. E., THE LAMINAR BOUNDARY LAYER ON A ROTATING BLADE, J. Aero. Sci., Vol. 18, No. 4, 1951, pp. 247-252.

5. Tan, H. S., ON LAMINAR BOUNDARY LAYER OVER A ROTATING BLADE, J. Aero. Sci., Vol. 20, No. 11, 1953, p. 780.

6. Graham, M. E., CALCULATION OF LAMINAR BOUNDARY LAYER FLOW ON ROTATING BLADES, Ph.D. Thesis, Cornell University, Ithaca, New York, 1954.

7. Rott, N.,and Smith, W. E., SOME EXAMPLES OF LAMINAR BOUNDARY LAYER FLOW ON ROTATING BLADES, J. Aero. Sci., Vol. 23, No. 11, 1956, pp. 991-996.

8. Liu, S. W., THE LAMINAR BOUNDARY LAYER FLOW ON ROTATING CYLINDERS, AFOSR TN 57-298, Parts I and II, Air Force Office of Scientific Research, Arlington, Va., 1957.

9. Banks, W. H. H., and Gadd, G. E., DELAYING EFFECTS OF ROTATION ON LAMINAR SEPARATION, AIAA J., Vol. 1, 1963, pp. 941-942.

10. Velkoff, H. R., A PRELIMINARY STUDY OF THE EFFECT OF A RADIAL PRESSURE GRADIENT ON THE BOUNDARY LAYER OF A ROTOR BLADE, Proceedings of the CAL/USAAVLABS Symposium on Aerodynamic Problems Associated with V/STOL Aircraft, Vol. III, 1966.

11. Dwyer, H. A., and McCroskey, W. J., CROSSFLOW AND UNSTEADY BOUNDARY-LAYER EFFECTS ON ROTATING BLADES, AIAA Paper 70-5, New York, 1970.

12. Young, W. H.,Jr., and Williams, J. C., THE BOUNDARY LAYER ON ROTATING BLADES IN FORWARD FLIGHT, AIAA Paper 70-49, New York, 1970.

13. Young, W. H.,Jr., LAMINAR BOUNDARY LAYER ON A LIFTING ROTOR IN FORWARD FLIGHT, Ph.D. Thesis, North Carolina State University, Raleigh, North Carolina, 1970.

14. Himmelskamp, H., PROFILUNTERSUCHUNGEN AN EINEM UMLAUFENDEN PROPELLER, Mitteibungen der Max-Planck Institut, No. 2, 1950.

LITERATURE CITED (Continued)

15. Harris, F. D., PRELIMINARY STUDY OF RADIAL FLOW EFFECTS ON ROTOR BLADES, J. Am. Helicopter Soc., Vol. 11, No. 1, 1966.

16. Schlichting, H., BOUNDARY LAYER THEORY, New York, N.Y., McGraw-Hill, 1960.

17. Pohlhausen, K., ZUR NAHERUNGSWEISEN INTEGRATION DER DIFFERENTIAL-GLEICHUNGEN DER LAMINAREN GRENZSCHICHT, ZAMM, Vol. I, 1921, pp. 252-268.

18. Cooke, J. C., ON POHLHAUSEN'S METHOD WITH APPLICATION TO A SWIRL PROBLEM OF TAYLOR, J. Aero. Sci., Vol. 19, 1952, pp. 486-490.

19. Prandtl, L., ON BOUNDARY LAYERS IN THREE-DIMENSIONAL FLOW, Min. Air. Prod. Repts. and Transl., Vol. 64, 1946.

20. Taylor, G. I., THE BOUNDARY LAYER IN THE CONVERGING NOZZLE OF A SWIRL ATOMIZER, Quart. J. Mech. and Appl. Math., Vol. 3, 1950, pp. 129-139.

21. Ralston, W., MATHEMATICAL METHODS FOR DIGITAL COMPUTERS, New York, N.Y., Wiley, 1960, pp. 95-109.

22. Mager, A., GENERALIZATION OF BOUNDARY LAYER MOMENTUM-INTEGRAL EQUATIONS TO THREE-DIMENSIONAL FLOWS INCLUDING THOSE OF A ROTATING SYSTEM, NACA Rept. 1067, 1952.

23. Theodorsen, T., and Garrick, I. E., GENERAL POTENTIAL THEORY OF ARBITRARY WING SECTION, NACA TR 452, 1933.

24. Abbott, I. H., and von Doenhoff, A. E., THEORY OF WING SECTIONS, New York, N.Y., Dover Publications, 1959.

25. Hoffman, J. D., A STUDY OF BOUNDARY LAYER FLOW OF HELICOPTER ROTOR BLADE TIPS, Master's Thesis, Ohio State University, Columbus, Ohio, 1971.

26. Champagne, F. H., Sleicher, C. A., and Wehrmann, O. H., TURBULENCE MEASUREMENTS WITH INCLINED HOT-WIRES, J. Fluid Mech., Vol. 28, Part 1, 1966, pp. 153-175.

27. Velkoff, H. R., Blaser, D. A., and Jones, K. M., BOUNDARY LAYER DISCONTINUITY ON A HELICOPTER ROTOR BLADE IN HOVERING, AIAA J. of Aircraft, Vol. 8, No. 2, 1971, pp. 101-107.

28. Gessow, A., and Myers, G. C., Jr., AERODYNAMICS OF THE HELICOPTER, New York, N.Y., Macmillan Company, 1952.

LITERATURE CITED (Continued)

29. Wills, J. A. B., THE CORRECTION OF HOT-WIRE READINGS FOR PROXIMITY TO A SOLID BOUNDARY, J. Fluid Mech., Vol. 12, Part 3, 1962, pp. 388-396.

30. Goldstein, S., MODERN DEVELOPMENTS IN FLUID DYNAMICS, New York, N.Y., Dover Publications, Inc., Vol. 1, 1965, pp. 251-252.

31. Batchelor, G. K., AXIAL FLOW IN TRAILING LINE VORTICES, J. Fluid Mech., Vol. 20, 1964, p. 649.

32. Spivey, Richard F., BLADE TIP AERODYNAMICS - PROFILE AND PLANFORM EFFECTS, paper presented at the 24th Annual National Forum of the American Helicopter Society, May, 1968.

33. Piziali, R., and Trenka, A., AN EXPERIMENTAL STUDY OF BLADE TIP VORTICES, Cal Report No. AC-2647-S-1, Buffalo, New York, January, 1970.

34. Spivey, W. A., and Morehouse, G. G., NEW INSIGHTS INTO THE DESIGN OF SWEPT-TIP ROTOR BLADES, paper presented at 26th Annual National Forum of the American Helicopter Society, Washington, D.C., June, 1970.

35. Carter, C. C., SIMPLE AERODYNAMICS AND THE AIRPLANE, New York, N.Y. The Ronald Press Company, 1940, pp. 126-129.

36. Velkoff, H. R., et al., EXPLORATORY STUDY OF THE NATURE OF HELICOPTER ROTOR BLADE BOUNDARY LAYERS, USAAVLABS Technical Report 69-50, U. S. Army Aviation Materiel Laboratories, Fort Eustis, Virginia, July, 1969, AD 860689.

APPENDIX I
CALIBRATION OF THE HOT-WIRE FLOW JET

In order to use the hot-wire calibration device shown in Figure 46, the device itself had to first be calibrated. The desired calibration data was to be of the form "air velocity versus chamber pressure". The first approach was to use an anemometer probe which was calibrated by the vendor as a standard reference. However, this approach was abandoned due to insufficient data supplied by the hot-wire probe manufacturer.

It was therefore decided to calibrate the nozzle by the use of a Pitot-static tube. A standard 1/8-inch-diameter probe was obtained, and calibration data were generated. Upon data reduction, it was noted that the nozzle efficiency was near unity at high velocities, but decreased significantly at lower velocities. At this point, the validity of the data became suspect. Since the diameter of the Pitot-static tube was one-third of the exit jet diameter, this method of measurement was believed to be altering the jet flow to the extent that the static pressure ports were prone to error. That is, the jet was forced to expand around the probe which presented diverging streamlines at the static pressure ports. The error introduced by this jet expansion is similar to a misalignment of the probe as discussed by Goldstein.[30]

The calibration data reduction indicated that nozzle efficiencies of 100 percent were evident over the full range of velocities from 0-500 fps. The 100-percent efficiency is good only to within 0.5 percent due to instrumentation readability and accuracy. Therefore, the isentropic relations could be applied directly to the chamber-to-atmospheric pressure ratio to obtain the exit velocity. The resulting calibration curve is shown in Figure 116.

Additional tests were conducted to define the exit velocity as a function of distance from the exit plane. These data were required to define the allowable band of distances from the exit over which the probe can be calibrated with accurate results. Figure 117 presents the results of these tests. It should be noted that p_o refers to the jet center line total pressure. Three chamber pressure levels were selected arbitrarily to show what effect the pressure level had on the exit jet. The total pressure in the stream is equal to the total pressure in the chamber from the exit plane to approximately 1.0 inch beyond the exit plane. The rate of center line total pressure decay increases with decreasing chamber pressure.

Finally, vertical and horizontal traverses of the exit jet were made using the small total head probe. These data were obtained at a chamber pressure of 50 inches of water, or a velocity of approximately 460 fps. Figure 118 shows the ratio of local velocity to center line velocity as a function of position at various distances from the nozzle exit. The velocity of the jet is nearly uniform at short distances

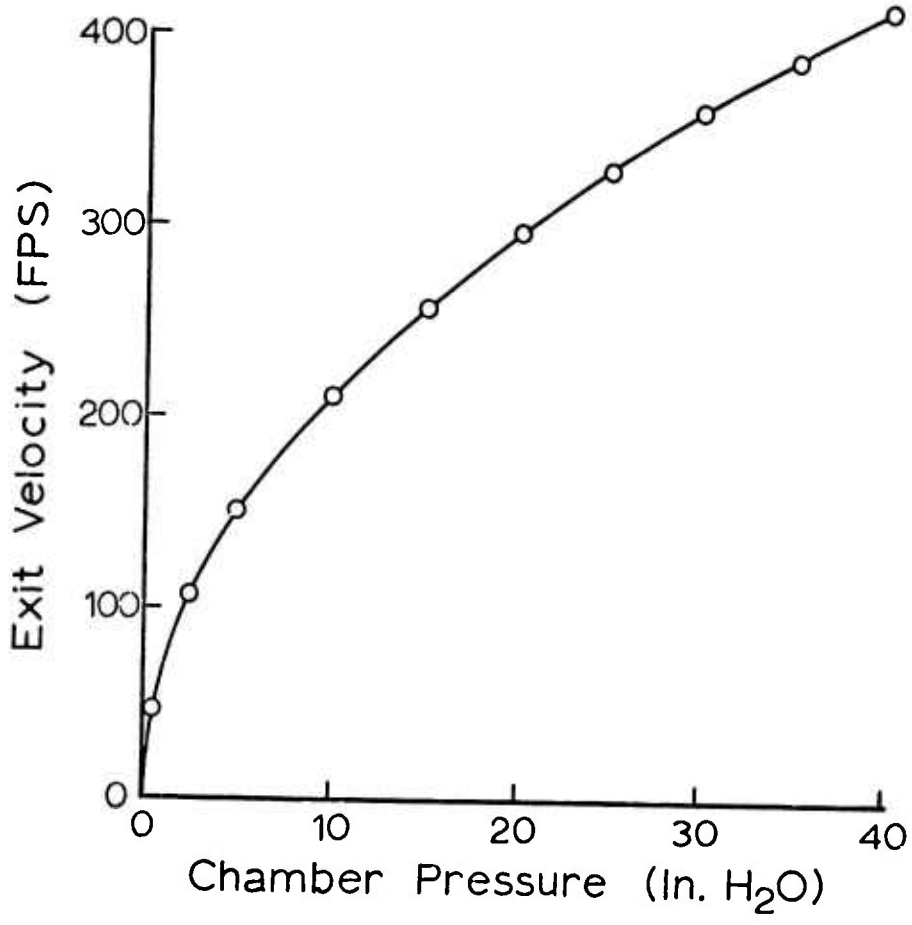

Figure 116. Exit Velocity Versus Chamber Pressure for Hot-Wire Calibration Device.

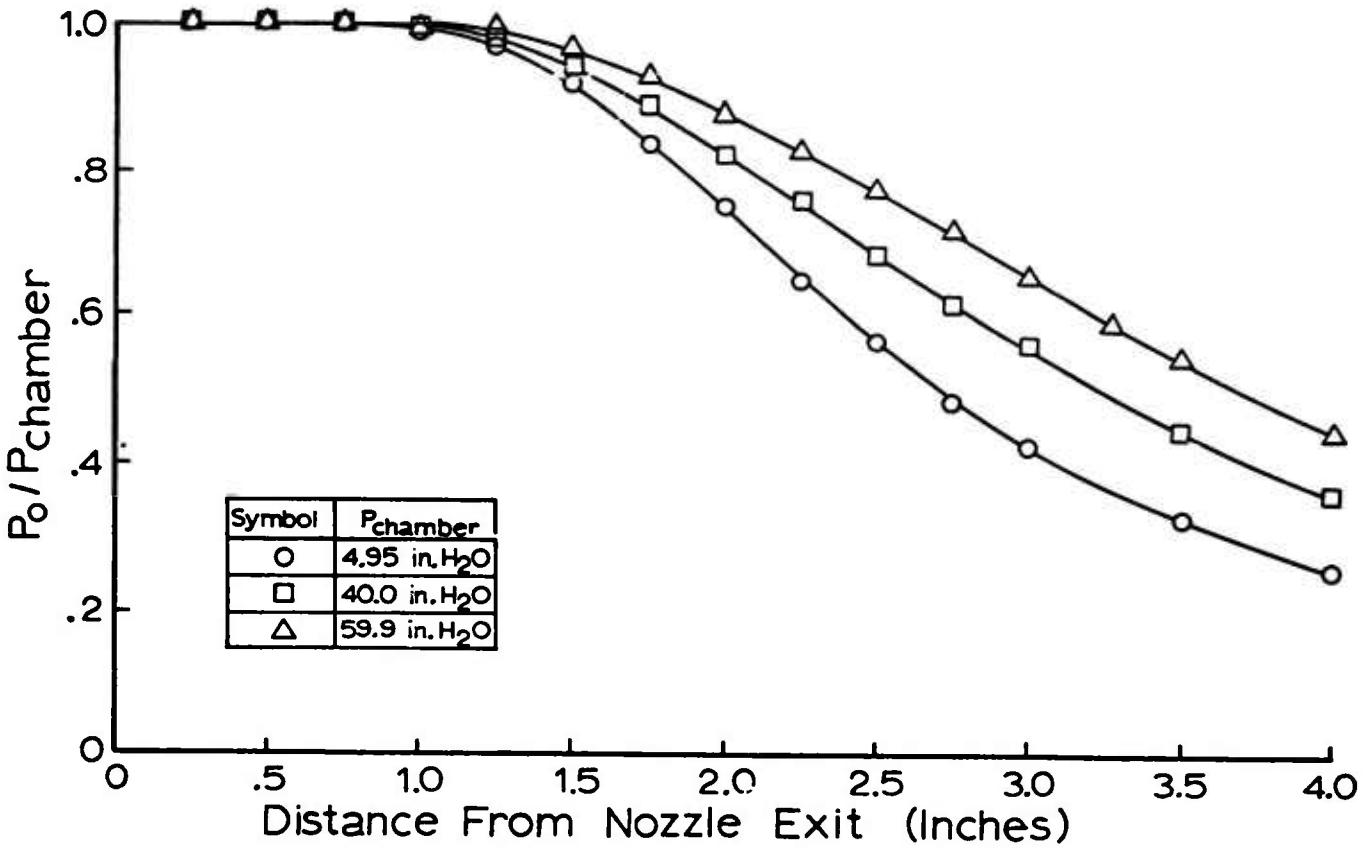

Figure 117. Center Line Pressure Decay Versus Distance From Jet Exit Plane.

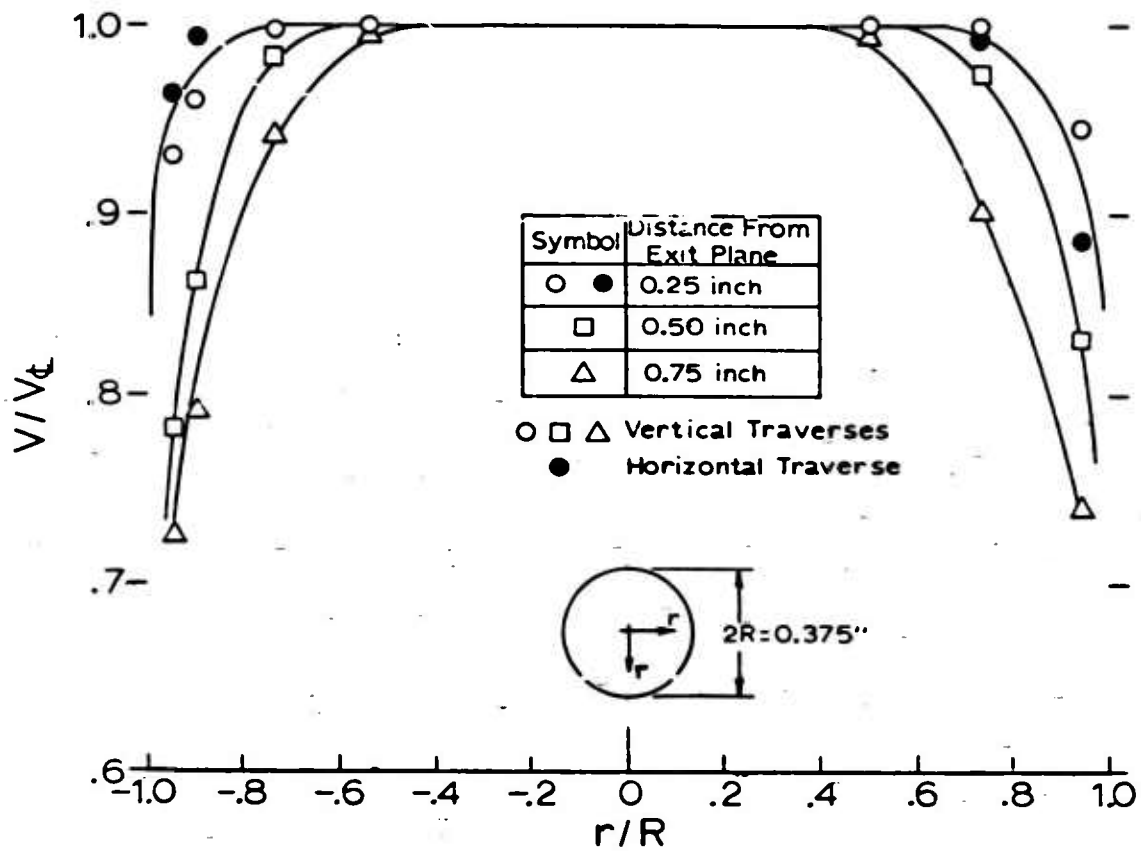

Figure 118. Velocity Profile of Jet at Various Distances From Jet Exit Plane.

from the exit, but starts to approach a parabolic type distribution at greater distances from the exit plane. For example, at 0.25 inch from the exit, the velocity is uniform over 75 percent of the exit area, whereas at 0.75 inch from the exit, the velocity is uniform over only 44 percent of the exit area.

The results of this calibration are as follows:

1. The exit velocity of the calibration nozzle may be calculated from isentropic relations with an accuracy of 0.5 percent.

2. The hot-wire probe must be mounted within 1 inch of the exit plane to maintain the exit plane center line velocity.

3. To assure that the complete hot-wire probe is within the potential core region of the nozzle (area of uniform velocity), the probe should be located at 0.25 inch from the nozzle exit and centered.

APPENDIX II
ADDITIONAL AMMONIA TRACE DATA--HOVER CONDITION

The ammonia trace data presented in Figures 57 through 59 were sufficient to describe the major results of the visualization portion of this study. However, additional trace data in hovering were obtained and are presented in Figures 119 through 124. The data presented in Figures 57 through 59 were obtained at θ = 12° and rotor speeds of 250, 700, and 990 rpm. Again, the ammonia was released at chordwise locations of 5, 10, 15, 20, 25, 30, 35, 40, 50, 60, and 75 percent chord.

The data in Figures 119 through 121 were obtained at θ = 13.5° and rotor speeds of 250, 700, and 920 rpm, respectively. The data in Figures 122 through 124 were obtained at θ = 15° and rotor speeds of 250, 700, and 855 rpm, respectively. Initially, it was hoped that data could be obtained at 1000 rpm; however, the limited hover stand power reduced the maximum rotor speeds to 990, 920, and 855 rpm at blade pitch angles of 12, 13.5, and 15°, respectively.

For the 250 rpm data, the only distinct flow discontinuities occur at 50 percent radius. The 60, 70, and maybe even 80 percent radius traces show indications of increased outflow in the vicinity of 10 percent chord. The most illustrative trace is at 50 percent radius in Figure 119. Although this trace is not as dark as the others in the vicinity of the discontinuity, the trace at 10 percent chord indicates that the flow is practically 100 percent spanwise outflow. This outflow pattern indicates the inconsistency of a small crossflow assumption in the vicinity of laminar separation.

For the ammonia traces at 99 percent radius, the data near the blade tip illustrate the same patterns of flow for all rotor speeds. It seems that the effect of the tip vortex on the rotor boundary layer flow is at most a weak function of rotor speed. The last three chordwise traces near the tip indicate a gradual lessening in the spanwise inflow. Again, this trend is similar in every hover condition at which data was obtained. A possible explanation could be that the tip vortex has started to separate from the blade at this chord position. If so, the effect of the vortex would tend to create an outflow near the blade surface.

The absence of flow discontinuities in the higher Reynolds number data indicates that transition may have occurred prior to the bubble formation. Since the resulting turbulent flow will not support a laminar separation bubble, it will separate in the more conventional and more gradual manner. Near the leading edge (at approximately the 1% chord position), the ammonia traces show a sudden expansion. This pattern of flow was discussed[27] and was hypothesized as the location of transition. If this hypothesis were true, it could explain the absence of discontinuities throughout most of the data.

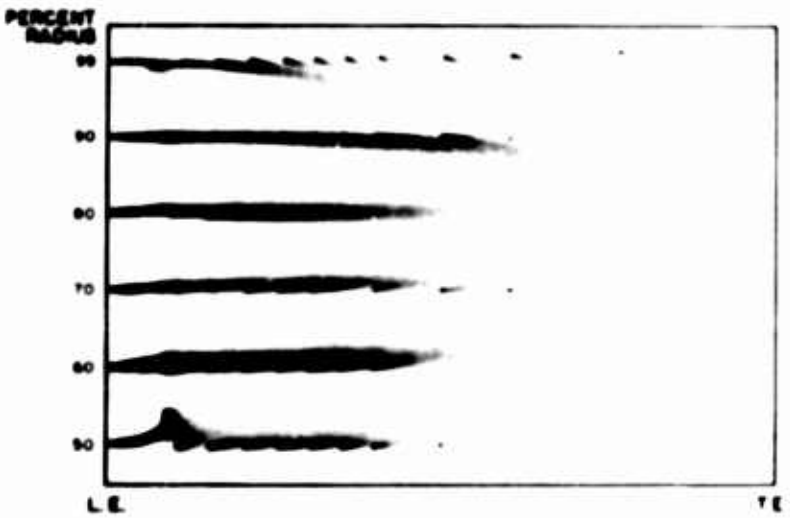

Figure 119. Ammonia Trace Data; θ = 13.5°, 250 rpm.

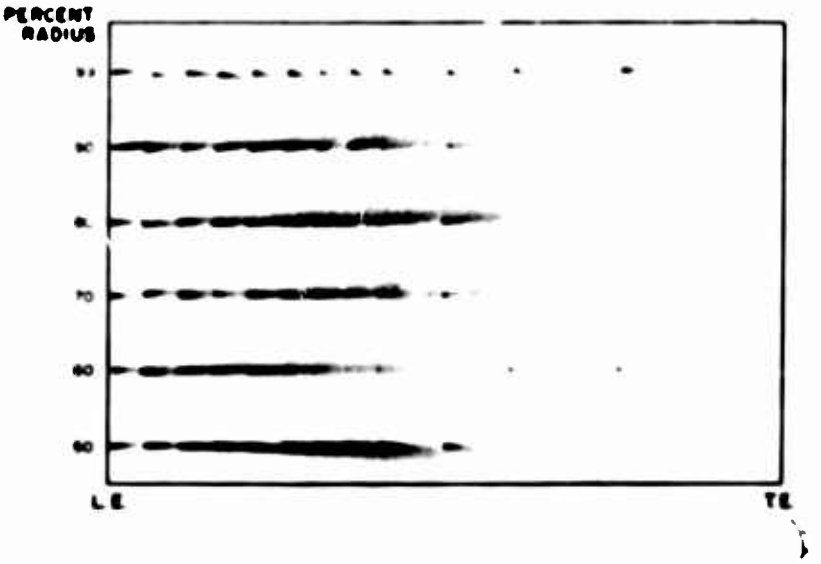

Figure 120. Ammonia Trace Data; θ = 13.5°, 700 rpm.

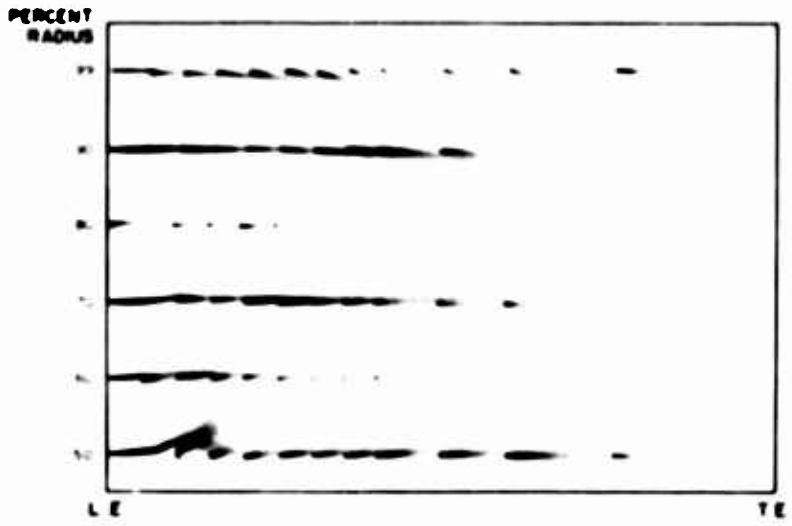

Figure 121. Ammonia Trace Data; θ = 13.5°, 920 rpm.

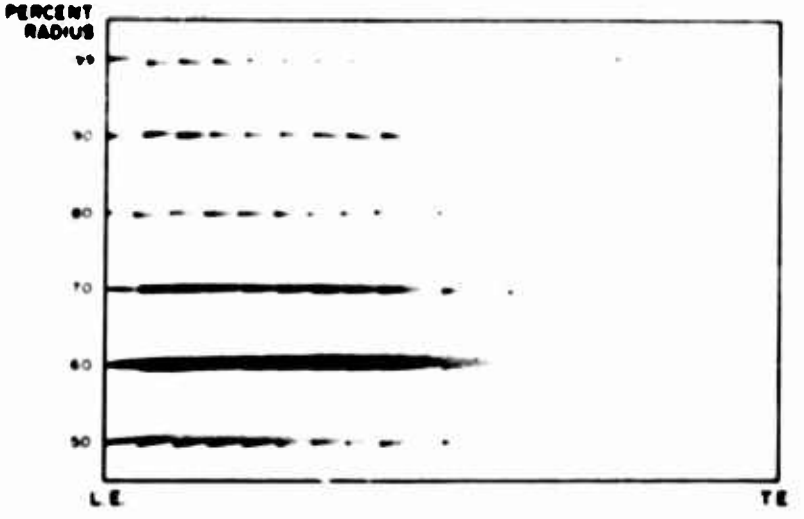

Figure 122. Ammonia Trace Data; $\theta = 15°$, 250 rpm.

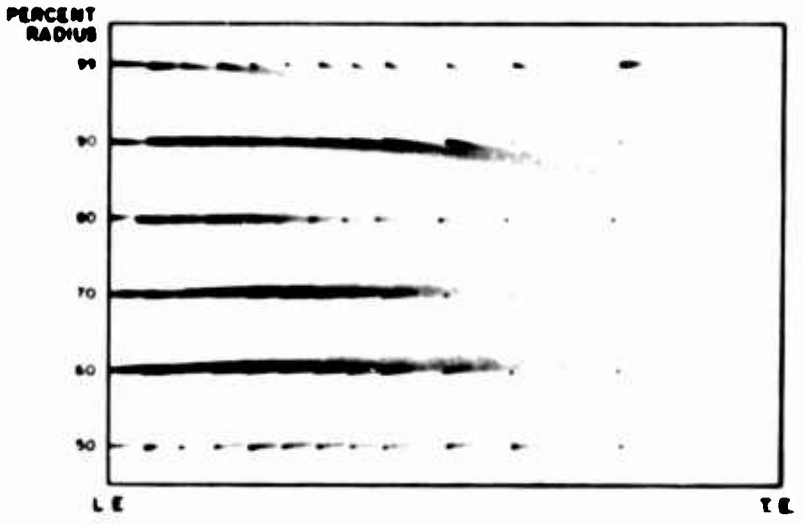

Figure 123. Ammonia Trace Data; θ = 15°, 700 rpm.

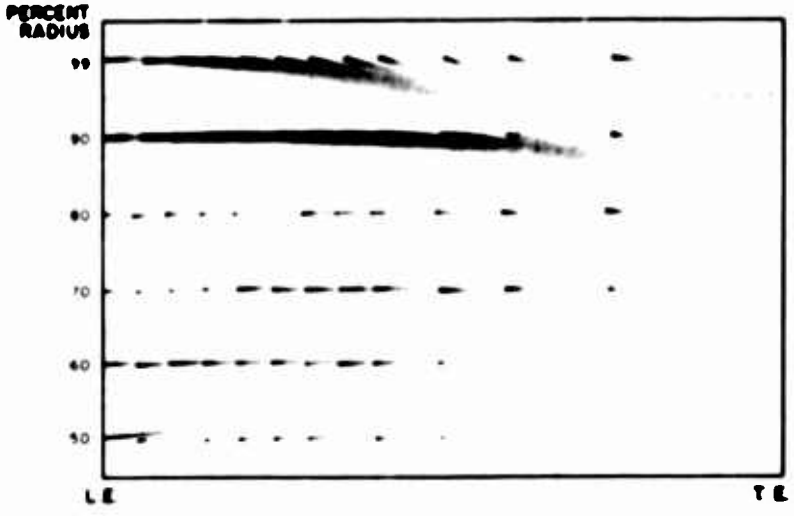

Figure 124. Ammonia Trace Data; θ = 15°, 855 rpm.

APPENDIX III
ADDITIONAL HOT-WIRE VELOCITY DATA--HOVER CONDITION

A large portion of the experimental data obtained in the hot-wire studies of the hovering blade boundary layer are presented in Figures 125 through 134. The form of presentation used is essentially identical to that of Figures 62 and 63. Thus, Figures 125, 126, 62, and 127 present a continuous sequence at 72% radius and 100 rpm; Figures 128, 129, 63, and 130 are a sequence at 72% radius and 400 rpm; Figures 131, 132, 133, and 134 present all data at 92% radius.

The data in Figures 125 through 127 are for pitch angles of 0, 5, and 15°, respectively. At θ = 0°, the chordwise profiles are "full" as the 25 percent chord position is approached. Very little spanwise outflow is observed, indicating that no separation bubble is present. A bubble could exist aft of the 25 percent chord position. At θ = 5°, the chordwise profiles are more similar to separation type profiles at 25 percent chord than the θ = 0° data. Also, at 25 percent chord, the spanwise outflow is quite large, indicating an action similar to the ammonia discontinuities. Next, recall that the data at θ = 10° presented in Figure 62 indicated large outflow at 20 percent chord. Now proceeding to the θ = 15° data of Figure 127, the trend of the hot-wire velocity profile data at 100 rpm can be completed. At this pitch angle, the variation of the chordwise profiles is reversed. That is, the profiles become fuller as the flow progresses from 10 to 25 percent chord. Very little outflow is observed in the spanwise profiles. This could indicate that a separation bubble exists in the flow just prior to the 10 percent chord position and that these data represent the development of reattached turbulent flow aft of the bubble.

The data at 100 rpm and pitch angles of 0, 5, 10, and 15° tend to confirm the trends of the location of the laminar separation bubbles that were observed with the ammonia trace technique. For example, ammonia data are presented[27] for a 4-inch-chord, 6-foot-diameter, NACA 0015 airfoil at 72 percent radius and 400 rpm. These data indicated that laminar separation occurred at chordwise positions of 46, 23, 15, and 10 percent chord at the corresponding pitch angles of 0, 5, 10, and 15°. A reexamination of Figures 125 through 127 and Figure 62 indicates velocity profile trends consistent with these locations of laminar separation.

Next, examine the data presented in Figures 128 through 130. These data were obtained at 72 percent radius, a rotor speed of 400 rpm, and pitch angles of 0, 5, and 15°, respectively. An increase in the boundary layer thickness can be observed in chordwise profiles as the flow progresses from 10 percent chord to 25 percent chord. Note how thin the boundary layer is at the 10 percent chord positions. This is a region of accelerated flow since the chordwise potential velocity is increasing. The θ = 15° data indicate a much increased boundary

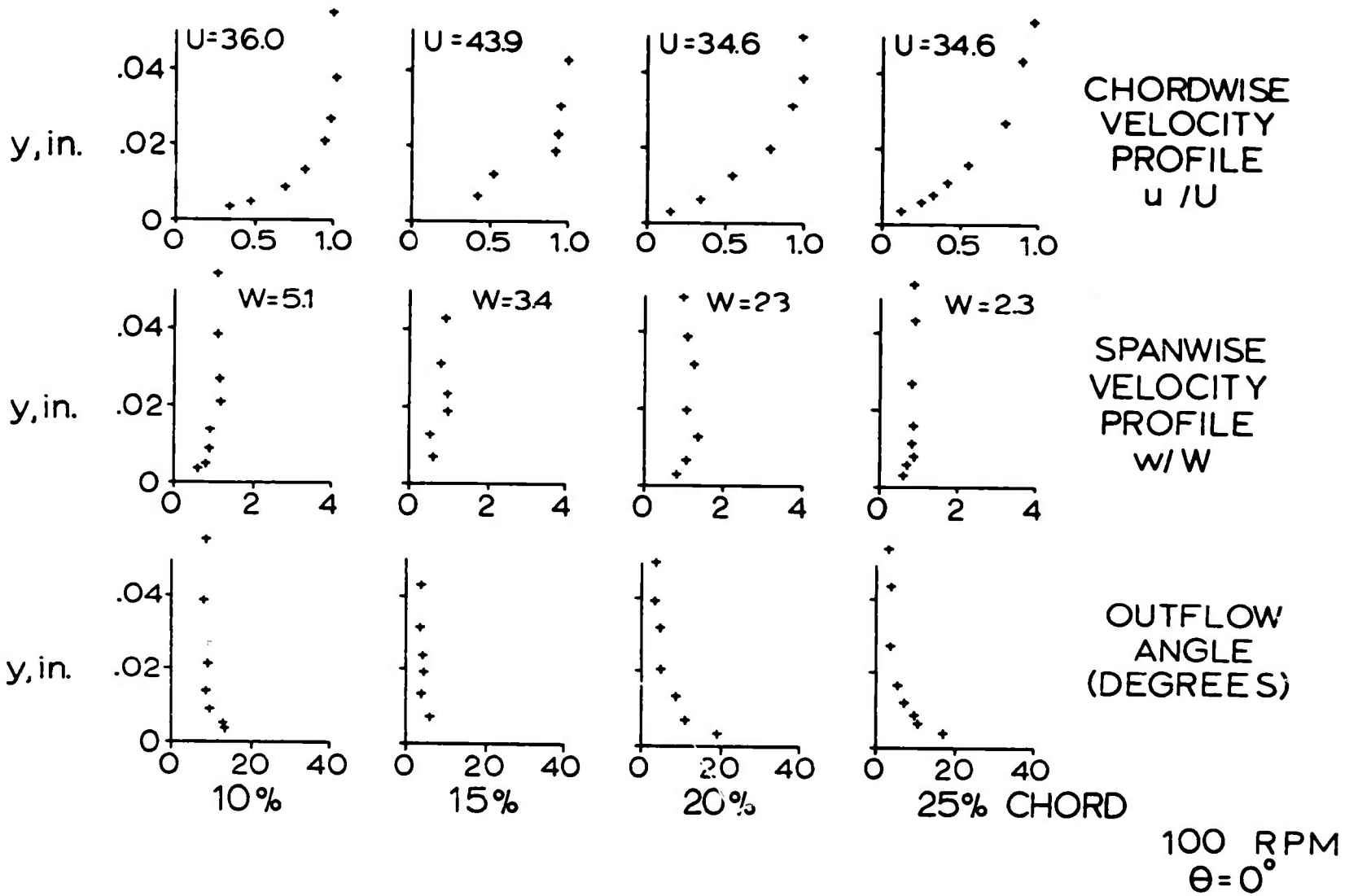

Figure 125. Velocity Data at 72% Radius, $\theta = 0°$, and 100 rpm.

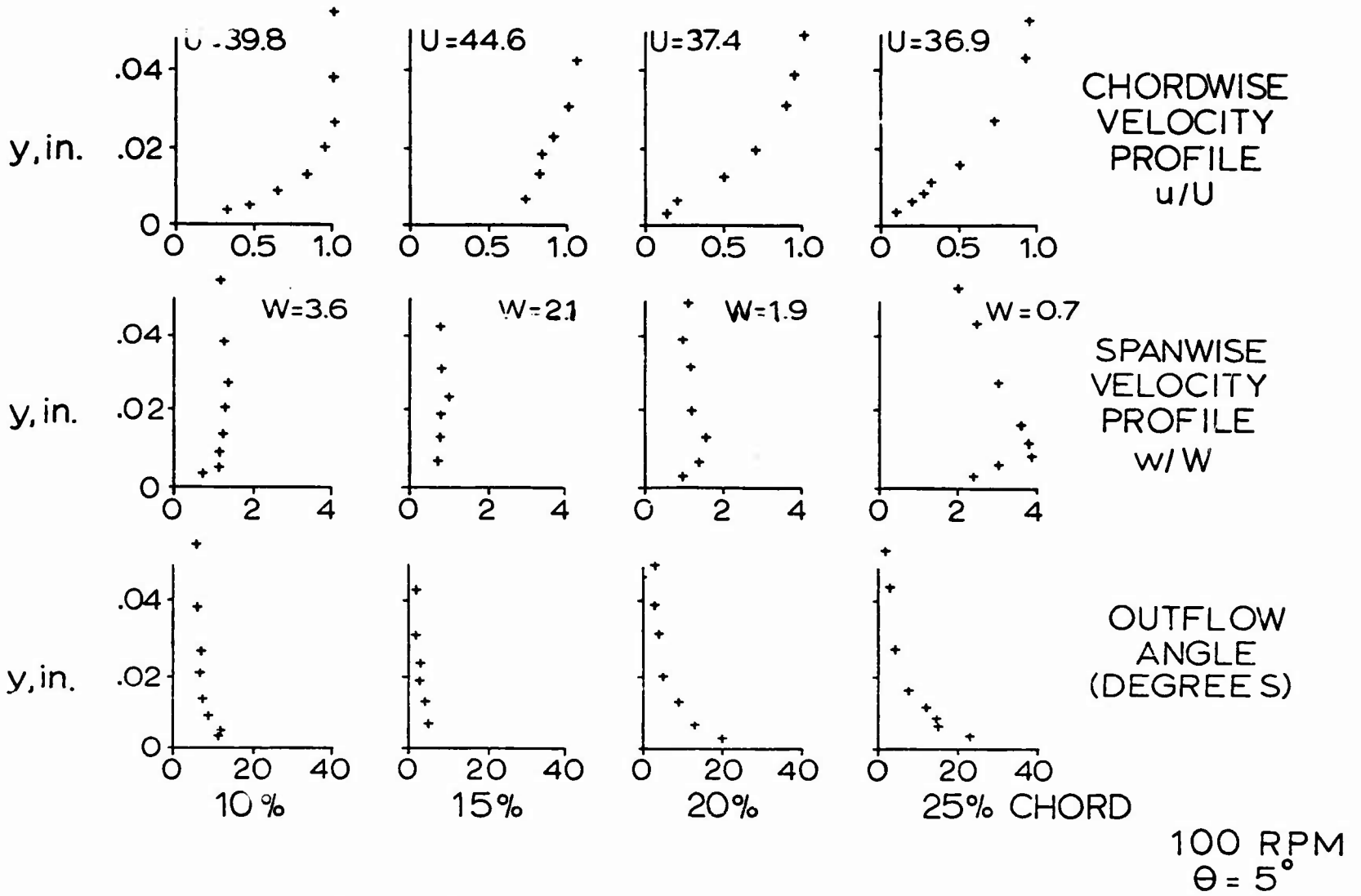

Figure 126. Velocity Data at 72% Radius, θ = 5°, and 100 rpm.

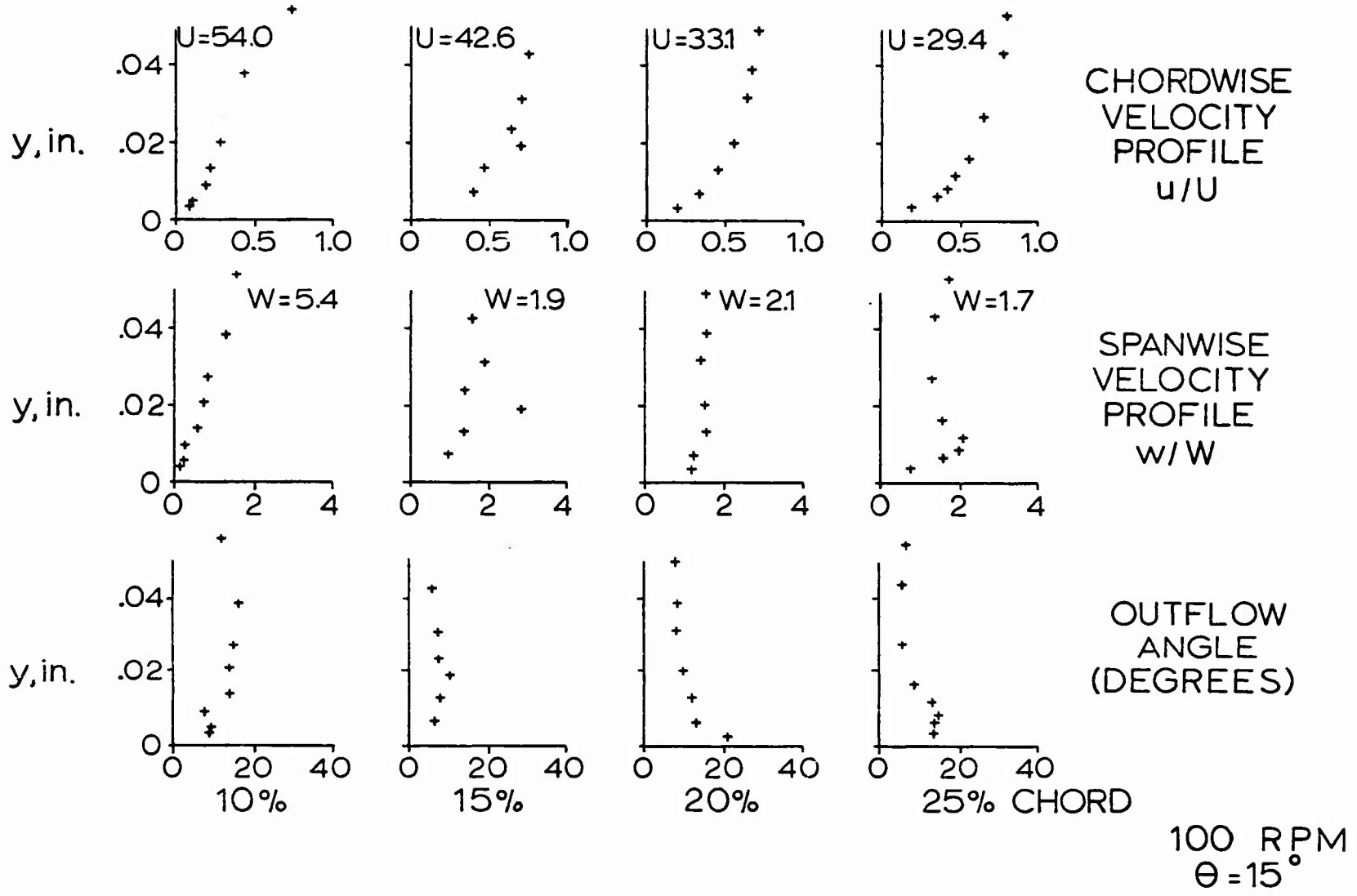

Figure 127. Velocity Data at 72% Radius, θ = 15°, and 100 rpm.

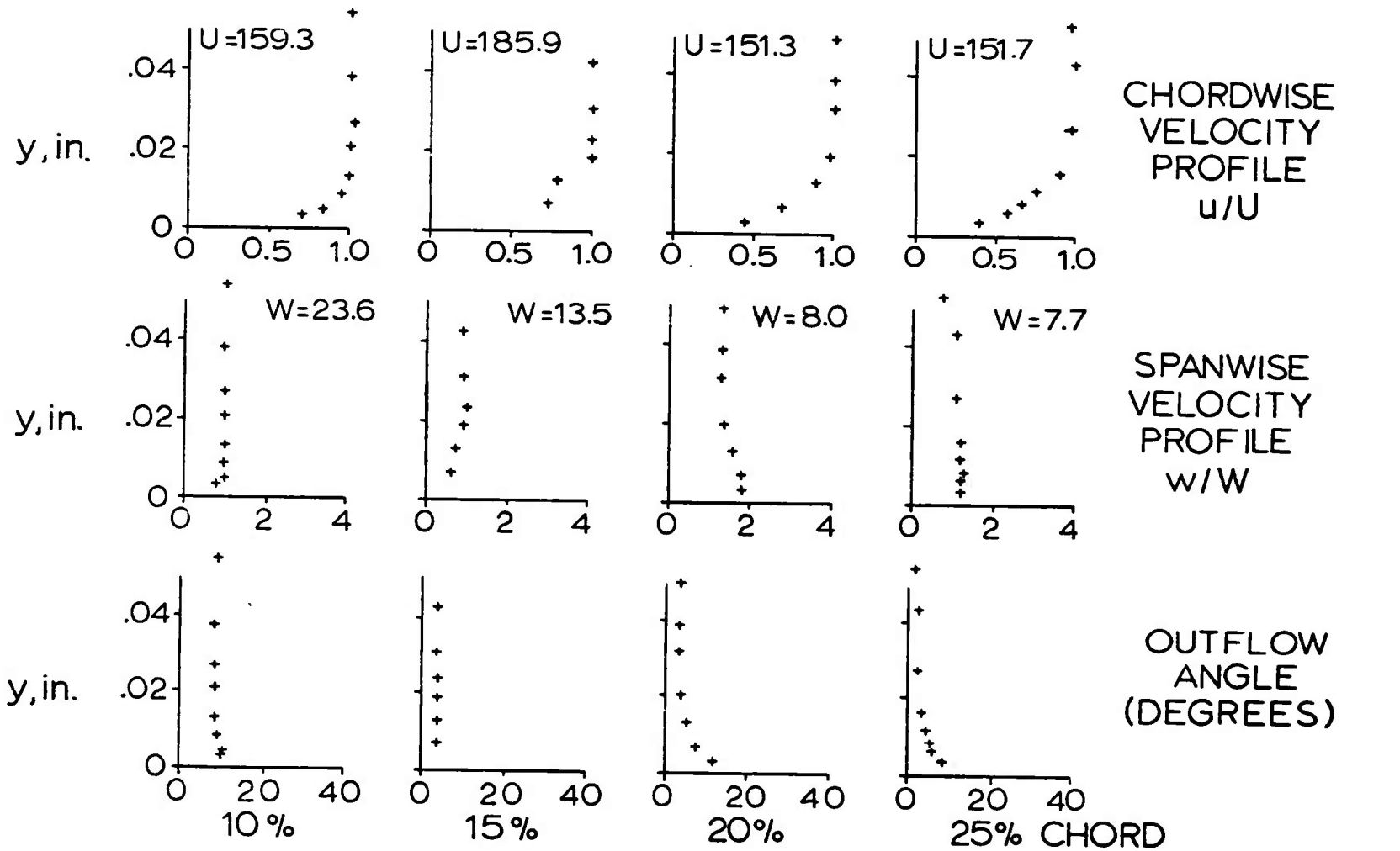

Figure 128. Velocity Data at 72% Radius, θ = 0°, and 400 rpm.

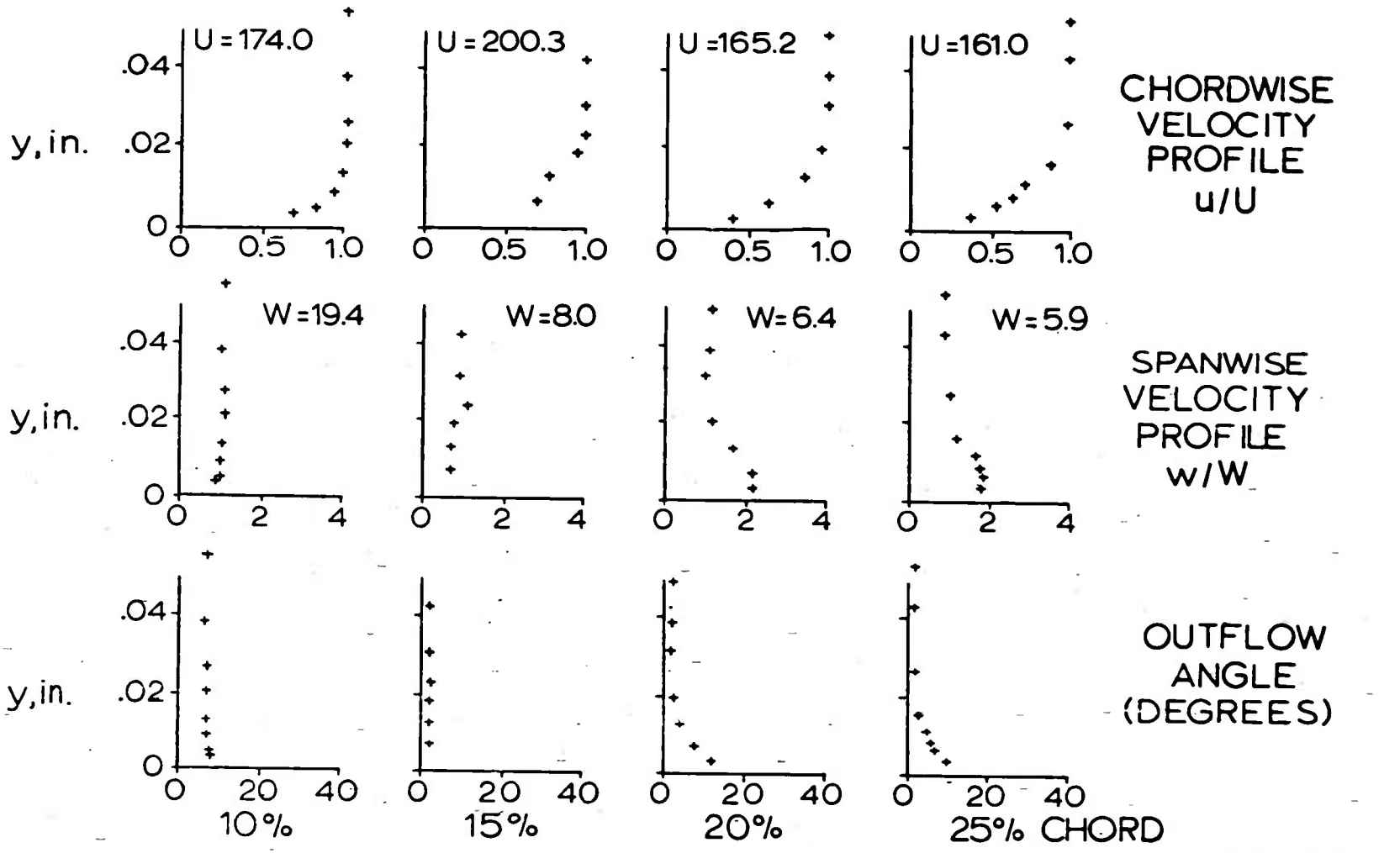

Figure 129. Velocity Data at 72% Radius, θ = 5°, and 400 rpm.

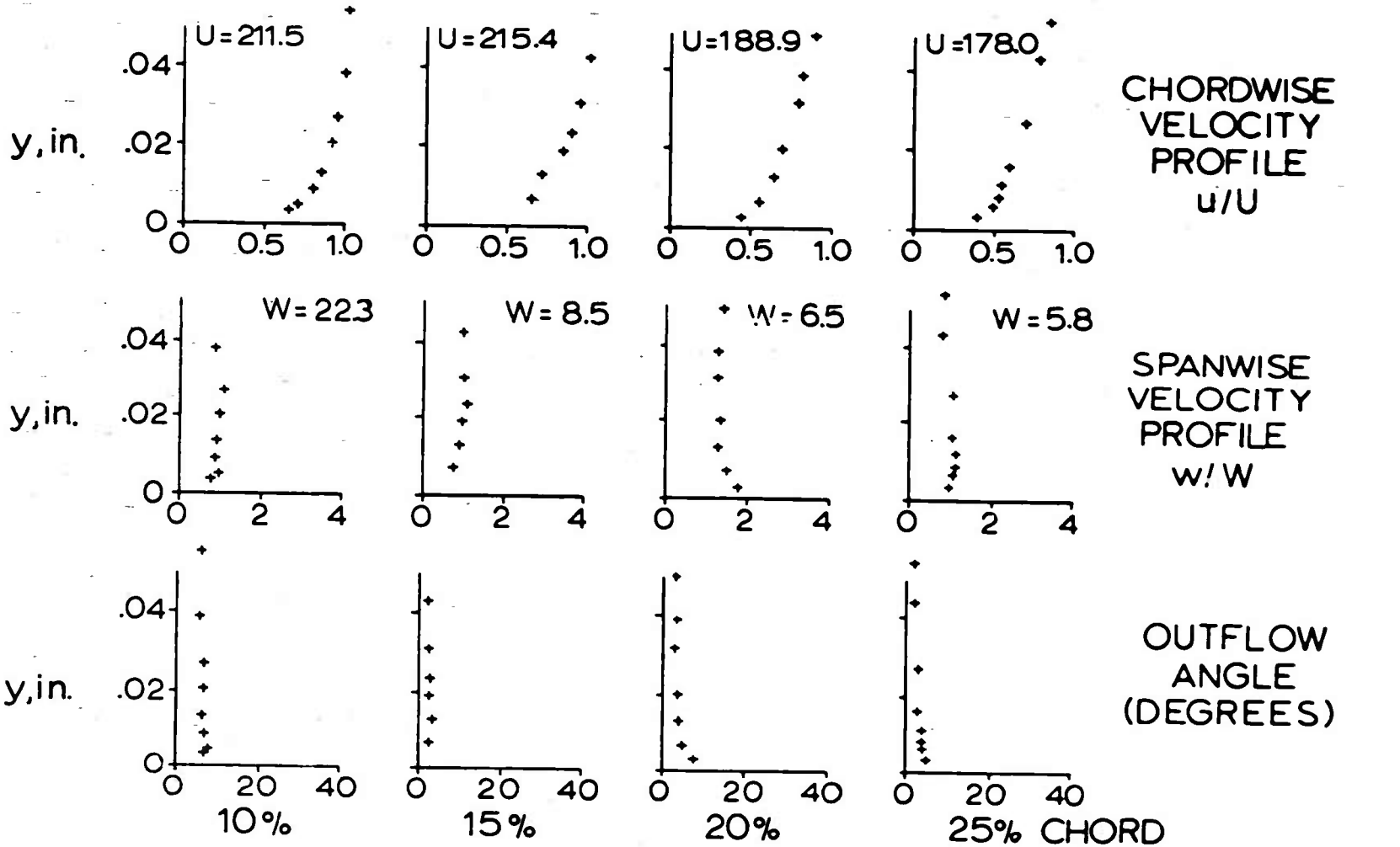

Figure 130. Velocity Data at 72% Radius, θ = 15°, and 400 rpm.

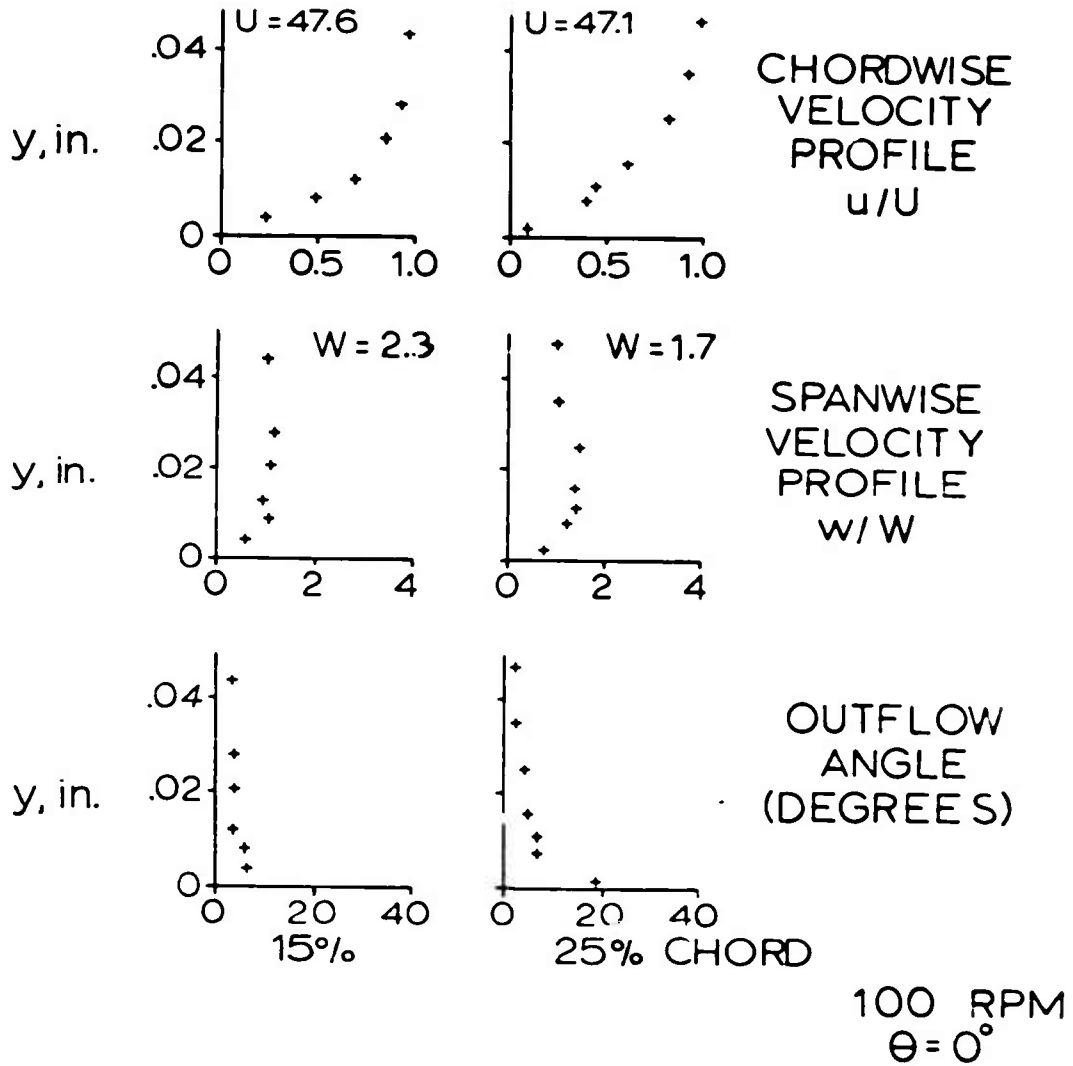

Figure 131. Velocity Data at 92% Radius, θ = 0°, and 100 rpm.

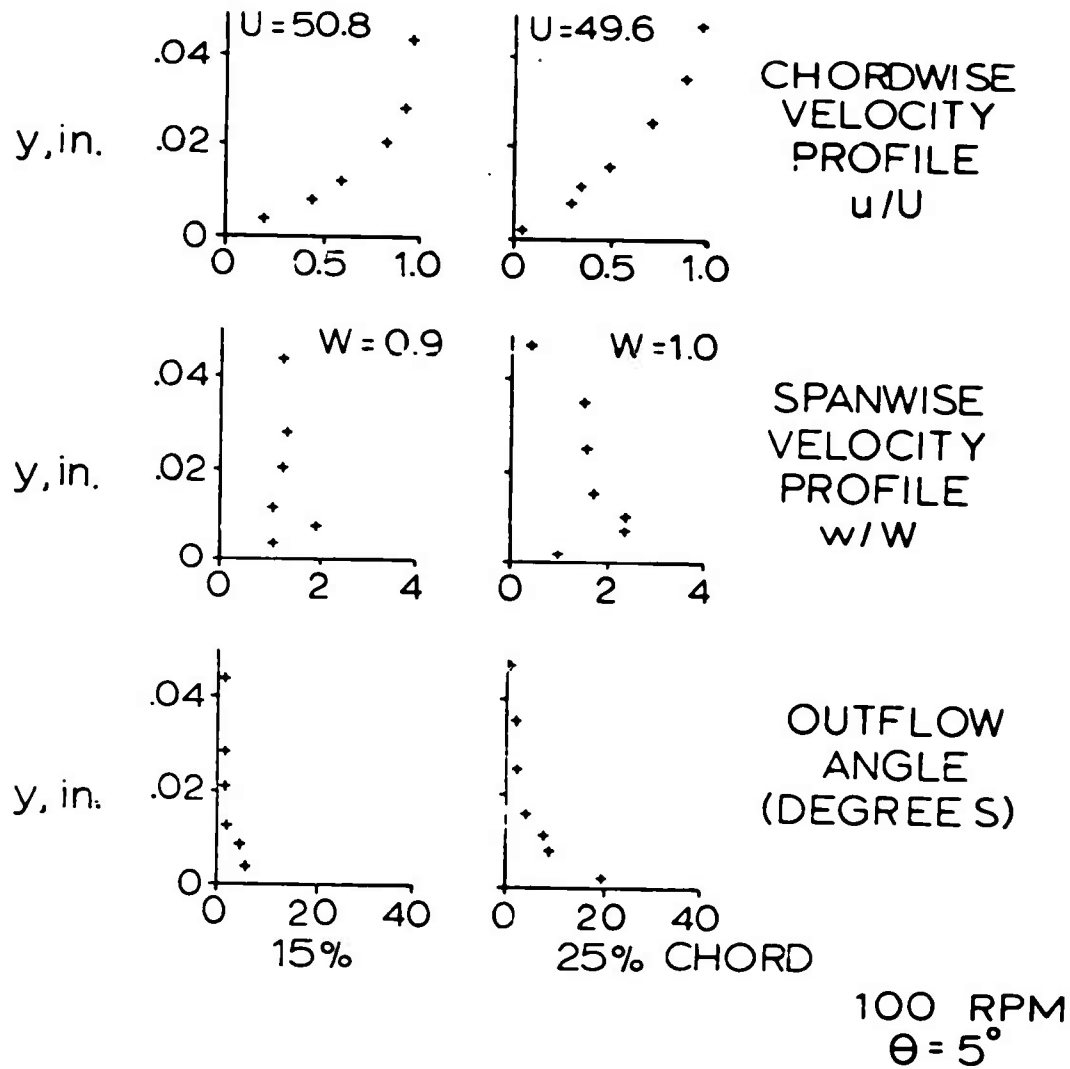

Figure 1 . Velocity Data at 92% Radius, θ = 5°, and 100 rpm.

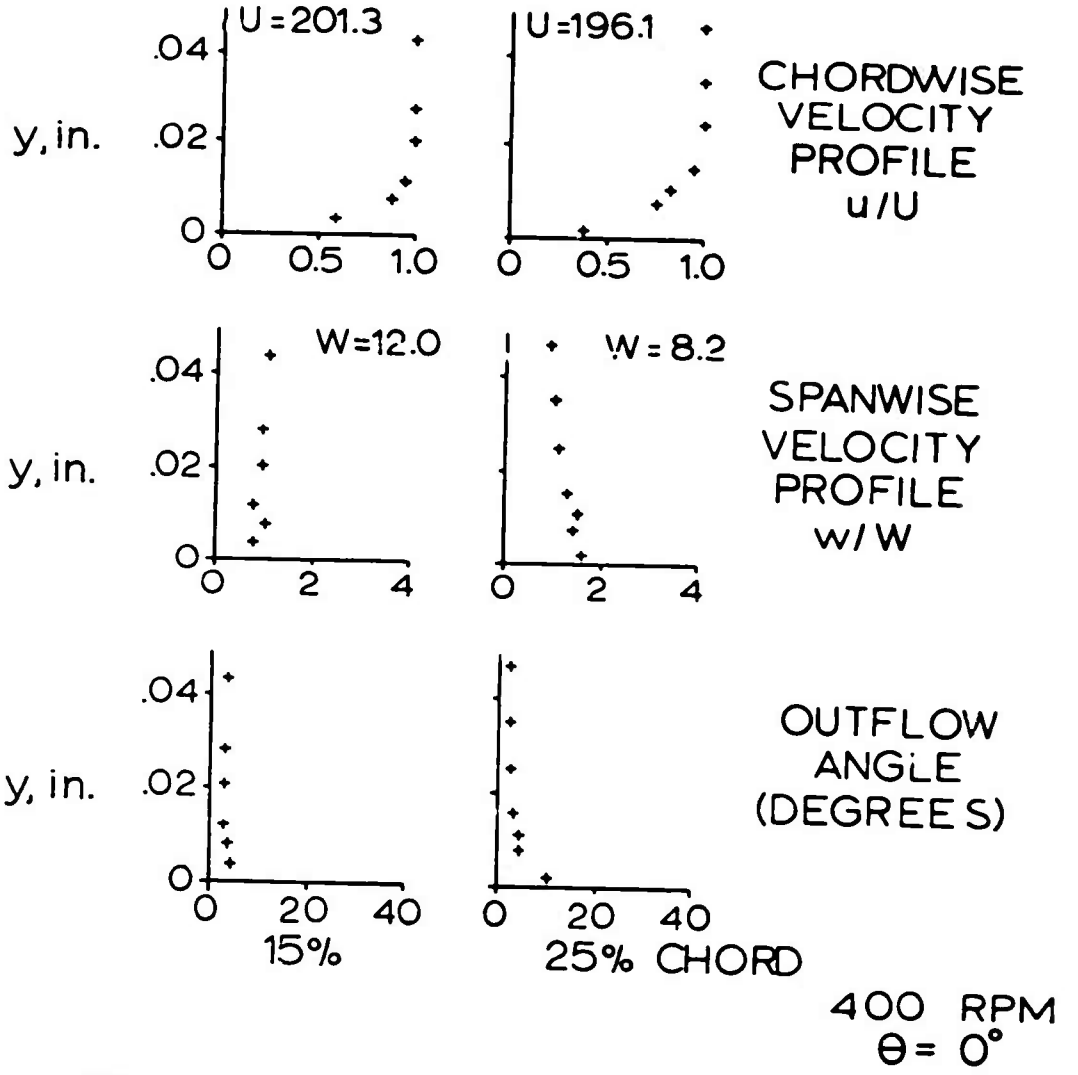

Figure 133. Velocity Data at 92% Radius, θ = 0°, and 400 rpm.

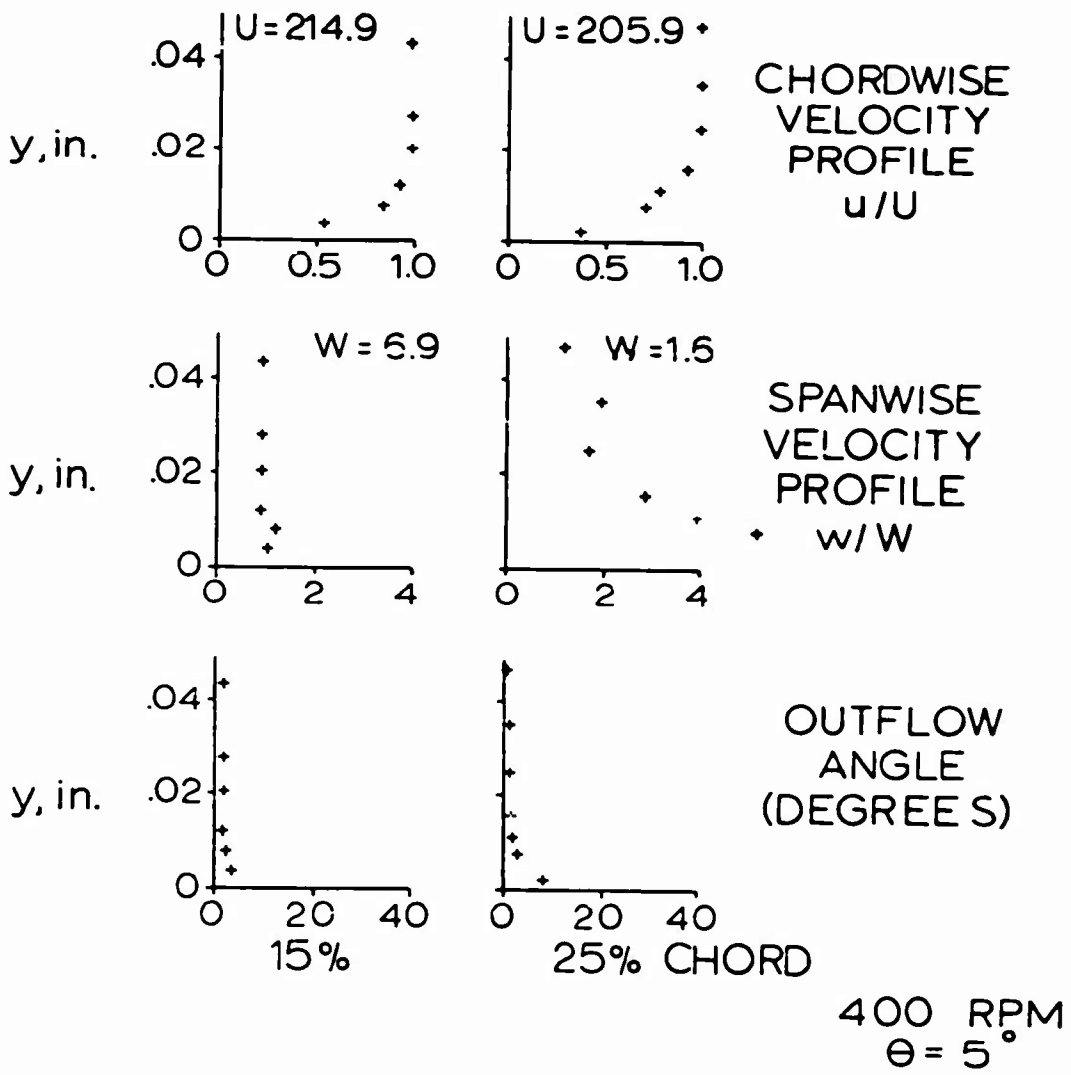

Figure 134. Velocity Data at 92% Radius, θ = 5°, and 400 rpm.

layer thickness; however, there are no indications of extremely large outflow in the 400 rpm data. The data in Figures 128 through 130 and Figure 63 could be aft of the point of transition.

Figures 131 through 134 present data obtained at 92 percent radius. The data in Figures 131 and 132 were obtained at a rotor speed of 100 rpm and pitch angles of 0 and 5°, respectively. Because of the increased spanwise location, these data are similar to data taken at 72 percent radius but at slightly increased rotor speeds. These data were obtained only at chordwise positions of 15 and 25 percent. The data at 92 percent radius indicate trends similar to the data already discussed; however, with only two chordwise positions, these trends are not as obvious. In Figure 134, a large outflow seems to be evident in these data at 25 percent chord. This large outflow may be attributed to the very small value of potential spanwise velocity. Since all velocities were divided by their corresponding potential components, they become quite large as this potential component becomes small.

APPENDIX IV
EVALUATION OF ACCURACY OF HOT-WIRE DATA

Because the findings on the magnitude and direction of the boundary layer flow constitute the most important result of this work, discussion of the possible magnitudes of errors is presented in this section. The main sources of error lie in the calibration of the probe, its use in measurements, and in data reduction.

1. Calibration

a) Readability of the voltmeter

The readability of the voltmeter was 0.01 volt for the high range of data and 0.001 volt for the low range. Using 200 fps (the maximum calibration velocity) as the full range for flow speed, the error can be determined to be (0.01 volt) x (50 fps/volt) - 0.5 fps or about 1% error.

b) Readability of the manometer

The manometer was readable to the nearest 0.05 inch of water at 8.9 inches of water or 200 fps. This represents an error of 0.56% in pressure and an error of 0.75% in velocity.

c) Readability of the protractor

The protractor used for setting and recording the angularity of the probe could be read to the nearest 0.25°, which represents an error of about 0.75% if one uses the maximum calibration angle as the reference (about 40°).

d) Accuracy of the regression curve fit

The numerical curve fit routine was accurate to within 1% for the velocity magnitudes up to 200 fps. The maximum curve fit error for flow angularity was about 2.5% up to angles of ±40°, which represents ±1° error.

2. Testing

a) Rotor speed setting

The rotor speed was only maintained to within about ±3 rpm during testing, which represents 3% error at a speed of 100 rpm. The velocity error introduced due to this rpm error would have been about 1.5 fps.

b) Readability of voltmeter

Readability was identical to that discussed under calibration, except near separation bubbles or at very high pitch angles, when rapid fluctuations in the output required a mental average to be taken.

c) Setting of probe relative to leading edge

The probe body was set perpendicular to the blade leading edge by viewing the probe through a 100X microscope. Through this optical method an angularity of ±0.5° could be obtained accurately. During the tests, centrifugal loads on the probe and probe supports could have caused enough deflection to alter this accuracy; however, the extent is not determinable. Additional error in the data could have been caused by the limited ability to set the plane of the sensors parallel to the surface of the blade. This would induce large errors in the measurements taken very near the blade surface.

3. Data Reduction

a) Interpolation of regression equations

The error due to the computerized interpolation of the regression equations was considerably under 1% and can be neglected.

b) Wall proximity corrections

Some of the error in the measurements near the surface was eliminated by using the results of Wills.[29] The corrections place the velocity profiles near the surface in nearly a straight line, as would be expected.

APPENDIX V
TIP SHAPES

The detailed shapes of the five tips used in the tip flow study are presented in this appendix. The orifice locations where the ammonia was emitted are shown in each figure, and the dimensions to the holes are indicated.

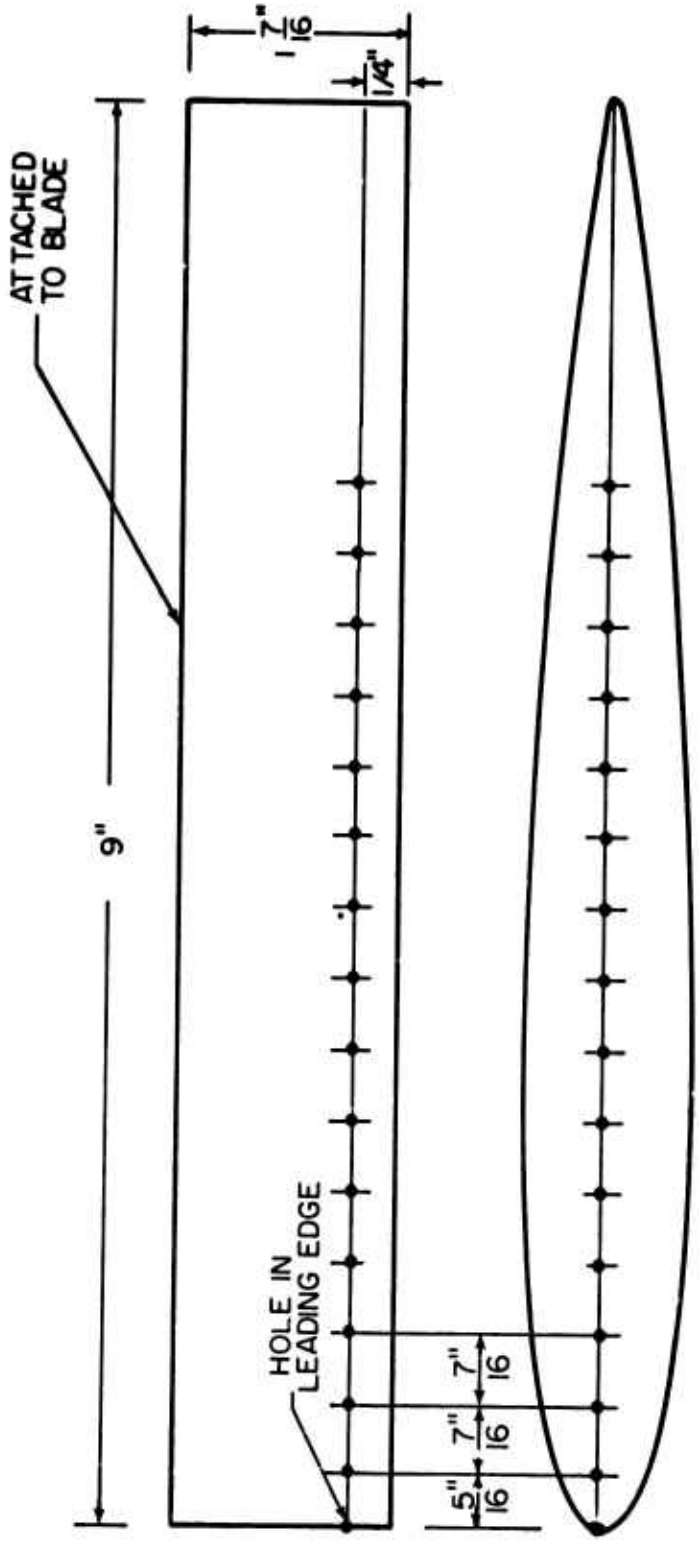

1 SQUARE TIP

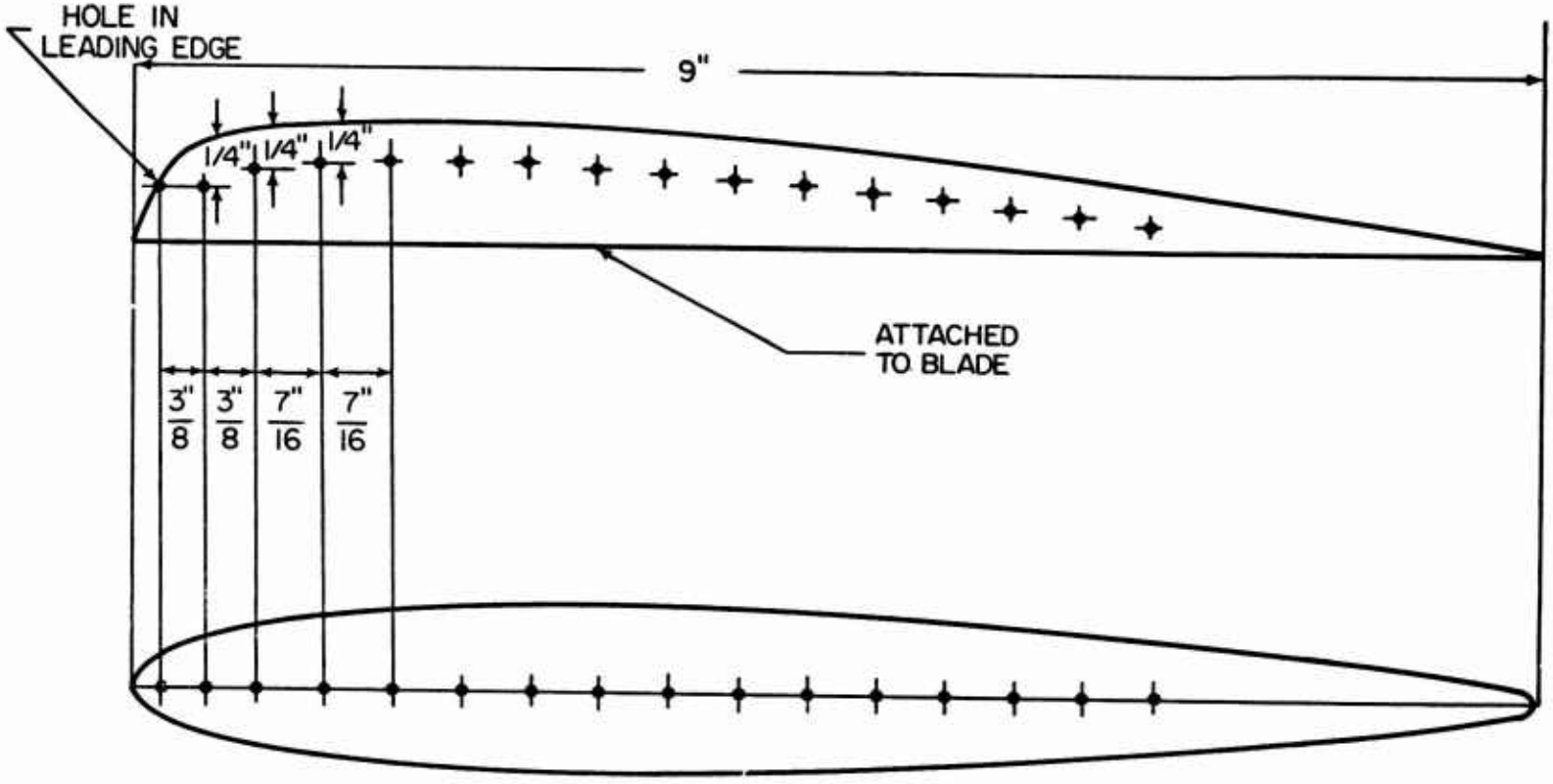

2 STANDARD TIP

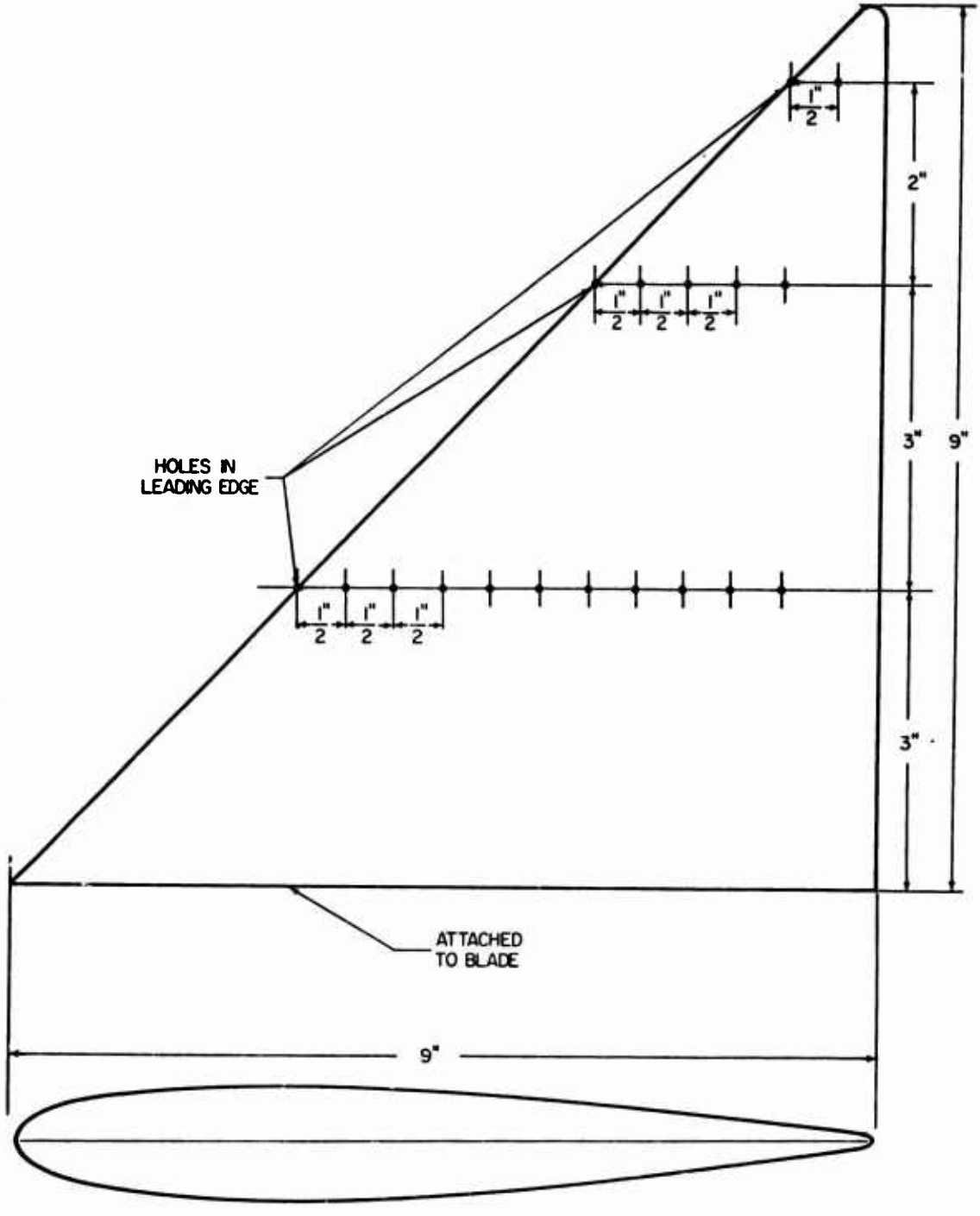

3 SWEPT-AFT TIP

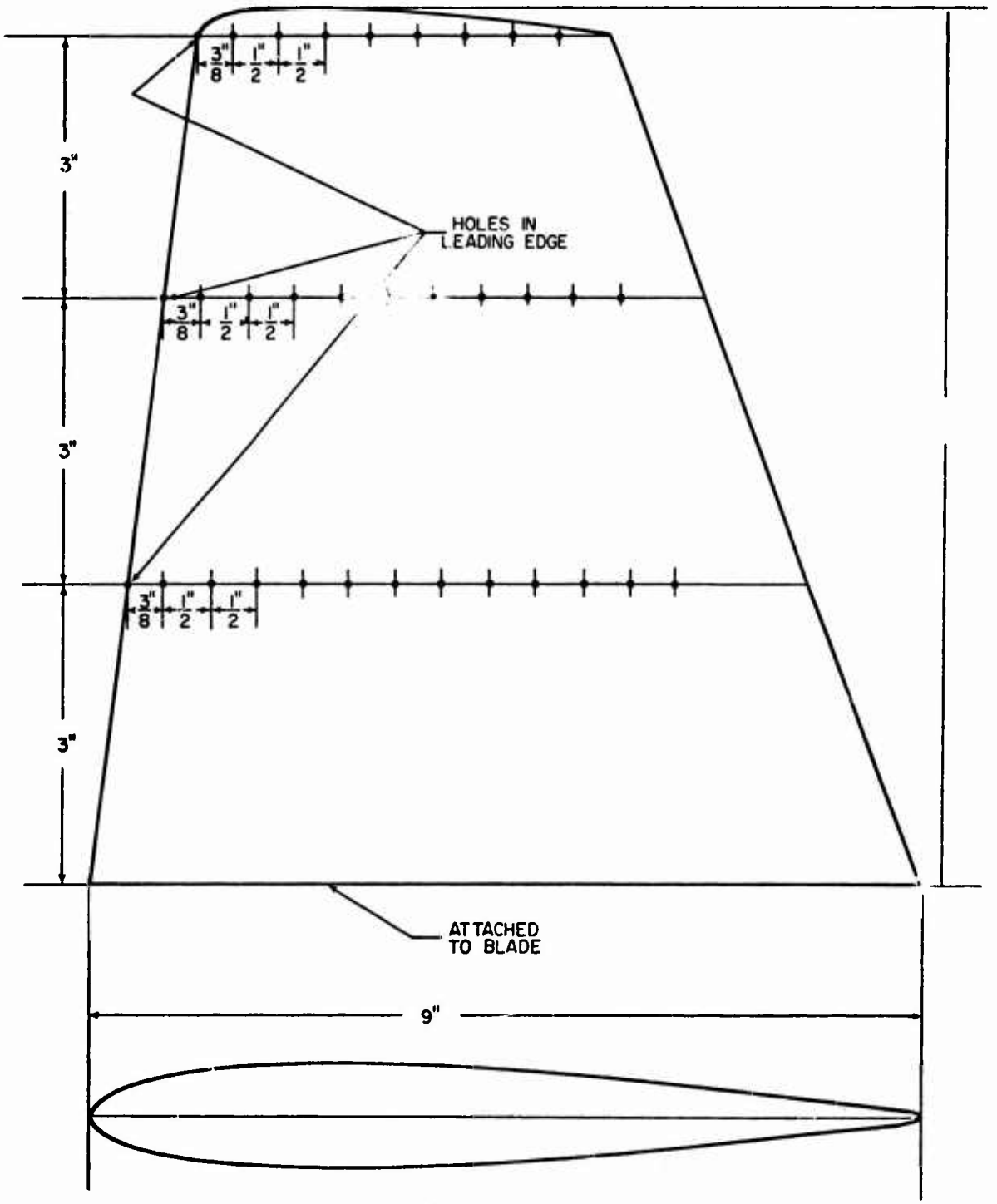

4 TRAPEZOIDAL TIP

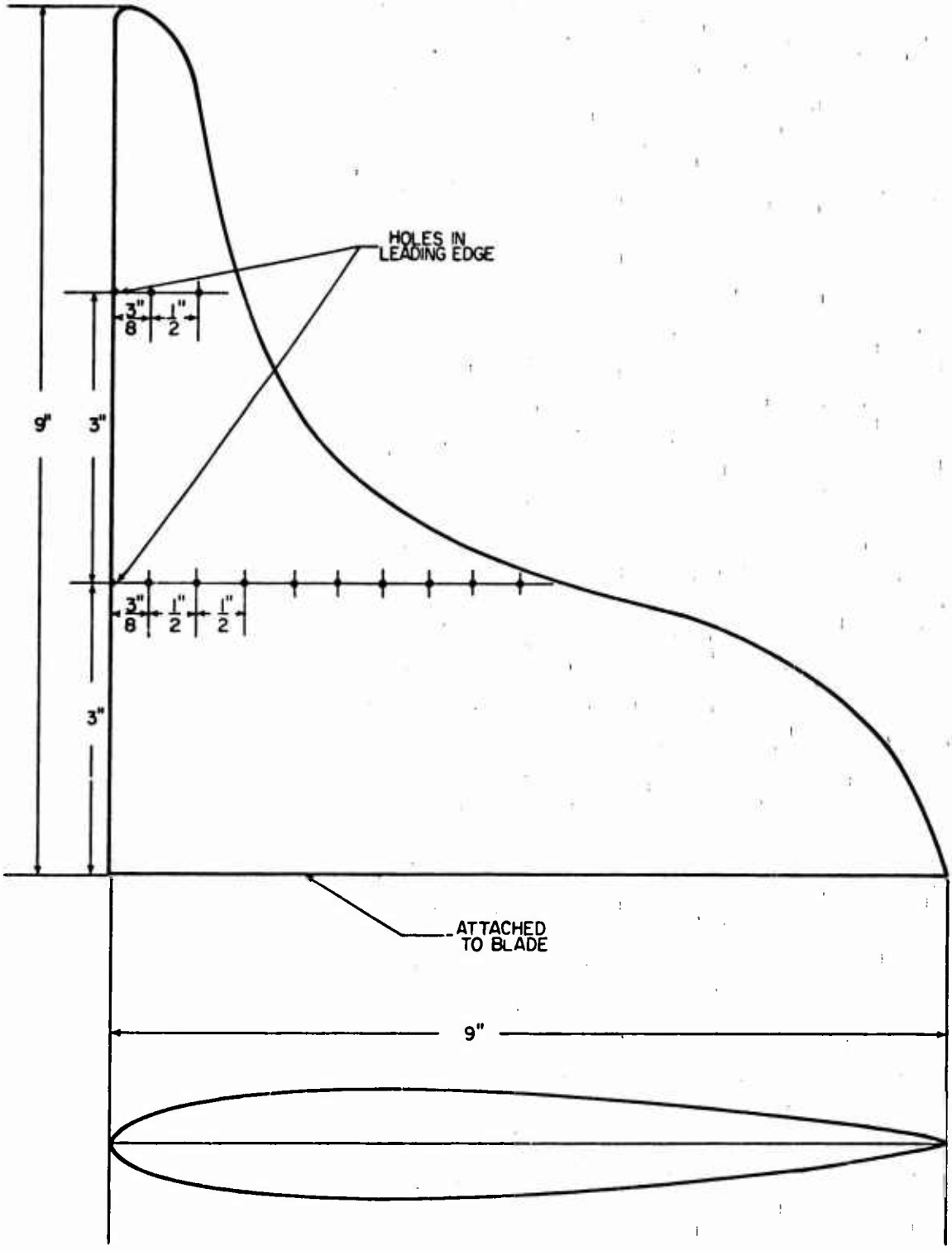

5 CUSPED TIP